Thermophoretic microswimmers: Interplay of phoresis, geometry and hydrodynamics

Inaugural-Dissertation

zur
Erlangung des Doktorgrades
der Mathematisch-Naturwissenchaftlichen Fakultät
der Universität zu Köln
vorgelegt von

Sergi Roca Bonet
aus Barcelona, Spanien

Köln
2021

Berichterstatter:	**PD Dr. Marisol Ripoll Hernando**
(Gutachter)	**Prof. Dr. Andreas Schadschneider**

Tag der mündlichen Prüfung: 18 Juni 2021

“We especially need imagination in science.
It is not all mathematic, nor all logic,
but it is somewhat beauty and poetry.”

Maria Mitchell
1818–1889

Acknowledgements

This thesis only has one author name, but it could not, for sure, be done just by one person. My deepest gratitude goes to my supervisor, PD Dr. Marisol Ripoll, for all her support and guidance through these long years and, ultimately, helping me get rid of the monkey. Thanks for all the scientific discussions, and all the meetings that started with a discussion about a figure and ended up in conversations in the fields of history, cinematography or botanics. Also, thanks for Fiona, she is still happy with us.

I also sincerely thank Prof. Dr. Gerhard Gompper for accepting me as a PhD student in his institute and giving me his support in the joining of the IHRS BioSoft graduate school, and for giving me the opportunity of giving guidance to a summer student. Thanks also to Prof. Dr. Schadschneider for accepting to be a reviewer of this dissertation in so short notice, to Prof. Dr. Annette Schmidt for accepting to be the chairwoman, and to Prof. Dr. Roland Winkler for being the secretary of my committee, along for the lectures on statistical physics. A special thanks goes to Dr. Thorsten Auth for the amazing coordination of BioSoft.

I would like to acknowledge the support of the DFG priority program SPP 1726 on "Microswimmers - from Single Particle Motion to Collective Behaviour" as well as gratefully acknowledge the computing time granted through JARA on the supercomputer JURECA at Forschungszentrum Jülich.

I can not miss to thank Prof. Dr. David Reguera, without whom I will not be writing these words now. I will never forget my fascination the first time I saw that virus. You opened my eyes and made me discover the amazing world of computer simulations. Thanks for all the patience and dedication during my Bachelor and Master times.

There is one person to thank for the smoothness of my start in this project, and this is Martin Wagner. Thank you Martin, for your patience and time during the time when you were where I am now. Without those three months with your tutoring, I would have had a rougher time landing here. I also want to thank Zihan Tan, for very fruitful discussions during my PhD, and all the time we spent in Jülich. Clara Abaurrea, thanks for all the insight you gave me both in the scientific and social world.

Part of this thesis will not be the same without Javier Oller. I am very proud of the work you performed in our group, the things you learned, and the ideas you gave to the triangular-shaped (binocular) trimers. Also thanks to Joscha Mecke, for your time in helping me understanding and implementing the AMC. In the end, the 2d saved the rotors.

I can only try to imagine what would have been this thesis without coffee, and I cannot forget the ones that accompanied so many caffeinated hours. Christina, although it lasted just a couple of months, I still miss our coffee breaks on the

couches. Ahmet, Andrea, thanks for all the “kahfmets” during these last years.

Working with simulations has its perks, but also its downsides. I need to thank all the support team from the Jureca supercomputer for their effective work, and always having the solution for any problem I encountered. Moreover, thanks to Dorothea Henkel for being always present and save the situation when something went wrong with my workstation. Moreover, the writing of this thesis would not have been the same without Scrivener and the person who recommended it to me. Thank you, Maria, for all these long morning conversations sharing a coffee and tea, and getting lost in so many worlds. Journey before destination. I would also like to thank Alexandra Elbakyan, for making science accessible for everyone. We need initiatives such yours to break more barriers in science.

An unconventional thanks goes to the party: Agatha, Mara, Martin and Shelldom. What began in a creepy, old and haunted house will not end in the big city. Redundantly, thanks Jordi, Raquel and Pau for the long hours spent either conquering the world or surviving it.

There are lots of names of people that have been alongside me during several years. I am proud of being able to call all of them my friends. All the ones that have been waiting for me when I came back to Barcelona, or the ones that couldn’t wait and came to visit Jülich. Long hours connected in Skype with all of you made the difference. At the risk of leaving some names behind… Ignacio, Guillem, Elena, Núria, Júlia, Kass, Laura, Meri, my mortal enemy Sergio, Claudia, Ferran, Nil, Lorena, Diego and Núria. I hope you could forgive me if you’re reading this, your name should be here and it is not. You are here. Thanks to all, for being there and keeping me sane, and sorry for my absences in the last months of my PhD.

A special and important place in my heart will always reserved for my family. My uncle and aunt, Joaquín and Maricarmen, for having been there since ever. My grandparents, Joaquín, Marcial, Maria and Pilar. You always believed in me, and what I could achieve. I am very sorry you won’t be able to see me now. I miss all of you. Especially, I am deeply thankful to my parents, Xavier and Mercè, for raising me the way you did, for always being by my side when I needed you the most and teach me the codes I try to live by. Thank you for teaching me how to walk before I could run. Moltes gràcies Urrians.

Time has come to thank one of the most important person in my life. Judit, words cannot express everything I feel. We met in a small city in the middle of nowhere, but we have created a whole amazing world here. Thanks for all the laughs, all the shared moments, the “burxaments”, and all the dreams. I want you to know that I would not have reached the end of this dissertation the way I did without your company, love and support. Now, the world awaits for us.

Sergi Roca Bonet, Jülich, March 2021.

Abstract

The term swimmer refers to biological or artificial structures that are capable of self-propel by drawing energy from the surrounding environment. The typical size of a swimmer ranges orders of magnitude, from the macroscopic world of a blue whale in the ocean, to the microscopic of a bacteria. Microscopic swimmers, or microswimmers, live in an environment where the viscosity of the fluid dominates their motion, suppressing the inertia that we are so familiar with. Phoresis refers to the physical mechanism in which colloidal particles migrate due to the presence of a solvent gradient, such as thermal, chemical or magnetic. Phoretic colloids have recently emerged as a promising avenue for the design of artificial microswimmers. Thermophoretic colloids are partially coated with a high heat conductivity material, such as gold, which heats faster under laser illumination, creating then a local thermal gradient. The non-coated surface reacts to the difference in temperatures and displays the thermophoretic response to it, driving the motion of the swimmer. The motion of colloids immersed in fluid produce long-ranged flows, which can infere in the motion of further colloids. These fluid-mediated interactions are known as hydrodynamic interactions. Since the colloid is found in solvent, phoresis and propulsion are linked to a hydrodynamic flow field. These fluid-mediated interactions are deeply influenced by the geometry and surface properties of the colloid, and play a major role in the interaction between swimmers.

This dissertation addresses the study of self-thermophoretic dimeric and trimeric colloidal swimmers by means of mesoscale computer simulations. In order to precisely understand the debated role of hydrodynamic interactions in these systems, two computational approaches are hereby presented. We use a full hydrodynamic approach, which includes thermophoresis, and a second method which neglects fluid-mediated effects while accounting for thermophoretic interactions. Hydrodynamic simulations are performed via the combination of molecular dynamics (MD) and multi-particle collision dynamics (MPC), which has proven to include hydrodynamics and heat transport. We furthermore propose a thermophoretic Brownian dynamics method for the dry systems, with phoresis implemented by means of pair potential interactions. The advantage of this method respect to regular Brownian methods is that the propulsion mechanism and intermolecular phoretic interactions are described by the same potential. This ensures a correct description of the thermophoretic interactions, disregarding only the hydrodynamics in the system, thus allowing for a fair comparative study.

In this thesis we have dealt with multimeric structures made of one heated bead, which creates a local thermal gradient, adjacent to one or two thermophoretic beads. Dimeric swimmers only have one phoretic bead, whereas trimers are build with two phoretic beads. The first trimers have been constructed with all the beads placed rod-like, with the heated bead in the middle. In order to achieve

ballistic motion, the two phoretic beads need to have different phoretic responses, thus the phoretic forces sharing orientation. Trimers can moreover be built with two phoretic beads of the same nature, in which the linear structure is no longer useful for propulsion. The three beads are then placed in a triangular lattice, recovering the ballistic propulsion. Changing one of the phoretic beads of this structure to the opposite phoretic behaviour leads to a rotational behaviour due to a phoretic torque, thus to a rotor swimmer.

Ensembles of dimeric and trimeric swimmers are studied besides the single swimmer properties, showing that the interplay of phoresis, hydrodynamics and geometry is key to the correct understanding of their collective behaviour. Thermophoresis either helps aggregation, as in the case of thermophilic swimmers, in which phoretic beads try to cluster around heat sources; or strongly prevents clustering when thermophobic beads get repelled by heat sources. These dimers and trimers change their hydrodynamic behaviour when varying the aspect ratio between the phoretic and heated beads' radii. Interestingly, the effects of hydrodynamics have shown to have distinct impacts on different systems. In some cases, hydrodynamics enhances aggregation, like it is the case for symmetric thermophilic dimers. In other cases, clustering is penalised due to repulsive fluid-mediated interactions, as it is the case for thermophobic dimers and triangular trimers. These effects are further enhanced or diminished by phoretic and steric effects. Furthermore, steric effects lead to alignment or aggregation on the system.

The results presented in this dissertation contribute to the understanding of thermophoretically driven artificial microswimmers. The large variety of behaviours which we have seen is which may offer more versatile tools in various systems such as micro-fluidic systems, or even devices with applications in medicine given the biocompatibility of small thermal gradients with most organisms.

Zusammenfassung

Der Begriff Schwimmer bezieht sich auf biologische oder künstliche Strukturen, die in der Lage sind, sich selbst anzutreiben, indem sie Energie aus der Umgebung beziehen. Die typische Größe eines Schwimmers reicht über Größenordnungen, von der makroskopischen Welt eines Blauwals im Ozean bis zur mikroskopischen eines Bakteriums. Mikroskopische Schwimmer, oder Mikroschwimmer, leben in einer Umgebung, in der die Viskosität der Flüssigkeit ihre Bewegung dominiert und die uns so vertraute Trägheit unterdrückt. Phoreses bezieht sich auf den physikalischen Mechanismus, bei dem ein kolloidales Teilchen aufgrund des Vorhandenseins eines Lösungsmittelgradienten, z. B. eines thermischen, chemischen oder magnetischen, wandert. Phoretische Kolloide haben sich in letzter Zeit als ein vielversprechender Weg für das Design künstlicher Mikroschwimmer herausgestellt. Thermophoretische Kolloide sind teilweise mit einem Material mit hoher Wärmeleitfähigkeit, wie z. B. Gold, beschichtet, das sich unter Laserbeleuchtung schneller erwärmt und dann einen lokalen Wärmegradienten erzeugt. Die nicht beschichtete Oberfläche reagiert auf den Temperaturunterschied und zeigt die thermophoretische Reaktion darauf, was die Bewegung des Schwimmers antreibt. Die Bewegung von Kolloiden, die in Flüssigkeit eingetaucht sind, erzeugt weitreichende Strömungen, die in die Bewegung weiterer Kolloide münden können. Diese flüssigkeitsvermittelten Wechselwirkungen werden als hydrodynamische Wechselwirkungen bezeichnet. Da sich der Kolloid in einem Lösungsmittel befindet, sind Phoreses und Propulsion mit einem hydrodynamischen Strömungsfeld verbunden. Diese fluidvermittelten Wechselwirkungen werden stark von der Geometrie und den Oberflächeneigenschaften des Kolloids beeinflusst und spielen eine große Rolle bei der Interaktion zwischen Schwimmern.

In dieser Dissertation wird die Untersuchung von selbstthermophoretischen Dimeren und Trimeren kolloidalen Schwimmern mittels mesoskaliger Computersimulationen untersucht. Um die umstrittene Rolle der hydrodynamischen Wechselwirkungen in diesen Systemen genau zu verstehen, werden zwei Berechnungsansätze vorgestellt. Wir verwenden einen vollständig hydrodynamischen Ansatz, der die Thermophorese einschließt, und eine zweite Methode, die fluidvermittelte Effekte vernachlässigt, aber thermophoretische Wechselwirkungen berücksichtigt. Hydrodynamische Simulationen werden über die Kombination von Molekulardynamik und Mehrteilchen-Kollisionsdynamik durchgeführt, die nachweislich Hydrodynamik und Wärmetransport einschließt. Wir schlagen eine thermophoretische Brownsche-Dynamik-Methode für die trockenen Systeme vor, bei der die Phorese durch Paar-Potential-Wechselwirkungen implementiert wird. Der Vorteil dieser Methode gegenüber regulären Brownschen Methoden ist, dass der Antriebsmechanismus und die intermolekularen phoretischen Wechselwirkungen durch das gleiche Potential beschrieben werden. Dies gewährleistet eine korrekte Beschreibung der

thermophoretischen Wechselwirkungen, wobei lediglich die Hydrodynamik im System vernachlässigt wird, was eine faire vergleichende Untersuchung ermöglicht.

In dieser Arbeit haben wir uns mit multimeren Strukturen beschäftigt, die aus einem beheizten Teilchen, das einen lokalen thermischen Gradienten erzeugt, neben einem oder zwei thermophoretischen Teilchen bestehen. Dimere Schwimmer haben nur ein phoretisches Teilchen, während Trimere mit zwei phoretischen Teilchen aufgebaut sind. Die ersten Trimere wurden so konstruiert, dass alle Teilchen stabförmig angeordnet sind, mit dem beheizten Teilchen in der Mitte. Um eine ballistische Bewegung zu erreichen, müssen die beiden phoretischen Teilchen unterschiedliche phoretische Antworten haben, so dass sich die phoretischen Kräfte die Orientierung teilen. Darüber hinaus können Trimere mit zwei gleichartigen phoretischen Teilchen gebildet werden, bei denen die lineare Struktur nicht mehr für den Vortrieb nützlich ist. Die drei Teilchen werden dann in einem Dreiecksgitter angeordnet, wodurch der ballistische Vortrieb wiederhergestellt wird. Ändert man eine der phoretischen Teilchen dieser Struktur in das entgegengesetzte phoretische Verhalten, führt dies zu einem Rotationsverhalten durch ein phoretisches Drehmoment, also zu einem Rotorschwimmer.

Neben den Eigenschaften der Einzelschwimmer werden auch Ensembles von Schwimmern untersucht, wobei sich zeigt, dass das Zusammenspiel von Phorese, Hydrodynamik und Geometrie der Schlüssel zum richtigen Verständnis des kollektiven Verhaltens ist. Die Thermophorese unterstützt entweder die Aggregation, wie im Fall von thermophilen Schwimmern, bei denen phoretische Teilchen versuchen, sich um Wärmequellen zu gruppieren; oder sie verhindert stark die Clusterbildung, wenn thermophobe Teilchen von Wärmequellen abgestoßen werden. Diese Dimere und Trimere ändern ihr hydrodynamisches Verhalten, wenn das Seitenverhältnis zwischen den Radien der phoretischen und der beheizten Teilchen variiert wird. Interessanterweise hat sich gezeigt, dass die Auswirkungen der Hydrodynamik unterschiedliche Auswirkungen auf verschiedene Systeme haben. In einigen Fällen verstärkt die Hydrodynamik die Aggregation, wie es bei symmetrischen thermophilen Dimeren der Fall ist. In anderen Fällen wird die Clusterbildung durch abstoßende, fluidvermittelte Wechselwirkungen benachteiligt, wie es bei thermophoben Dimeren und dreieckigen Trimeren der Fall ist. Diese Effekte werden durch phoretische und sterische Effekte weiter verstärkt oder abgeschwächt. Darüber hinaus führen sterische Effekte zu einer Ausrichtung oder Aggregation am System. Die in dieser Dissertation vorgestellten Ergebnisse tragen zum Verständnis von thermophoretisch angetriebenen künstlichen Mikroschwimmern bei. Die große Vielfalt an Verhaltensweisen, die wir gesehen haben, kann vielseitigere Werkzeuge in verschiedenen Systemen wie mikrofluidischen Systemen oder sogar Geräte mit Anwendungen in der Medizin bieten, da die Biokompatibilität von kleinen thermischen Gradienten mit den meisten Organismen gegeben ist.

Contents

List of Figures

List of Tables

Chapter 1

Introduction

1.1 Soft Matter

In nature, complex systems are common. Every time we bleed, we see one of these systems where micrometric, disk-like cells immersed in a fluid made of far way smaller particles just abandon small capillaries. This complex fluid called blood is a clear example of a biological suspension, crucial for the survival of mostly all animals in the planet. Another fluid with similar properties is milk, produced by animals to feed their younglings during the first weeks of their life.

These mentioned systems are examples of *soft matter* systems, definition of a subfield of condensed matter that encompasses "squishy" materials, such as the previously mentioned complex fluids, *e.g.*, colloidal suspensions, polymer solutions, liquid crystals, gels, foams or membranes. The term soft matter was first employed by Pierre-Gilles de Gennes, considered the founding father of this field [1, 2]. He showed how diverse problems shared by physics, chemistry and biology share many key features that can be treated with statistical mechanics and thermodynamic approaches [1]. Another common feature in these systems is the relevance of thermal fluctuations. Soft matter structures typically have bond energies of similar scale as thermal energies, being then influenced to a high degree by thermal fluctuations, undergoing then Brownian motion [3]. Moreover, the length scales of the structures within most soft matter systems range from the nanometer (10^{-9} m) to the micrometer (10^{-6} m) scales.

A fascinating subset of soft matter encompasses such systems in which energy is drawn from the surrounding environment and gets dissipated at the particle-level, leading to systems inherently far from equilibrium. Such systems are known as *soft active matter* [4, 5, 6, 7], in contrast to passive systems, which only propagate due to pure Brownian random motion [8]. The dissipated energy is mostly used for a wide variety of purposes, *e.g.*, locomotion, replication and growth [9].

1.2 Swimming at the microscale

In nature, active locomotion is a key element of the survival of many biological organisms. Active locomotion can be used as a mechanism for finding sources of aliment (chemotaxis), along with to find environments with favourable and flourishing conditions regarding temperature (thermotaxis), light (phototaxis), gravity (gravitaxis) or acidity. Other important factors for locomotion encompass reproduction or avoiding possible predators [6, 10].

Several microscopic biological organisms are able to propel and move, which allow them to fulfillthe basic needs for life survival and reproduction. These microorganisms, such as viruses, bacteria and individual eukariotic cells, live and swim in nearly intertia-free fluid environments. This regime is determined by the Reynolds number of the fluid, defined by the ratio between the inertia and viscous effects. In a microscopic world, where this Reynolds number is low, viscous forces are dominant. Thus the organisms need to employ different swimming strategies in order to achieve direction motion, different from the ones for our macroscopic more intuitive world. This problem was studied by Purcell, who proposed the so-called *scallop theorem* [11], where he stated that any mechanical motion at low Reynolds numbers shall be asymmetric and not reciprocal in time. The term microswimmers encompasses organisms and artificial structures that are able to sustain motion through a viscous fluid in the absence of external forces or torques. Biological microswimmers typically achieve motion by deforming their bodies [10], whereas their artificial counterparts typically require the presence of environmental gradients.

Most of these biological agents feature external structures that allow them to self-propel in such environments. These structures usually are long or short flagella or cilia. Flagella are elongated filaments made out of microtubules that rotate and beat, allowing bacteria to achieve directed motion [12, 20]. A characteristic motion performed by such organisms is of *run-and-tumble*, a random walk achieved by swimming in one direction, then perform a change of orientation to continue swimming afterwards [21]. Bacteria such as *Escherichia coli* and *Salmonella enterica* use the helical rotation of a flagellar bundle, as shown in Fig. 1.1a and b. Organisms propelling by means of flagella are, *e.g.*, spermatozoa [13], which uses a wiggling single flagellum (shown in Fig. 1.1c), and *Chlamydomonas reinhardtii*, which uses two coordinated flagella. Other organisms, such as *Paramecium*, are covered of short filaments called cilia, which perform coordinated strokes, inducing the cell motion [14] (example in Fig. 1.1d).

The motion due to flagella and cilia creates flow fields around the microorganisms, which influence their mutual interactions and also modify the rheology of the surrounding environment [22, 23]. These flow fields are used by the microorganisms for locomotion, but also for feeding [24], or prey-predator interactions, and

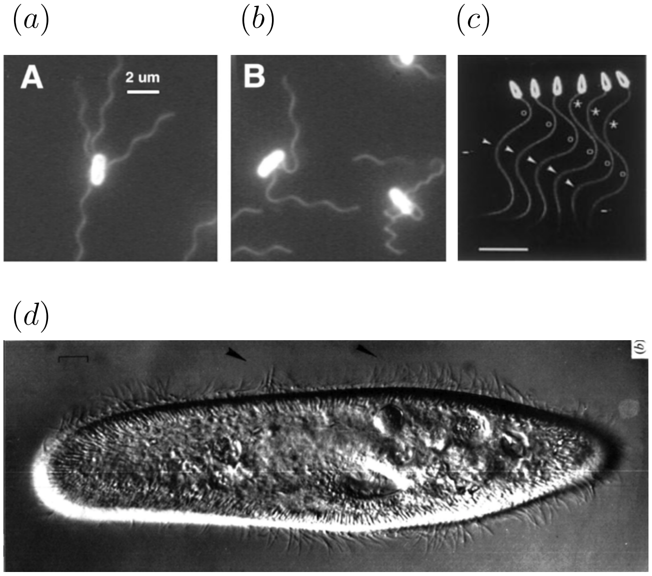

Figure 1.1: Examples of three microorganisms with flagellar and ciliary propulsion mechanisms. (*a*) and (*b*) are flagellated *E. coli* bacteria, which achieve the motion by the beating of flagellar bundles (from [12], with the permission of the American Society of Microbiology), (*c*) corresponds to a sea urchin spermatozoa, and shows the beating pattern of its flagellum (reproduced from [13] with the permission of John Wiley and Sons) and (*d*) a ciliated *Paramecium*, which swims due to whiplash movements of the cilia in its surface (reproduced from [14] with permission of J. Exp. Biol.).

interactions between mates [25]. Moreover, faster and bigger organisms tend to produce stronger flow fields, which is not always advantageous. Some organisms try to minimise the disturbances of the flow in order to hide from predators [25]. Theoretical modelling of the flow fields of flagellates and ciliates can be broadly found in literature [23, 26]. One of these models is the so called squirmer model, which was introduced by Lighthill [27] and later revised by Blake [28], and now is widely used to describe the flow field generated by ciliates, and implemented by enforcing a velocity field surrounding the body [6, 23, 29].

Although the environments of swimming microorganisms and biological organisms of the macroscopic world are vastly different, they display similarities in their collective behaviour. In both scale systems, non-equilibrium collective phenomena emerge on ensembles of actively moving organisms, such as swarming behaviour [15], motility-induced phase separation (MIPS) [19], schooling or lane formation, among others. Some of these patterns are very similar for bacterial ensembles and macroscopic animals such as birds, sheep or fish. Different collective behaviours of both macro- and micoorganisms are shown in Fig. 1.2.

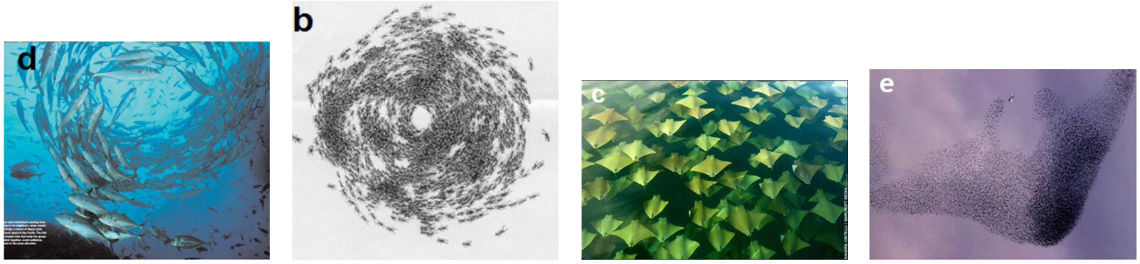

(a) Vortex formation in a swarm of fish. Reprinted from [15] with permission from Elsevier.

(b) Rotating colony of army ants, forming a vortex. Reprinted from [15] with permission from Elsevier.

(c) Swarming behaviour of golden rays. Reprinted from [15] with permission from Elsevier.

(d) Swarming of thousands of starlings. Reprinted from [15] with permission from Elsevier.

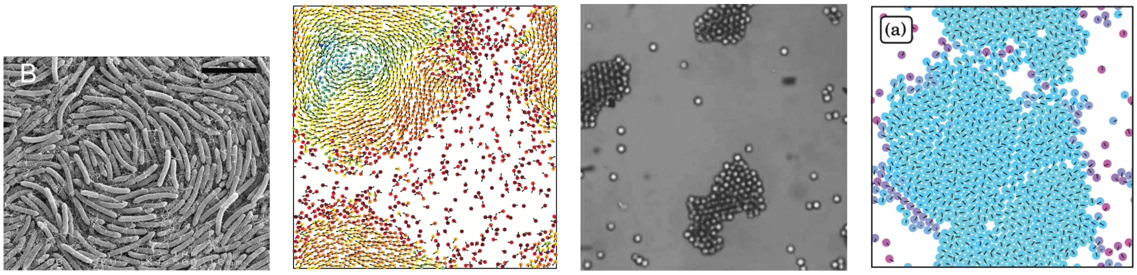

(e) Electron microscope image of an ensemble of *Paenibacillus vortex* forming a vortex. Reprinted from [16].

(f) Vortex formation in a simulation of active colloids. Reprinted with the permission of [17].

(g) Experimental realisaton of Janus colloids displaying MIPS. Reprinted with permission from [18] ©2013 by the American Physical Society.

(h) Motility-induced phase separation on active colloidal simulations (squirmers). Image from [19] - Published by The Royal Society of Chemistry.

Figure 1.2: Examples of collective motion of macro- and microorganisms.

1.3 Artificial microswimmers

Active colloids are synthetic structures able to self-propel by means of the beating or twisting of artificial flagella, different kinds of interactions with gradients (phoresis), or other mechanisms, such as bubble ejection [33, 34]. These kind of swimmers are very promising candidates to serve as synthetic microrobots with possible biomedical implications *à la* “Fantastic Voyage” film from 1966 [35]. These microrobots are small artificial machines or swimmers that can travel and traverse within bigger biological organisms and perform various complex tasks [36]. Examples of self-assembly of swimming structures are by electric or magnetic field manipulation [37, 38, 39], random formation of the structures aided by light [40], top-down approaches using DNA molecule adhesion [41, 42, 43, 44] or spontan-

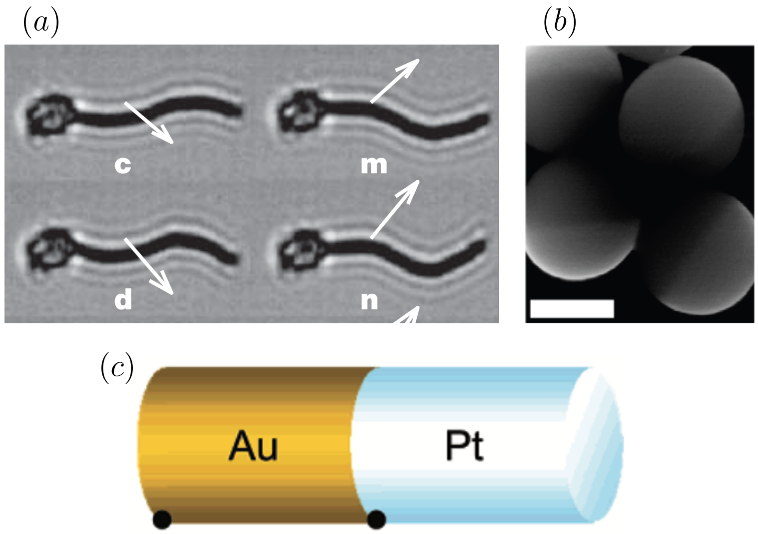

Figure 1.3: Examples of artificial microswimmers. Artificial sperm, (*a*), constructed by attaching a flexible magnetic filament to an erythrocyte ([30] reprinted with permission from Nature ©2005), (*b*) a colloidal Janus particle made of latex and half-coated with platinum (reprinted with permission from [31] ©2010) and (*c*) a scheme of a bimetallic Janus nanorod (reprinted with permission from [32] ©2004).

eously clustering, depending on geometrical considerations of the swimmer [45], hydrodynamics [46], or the process of injection of energy into the system [47].

The first artificial microswimmer constructed to mimic a biological mechanism was the one of Dreyfus *et al.* [30]. In this work, they stated that a manmade microswimmer must fulfil two conditions, see that energy must be injected into the systems, and used to mechanically deform the device of propulsion. Secondly, the sequence of deformations of the system must be cyclic and time irreversible, as the scallop theorem stated. This last condition is required due to the low Reynolds number condition, when viscosity overrules inertia. They attached a linear chain of magnetic colloidal particles to a erythrocyte, creating an artificial spermatozoid. The propulsion was then achieved by an oscillating magnetic field, which induced a wiggling motion to the artificial magnetic filament, mimicking the flagellum beating of a biological sperm cell. This construction is shown in Fig. 1.3a.

One of the first artificial microswimmers which did not directly aim at mimicking a biological locomotion process was introduced by Paxton *et al.* [32]. They constructed a bimetallic nanorod, half platinum covered and half gold covered, immersed in a hydrogen peroxide solution, shown in Fig. 1.3c. The decomposition of the hydrogen peroxide is catalised by the platinum end, and the resulting reactants interact with the gold end, leading to self-propulsion. Nevertheless, the precise details of how this mechanism takes place is still an open issue [6].

Similar artefacts have been constructed with spherical particles. These particles are made of two halves coated with different materials (see Fig. 1.3b), and are known as Janus particles in honour of the ancient, double-faced, Roman god, with one face pointing towards the past, and the other towards the future. The term "Janus particle" was coined by the science-fiction author Leonard Wibberley in this novel *The Mouse on the Moon* in 1962 as a science fiction device for space travel, but saw its first use in the scientific world by C. Casagrande *et al.* in 1988 [48]. Similar to the nanorod, catalytic Janus particles are half coated with platinum and gold, and immersed in a hydrogen peroxide solution, which gets catalised by the platinum surface. Experimental realisation of catalytic Janus particles have been realised by Howse *et al.* [49], based on the theoretical considerations of Golestanian *et al.* [50].

Catalytic-driven swimmers are one example of systems that achieve locomotion due to the *phoretic* effect. The term phoresis was coined back in 1896 to describe commensalism between animals, more specifically, the relationship in which one organism (the phoretic, or *phoront*), such as a nematode or mite, attaches to another organism (the host), such as a fly or bee, for the only purpose of achieving motion [51, 52]. The root of the name comes from the greek *phoras*, which means to bear, and at the same time is influenced by the word *phor*, meaning thief [51]. This term is nowadays also extensively used to describe the effect in which colloidal particles migrate due to the reaction to a gradient of a field. The physical nature of the field determines the phoresis. In the case of the mentioned catalytic Janus particle, this gradient may just be a concentration gradient of the reactants from the decomposition of the hydrogen peroxide. This gradient is by itself enough to achieve self-propulsion due to the different interactions that each of the components has on the colloid surface [53, 54]. Other gradients that also lead to self-propelled colloids are temperature (thermophoresis) [55, 56, 57], light (phototaxis) [58], electric (electrophoresis) [59, 60, 61, 62, 63] or magnetic (magnetophoresis) [64, 65, 66]. The process in which the phoresis is based solely due a concentration gradient is termed diffusiophoresis.

Swimmers with geometries different than spherical or rod-like have also been synthesised, following the Janus idea. By separating the platinum and gold halves of the Janus into two different beads (with one of them the phoretically active), the resulting dimer construct was suggested in simulation studies by Rückner and Kapral [67] to behave similarly as the Janus particle. Later on, Valadares *et al.* [68] synthesised platinum/silica dimers via deposition of silica microspheres of a flat platinum/silica subtract, and then added a layer of chromium and a thicker layer of platinum. These structures are shown in Fig. 1.4a. Similar structures of simulated thermophoretic dimers are shown in Fig. 1.4b and Fig. 1.4c. On

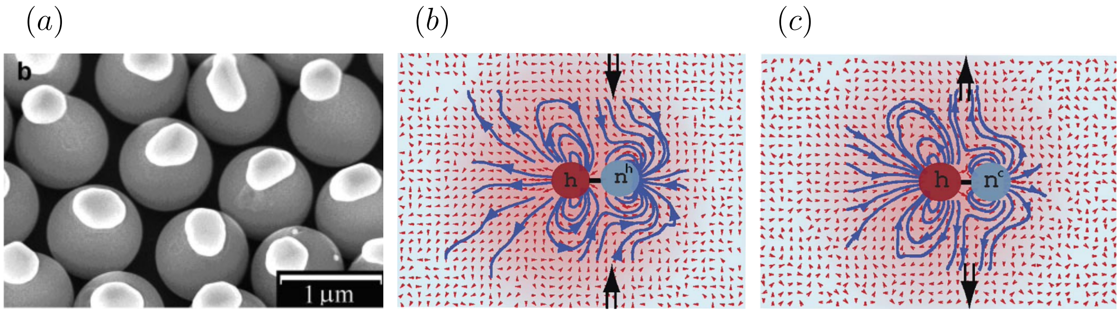

Figure 1.4: Examples of dimeric phoretic microswimmers. (*a*) Experimental realisation of a chemically-driven dimeric microswimmer (reprinted from [68] with the permission of John Wiley and Sons), (*b*) and (*c*) simulated flow fields of two thermophoretic dimeric swimmer, philic and phobic, respectively (reprinted with permission from [74] ©2014 by the Royal Society of Chemistry).

annealing the samples, the half-chromium half-platinum shells dewet, forming a metallic, platinum covered, spherical particle on top of the silica colloid [69]. They performed an experimental realisation of this phoretically driven microswimmers, which showed typical velocities in the μm$/s$ range [7]. Other dimeric colloids have also been synthesised with tunable shapes, geometry and interfacial anisotropy, along with other materials, such as platinum-polystyrene electrophoretic colloids, synthesised via seeded emulsion polymerisation [70], or "patchy" particles with gold coating made by surfactant-aided dewetting [71].

Further multimeric colloidal structures have been already synthesised. Yang *et al.* [72] achieved linear and triangular trimeric colloidal structures (with same sized beads) by monomer swelling and phase separation during polymerisation. Kim *et al.* [73] showed that larger colloidal structures can be prepared by site-selective attraction, which lead to the dimpled particles under study to cluster into dumbbells or trimers. Gonzalez and Soto [36] presented a proof of concept for the directed assembly of catalytic dimers and triangular-shaped trimers. It was achieved by transporting monomers (A and B, with different phoretic nature) via an external concentration field with a geometry which focused on a specific reaction zone.

1.4 Thermophoresis

Thermodiffusion, or Ludwig-Soret effect, describes the phenomenon of mass transport due to the presence of a temperature gradient on a liquid mixture, leading to a partial segregation of the compounds of the mixture. This phenomenon was first reported by Carl Ludwig in 1856 [75]. During the two decades after the discovery, this effect was systematically investigated in electrolyte solutions by Charles Soret [76], who developed phenomenological equations to describe thermodiffusion in terms of Fick's diffusion equations.

This thesis focuses on computational artificial colloidal microswimmers, dimers and trimers, driven by thermophoresis. Thermophoresis refers to the physical phenomenon in which colloidal nanoparticles move due to the presence of a thermal gradient. This is the colloidal analog to thermodiffusion, in which one of the components in the mixture is orders of magnitude larger than the other. It is usually referred to aerosol mixtures whose mean free path, λ, is comparable to the characteristic length scale of the colloid [77]. This effect is usually observed at scales smaller than the milimeter, being a naked-eye example of it the interaction between tobacco smoke and a metal hot rod of an electric heater, in which is clear that the smoke moves away from the immediate vicinity of the rod.

Thermophoresis, or Soret effect, is commonly characterised by the so-called Soret coefficient, S_T, which describes how the colloid reacts towards the temperature gradient. The sign of this coefficient relates to the direction of the motion. The current convention says that it is positive for thermophobic, thus moving towards colder areas, or negative for thermophilic colloids, which move towards heat sources. The sign of the Soret coefficient, as well as its magnitude, depends on multiple factors. It is seen that, typically, the heavier or larger particles in a mixture exhibit positive thermophoretic behaviour, or thermophobic nature, while the smaller or lighter ones display thermophilic nature, or negative behaviour. Other factors include the charge of the particles, their moment of inertia, the heat conductivity and heat absorption of the colloids as well as the particular interaction details between colloid and fluid environment [78]. Moreover, Braun *et al.* [79, 80] have suggested that the charge and entropy of the hydration shell of the colloids also play a major role in the thermophoretic nature of biomolecules in aqueous solutions. Another key element that influences the thermophoretic behaviour is the precise inter-particle interactions at the molecular level. On one hand, the overall combination and dependency of all these factors leads to a theoretical description of thermophoresis being very complex, which detailed microscopic description is still a matter of ongoing research. On the other hand, the intricate influences of the multiple dependencies also implies that a system employing the thermophoretic effect is highly tunable [78].

Thermophoresis might be advantageous in some applications over diffusiophoresis, given that it does not require a specific solvent chemistry. This means that no toxic chemicals are needed in order to achieve phoretic motion, thus is a promising venue for applications in biological organisms. One way to activate and control thermophoresis is by laser illumination. Laser sources allow for a very precise control over the applied heating mechanism in both time and space.

Thermophoresis was first applied to microswimmers by Jiang *et al.* [81]. They build a Janus particle by gold-coating polystyrene and silica particles via deposition. Thermophoretic thrust was achieved via laser illumination over the sample, inducing self-phoresis. Simulations on a thermophoretic Janus were performed by Yang *et al.* [74], along with similar thermophoretic dimeric swimmers [82]. These dimer constructions are of considerable interest, since their increased inherent complexity compared to the spherical Janus particle leads to additional degrees of freedom.

The shape of the microswimmer plays an important role on the hydrodynamics of the swimmer. The complex interplay of these hydrodynamic interactions with phoretic effects, steric interactions, propulsion and thermal fluctuations are of crucial relevance to the collective dynamics of these swimmers. The temperature gradient, with source on the heated surface of the swimmer, obeys Fourier law, following a decay proportional to $1/r$. Phoretic interactions are proportional to the field gradient, and show a dependency of $1/r^2$ with the distance. Hydrodynamic interactions have a strong dependency on the shape of the swimmer. Simulations on Janus particles showed that their flow field decays as $1/r^3$, such that the hydrodynamic interactions in these systems are less relevant than phoretic effects [74]. This is not the case for the dimeric structures, whose flow field is shown to decay as $1/r^2$, *i.e.*, the same as the phoretic interactions. The combination of both effects results in very interesting collective dynamics, which are investigated in this dissertation.

1.5 Outline of this thesis

This dissertation focuses on thermophoretically active dimers and trimers in the presence and absence of hydrodynamic interactions, from their single to collective behaviour in 3d-bulk and quasi-2d confined systems.

Chapter 2 provides the required theoretical framework, encompassing theory from passive colloids, to active colloids, and notions of thermophoresis and hydrodynamics.

In chapter 3, the methods to set up the simulations used in this work are introduced in detail. The simulation methods explained are molecular dynamics (MD), multi-particle collision dynamics (MPC) and Brownian dynamics (BD).

Chapter 4 contains the study of the swimming behaviour of single dimers and trimers in 3d bulk conditions and in quasi-2d confinement, along with the hydrodynamic study of these single swimmers in 3d-bulk conditions.

Chapters 5 and 6 contain the study of quasi-2d confined ensembles of dimers and trimers, respectively, and the comparison of simulations with and without hydrodynamic interactions to precisely quantify the effects of hydrodynamics. The studied dimers have thermophobic and thermophilic properties, for two different dimer geometries. Two very different geometries are investigated for trimeric active colloids. Section 6.1 studies trimers with two beads of the same phoretic nature and one heated, positioned in a triangular shape, leading to a modified version of the dimers. Section 6.2 contains the study of linear trimers, with one bead philic and the other phobic, leading to a rod-like swimmer.

The last chapter of results is chapter 7, where rotors have been studied. Rotors are heterogeneous trimers placed instead of in rod-like shape, in triangular formation. This leads to a net torque on the structure, thus a rotational motion.

Finally, in chapter 8 there are the summary and outlook of this work.

All the snapshots of the simulations have been rendered with VMD [83], and all the plots have been generated with Matplotlib in Python [84].

Chapter 2

Theoretical framework

This chapter contains the theoretical basis for the topic of this dissertation. First introduced are the dynamics of passive colloidal particles, or Brownian motion, and the dynamics of active colloids, which describe the swimming behaviour of the self-propelled microswimmers. Thermophoresis is then characterised by the drift velocity and the description of the thermophoretic force. The last section treats hydrodynamics, from the derivation of the Navier-Stokes equations from the conservation laws of a fluid, to some particular solutions and the introduction to hydrodynamic flow fields.

2.1 Colloidal dynamics: Langevin equation

The word colloid comes from the greek $\kappa\acute{o}\lambda\lambda\alpha$, which means glue. This term was coined by Thomas Graham on his first publications in systematic research about colloidal systems in 1861. In his work, Graham made a distinction between two kinds of solutions depending on the size of the solute. The first category included solutions in which the solute particles were small enough to be able to diffuse through a membrane. The second category corresponded to solutions where there is no diffusion observed through a membrane, due to the solute particles being too big to fit through the pores of the membrane.

The botanist Robert Brown observed in 1827 that pollen particles of the plant *Clarkia pulchella* showed an irregular motion when found in water. This motion is now known as the Brownian motion, and is interpreted as the result of random collisions between the small solvent molecules and the large solute pollen colloids. Jean Perrin verified in 1910 that these colloids were "large molecules", thus their irregular motion was identified as thermal noise.

With that assumption, one can define the size range of colloidal particles. The surface of a single colloid is assumed to interact simultaneously with many solvent particles. We then require that the interactions between the solvent particles and the colloid are treated only in an averaged way. These interactions can be described by a continuum limit description, which are the macroscopic equations of motion for the fluid. In order to solve the solvent flow on the surface, boundary conditions must be furthermore considered. The macroscopic properties of the solvent, such as temperature or viscosity, characterise then the Brownian motion of the colloid. This construction is only feasible if one assumes that the size of the colloid is at least about ten times the size of the solvent molecules, *i.e.*, $\simeq 1$nm.

Once we have the minimum size of the colloid, the maximum is let to be determined. To obtain this limit, the requirement is that the colloid should behave as a "large molecule", as Perrin postulated in 1910. That means that it must show a vivid thermal motion, *i.e.*, Brownian motion. For thermal motion to be relevant on a system, the displacements must be a sizeable fraction of the linear dimension of the particle, setting this upper limit to $\simeq 10\mu$m [85]. With this, we can consider that a colloid is any particle of size $\simeq 1\text{nm} - 10\mu\text{m}$.

Moreover, there is also a time scale difference between solute and solvent. The typical scale of the relaxation time of the solvent is of the order of 10^{-14}s, whereas the relevant time scale for colloidal motion is of the order of 10^{-9}s [85].

In order to derive an equation to predict the colloidal motion, one has to assume that all interactions between the fluid and the colloid are experienced in an averaged and stochastic way. A spherical colloid of mass m experiences a random force, $\boldsymbol{\xi}$, accounting for the random kicks exerted to the particle through thermal fluctuations. Moreover, it also experiences a drag force, or friction, in the direction of movement due to the viscosity of the fluid, η. This force is proportional to the velocity of the colloid, with a constant known as the translational friction coefficient γ_f. With these two assumptions, the motion equation of a colloidal particle reads

$$m\ddot{\boldsymbol{r}} = -\gamma_f \boldsymbol{v} + \boldsymbol{\xi} + \boldsymbol{F} \ , \tag{2.1}$$

which is the so-called *Langevin equation*. In Eq. (2.1), $\boldsymbol{F}$ describes the total sum of external forces on the colloid. Due to the difference in both time and length scales between the colloid and the fluid particles, the random force $\boldsymbol{\xi}$ accounting for the thermal fluctuations is assumed to be a Gaussian and Markovian white noise,

$$\langle \boldsymbol{\xi}(t) \rangle = 0 \ , \tag{2.2}$$

$$\langle \boldsymbol{\xi}(t) \cdot \boldsymbol{\xi}(t') \rangle = \boldsymbol{\Xi} \delta(t - t') \ , \tag{2.3}$$

with $\boldsymbol{\Xi}$ the strength of the fluctuations. This parameter can be evaluated by using the fluctuation-dissipation theorem, leading to

$$\boldsymbol{\Xi} = 2\gamma_f k_B T \ \mathbb{I} \ ,$$

with $\mathbb{I}$ the identity matrix, k_B the Boltzmann constant, T the temperature of the system and γ_f the friction coefficient. This means that the noise does not have any preferred direction, and that the strength of the fluctuations increases proportionally with both the temperature and friction.

In most soft matter systems, the friction that the fluid exerts on the colloid is considerably higher than the mass of the colloidal particle, $m/\gamma_f \to 0$, which leads to the assumption that in these systems, the inertia terms play no role on the motion equations. This allows us to neglect the acceleration term of Eq. (2.1), thus obtaining the *overdamped* limit of the Langevin equation,

$$0 = -\gamma_f \boldsymbol{v} + \boldsymbol{\xi} + \boldsymbol{F} \ ,$$

where we no longer have any mass-dependent term. Physically, this is interpreted as that the colloid's motion is not influenced by the inertia relaxation, due to the short-ranged time scale of this phenomenon, and the average velocity of the colloid vanishes instantaneously due to the system's temperature and friction, *i.e.*, noise.

The Brownian motion [86] is purely diffusive, which means that, in the absence of external forces, the first moment of the displacements, or mean displacement, is zero, $\langle \boldsymbol{r}(t) - \boldsymbol{r}(0) \rangle = 0$, and in order to quantify the diffusion of a colloid one can look at the second moment, known as the mean square displacement, or MSD, of the diffusing particle,

$$\Delta \boldsymbol{r}^2(t) = \langle [\boldsymbol{r}(t) - \boldsymbol{r}(0)]^2 \rangle \ . \tag{2.4}$$

Defining $\tau \equiv m/\gamma_f$ as the timescale of the momentum relaxation, with m the mass of the colloid and γ_f the friction coefficient, one can identify two regimes of Eq. (2.4). At short time ranges, $t < \tau$, the mean square displacement behaves as MSD $\propto t^2$ due to momentum relaxation. Nonetheless, when studying Brownian systems, this time scale is commonly omitted due to the non-inertial framework. At larger time ranges, the mean square displacement behaves linearly with time, showing the diffusive term and allowing us to define the diffusion coefficient D as

$$D \equiv \lim_{t \to \infty} \frac{\Delta \boldsymbol{r}^2(t)}{2dt} \ ,$$

with d the dimensionality of the system. This coefficient is one of the most important quantitative measures of molecular diffusion. Physically, it defines the average distance that a particle can travel in a time t, $l \sim \sqrt{Dt}$, being then analogous to the classical mechanics description of the velocity. For a passive Brownian particle in a homogeneous and diluted three dimensional system, the motion is characterised by two independent motions, the translational and the rotational motions [7]. The translational motion is defined by the translational diffusion coefficient, defined by the Stokes-Einstein equation

$$D_T = \frac{k_B T}{6\pi\eta\sigma_c} \ , \tag{2.5}$$

where σ_c is the colloid's radius, η is the viscosity of the fluid and $6\pi\eta\sigma_c = \gamma_f$ is the viscous friction of a spherical particle. Moreover, the colloid also undergoes rotational diffusion with a characteristic time scale τ_R. This time scale is the inverse of the rotational diffusion coefficient,

$$D_R = \frac{k_B T}{8\pi\eta\sigma_c^3} \ . \tag{2.6}$$

Then, with these definitions, the mean square displacement of a Brownian particle in a d-dimensional system reads

$$\Delta \boldsymbol{r}^2(t) = 2dD_T t \ , \tag{2.7}$$

where only the translational diffusion coefficient is taken into account given that, for a passive colloid, only the thermal fluctuations are relevant to its motion. Nonetheless, the description of the rotational motion is of crucial importance when a propulsion is present. Similarly to the MSD, the rotational motion can be described by the rotational mean square displacement, given by [85]

$$\Delta \boldsymbol{e}^2 \equiv \langle (\boldsymbol{e}(t) - \boldsymbol{e}(0))^2 \rangle = 2\left(1 - e^{-(d-1)D_R t}\right) \ . \tag{2.8}$$

From Eq. (2.5) and Eq. (2.6) we can see that the translational diffusion scales linearly as the radius of the colloid, while the rotational diffusion scales with the volume of the particle.

In the case of crowded systems, such as large and dense ensambles of colloids or inside the cell's cytoplasm, this description becomes more complex and density dependent [86]. At a given density, the MSD does not longer behave linearly with time, and two time ranges can be distinguished; a short-time and long-time regimes, with their corresponding diffusion coefficients, D_s and D_l, respectively. Between these two regimes, a third region, know as *anomalous* diffusive regime, can frequently been identified with a time-dependent diffusion coefficient,

$$D(t) = \frac{\Delta \boldsymbol{r}^2(t)}{2dt} = \gamma_f t^{\alpha-1} \ ,$$

with γ_f the generalised transport, or anomalous diffusion, coefficient and α the exponent of anomaly. If $\alpha > 1$, the system is referred as superdiffusive, while if $\alpha < 1$ it is called anomalous subdiffusion, as most crowded systems show.

2.2 Active colloids: Self-propelled swimmers

Active colloids are those colloidal particles that in the absence of any external force are able to enhance their diffusive motion, *i.e.*, propel themselves, by consuming internal energy or extract energy from the surrounding environment [87, 88]. Given the constant flow of energy between environment and colloid, thus being far from thermal equilibrium, their behaviour can only be understood within the framework of non-equilibrium physics [7]. As a result of the swimming, the direction $\boldsymbol{e}$ is an intrinsic property of the individual colloidal swimmer, instead of being determined by external conditions. Therefore, on the description of the colloidal motion we have to add both the action of the self-propulsion force along with the orientation of the motion. A model of a self-propelled spherical colloid is the active Brownian particle (ABP), which considers a fixed velocity v_0 and where the orientation of the directed motion is subject to rotational diffusion. For this system, the Langevin description is given by the stochastic differential equations for the velocity and the orientation [87, 17, 89]. The translational motion is given by

$$\dot{\boldsymbol{r}}(t) = \boldsymbol{v}(t) + \frac{1}{\gamma}\left(\boldsymbol{F}(t) + \boldsymbol{\xi}(t)\right) \ , \tag{2.9}$$

with $\boldsymbol{v}(t) = v_0\boldsymbol{e}(t)$, $\gamma = k_BT/D_T$ the translational friction, $\boldsymbol{F}(t)$ the total sum of external forces and where the thermal fluctuations are captured by $\boldsymbol{\xi}(t)$, a Gaussian and Markovian white noise force given by Eq. (2.2) and Eq. (2.3). The change on the orientation has no dependency on the position and velocity of the colloid, thus the rotational motion is independent of the translation,

$$\dot{\boldsymbol{e}}(t) = \boldsymbol{\xi}_R(t) \times \boldsymbol{e}(t) \ , \tag{2.10}$$

where $\boldsymbol{\xi}_R(t)$ is a Gaussian and Markovian stochastic process,

$$\begin{aligned} \langle \boldsymbol{\xi}_R(t) \rangle &= 0 \ , \\ \langle \boldsymbol{\xi}_R(t) \cdot \boldsymbol{\xi}_R(t') \rangle &= 2(d-1)D_R\delta(t-t') \ , \end{aligned}$$

with D_R the rotational diffusion coefficient from Eq. (2.6) and d the dimensionality of the system. D_R is generally non dependent on D_T. Moreover, D_R can also be of non-thermal origin, such as the tumbling of bacteria [87].

Two correlation functions rise from Eq. (2.9) and Eq. (2.10), respectively. The velocity and orientation autocorrelation functions read [87, 88]

$$\begin{aligned} \langle \boldsymbol{v}(t) \cdot \boldsymbol{v}(t') \rangle &= v_0^2 e^{-(d-1)D_R|t-t'|} \ , \\ \langle \boldsymbol{e}(t) \cdot \boldsymbol{e}(t') \rangle &= e^{-(d-1)D_Rt} \ . \end{aligned} \tag{2.11}$$

Given that, for an active colloidal Brownian particle, the rotational motion is of crucial importance, the MSD has both contributions; rotational and translational.

In order to derive the expression [87], we need to integrate Eq. (2.9) in the force-free case, $\boldsymbol{F}(t) = 0$,

$$\boldsymbol{r}(t) - \boldsymbol{r}(0) = \int_0^t \left(\boldsymbol{v}(t') + \frac{\boldsymbol{\xi}(t')}{\gamma} \right) \mathrm{d}t' \ . \tag{2.12}$$

The mean square displacement is then be obtained from Eq. (2.12),

$$\begin{aligned} \Delta \boldsymbol{r}^2(t) &= \langle (\boldsymbol{r}(t) - \boldsymbol{r}(0))^2 \rangle \\ &= \frac{6k_BT}{\gamma} t + \int_0^t \int_0^t \langle \boldsymbol{v}(t') \cdot \boldsymbol{v}(t'') \rangle \mathrm{d}t' \mathrm{d}t'' \qquad (2.13) \\ &= 2dD_T t + \frac{2v_0^2}{\gamma_R^2} \left(\gamma_R t + e^{-\gamma_R t} - 1 \right) \ , \qquad (2.14) \end{aligned}$$

where we used the definition of the velocity autocorrelation function from Eq. (2.11) in Eq. (2.13), and the damping factor is related to the rotational diffusion coefficient as $\gamma_R = (d-1)D_R$. This is the generalisation for a d-dimensional system of the MSD, derivations and examples for 2d biological and artificial systems can be found in references [90, 49], respectively. The equation of the MSD, Eq. (2.14), holds whenever the activity on the colloid is characterised by an exponential decay. The MSD can be studied in two time regimes [7, 87], short and long respectively,

$$\begin{aligned} \Delta \boldsymbol{r}^2 &= 2dD_T t + v_0^2 t^2 \ , & \gamma_R t \ll 1 \ ; \\ \Delta \boldsymbol{r}^2 &= \left(2dD_T + \frac{2v_0^2}{\gamma_R} \right) t \ , & \gamma_R t \gg 1 \ . \end{aligned}$$

These equations physically express that for shorter times the motion performed by the active colloid is of ballistic nature, or superdiffusive, while a diffusive motion is observed for larger times because of the randomisation of the orientation due to rotational diffusion on the propulsion direction, leading to a random walk motion.

In this scope, it is important to highlight that rotational noise is of high importance. In order to emphasise the difference between the motion of a passive and an active Brownian particle, one can consider the average particle trajectory. For the passive case, $\langle \boldsymbol{r}(t) \rangle = 0$ by symmetry. Nonetheless, in the case where activity is present, the average displacement does not vanish at all times. Instead, it results in a straight line along the activity direction at small times [7],

$$\begin{aligned} \langle \boldsymbol{r}(t) \rangle &= \frac{v_0}{D_R} \left(1 - e^{-D_R t} \right) \\ &= v_0 \tau_R \left(1 - e^{-t/\tau_R} \right) \ , \end{aligned}$$

implying that the trajectory only turns due to rotational effects, and that for a characteristic time, τ_R, the particle moves in a straight line in the direction of the activity for a finite persistence length $L = v_0/D_R = v_0\tau_R$.

In order to further characterise the importance of the directed motion in front of the diffusion for an active Brownian particle, or ABP, one can define the dimensionless Péclet number, which quantifies the importance of the diffusion compared to the directed swimming motion [88, 7, 91].

$$\mathrm{Pe} \equiv \frac{v_0}{\sigma_c D_R} \ , \tag{2.15}$$

where σ_c is a factor related to the swimmer relevant size. Here we take that σ_c is the colloid radius, but it can also be chosen to be any characteristic length relevant on the system. If Pe is small, it means that the diffusive term governed by the rotational diffusion coefficient overtakes the directed motion, leading to a diffusive motion; while if Pe is large, the motion is ballistic, prevailing the directed motion in front of the rotational diffusion [7, 87, 88].

Moreover, as done for the MSD, the $\Delta\boldsymbol{e}^2$ (Eq. (2.8)) can be treated for small times ($\gamma_R t \ll 1$), resulting in

$$\langle(\boldsymbol{e}(t) - \boldsymbol{e}(0))^2\rangle = 2(d-1)D_R t \ .$$

2.3 Thermophoresis

Brownian motion describes the dynamics of a colloidal system in a homogeneous fluid. When an inhomogeinity is added in said fluid, such a gradient, the motion is no longer completely random, and the colloids might experience a drift. This phenomenon is called inhomogeneous Brownian motion. A general description of the diffusion of such Brownian particles in an inhomogeneous fluid was obtained by van Kampen in 1988 [92]. One example of inhomogenous Brownian motion is thermophoresis, which describes the phenomenon of mass transport driven by the effect of an applied temperature gradient on the colloidal system [7, 56, 57], and can be understood as the colloidal analog of the molecular thermodiffusion. We then refer to thermophoresis to the physical effect in which a colloidal particle suspended in a fluid performs a steady drift motion towards the cold or warm areas due to the presence of a temperature gradient [93]. The creation of a temperature gradient applied to a fluid suspensions leads to two main non-equilibrium effects. The first of them is heat conduction, *i.e.*, the transport of energy, which always happens in the same direction than the gradient (from warm to cold areas) and with a timescale given by the heat diffusivity. The second effect is the thermodiffusion, also known as thermal diffusion or Soret effect, named after Charles Soret (1854-1904). This refers to the phenomenon describing the mass transport on a fluid, *e.g.*, a colloidal particle under a temperature gradient. Although this phenomenon is more common to occur towards the direction to cold areas, it has also been observed in the opposite direction. These two processes are decoupled given that the timescale for diffusion is typically two orders of magnitude slower than the one for the heat conduction. A colloid reacting to a gradient behaves as if it experiences an external force. One can use this similarity in order to approach the thermal transport coefficients and thus derive an effective field in order to understand the effect of the temperature gradient [56]. Nonetheless, this procedure is not trivial. The nature of thermophoresis is not defined by the particle's general bulk or surface physical properties [56], such as material, size, or thermal conductivity, but it appears to be subtly related to the microscopic nature of the particle-solvent interactions.

2.3.1 Drift velocity in inhomogeneous systems

When a single colloidal particle is suspended in a homogeneous fluid at low Reynolds numbers and is subject to a driving force $\boldsymbol{f}$, it experiences a drift velocity which, at the stationary state, exactly balances the viscous drag, $\boldsymbol{v}_d = \mu \boldsymbol{f}$, with μ the mobility of the colloid. Nonetheless, when the fluid is no longer homogeneous, this relation breaks down due to an additional contribution to the drift velocity proportional to the gradient of the diffusion coefficient, $\propto \nabla D$ [94].

In order to understand this problem, the flux equation must be derived. Starting with the diffusion equation for the probability density of a colloidal particle within a homogeneous medium, $P(\boldsymbol{r},t)$, under the presence of an external stationary potential, $U(\boldsymbol{r})$, is given by the Fokker-Plank or Smoluchowski equation

$$\frac{\partial P(\boldsymbol{r},t)}{\partial t} = \nabla \cdot \left[(\mu \nabla U(\boldsymbol{r}))P(\boldsymbol{r},t) + D\nabla P(\boldsymbol{r},t)\right] \ , \tag{2.16}$$

with D the diffusion coefficient, obtained via the Einstein's relation. In the presence of an inhomogeneous medium, van Kampen considered that the temperature T, the diffusion coefficient D and the mobility μ were dependent on the spatial coordinates, $\boldsymbol{r}$. The generalisation of Eq. (2.16) is

$$\frac{\partial P(\boldsymbol{r},t)}{\partial t} = \nabla \cdot \left[\mu(\boldsymbol{r})\nabla U(\boldsymbol{r})P(\boldsymbol{r},t) + \nabla (D(\boldsymbol{r})P(\boldsymbol{r},t))\right] \ , \tag{2.17}$$

which can in turn be rewritten as

$$\frac{\partial P(\boldsymbol{r},t)}{\partial t} = \nabla \cdot \left[(\mu(\boldsymbol{r})\nabla U(\boldsymbol{r}) + \nabla D(\boldsymbol{r}))P(\boldsymbol{r},t) + D(\boldsymbol{r})\nabla (P(\boldsymbol{r},t)\right] \ ,$$

where $\nabla D(\boldsymbol{r})P(\boldsymbol{r},t)$ describes the additional term introduced by the inhomogeneities of the fluid. In order to specifically derive the diffusion equation, van Kampen

[92] proposed to use the model of a Brownian particle. The starting point was Kramer's equation [95, 96, 97], valid in the linear response regime, for a Brownian colloid. This equation determines the evolution of the joint probability of the position and the velocity, which in one dimension gives for the probability density $G(\boldsymbol{r}, \boldsymbol{v}, t)$,

$$\begin{aligned}\frac{\partial G(x,v,t)}{\partial t} = &- v\frac{\partial G(x,v,t)}{\partial x} + \frac{\partial U(x)}{\partial x}\frac{\partial G(x,v,t)}{\partial v} \\ &+ \zeta\left(\frac{\partial}{\partial v}vG(x,v,t) + T\frac{\partial^2 G(x,v,t)}{\partial v^2}\right) \,, \end{aligned} \tag{2.18}$$

with $\frac{\partial U(x)}{\partial x} = -f$ the force resulting from the potential U and $\zeta = 1/\mu$ the friction coefficient. The last term of Eq. (2.18) dominates for high values of ζ, in which case one may expand the equation in terms of $1/\zeta$, in the spirit of the Chapman-Enskog procedure [97, 98]. In the zeroth approximation, $G(x, v, t)$ is locally a Maxwellian in v, uniquely determined by the spatial density,

$$P(x,t) = \int_{-\infty}^{\infty} G(x,v,t)\mathrm{d}v \,.$$

The lowest non-vanishing order, considering $\mu(x) = 1/\zeta(x)$ and $D(x) = k_B T(x)/\zeta(x)$, leads to [99]

$$\frac{\partial P(x,t)}{\partial t} = \frac{\partial}{\partial x}\left[\mu(x)\frac{\partial U}{\partial x}P(x,t) + \mu(x)\frac{\partial}{\partial x}k_B T(x)P(x,t)\right] \,, \tag{2.19}$$

which takes neither the form of Eq. (2.16) nor Eq. (2.17), but is a hybrid. A reformulation would be possible in order to write it in either form, provided an extra drift term is added [92]. Finally, the expression of Eq. (2.19) in 3d takes the form

$$\frac{\partial P(\boldsymbol{r},t)}{\partial t} = \nabla\left[\mu(\boldsymbol{r})P(\boldsymbol{r},t)\nabla U(\boldsymbol{r}) + \mu(\boldsymbol{r})\nabla(k_B T(\boldsymbol{r})P(\boldsymbol{r},t))\right] \,. \tag{2.20}$$

In the same article, van Kampen writes Eq. (2.16) as a continuity equation,

$$\partial_t P(\boldsymbol{r},t) = -\nabla \boldsymbol{J}(\boldsymbol{r},t) \,, \tag{2.21}$$

where the flux $\boldsymbol{J}$ is assumed to consist of two terms. The first term considers the average drift of the particles proportional to the force, $\boldsymbol{J}_{\mathrm{drift}}$, while the second term stands for the diffusion, as given by Fick's law, $\boldsymbol{J}_{\mathrm{diff}}$. Combining equations Eq. (2.20) and Eq. (2.21), we obtain an expression for the particle flux with both drift and diffusion terms, known as the van Kampen flux equation [92, 97, 100]

$$\boldsymbol{J}(\boldsymbol{r},t) = -\left[\mu(\boldsymbol{r})\nabla U(\boldsymbol{r})\right]P(\boldsymbol{r},t) - \mu(\boldsymbol{r})\nabla\left[k_B T(\boldsymbol{r})P(\boldsymbol{r},t)\right] \,. \tag{2.22}$$

Now, substituting the particle probability density function $P(\boldsymbol{r},t)$ by the particle number density, n, and the potential $U(\boldsymbol{r})$ to the force $\boldsymbol{f}(\boldsymbol{r})$ on Eq. (2.22), the flux can be expressed as a version of the Fick's law in the presence of a temperature gradient and driving force,

$$\boldsymbol{J}(\boldsymbol{r},t) = \mu(\boldsymbol{r})\boldsymbol{f}(\boldsymbol{r})n(\boldsymbol{r}) - \mu(\boldsymbol{r})\nabla\left[n(\boldsymbol{r})k_B T(\boldsymbol{r})\right] \ , \tag{2.23}$$

where the force in this case considers both forces resulting from external potentials as well as mechanical driving forces on the colloid, resulting from the surrounding fluid. This equation can be understood as a balance between two forces acting on a volume element [101, 102]. One of the forces is represented by the term $\nabla\left[n(\boldsymbol{r})k_B T(\boldsymbol{r})\right]$, which is related to the Brownian noise, or the gradient of the ideal gas osmotic pressure [101, 103], and arises from the momentum change in the volume element due to the particle flux from said element.

Finally, the drift velocity can be obtained from Eq. (2.23) by adding and subtracting the term $k_B T(\boldsymbol{r})\nabla\mu(\boldsymbol{r})$ to both terms as

$$\boldsymbol{J}(\boldsymbol{r}) = n(\boldsymbol{r})\boldsymbol{v}_d - \nabla\left[n(\boldsymbol{r})D_s(\boldsymbol{r})\right] \ , \tag{2.24}$$

from which the drift velocity arises as

$$\boldsymbol{v}_d = \mu(\boldsymbol{r})\boldsymbol{f}(\boldsymbol{r}) + k_B T(\boldsymbol{r})\nabla\mu(\boldsymbol{r}) \ . \tag{2.25}$$

Eq. (2.25) is the drift velocity of a Brownian particle in a homogeneous environment plus an extra term due to the inhomogeneity created by a thermal gradient. Nevertheless, this extra term is seen to be proportional to the mobility, μ, rather than the gradient of the diffusion coefficient, as predicted, which is very relevant in the case of non-isothermal systems. Therefore, the expression of the drift velocity here obtained can be considered a general case for both isothermal and non-isothermal inhomogeneous systems, as long as the system is in the linear response regime.

2.3.2 Thermophoretic force

In order to derive the expression for the thermophoretic force, the phenomenological expression of the mass flux is needed. The total diffusive particle flux, or mass flux, of one component in a homogeneous mixture or suspension is given by the Fick's law and determined by the gradient of concentration, c, [104],

$$\boldsymbol{J} = -D_s\nabla c \ . \tag{2.26}$$

Nonetheless, in the presence of a temperature gradient, one must take into account the effect of thermodiffusion as an extra term on equation Eq. (2.26), known as the thermodiffusion contribution.

In the framework of non-equilibrium thermodynamics, the entropy production, σ, in a n-component mixture system can be written as [105]

$$\sigma = -\frac{1}{T^2}\boldsymbol{J}_q \cdot \nabla T - \frac{1}{T}\sum_k \boldsymbol{J}_k \cdot \nabla_T \mu_k \ ,$$

with $\boldsymbol{J}_q$ the heat flux, $\boldsymbol{J}_k$ the mass flux of the k component, ∇T the thermal gradient and $\nabla_T \mu_k$ the chemical potential gradient of the component k. The expressions of the heat and mass fluxes derive from Fourier's law, and taking an example of a binary mixture ($k = 1, 2$) with $k = 1$ as the solute, the fluxes read

$$\begin{aligned} \boldsymbol{J}_q &= -L_{qq}\frac{\nabla T}{T^2} - L_{q1}\frac{\nabla_T(\mu_1 - \mu_2)}{T} \\ \boldsymbol{J}_1 &= -L_{1q}\frac{\nabla T}{T^2} - L_{11}\frac{\nabla_T(\mu_1 - \mu_2)}{T} \ , \end{aligned} \tag{2.27}$$

where L_{ij} are the phenomenological coefficients fulfilling the Onsager reciprocal relations [105]. For this example of a binary mixture, thermodiffusion can be phenomenologically described by the total flux of particles of one component in the direction of the temperature gradient, in this case, the solute $k = 1$. Then, the total mass flux from Eq. (2.27) can be rewritten as [56, 105, 106]

$$\boldsymbol{J}_x = -\overline{n} D_m \nabla x - \overline{n} D_T x(1-x)\nabla T \ , \tag{2.28}$$

where $\overline{n} = n + n'$ is the average total number density, with n and n' the densities of the two components (solute and solvent, respectively), $x = n/\overline{n}$ the molar fraction of one of the components, D_m the mutual diffusion coefficient and D_T the thermal diffusion coefficient, which takes the form

$$D_m = L_{11}\frac{\nabla_T(\mu_1 - \mu_2)}{T\overline{n}\nabla x} = \frac{L_{11}}{\overline{n}(1-x)T)}\frac{\partial \mu_1}{\partial x} \ , \tag{2.29}$$

$$D_T = \frac{1}{\overline{n}x(1-x)T^2}L_{1q} \ . \tag{2.30}$$

From these two coefficients, the so-called Soret coefficient is defined as

$$S_T \equiv \frac{D_T}{D_m} \ ,$$

whose magnitude indicates how strongly the two components separate in the mixture. The particle flux $\boldsymbol{J}$ vanishes in the stationary state, allowing us to obtain an expression for the Soret coefficient from the molar fraction, x, and temperature distribution, T, with Eq. (2.29) and Eq. (2.30) applied on Eq. (2.28),

$$S_T = -\frac{x}{x(1-x)}\frac{\nabla x}{\nabla T} \ . \tag{2.31}$$

The Soret coefficient, Eq. (2.31), can take both positive and negative values. By convention, positive values of S_T lead to a net mass flux towards cold areas, displaying the more commonly observed thermophobic behaviour. On the other hand, negative values of this coefficient lead to particle accumulation on the hot areas, being then of thermophilic nature. Eq. (2.28) represents the standard method to quantify the thermodiffusion phenomena in concentrated mixtures.

The relation between the drift velocity Eq. (2.25) and the thermal diffusion coefficient of a dilute mixture, D_T, is of essential importance not only from a conceptual viewpoint, but also for experimental studies. The dilute regime is characterised by a low solute density, *i.e.*, $n \ll n'$, thus the mutual diffusion coefficient can be considered equivalent to the solute self-diffusion coefficient, $D_m \simeq D_s$ [107]. In this scenario, the mass flux from Eq. (2.28) can be compared to Eq. (2.24) [108], leading to

$$\boldsymbol{v}_d = -D_T \nabla T + \nabla D_s - D_s \beta \nabla T \ ,$$

with $\beta \equiv (-1/n')\partial_T n'$ being the solvent thermal expansion coefficient [106, 109]. When this expression is compared to the extensively used definition of the thermophoretic velocity [56, 57, 79]

$$\boldsymbol{v}_T \equiv -D_T \nabla T \ , \tag{2.32}$$

which depends linearly only with the thermal gradient and the thermal diffusion coefficient. Thus, the drift velocity can only be considered equivalent to this thermophoretic velocity when $|D_T| \gg |\partial D_s/\partial T - D_s\beta|$, which is indeed the most common case in complex fluids [57, 79, 110]. With this velocity, and a characteristic length of the thermophoretic colloid, *e.g.*, the radius σ, we can define the ballistic time as $\tau_B = \sigma/v_T$, which describes the time a colloid takes to move a distance equivalent to σ. This time also has the advantage to be easily compared with experiments.

Besides the propulsion velocity of a colloid, the driving thermophoretic force is also a very important tool to characterise thermophoretic systems. This force is also linear with the thermal gradient, as well as the Soret coefficient [82, 110],

$$\boldsymbol{f}_T = -\alpha_T k_B \nabla T \ , \tag{2.33}$$

where $\alpha_T = T S_T$ is the thermodiffusion coefficient, or dimensionless thermal diffusion factor, which provides the linear proportionality constant relating the gradients to the colloid's response [108].

2.4 Hydrodynamics

The motion of a viscous fluid is described by the well-known Navier-Stokes equation, named after Claude-Louis Navier (1785-1836) and George Gabriel Stokes

(1819-1903), which characterises a fluid by its mass density $\rho(\boldsymbol{r},t)$, pressure $p(\boldsymbol{r},t)$ and flow velocity $\boldsymbol{u}(\boldsymbol{r},t)$. The derivation of these equations lies in two key elements, the local conservation of mass and momentum.

2.4.1 Conservation of mass

In order to derive the conservation of mass equation, one needs to first adress the equation which describes the fluid density. A volume element of fluid, $V(t)$, describing the volume containing a specific collection of fluid particles, is considered [111]. The fluid density ρ in this volume element is a constant over time and space. This condition imposes a restriction on the nature of the fluid flow, given that within the volume element the number of fluid particles must be a constant [85].

A general property $g(\boldsymbol{r},t)$ of a random material volume evolves in time via

$$g(\boldsymbol{r}+\boldsymbol{u}\Delta t, t+\Delta t) = g(\boldsymbol{r},t) + \Delta t\left(\frac{\partial g}{\partial t} + \boldsymbol{u}\cdot\nabla g\right) + \mathcal{O}(\Delta t^2)\ ,$$

which includes the so-called material derivative of g,

$$\frac{\mathrm{D}g}{\mathrm{D}t} = \frac{\partial g}{\partial t} + \boldsymbol{u}\cdot\nabla g\ ,$$

where $\boldsymbol{u}$ is the fluid velocity. The mass of a volume element is $M = \int_{V(t)} \rho \mathrm{d}V$, which is a constant in time, $\mathrm{d}M/\mathrm{d}t = 0$. Following this procedure, we need to obtain the time derivative of the intergral $\int_{V(t)} \rho \mathrm{d}V$ with a time-dependent integral range. This can be obtained via the three dimensional generalisation of the Leibniz integral rule, also known as Reynolds transport theorem [112], which applied to g leads to

$$\frac{\mathrm{d}}{\mathrm{d}t}\int_{V(t)} g(\boldsymbol{r},t)\mathrm{d}V = \int_{V(t)} \frac{\partial g(\boldsymbol{r},t)}{\partial t}\mathrm{d}V + \int_{V(t)} g(\boldsymbol{r},t)\boldsymbol{u}(\boldsymbol{r},t)\cdot\boldsymbol{n}\mathrm{d}A\ , \tag{2.34}$$

with $\boldsymbol{u}(\boldsymbol{r},t)$ being the surface fluid velocity, which also corresponds to the fluid velocity of the material volume [112]. Applying Eq. (2.34) to the mass density ρ and using Gauss' theorem on the integration, we obtain

$$0 = \frac{\mathrm{d}}{\mathrm{d}t}\int_{V(t)} \rho \mathrm{d}V = \int_{V(t)} \left[\frac{\partial \rho}{\partial t} + \nabla\cdot(\rho\boldsymbol{u})\right]\mathrm{d}V\ . \tag{2.35}$$

Given that Eq. (2.35) must stand for any arbitrary volume element $V(t)$, this means that the integrand must be zero. This allows us to finally obtain the continuity equation, which states that the mass flow throughout a volume element $\mathrm{d}V$ is zero,

$$\frac{\mathrm{d}\rho}{\mathrm{d}t} + \rho\left(\nabla\cdot\boldsymbol{u}\right) = 0\ . \tag{2.36}$$

The density ρ is here considered constant throughout time, thus the first term of the left-hand side of Eq. (2.36) vanishes, leading to the condition for the mass conservation,

$$\nabla \cdot \boldsymbol{u} = 0 \, , \tag{2.37}$$

of an incompressible fluid.

2.4.2 Conservation of momentum

The main ingredient for the derivation of the Navier-Stokes equations is the local momentum conservation in a volume element $\mathrm{d}V$. The starting point is to consider Newton's second law $\boldsymbol{F} = m\boldsymbol{a}$ to fluid motion,

$$\rho \frac{\mathrm{D}\boldsymbol{u}}{\mathrm{D}t} = \boldsymbol{F} = \boldsymbol{F}_{\text{bulk}} + \boldsymbol{F}_{\text{surface}} \, . \tag{2.38}$$

where $\boldsymbol{F}_{\text{bulk}} = \boldsymbol{f}$ is the total force on the bulk fluid in a volume element $\mathrm{d}V$ due to external factors, $\boldsymbol{F}_{\text{surface}} = \boldsymbol{F}_{\text{pressure}} + \boldsymbol{F}_{\text{viscous}}$, with σ_{ij} the stress tensor, and $\mathrm{D}/\mathrm{D}t$ refers to the material derivative. Note that no force connected to sources/sinks has been taken into account.

The general deformation law of Newtonian viscous fluids given by Stokes [113], in which the stress in the fluid is assumed to be the sum of a diffusing viscous and a pressure term, allows us to rewrite the stress tensor as

$$\sigma_{ij} = -p\delta_{ij} + \eta \left(\frac{\partial u_i}{\partial x_j} + \frac{\partial u_j}{\partial x_i} \right) + \delta_{ij} \lambda \nabla \cdot \boldsymbol{u} \, , \tag{2.39}$$

where p is the pressure and η is the shear viscosity of the fluid, which measures the resistance of the fluid against shearing. Note that this description is not general, and does not stand for viscoelastic fluids. The condition of being a Newtonian fluid is mandatory, and is the relevant case for this thesis.

In Eq. (2.39) we can apply the condition of an incompressible fluid Eq. (2.37), which makes the last term on the right-hand side of Eq. (2.39) to vanish. Then, Eq. (2.38) is rewritten as

$$\begin{aligned} \rho \frac{\mathrm{D}\boldsymbol{u}}{\mathrm{D}t} &= \boldsymbol{f} + \nabla \sigma_{ij} \\ &= \boldsymbol{f} - \nabla p + \frac{\partial}{\partial x_i} \left[\eta \left(\frac{\partial u_i}{\partial x_j} + \frac{\partial u_j}{\partial x_i} \right) \right] \, . \end{aligned}$$

We then arrive at the common expression of the Navier-Stokes equation,

$$\rho \frac{\mathrm{D}\boldsymbol{u}}{\mathrm{D}t} = \rho \left(\frac{\partial \boldsymbol{u}}{\partial t} + \boldsymbol{u} \cdot \nabla \boldsymbol{u} \right) = \boldsymbol{f} - \nabla p + \eta \nabla^2 \boldsymbol{u} \, . \tag{2.40}$$

for an incompressible fluid under an external force $\boldsymbol{f}$, where the fluid velocity $\boldsymbol{u}$, the pressure field p and the external forces $\boldsymbol{f}$ are spatio-temporal dependent, *i.e.*, $\boldsymbol{u}, p, \boldsymbol{f} = f(\boldsymbol{r}; t)$.

These equations present a problem. Despite the information they contain and their pratical uses in both science and engineering, there is still not proof whether their solutions always exist in three dimensional systems. Even if they do exist, it is not even proved if they are smooth, *i.e.*, they are infinitely differentiable at all points in the domain. In order to analytically solve these equations in three dimensions, several approximations are necessary.

2.4.3 Conservation of energy and heat transport

For non-isothermal systems, or conditions in which the transport of energy is relevant, one needs to address the thermal energy conservation. The conservation of the total internal (thermal) energy per unit mass, e, requires that the rate of variation of energy in a volume element V,

$$\frac{\mathrm{D}}{\mathrm{D}t}\int_V \rho\left(e+\frac{u^2}{2}\right)\mathrm{d}V = \int_V \rho\frac{\mathrm{D}}{\mathrm{D}t}\left(e+\frac{u^2}{2}\right)\mathrm{d}V \ ,$$

with the equality due to the kinematic transport theorem, is equal to the sum of the rate of heat flux into the element,

$$-\int_V \frac{\partial Q_i}{\partial x_i}\mathrm{d}V \ , \tag{2.41}$$

with $\boldsymbol{Q}$ being the heat flux described by Fourier's law, $\boldsymbol{Q} = -\kappa_T \nabla T$, with κ_T the heat conductivity, and the rate of work due to bulk and surface forces,

$$\int_V \rho \boldsymbol{f}\cdot\boldsymbol{u}\mathrm{d}V + \int_V \frac{\partial \sigma_{ij} u_j}{\partial x_i}\mathrm{d}V \ . \tag{2.42}$$

Given that both Eq. (2.41) and Eq. (2.42) are expressed as volume integrals over arbitrary volume elements, the total equation must be true at every point in space. This, together with the conservation of linear momentum, leads to the conservation of energy equation [114]

$$\rho\frac{\mathrm{D}e}{\mathrm{D}t} = -\nabla\boldsymbol{Q} + \sigma_{ij}\nabla\boldsymbol{u} \ . \tag{2.43}$$

Finally, since $e = C_p T$, being C_p the specific heat of the fluid, Eq. (2.43) can be rewritten as

$$\rho C_p \frac{\mathrm{D}T}{\mathrm{D}t} = \kappa_T \nabla^2 T + \boldsymbol{\sigma}\cdot\nabla\boldsymbol{u} \ ,$$

with κ the heat conductivity.

Heat in a fluid is transported by three main mechanisms; conduction, convection and radiation. Radiation is disregarded in this discussion given that it is typically only important for very hot materials or systems with a large temperature difference, which is not the case in this dissertation. Thermal conduction, or heat diffusion, refers to the transfer of internal energy by momentum transfer, *i.e.*, microscopic collisions between fluid particles. This process is described by Fourier's law, also known as the law of heat conduction,

$$\frac{\partial Q}{\partial t} = -\kappa_T \oint_S \nabla T \cdot \mathrm{d}S \ .$$

Convective heat transfer, or simply convection, refers to the transfer of heat due to mass transfer within a fluid due to the physical movement of fluid elements, and is given by

$$\boldsymbol{Q} = \rho C_p \boldsymbol{u}(T - \overline{T}) \ ,$$

being $\overline{T}$ a reference temperature.

2.4.4 Creeping flow limit: Stokes equations

The physics of swimming in the microscopic world differs significantly compared to what we experience in the macroscopic world. To put a daily example, in order to swim, a human needs to transfer momentum to the water by moving arms and legs, whereas fish have evolved more advanced techniques, using the tail and fins to swim on the seas and rivers. Nonetheless, in the world of microscopic organisms, viscous damping is paramount. Microorganisms need other strategies to accomplish swimming in such systems [10, 115, 116, 117].

We can rewrite the Navier-Stokes equations Eq. (2.40) in terms of a characteristic length scale l_0, and a characteristic flow velocity u_0. This characteristic length scale depends on the system, *e.g.*, for the case of a spherical colloid suspended in water, l_0 could refer to the colloid's radius or diameter, while the characteristic velocity can refer to the fluid velocity at infinity, $u_0 = u(r \to \infty)$ [118]. By doing this, we are implicitly choosing a characteristic timescale defined as $t_0 = l_0/u_0$. Now, we can use this three characteristic scales in order to rescale the main variables of Eq. (2.40). The rescaled variables are $\boldsymbol{u}' = \boldsymbol{u}/u_0$, $t' = t/t_0$, $\boldsymbol{f}' = \boldsymbol{f} l_0^2/(\eta u_0)$ and $\nabla' = l_0 \nabla$, such that Eq. (2.40) reads now

$$\frac{\rho u_0 l_0}{\eta} \left(\frac{\partial \boldsymbol{u}'}{\partial t'} + \boldsymbol{u}' \cdot \nabla' \boldsymbol{u}' \right) = \boldsymbol{f}' - \nabla' p + \eta \nabla^{2\prime} \boldsymbol{u}' \ , \tag{2.44}$$

where the pre-factor is defined as the dimensionless Reynolds number

$$\mathrm{Re} \equiv \frac{\rho u_0 l_0}{\eta} \ . \tag{2.45}$$

This dimensionless Reynolds number, Re, was first introduced in 1851 by George Stokes [113], but its name was coined by Arnold Sommerfeld in 1908 [119]. He called it Reynolds number after Osborne Reynolds, who popularised its use in 1883 [120, 121]. It qualitatively captures the characteristics of the flow regime described by the Navier-Stokes equation, Eq. (2.40), defining the ratio between the inertia terms of Eq. (2.40), $\sim \rho \boldsymbol{u} \cdot \nabla \boldsymbol{u}$, and the viscous forces per unit volume, $\simeq \eta \nabla^2 \boldsymbol{u}$ [10]. Moreover, this quantity defines which is the dominating transport mechanism in a fluid. The typical time scale for convection in a fluid is $t_{\mathrm{conv}} \simeq l_0/u_0$, *i.e.*, the time scale of a local perturbation in the fluid to be transported by convection by the flow. On the other hand, the typical time scale for this perturbation to diffuse away due to viscosity is $t_{\mathrm{diff}} \simeq \rho l_0^2/\eta$ [10]. Therefore, the Reynolds number can also be defined as

$$\mathrm{Re} \equiv \frac{t_{\mathrm{diff}}}{t_{\mathrm{conv}}} \ . \tag{2.46}$$

In the macroscopic world of the swimming fish and flying birds, inertia dominates over viscous forces, with Re $\gg 1$. In contrast, most of soft matter systems, such as most microswimmers, the inertia is negligible compared to the viscous terms, and Re $\ll 1$, thus the viscous forces dominate in the fluid [11]. In this low Reynolds number approximation, Re $= 0$, also called the creeping flow limit, laminar flow, or Stokes limit, the fluid transport is dominated by the viscous diffusion, as we can see from Eq. (2.46). For these systems, the left hand side of Eq. (2.44) vanishes, leading to the Stokes equations

$$\begin{aligned} \nabla p - \eta \nabla^2 \boldsymbol{u} &= \boldsymbol{f} \ , \\ \nabla \cdot \boldsymbol{u} &= 0 \ , \end{aligned} \tag{2.47}$$

where p is the pressure field and $\boldsymbol{u}$ is the velocity field of the fluid. Due to the absence of inertia, the linearity and time independence of Eq. (2.47) manifest kinematic reversibility [23]. This equation can now be solved, given the adequate boundary conditions.

2.4.5 Dimensionless numbers

Dimensionless numbers are of key importance to adimensionalise the simulation results in order to compare them with real experimental units. Some relevant dimensionless numbers have already been defined, as the Péclet number, Eq. (2.15), or the Reynolds number, Eq. (2.45). Other relevant dimensionless numbers for this work are hereby described. The dimensionless Schmidt number,

$$\mathrm{Sc} \equiv \frac{\nu}{D_f} \, ,$$

characterises the rate of diffusive momentum transfer, measured by the kinematic viscosity ν, relative to the rate of diffusive mass transport, measured by the self-diffusion coefficient of a fluid particle, D_f. In other words, it represents the ratio between collisional and kinetic momentum transport. In liquids, momentum transport is dominated by interparticle collisions, thus $\mathrm{Sc} \gg 1$, while in diluted gases, the momentum transport is governed by mass diffusion, with $\mathrm{Sc} \sim 1$. In simulations, values of the Schmidt number $10 < \mathrm{Sc} < 100$ are typically employed, which nicely account for the separation of mass and momentum transport, allowing us to recover the hydrodynamic behaviour reminiscent of liquids [122].

Systems in which thermal processes play a major role, the Prandtl number,

$$\mathrm{Pr} \equiv \frac{\nu}{D_T} \, ,$$

characterises the rate of viscous over thermal diffusion. The typical value of the Prandtl number of water at around 15°C is $\mathrm{Pr} = 7.82$ [123].

The Mach number describes the ratio between the speed of solvent (or solute flow), v_s, and the speed of sound $c_f = \sqrt{(5/3)(k_B T/m)}$,

$$\mathrm{Ma} \equiv \frac{v_s}{c_f} \, .$$

This number, in contrast to other numbers that are an intrinsic property of the fluid, has a direct dependency on the flow velocity. Given the presence of the speed of sound on its definition, the Mach number measures compressibility effects on the fluid [124]. The sound speed c_f is in the order of 10^3 m/s in most liquids, leading to overall small Mach numbers in colloidal systems under normal achievable flow conditions [124]. Moreover, this number can also be related to the Reynolds number, Eq. (2.45), as

$$\mathrm{Re} = \sqrt{\frac{5}{3}} \mathrm{Ma} \left(\frac{\sigma_c}{a} \right) \left(\frac{\nu_0}{\nu} \right) \, ,$$

with σ_c the radius of a colloid in suspension on the fluid.

Finally, the Knudsen number characterises rarefaction effects [124], and it is given by

$$\mathrm{Kn} \equiv \frac{\lambda_f}{l_0} \, ,$$

with λ_f the mean free path of a fluid particle and l_0 a characteristic length scale. Large Knudsen numbers, $\mathrm{Kn} \geq 10$, the continuum Navier-Stokes equations completely break down, but even for smaller Kn, rarefaction effects can be seen [124]. These effects, known as Knudsen effects, could find important applications in microfluidics or micromechanical devices, where they play an important role [125, 126].

2.4.6 Hydrodynamic interactions: flow fields

The relative motion of a colloid perturbs the surrounding fluid, which is characterised by the so-called flow field. The flow fields are the solutions of the Navier-Stokes equations under certain assumptions and boundary conditions, obtaining the fluid particle velocity field around the colloid. Given that this work only focuses on the low Reynolds number approximation, the Navier-Stokes equations gets reduced to the Stokes equation, Eq. (2.47).

A first solution is when the external force is a point force, $\boldsymbol{f} = \boldsymbol{f}_0 \delta(\boldsymbol{r} - \boldsymbol{r}')$. Since the Stokes equations are linear, the fluid velocity at an arbitrary point $\boldsymbol{r}$ in the fluid has to be proportional to the point force in $\boldsymbol{r}'$ [85]. Hence

$$\boldsymbol{u}(\boldsymbol{r}) = \mathbb{T}(\boldsymbol{r} - \boldsymbol{r}') \boldsymbol{f}_0 \delta(\boldsymbol{r} - \boldsymbol{r}') \ , \tag{2.48}$$

with $\mathbb{T}(\boldsymbol{r} - \boldsymbol{r}')$ a tensor known as Oseen tensor, which connects the point force $\boldsymbol{f}(\boldsymbol{r}')$ to the resulting fluid velocity at $\boldsymbol{r}$ [85]. The fact that the Oseen tensor does only depend on the relative position $\boldsymbol{r} - \boldsymbol{r}'$ arises from the translational invariance. Similarly, the pressure field is also linear with the force, hence

$$p(\boldsymbol{r}) = \boldsymbol{w}(\boldsymbol{r} - \boldsymbol{r}') \cdot \boldsymbol{f} \ , \tag{2.49}$$

with $\boldsymbol{w}(\boldsymbol{r} - \boldsymbol{r}')$ known as the pressure vector. Solving Eq. (2.47) with the assumptions from Eq. (2.48) and Eq. (2.49) leads to the solution known as the Stokeslet,

$$\boldsymbol{u}(\boldsymbol{r}) = \frac{1}{8\pi\eta r} \left(\mathbb{I} + \frac{\boldsymbol{r}\boldsymbol{r}}{r^2} \right) \ , \tag{2.50}$$

with $\boldsymbol{r}\boldsymbol{r} \equiv \boldsymbol{r}\boldsymbol{r}^{\intercal}$, which describes the fluid velocity field due to an externally applied point force. Examples characterised by these flows are, *e.g.*, particles under gravity, or other external fields. Note that the flow from Eq. (2.50) decays with r^{-1}, which is very slow and results then in long-ranged hydrodynamic interactions between colloids at distant locations.

Other solutions to Eq. (2.47) can be found in literature, one of the most known being the force dipole or stresslet. This flow field is force-free, and is broadly observed on biological active microswimmers, which can autonomously move without the presence of an externally applied force. This solution is obtained by superposing two Stokeslets solutions of forces of strength f_0 applied at $\boldsymbol{r} = \boldsymbol{r}_0 \pm l/2$, with $\boldsymbol{r}_0$ the centre of the body and l the distance between the applied forces. These two forces have to be aligned with the dipole axis, pointing in opposite orientations, leading to

$$\boldsymbol{u}(\boldsymbol{r}) = \frac{\alpha}{8\pi\eta r^3}\left(3\frac{\boldsymbol{r}\boldsymbol{r}}{r^2} - \mathbb{I}\right)\boldsymbol{r} \ ,$$

with $\alpha = \pm f_0 l$. This velocity field has two solutions, the positive one ($\alpha > 0$) leads to forces pointing outwards the body, whereas the negative solution ($\alpha < 0$) leads to forces pointing inwards the body. These differences lead to different hydrodynamic interactions, and are the origin of the puller/pusher flow fields.

An extra solution is that of a fixed colloid under the presence of a thermal gradient [127], implying a thermophoretic force, Eq. (2.33). Three boundary conditions can then be imposed, see, a vanishing velocity field at $r \to \infty$, a vanishing normal component of the flow field at the particle surface, $r \to \sigma_c$, and the integral of the stress tensor over the particle surface corresponding to $\boldsymbol{f}_T$. The stationary flow field they obtained was the superposition of a Stokeslet with a source-dipole term decaying with $1/r^3$,

$$\boldsymbol{u}(\boldsymbol{r}) = -\frac{1}{8\pi\eta r}\left(\mathbb{I} + \hat{\boldsymbol{r}}\hat{\boldsymbol{r}}\right)\cdot\boldsymbol{f}_T + \frac{\sigma_c^2}{8\pi\eta r^3}\left(3\hat{\boldsymbol{r}}\hat{\boldsymbol{r}} - \mathbb{I}\right)\cdot\boldsymbol{f}_T \ ,$$

with $\hat{\boldsymbol{r}} = \boldsymbol{r}/\left|\boldsymbol{r}\right|$, $\hat{\boldsymbol{r}}\hat{\boldsymbol{r}} \equiv \hat{\boldsymbol{r}}\hat{\boldsymbol{r}}^{\mathsf{T}}$, σ_c the colloid's radius and η the fluid dynamic viscosity.

Chapter 3

Simulation methods

Complex fluids introduced in the first chapter frequently relate to colloidal or polymer suspensions. These solutions contain billions of particles with sizes ranging from a tenth of a nanometer to a micrometer. The characteristic length and time scales of the different components of these suspensions differ by orders of magnitude. These systems are really tough to study under experimental set-ups, where monitoring both the colloids and the fluid particles is virtually impossible. In this regard, computer simulations have shed light into the understanding of these systems, where both the fluid and colloidal particles are step-by-step monitored by integrating the motion equations. The ideal case would be to study the system with the maximum level of detail, although an atomistic description is impossible due to a lack of resources. The time scales, described by the diffusion of the component, also differ significantly, being around $10^{-7} - 10^{-3}$ s for the colloid and $10^{-14} - 10^{-12}$ s for the fluid. In order to bridge the length and time scales from the fluid and the solute, the system can be coarse-grained into a new system in which we pay the price of losing atomistic detail. These simulations are called mesoscale methods, and nowadays are broadly used in soft matter systems. Hereby, we have coarse-grained both our solute and solvent, treating the colloids as bound spheres which are simulated via molecular dynamics (MD) with an interatomic, pair-wise potential. Moreover, the fluid has been modelled via multiparticle collision dynamics (MPC) [128] with the stochastic rotational dynamics approach (SRD), which conserves both the energy and linear momentum. Colloidal systems without hydrodynamic interactions have been simulated with full Brownian dynamics (BD).

3.1 Multiparticle Collision Dynamics

Some simulation methods, such as molecular dynamics, can provide a precise description of a fluid, being even able to simulate the structure of, *e.g.*, water molecules. Nevertheless, these methods tend to be computationally very expensive. Colloidal suspensions are characterised by the difference in scales, thus for a single colloid, the number of fluid particles of the system increases exponentially. Thus, other methods, with different approaches to the description of the fluid, are required in order to simulate fluids along with colloids in an efficient way, ensuring a good description of the system.

Firstly, one of the most used nowadays is the so-known Lattice-Boltzmann method (LB) [129, 130, 131]. It was first developed empirically in 1988 [132] from the lattice-gas automata method (LGA) [133, 134, 135, 136], and later directly derived from the Boltzmann equation [137]. This approach does not solve the Navier-Stokes equations directly, but simulates a fluid density on a lattice via a streaming and a collision processes [129]. Particle distributions propagate from node to node of the lattice, while interchanging mass and momentum with other particle distributions in the node before the next propagation step. One of the main drawbacks of the LB method, in its original and most extended formulation, is that energy conservation is not fulfilled, thus being restricted to isothermal systems. Morevoer, thermal fluctuations, which are a required element in the correct description and understanding of multiple physical phenomena, are not included.

Dissipative particle dynamics, or DPD, is a method first introduced on 1992 by Hoogerbrugge and Koelman [138] as an attempt to free LGA from the inherent lattice-induced artefacts. The two main ideas of this method are to consider soft and finite interactions into a standard simulation with Newtonian MD, and the second is to consider these interactions to have a soft, finite range conservative term, and a dissipative and stochastic contributions linked by the fluctuation-dissipation theorem, as introduced by Español and Warren in 1995 [139]. This method includes both hydrodynamics and thermal fluctuations [124]. The dissipative and stochastic contributions are understood given that a DPD particle corresponds to the coarse-graining of several fluid particles, still subject to thermal fluctuations. With this, larger time and spatial scales than those from MD can be reached. Together, these two dissipative and random forces can act as a Galilean-invariant thermostat to the system that conserves momentum, thus generating the correct Navier-Stokes hydrodynamics in the continuum limit [124]. The conservation of energy is not fulfilled by the basic algorithm, but by adding an internal energy variable it can be solved (DPD+e) [140, 141, 142].

On 1999, Malevanets and Kapral [128, 143] derived a new mesoscale simulation technique which allowed to simulate mesoscopic fluid systems. This method is known as Multiparticle Collision dynamics (MPC). The main idea was to modify an already existing method for the simulation of gas flows known as Direct Simulation Monte Carlo (DSMC) by replacing the binary collisions by multi-particle collisions within a predefined collision volume [124]. This method employs an off-lattice description of a fluid coarse-grained in both time and space dimensions. The fluid is described by N point particles, characterised by their positions and velocities, $\boldsymbol{r}_k$ and $\boldsymbol{v}_k$, which are treated as continuous variables and are subject to Newton's laws of motion [124].

3.1.1 MPC-SRD Algorithm

The particles which constitute the MPC fluid are treated as N point particles, and their interparticle interactions are instead accounted by means of coarse-grained collisions between pre-defined cells, called *collision cells*. This method is based on two steps; the first step is performed by propagating the positions of the fluid particles during a timestep known as collision time, h. In this work, the collision time is chosen as $h = 0.1$. In the second step, the interactions between fluid particles are taken into account by means of a coarse-grained, averaged rotation of relative velocities. In the streaming step all interactions are neglected, and the positions of the fluid particles are updated by means of pure streaming, as shown in Fig. 3.1a,

$$\boldsymbol{r}_k(t+h) = \boldsymbol{r}_k(t) + h\boldsymbol{v}_k(t) \ , \tag{3.1}$$

where k corresponds to the index of the streamed particle. The second step is the so-known collision step, in which the particles interchange momentum via the interactions between fluid particles, treated via a coarse-grained effective collision. To perform this part of the algorithm, the simulation space is divided in cubic cells my means of defining a grid of cell size a as depicted in Fig. 3.1b. In each of these cells, the collision takes place in the form of the rotation of the relative velocity of each particle with respect to the centre of mass velocity of the particles in the cell i, $\boldsymbol{v}_{cm,i}$,

$$\boldsymbol{v}_k(t+h) = \boldsymbol{v}_{cm,i}(t) + \mathbb{R}(\alpha)\left[\boldsymbol{v}_k(t) - \boldsymbol{v}_{cm,i}(t)\right] \ , \tag{3.2}$$

with $\mathbb{R}(\alpha)\left[\boldsymbol{v}_k(t) - \boldsymbol{v}_{cm,i}(t)\right]$ the collision operator, $\mathbb{R}(\alpha)$ the rotation matrix, α the rotation angle and

$$\boldsymbol{v}_{cm,i}(t) = \frac{\sum_k^{(i,t)} m_k \boldsymbol{v}_k}{\sum_k^{(i,t)} m_k} \ , \tag{3.3}$$

the centre of mass velocity of the collision cell i containing the particles k. To perform the rotation, several approaches are available, depending on the axis chosen

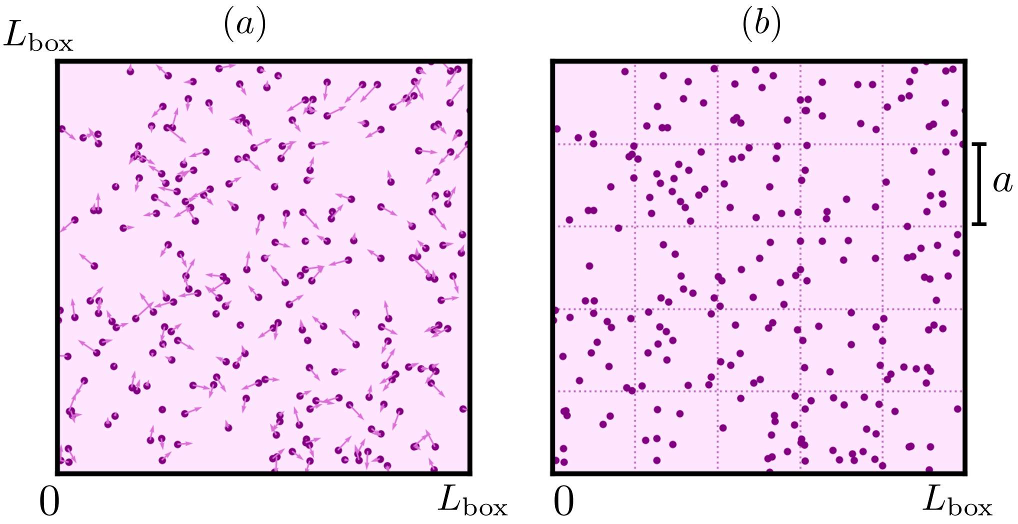

Figure 3.1: Scheme of the two steps of the MPC-SRD algorithm. (*a*) shows the streaming step (Eq. (3.1)), when the particles only move ballistically with their instantaneous velocity. (*b*) shows the collision step (Eq. (3.2)), where the particles are sorted in collision cells and their velocities are updated.

to define the rotation. One possibility is to choose one of the three main axis and perform the rotation with $\pm\alpha$, leading to six rotation matrices from which one needs to choose one randomly for each collision cell. Although this approach is relatively easy to implement, given that the three main axis are fixed, this implementation leads to an intrinsic isotropy in the system due to the underlying lattice. Another approach, and the one used in this work, has been to choose a random axis for each collision cell and each collision step [144]. This approach, given by Eq. (3.2), is known as MPC-SRD scheme, standing for the term stochastic rotational dynamics, and although it is more costly to implement, minimises the isotropy effect of the collision grid. The rotation itself is performed by the rotation matrix $\mathbb{R}(\alpha)$, with α being the angle used to rotate the particles, typically taken as 120° for this work. In the MPC-SRD approach for a 3d system, this matrix takes the shape

$$\mathbb{R}(\alpha) = \begin{pmatrix} n_x^2(1-c)+c & n_xn_y(1-c)-n_zs & n_xn_z(1-c)+n_ys \\ n_yn_x(1-c)+n_zs & n_y^2(1-c)+c & n_yn_z(1-c)-n_xs \\ n_zn_x(1-c)-n_ys & n_zn_y(1-c)+n_xs & n_z^2(1-c)+c \end{pmatrix} , \tag{3.4}$$

with $c \equiv \cos\alpha$, $s \equiv \sin\alpha$, and the random unit vector $\hat{\boldsymbol{n}} = (n_x, n_y, n_z)^T$ is randomly chosen for each collision step and cell [128, 145, 146] according to

$$n_x = \sqrt{1-\zeta^2}\cos\phi\ , \qquad n_x = \sqrt{1-\zeta^2}\sin\phi\ , \qquad n_z = \zeta\ ,$$

where $\phi \in [0, 2\pi]$ and $\zeta \in [-1, 1]$ are uniformly distributed and uncorrelated random numbers [111].

3.1.1.1 Energy and momentum conservation

The choice of the collision rule Eq. (3.2) ensures the local conservation of both kinetic energy and linear momentum for the MPC fluid, for which we provide a detailed proof in the following. The first quantity to prove is the linear momentum, $\boldsymbol{p} = m\boldsymbol{v}$, for an arbitrary cell on the system. This quantity is conserved on this cell, thus in the overall system.

Proof. Taking a collision cell i at a time step t, and defining the particles within this box with the index j, we can define the total linear momentum of cell i at the next time step, $t+h$, as

$$\begin{aligned}\sum_k^{(i,t+h)} m_k \boldsymbol{v}_k(t+h) &= \sum_k^{(i,t)} m_k \boldsymbol{v}_k(t) \\ &= \sum_k^{(i,t)} m_k \Big(\boldsymbol{v}_{cm,i}(t) + \mathbb{R}(\alpha)\left[\boldsymbol{v}_k(t) - \boldsymbol{v}_{cm,i}(t)\right]\Big)\ .\end{aligned}$$

Applying the definition of the centre of mass velocity Eq. (3.3), we inmediately obtain, with some arrangement, the conservation of the linear momentum,

$$\begin{aligned}\sum_k^{(i,t)} m_k \boldsymbol{v}_k(t+h) &= \boldsymbol{v}_{cm,i}(t)\sum_k^{(i,t)} m_k + \mathbb{R}(\alpha)\left[\sum_k^{(i,t)} m_k \boldsymbol{v}_k(t) - \boldsymbol{v}_{cm,i}(t)\sum_k^{(i,t)} m_k\right] \\ &= \boldsymbol{v}_{cm,i}(t)\sum_k^{(i,t)} m_k \\ &= \sum_k^{(i,t)} m_k \boldsymbol{v}_k(t)\end{aligned}$$

□

The same procedure can be done for the kinetic energy of an arbitrary cell i at a time t and $t+h$. This energy is $K = \frac{1}{2}mv^2$.

Proof. Starting with the cell i at time t, with the fluid particles within cell i denoted by the index j, then the kinetic energy of said cell at time $t+h$ is defined as

$$\begin{aligned}
\sum_{k}^{(i,t)} \frac{m_k}{2} v_k^2(t+h) &= \sum_{k}^{(i,t)} \frac{m_k}{2} \Big(\boldsymbol{v}_{cm,i}(t) + \mathbb{R}(\alpha) \left[\boldsymbol{v}_k(t) - \boldsymbol{v}_{cm,i}(t) \right] \Big)^2 \\
&= \sum_{k}^{(i,t)} \frac{m_k}{2} \Big(v_{cm,i}^2(t) + v_k^2(t) - 2\boldsymbol{v}_{cm,i}(t) \cdot \boldsymbol{v}_k(t) \Big) \\
&= v_{cm,i}^2(t) \sum_{k}^{(i,t)} m_k + \sum_{k}^{(i,t)} \frac{m_k}{2} \boldsymbol{v}_k^2(t) - 2\boldsymbol{v}_{cm,i}(t) \sum_{k}^{(i,t)} \frac{m_k}{2} \boldsymbol{v}_k(t) \\
&= \boldsymbol{v}_{cm,i}(t) \sum_{k}^{(i,t)} m_k \boldsymbol{v}_k(t) + \sum_{k}^{(i,t)} \frac{m_k}{2} \boldsymbol{v}_k^2(t) - \boldsymbol{v}_{cm,i}(t) \sum_{k}^{(i,t)} m_k \boldsymbol{v}_k(t) \\
&= \sum_{k}^{(i,t)} \frac{m_k}{2} v_k^2(t)
\end{aligned}$$

where $\mathbb{R}(\alpha)^2 = 1$ has been used as well as the expression

$$\begin{aligned}
v_{cm,i}^2(t) \sum_{k}^{(i,t)} m_k &= \boldsymbol{v}_{cm,i}(t) \cdot \boldsymbol{v}_{cm,i}(t) \sum_{k}^{(i,t)} m_k \\
&= \boldsymbol{v}_{cm,i}(t) \sum_{k}^{(i,t)} m_k \boldsymbol{v}_k(t) \ .
\end{aligned}$$

With this, the conservation of the kinetic energy in cell i is proved. □

3.1.1.2 Restore Galilean invariance: grid shift

The imposition of a grid on the collision step, Eq. (3.2), can lead to some physical issues. Moreover, the collision grid induces an unphysical behaviour of the fluid when considering MPC fluid particles with mean free paths smaller than the collision cell's size, $\lambda < a$. This leads to a system in rest and another system moving at a constant speed to not be exactly equivalent, thus breaking the Galilean invariance, or Galilean relativity, which states that the laws of motion are the same for all inertial frames. The approach proposed to solve this has been the application of a shifting in the predefined grid [147, 148]. This shift displaces the grid by a random number $\zeta \in [-a/2, a/2]$, or similarly, $\zeta \in [0, a]$. By doing so, we are reshuffling the particles into different cells at each collision step by moving the grid randomly. This randomisation is the same for a system at rest and a system at a constant speed, which ultimately leads to the recover of the Galilean invariance[1].

When considering systems confined by walls, a random grid shift leads to collision cells overlapping with the walls, thus with a lower particle density. The decrease of fluid particles in some cells leads to unphysical behaviours in the vicinity of the wall, given that the fluid density ρ determines the physical properties of the fluid. In order to compensate these lower densities, additional virtual particles are typically considered. These particles are added on the cells which overlap with the walls in order to restore the particle density ρ of said cell. The velocity of the virtual particles is taken from a Maxwell-Boltzmann distribution with the fluid's average temperature, $\overline{T}$ [149].

3.1.1.3 Temperature gradients

The presence of thermal gradients in a fluid is essential for this work. These temperature gradients have been implemented in confined MPC fluid by Lüsebrink and Ripoll [150] via two approaches. The first one consists on reescalating the fluid's temperature in short layers close to the confining walls. The authors chose to define a *cold* wall, at temperature T_c, and a *warm* wall, at T_h, with $T_h > T_c$. The fluid particles then see their velocities rescaled on these regions to approach both temperatures. This method is also used in other studies (including this thesis), where the rescaling of velocities has been applied around an asymmetric colloidal surface, creating local temperature gradients [108]. The second approach used by Lüsebrink and Ripoll was to consider the virtual particles discussed in the previous section (see section 3.1.1.2). As explained there, the virtual particles see their velocity drawn from a Maxwell-Boltzmann distribution, via the average fluid's temperature. These velocities can also be drawn by using a defined temperature, such as $T_h > \overline{T}$, thus using the walls as thermostats, creating stable linear temperature gradients.

One can also use the Müller-Plathe approach for non-equilibrium molecular dynamics [151]. This method creates the temperature gradient by defining two regions, cold and warm, within the periodic system. Then, the velocities of the hottest (fastest) particle or particles of the cold region are then exchanged by the velocities of the coldest (slowest) particle or particles of the warm region. This method creates a linear and stable temperature gradient, along with conserving the total energy and momentum. Although this method was originally introduced for MD simulations, it is also proven to be a suitable thermostat for MPC fluids [150].

---

[1] On a typical MPC-SRD code, one may, instead of displacing the grid, displace the temporary position of the fluid particles by a random number $\boldsymbol{\zeta} = (\zeta_x, \zeta_y, \zeta_z)$ in each axis, and apply boundary conditions to restore the particles in the simulation box.

3.1.2 Transport coefficients in MPC-SRD fluids

Two material elements in a fluid with different properties, not initially uniform, exchange some of these mechanical or thermal properties. This group of exchanges constitutes the so-called transport phenomena, from which we can highlight the transfer of matter, energy and momentum [114], characterised by the diffusivity, the thermal conductivity and the viscosity, respectively.

Mass transport in a gas is mostly dominated by the random motion of the actual gas molecules, whereas in liquids, mass transport can be regarded as an interplay between a rapid translation comparable to the particle's diameter, and a slower migrational motion of temporal coordinated clusters of liquid molecules. This leads to gas diffusion coefficient being orders of magnitude higher than the liquid ones, *e.g.*, being the diffusion coefficient of NaCl in water $D_{\mathrm{NaCl}} \sim 10^{-5}\mathrm{cm}^2/\mathrm{s}$, while for nitrogen at 15°C is $D_{\mathrm{N}_2} \sim 0.2$ [114].

The transport of heat in fluids is achieved by the direct exchange of energy and momentum between particles within the range of each other's force fields [114]. It is characterised by the thermal diffusivity, κ_H, which for most liquids is of the order $10^{-3}\mathrm{cm}^2/\mathrm{s}$ (for water at 15°C is $\kappa_H = 1.4 \times 10^{-3}\mathrm{cm}^2/\mathrm{s}$), while for air is a factor 145 higher [114]. However, the thermal conductivity, k_T, weights the thermal diffusivity with the fluid density, ρ, via $\kappa_h = k_T/\rho c_p$, with c_p the specific heat capacity. This leads to that the heat flux per unit of temperature gradient is much higher in liquids than in gases.

The most relevant contribution in momentum transport seems to be the constant reorganisation of clusters of molecules, and the consequent dissipation of energy into heat [114].

The next sections characterise the transport properties of the MPC-SRD fluid, such as the self-diffusion coefficient or the kinematic viscosity. By tuning the MPC parameters, normally the density ρ, the rotational angle α, and the collision time h, the MPC-SRD model can vary the value of its transport coefficients, allowing us to use it to simulate both liquids and gases.

3.1.2.1 Units and the dimensionless mean free path

In this work, lengths are expressed in terms of the collision cell size, a, energies in units of the thermal energy, k_BT, and masses in units of the fluid particle mass, m. This means that these values are the simulation units, taken equal to unity; $a = k_BT = m = 1$. In this scope, time is expressed in units of $t_0 = a\sqrt{m/k_BT}$. The mean free path provides an average fraction of the cell size a travelled by a fluid particle between two collision steps,

$$\lambda = \frac{h}{a}\sqrt{\frac{k_BT}{m}} = \frac{h}{t_0} \; .$$

Note that λ is directly related to h, and it is used in the definition of different fluid properties.

3.1.2.2 Self-diffusion coefficient

The self-diffusion coefficient can be estimated by the Green-Kubo formalism as $D_f = \frac{1}{3}\int_0^\infty \langle \boldsymbol{v}(t)\boldsymbol{v}(t')\rangle \mathrm{d}t$, such that for a discretised time this expression has to be replaced by [122, 148]

$$D_f = \frac{1}{3}\left[\frac{1}{2}\langle \boldsymbol{v}^2(0)\rangle h + \sum_{k=1}^{\infty}\langle \boldsymbol{v}(nh)\cdot\boldsymbol{v}(0)\rangle\right] h \ ,$$

which presents the problem of estimating the term $\langle \boldsymbol{v}(nh)\cdot\boldsymbol{v}(0)\rangle$. Ripoll *et al.* [122] used a molecular chaos approximation of the velocity autocorrelation function. By doing so, the self-diffusion coefficient of a fluid particle reads

$$\frac{D_f}{D_0} = \lambda\left[\frac{3}{2(1-\cos\alpha)}\left(\frac{\rho}{\rho-1}\right) - \frac{1}{2}\right] \ , \tag{3.5}$$

with $D_0 = a\sqrt{k_B T/m}$ and the fluid number density ρ. In this thesis, this density has been chosen as $\rho = 10$ for all systems under study.

The self-diffusion coefficient of a heavier tagged particle of mass M in the MPC-SRD fluid can be similarly obtained as [122, 148]

$$\frac{D_t}{D_0} = \frac{\lambda m}{M}\left[\frac{3}{2(1-\cos\alpha)}\left(\frac{\rho + M/m}{\rho-1}\right) - \frac{1}{2}\right] \ , \tag{3.6}$$

which does not reduce to Eq. (3.5) when $M/m \to 1$ due to the differences in the approximations, although the discrepancies decrease with increasing ρ [124]. Note that Eq. (3.6) is accurate for large mean free paths, where the molecular chaos approximation is valid. Nonetheless, it starts to show deviations for $\lambda \leq 0.6$ due to long-time kinetic correlations, which create hydrodynamic interactions, enhancing the diffusion of a fluid particle [122].

3.1.2.3 Kinematic viscosity

The kinematic viscosity of an MPC-SRD fluid, ν, has been calculated theoretically by means of the kinetic theory [128, 147, 148, 152, 153, 154] and validated by simulations [122]. A velocity fluctuation $\delta\boldsymbol{v}(\boldsymbol{r})$ spreads in a fluid following a diffusion equation,

$$\frac{\partial\delta\boldsymbol{v}(\boldsymbol{r})}{\partial t} = \nu\nabla^2\delta\boldsymbol{v}(\boldsymbol{r}) \ ,$$

where ν is the kinematic viscosity and describes the rate at which vorticity or momentum dissipate or diffuse away on a fluid [124]. The corresponding units are $\nu_0 = a^2/t_0 = a\sqrt{k_B T/m}$, being the same as those for the self-diffusion coefficient, *i.e.*, $\nu_0 = D_0$.

In order to obtain an expression for the kinematic viscosity, first the momentum transport mechanism has to be addressed. In MPC-SRD fluids, momentum is transferred by two main mechanisms [124]. Firstly, by particles ballistically streaming between collision steps, which leads to a kinetic term of the viscosity, ν_{kin}. This is a gas-like contribution, given that the momentum is transferred only due to particle motion, leading to a viscosity scaling as the particle self-diffusion coefficient D_f, *i.e.*, $\nu_{\text{kin}}/\nu_0 \sim \lambda$. Secondly, momentum is also transferred during the collision step via redistribution among the fluid particles of each cell during said step, which leads to a collisional viscosity, ν_{col}. This term mimics the transfer of momentum due to interparticle collisions, a process which is dominant in dense fluids such water at standard temperature and pressure [124]. The scaling of this term can easily be done by a random walk argument. On a collision step, momentum is distributed among all the particles within the same collision cell. Given that there are $1/\lambda$ collision steps per unit time t_0, this suggests that $\nu_{\text{col}}/\nu_0 \sim 1/\lambda$.

Analytical expressions for these viscosities in three dimensions of MPC-SRD have been derived [147, 148, 152, 153, 154], and given by

$$\begin{aligned}
\frac{\nu_{\text{kin}}}{\nu_0} &= \lambda \left[\frac{1}{(4 - 2\cos\alpha - 2\cos 2\alpha)} \frac{5\rho}{\rho - 1} - \frac{1}{2} \right] , \\
\frac{\nu_{\text{col}}}{\nu_0} &= \frac{1}{\lambda} \frac{(1 - \cos\alpha)}{18} \left(1 - \frac{1}{\rho} \right) .
\end{aligned}$$

Note that these expressions only depend weakly on the particle density ρ for the typical parameter set used in simulations [124].

3.1.3 Angular momentum conservation

In spite of conserving both linear momentum and kinetic energy, the MPC-SRD collision rule, Eq. (3.2), does not conserve the angular momentum of each cell. This violation does not have a deep impact on the generic form of the hydrodynamic equations [124, 154, 155, 156], but the fluid stress tensor, Eq. (2.39), is no longer symmetric [114, 154, 157, 158, 159]. The absence of AMC leads to an unphysical contribution in some cases such as for the fluid torque in Couette flow simulations [159]. Thus, AMC has an important role in systems with an inherent rotation, whereas is expected to be irrelevant for non-rotating systems, such as directed swimmers.

In order to circumvent this problem, the collision rule requires an extra correction as suggested by [111, 160], which accounts for the correction of the angular momentum conservation in the bulk fluid. This correction is typically considered in a variant of the MPC method known as the MPC-AT, where AT stands for Andersen thermostat. The MPC-AT collision conserves linear momentum but not kinetic energy, such that it is not appropriate for the non-isothermal conditions employed in this thesis. The AMC correction for MPC-AT is computationally costly, but reasonable. In the case of MPC-SRD, the AMC correction is more elaborate since it needs to ensure the conservation of the three quantities (linear and angular momentum, together with kinetic energy), and results to be computationally more costly.

Yang *et al.* [161] suggested a second method to ensure the conservation of the angular momentum in two dimensional systems, which can also be applied for quasi-two dimensionally confined systems with a 2d confined rotation. This is then achieved by only conserving the angular momentum in the z-direction. The suggested algorithm modifies the rotation matrix $\mathbb{R}(\alpha)$ (Eq. (3.4)) by using another definition of $\cos\alpha$ and $\sin\alpha$,

$$\cos\alpha = \frac{A^2 - B^2}{A^2 + B^2} \tag{3.7}$$

$$\sin\alpha = \frac{2AB}{A^2 + B^2} \tag{3.8}$$

where

$$\begin{aligned} A &= \sum_{k\in\text{cell}} \left\{ \boldsymbol{r}_k \times \Big(\boldsymbol{v}_k - \boldsymbol{v}_k \cdot \boldsymbol{nn} \Big) \right\} \boldsymbol{e}_z \;, \\ B &= \sum_{k\in\text{cell}} \left\{ \boldsymbol{r}_k \times \left[\boldsymbol{n} \Big(\boldsymbol{v}_k - \boldsymbol{v}_k \cdot \boldsymbol{nn} \Big) \right] \right\} \boldsymbol{e}_z \;, \end{aligned}$$

with $\boldsymbol{r}_k$ and $\boldsymbol{v}_k$ the position and velocity of the fluid particle k respect the centre of mass position of cell c and $\boldsymbol{nn} \equiv \boldsymbol{n} \otimes \boldsymbol{n} \equiv \boldsymbol{nn}^\intercal = \sum_i \sum_j n_i n_j \boldsymbol{e}_i \boldsymbol{e}_j$ the dyadic or tensor product.

With these descriptions, the first step is to calculate the product $\boldsymbol{V}_k \equiv \boldsymbol{v}_k - \boldsymbol{v}_k \cdot \boldsymbol{nn}$,

$$\boldsymbol{V}_k = \boldsymbol{v}_k - \begin{pmatrix} v_x & v_y & v_z \end{pmatrix} \begin{pmatrix} n_x n_x & n_y n_x & n_z n_x \\ n_x n_y & n_y n_y & n_z n_y \\ n_x n_z & n_y n_z & n_z n_z \end{pmatrix}$$

Given that we are restricting the rotation in the xy plain, this method only takes into account the z axis components. Thus, the parameter A results in

$$A = \sum_{k \in \text{cell}} \left[r_x \Big(v_y - v_x n_y n_x - v_y n_y n_y - v_z n_y n_z \Big) \right. \\ \left. - r_y \Big(v_x - v_x n_x n_x - v_y n_x n_y - v_z n_x n_z \Big) \right] .$$

Now, we only need to obtain B to implement the AMC. In order to do so, we need to calculate the two cross products, $\boldsymbol{n} \times \boldsymbol{V}_k$, and $\boldsymbol{r}_k \times (\boldsymbol{n} \times \boldsymbol{V}_k)$, which leads to

$$B = \sum_{k \in \text{cell}} \left[r_x \Big\{ n_z \Big(v_x - v_x n_x n_x - v_y n_x n_y - v_z n_x n_z \Big) \right. \\ - n_x \Big(v_z - v_z n_y n_x - v_y n_z n_y - v_z n_z n_z \Big) \Big\} \\ - r_y \Big\{ n_y \Big(v_z - v_x n_z n_x - v_y n_z n_y - v_z n_z n_z \Big) \\ \left. - n_y \Big(v_y - v_x n_y n_x - v_y n_y n_y - v_z n_y n_z \Big) \Big\} \right] .$$

Then, substituting both A and B on Eq. (3.7) and Eq. (3.8) and using these parameters on the collision rule, one assures the conservation of the angular momentum on the z direction. The gain of this method is the minimisation of loops over the fluid particles in its implementation, being computationally cheaper than the full AMC algorithm for MPC-SRD. This implementation modifies then the collision rule in Eq. (3.2). Conservation of linear momentum and energy still applies, but since the rotation angle is not constant, the calculation of the transport properties does not apply anymore. In order to estimate the new viscosity, flow simulations have been made on a two wall slit, from which the parabolic flow profile has been obtained. These simulations have been made with vertical box size between the walls of $L = 20$, $\rho = 10$ and forces $f \in [10^{-5}, 10^{-4}]$, from which the viscosity has been obtained by fitting Eq. (3.9). This flow profile is known as Hagen-Poiseuille flow, and it is described in the linear response regime by [162]

$$v_x(z) = \frac{f\rho}{2\eta}(L - z)z \, , \tag{3.9}$$

with f the external applied force on the x direction, L the simulation box size and z the vertical coordinate along the short side of the cylinder. The results of both

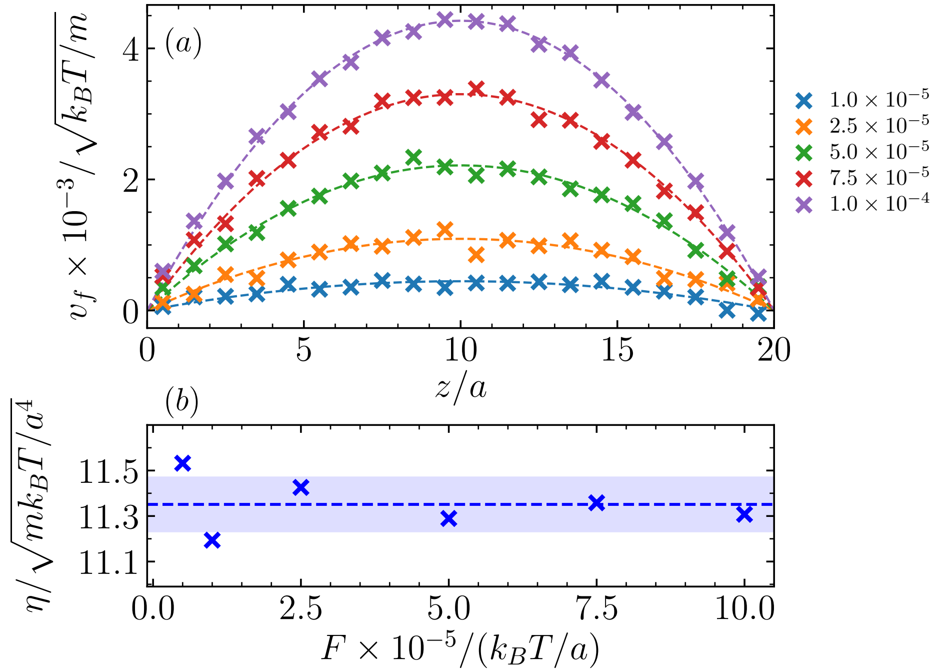

Figure 3.2: Quantification of the effects of AMC in MPC-SRD. (a) Poiseuille flow profile as a function of the force (different colour symbols) in the linear response regime. Symbols correspond to simulation results, while dashed lines correspond to the fit of the simulations to Eq. (3.9). (b) Estimation of the viscosity from (a) as a function of the force, with the dashed line corresponding to the average value and the blue region as the standard deviation.

the Hagen-Poiseuille parabolic flow and the estimation of the viscosity at different forces are shown in Fig. 3.2. The obtained viscosity $\eta \sim 11.35$ differs significantly with that from the MPC-SRD-a with $\alpha = 120$, $\eta = 7.92$. With this η value, the Schmidt number results in Sc = 97.3 and the Prandlt number in Pr = 6.3, which is very close to that of water at 18°C, Pr = 7.56 [163].

3.2 Molecular dynamics

The complexity of some systems causes that the fully experimental analysis is not sufficient to gain a deep understanding of the processes of the microscale in that system. Moreover, analytical descriptions of these systems are out of the equation, due to the impossibility of obtaining the properties of such complex systems due to the vast amount of particles, *i.e.*, degrees of freedom in the analytical equations. In order to circumvent these challenges, a new method emerged. Instead of using analytical methods, one can use numerical methods by means of computer simulations. Molecular dynamics is then used, as its name indicates, to study the motion of particles by integrating Newton's equations numerically. Nevertheless, computer simulations can induce cumulative errors due to the numerical integration of equations, which need to be minimised by the choice of a proper algorithm.

Molecular dynamics (MD) was introduced in the early 1950s as a way to solve the time evolution of N-body systems, a trouble Newton already faced and that extended in the XVI century due to the deep interest in the dynamics of the celestial bodies of the solar system. The first application of MD was in materials science, but since the 1970s it was also introduced and commonly used in biophysics and biochemistry. Nowadays, molecular dynamics is one of the most broadly used simulation method in a wide variety of fields in science.

3.2.1 Algorithm

A molecular dynamics simulation algorithm can be summarised in two main parts. The first one is the numerical integration of the motion equations, Newton's second law, by means of an integrator. The second part is the determination of the pairwise interactions between the many particles under study, obtaining then the total force acting upon each of these particles. In order to choose a proper integrator, several details must be taken into account. The easiest to implement is the common Euler integrator, which is just an update of both positions and velocities, assuming linear time evolution. This integrator induces an energy drift due to the lack of symmetry under time reversal, only being symmetric at $\Delta t \to 0$, thus not being adequate for most systems, given that large simulation times would require an excessive amount of timesteps.

One of the most widely used MD integrators is the velocity-Verlet [164], for its simplicity to implement, its stability to higher Δt and to be symplectic [165, 166]. This algorithm reads [165, 167]

$$\boldsymbol{r}_k(t+\Delta t) = \boldsymbol{r}_k(t) + \boldsymbol{v}_k(t)\Delta t + \frac{1}{2m_k}\boldsymbol{f}_k(t)\Delta t^2 \ , \tag{3.10}$$

$$\boldsymbol{v}_k(t+\Delta t) = \boldsymbol{v}_k(t) + \frac{1}{2m_k}\left[\boldsymbol{f}_k(t+\Delta t) + \boldsymbol{f}_k(t)\right]\Delta t^2 \ , \tag{3.11}$$

with $\boldsymbol{r}_k$, $\boldsymbol{v}_k$ and $\boldsymbol{f}_k$ the positions, velocities and forces of the particle k, respectively, evaluated in two consecutive time steps, t and $t+\Delta t$, and m_k the mass of said particle. This algorithm is indeed symmetric under time reversal, therefore ensuring the energy conservation.

Proof. $\Delta t \to -\Delta t$

$$\boldsymbol{r}_k(t-\Delta t) = \boldsymbol{r}_k(t) - \boldsymbol{v}_k(t)\Delta t + \frac{1}{2m_k}\boldsymbol{f}_k(t)\Delta t^2 \ , \tag{3.12}$$

$$\boldsymbol{v}_k(t-\Delta t) = \boldsymbol{v}_k(t) - \frac{1}{2m_k}\left[\boldsymbol{f}_k(t-\Delta t) + \boldsymbol{f}_k(t)\right]\Delta t^2 \ . \tag{3.13}$$

Now $t-\Delta t \to t$ and $t \to t+\Delta t$, equations Eq. (3.12) and Eq. (3.13) lead to

$$\boldsymbol{r}_k(t) = \boldsymbol{r}_k(t+\Delta t) - \boldsymbol{v}_k(t+\Delta t)\Delta t + \frac{1}{2m_k}\boldsymbol{f}_k(t+\Delta t)\Delta t^2 \ ,$$

$$\boldsymbol{v}_k(t) = \boldsymbol{v}_k(t+\Delta t) - \frac{1}{2m_k}\left[\boldsymbol{f}_k(t) + \boldsymbol{f}_k(t+\Delta t)\right]\Delta t^2 \ .$$

Reordering the elements, the velocity recovers its form from Eq. (3.11), and the position yields

$$\boldsymbol{r}_k(t+\Delta t) = \boldsymbol{r}_k(t) + \boldsymbol{v}_k(t+\Delta t)\Delta t - \frac{1}{2m_k}\boldsymbol{f}_k(t+\Delta t)\Delta t^2 \ . \tag{3.14}$$

Substituting the velocity, Eq. (3.11), on the positions, Eq. (3.14),

$$\begin{aligned}\boldsymbol{r}_k(t+\Delta t) &= \boldsymbol{r}_k(t) + \left[\boldsymbol{v}_k(t) + \frac{1}{2m_k}\left[\boldsymbol{f}_k(t) + \boldsymbol{f}_k(t+\Delta t)\right]\Delta t^2\right]\Delta t \\ &\quad - \frac{1}{2m_k}\boldsymbol{f}_k(t+\Delta t)\Delta t^2 \\ &= \boldsymbol{r}_k(t) + \boldsymbol{v}_k(t)\Delta t + \frac{1}{2m_k}\boldsymbol{f}_k(t)\Delta t^2 \ ,\end{aligned}$$

we recover the equation of the position update Eq. (3.10). □

In this work, this algorithm is chosen to update the positions and velocities of the colloidal particles, with a time step of $\Delta t = 10^{-3}$.

3.2.2 Forces

When simulating molecules or colloidal ensembles with a well determined structures such as polymers, rod-like colloids, or even helical or protein-like structures, intramolecular interactions need to be considered in order to keep the defined structure.

In this work, the dimers and trimers are held together via a stretching and bending interactions in the shape of harmonic potentials. Intermolecular interactions are described by both the steric interactions defined by a Mie-like potential, similar to the MD case for the hydrodynamic simulations, and thermophoretic interactions between the heated and phoretic beads of both the same and different swimmers. No external forces have been applied.

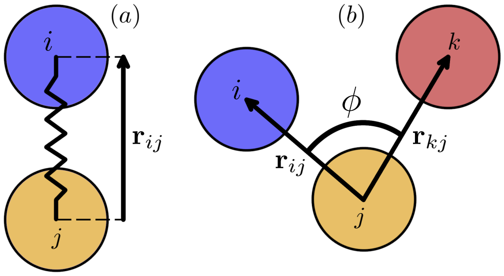

Figure 3.3: Scheme of (*a*) the stretching potential used to connect the beads of the same swimmer via a harmonic spring and (*b*) the bending potential in order to give shape to the trimeric swimmer (linear, $\phi_0 = \pi$, or v-shaped, $\phi_0 = 2\arcsin\left[s_p/(s_p + s_h)\right]$).

3.2.2.1 Intramolecular forces

In order to keep the beads of a polymer together, or in our case, keep the heated and the phoretic beads connected, a stretching term between the beads is considered. We employ a harmonic potential, which results in a linear force

$$\boldsymbol{F}_{\text{bond}} = -2\kappa_b(|\boldsymbol{r}_{ij}| - r_0)\hat{\boldsymbol{n}} \ , \tag{3.15}$$

where κ_b is the spring constant, $\boldsymbol{r}_{ij} = \boldsymbol{r}_i - \boldsymbol{r}_j$ is the distance between the centres of two connected beads, r_0 is the equilibrium distance, usually the sum of the radii of the beads, and $\hat{\boldsymbol{n}}$ the normal direction bead-bead, *i.e.*, $\boldsymbol{r}_{ij}/|\boldsymbol{r}_{ij}|$ (see Fig. 3.3a).

When rigidity needs to be considered, this is done by means of a bending term in the forces, which in this work is used to study systems of three beads with a defined angle between them. We implemented the standard three-body harmonic interaction potential [168] using the angle formed by three consecutive beads (see Fig. 3.3b), corresponding to the phoretic (i, k) and the heated (j) beads. This potential has the form

$$U_\phi(r) = \kappa_\phi(\cos\phi - \cos\phi_0)^2 \ ,$$

being κ_ϕ the spring constant of the bending term, and ϕ_0 the preferred angle, which was set to $\phi_0 = \pi$ for linear trimers and $\phi_0 = 2\arcsin\left[s_p/(s_p + s_h)\right]$ for v-shaped trimers, with s_p and s_h the radius of the phoretic and heated beads, respectively. The bending force is equal to minus the gradient of the potential, *i.e.*,

$$\boldsymbol{F}_\phi = -\nabla_{\boldsymbol{r}} U_\phi = -\nabla_{\boldsymbol{r}}\phi \frac{\partial U_\phi}{\partial \phi} \ .$$

However, since $\phi = \arccos\left(\frac{\boldsymbol{r}_i \cdot \boldsymbol{r}_j}{|\boldsymbol{r}_i||\boldsymbol{r}_j|}\right)$ and $\nabla_{\boldsymbol{r}}\phi \propto \sin^{-1}\phi$, this expression presents a singularity for angles $\phi = 0$ and π. We use a solution to this issue given by

Swope and Ferguson [169]. The expression of the bending force is now rewritten as

$$\boldsymbol{F}_\phi = -\frac{\partial U_\phi}{\partial \phi}\frac{\partial \phi}{\partial \cos\phi}\nabla_{\boldsymbol{r}} \cos\phi,$$

with

$$\frac{\partial U_\phi}{\partial \phi} = -2\kappa_\phi(\cos\phi - \cos\phi_0)\sin\phi,$$

and

$$\frac{\partial \phi}{\partial \cos\phi} = \frac{-1}{\sin\phi}.$$

Then, the angular forces due to the angle bending that acts upon the monomers result in

$$\begin{aligned}\boldsymbol{F}_\phi &= -2\kappa_\phi(\cos\phi - \cos\phi_0)\nabla_{\boldsymbol{r}} \cos\phi \\ &\equiv F_\phi \nabla_{\boldsymbol{r}} \cos\phi,\end{aligned}$$

with $F_\phi \equiv -2\kappa_\phi(\cos\phi - \cos\phi_0)$ defined as the strength of the bending force.

In order to evaluate the cosine and its gradient, we use the vectors connecting the monomer j with its consecutive beads $i = j - 1$ and $k = j + 1$. Then, $\boldsymbol{r}_{ij} = \boldsymbol{r}_i - \boldsymbol{r}_j$ and $\boldsymbol{r}_{kj} = \boldsymbol{r}_k - \boldsymbol{r}_j$ (see Fig. 3.3). In terms of the two vectors, we calculate the cosine of the angle between those beads as

$$\cos\phi = \frac{\boldsymbol{r}_{ij} \cdot \boldsymbol{r}_{kj}}{|\boldsymbol{r}_{ij}||\boldsymbol{r}_{kj}|}.$$

The components of the gradient result from the derivation of the previous equation with respect to both vectors,

$$\begin{aligned}\nabla_\mu \cos\phi &= \hat{\boldsymbol{x}}\frac{\partial \cos\phi}{\partial x_{\mu j}} + \hat{\boldsymbol{y}}\frac{\partial \cos\phi}{\partial y_{\mu j}} + \hat{\boldsymbol{z}}\frac{\partial \cos\phi}{\partial z_{\mu j}}\ , \\ \nabla_j \cos\phi &= -\,\hat{\boldsymbol{x}}\left(\frac{\partial \cos\phi}{\partial x_{ij}} + \frac{\partial \cos\phi}{\partial x_{kj}}\right) \\ &\quad -\,\hat{\boldsymbol{y}}\left(\frac{\partial \cos\phi}{\partial y_{ij}} + \frac{\partial \cos\phi}{\partial y_{kj}}\right) \\ &\quad -\,\hat{\boldsymbol{z}}\left(\frac{\partial \cos\phi}{\partial z_{ij}} + \frac{\partial \cos\phi}{\partial z_{kj}}\right),\end{aligned}$$

where $\mu = i, k$.

Finally, the last expression that we need is the derivative of the cosine with respect to each coordinate, which reads

$$\frac{\partial \cos\phi}{\partial x^{\nu}_{ij}} = \frac{1}{|\boldsymbol{r}_{ij}|}\left(\frac{x^{\nu}_{kj}}{|\boldsymbol{r}_{kj}|} - \frac{x^{\nu}_{ij}}{|\boldsymbol{r}_{ij}|}\cos\phi\right),$$

$$\frac{\partial \cos\phi}{\partial x^{\nu}_{kj}} = \frac{1}{|\boldsymbol{r}_{kj}|}\left(\frac{x^{\nu}_{ij}}{|\boldsymbol{r}_{ij}|} - \frac{x^{\nu}_{kj}}{|\boldsymbol{r}_{kj}|}\cos\phi\right),$$

with $\nu = 1, 2, 3$ representing the three Cartesian coordinates (x, y, z).

Thus, putting all the pieces together, the force term related to the bending rigidity of our polymeric chain is

$$F^{\nu}_{i} = F_{\phi}\frac{1}{|\boldsymbol{r}_{ij}|}\left(\frac{r^{\nu}_{kj}}{|\boldsymbol{r}_{kj}|} - \frac{r^{\nu}_{ij}}{|\boldsymbol{r}_{ij}|}\cos\phi\right),$$

$$\begin{aligned} F^{\nu}_{j} = F_{\phi}\Bigg[&\frac{1}{|\boldsymbol{r}_{ij}|}\left(\frac{r^{\nu}_{ij}}{|\boldsymbol{r}_{ij}|}\cos\phi - \frac{r^{\nu}_{kj}}{|\boldsymbol{r}_{kj}|}\right) \\ &+ \frac{1}{|\boldsymbol{r}_{kj}|}\left(\frac{r^{\nu}_{kj}}{|\boldsymbol{r}_{kj}|}\cos\phi - \frac{r^{\nu}_{ij}}{|\boldsymbol{r}_{ij}|}\right)\Bigg], \end{aligned}$$

$$F^{\nu}_{k} = F_{\phi}\frac{1}{|\boldsymbol{r}_{kj}|}\left(\frac{r^{\nu}_{ij}}{|\boldsymbol{r}_{ij}|} - \frac{r^{\nu}_{kj}}{|\boldsymbol{r}_{kj}|}\cos\phi\right),$$

where the sinus on the denominator has been cancelled, eliminating all possible divergences for $\phi = 0, \pi$.

Although this is applied to systems of only three beads each, this description is generalised, and can be perfectly used for polymeric chains of N monomers, where $i = j - 1$ and $k = j + 1$.

3.2.2.2 Excluded volume interactions

In order to avoid overlapping between different swimmers, excluded volume effects are accounted for using the same intermolecular Mie-like potential, with $n = 24$. The interaction force then yields,

$$\boldsymbol{F} = -\frac{96\epsilon}{r}\left[2\left(\frac{\sigma}{r}\right)^{48} - \left(\frac{\sigma}{r}\right)^{24}\right]\hat{\boldsymbol{r}}\ . \qquad (3.16)$$

where the distance $\sigma = s_i + s_j + \delta$, with $\delta = 0.2(s_i + s_j)$ in order to reproduce the results from the full hydrodynamic simulations, where this extra distance has to be introduced in order to avoid depletion effects between the colloids [108] [2]. Then, Eq. (3.16) can be rewritten as

$$\boldsymbol{F} = -96\epsilon\sigma^{24} r_i^2 r_i^{24} \left[\sigma^{24} r_i^{24} - 1\right] \hat{\boldsymbol{r}} \ , \tag{3.17}$$

where the same procedure as Eq. (3.17) has been done for σ, and where $\delta\boldsymbol{r}$ is again the normalised distance between particles.

3.2.2.3 Intermolecular interactions

Intermolecular interactions in nature are very complex, and so far no exact theoretical expression has been derived. This arises from the fact that we can not obtain a closed-form analytical solution for the three-body problem, *i.e.*, the interaction between three bodies at once. This is the so-known N-body problem. The relevance of this issue is determining on molecular simulations, given the amount of interacting particles under study. Thus, the N-body potential interactions must be approximated by other approaches. One approximation is to describe the non-bonded potential interactions by splitting the potential into a sumatory of k-body terms, with k the number of particles involved in the interaction [167],

$$U(\boldsymbol{r}^N) = \sum_k u(\boldsymbol{r}_k) + \sum_i \sum_{j>i} v(\boldsymbol{r}_i, \boldsymbol{r}_j) + \mathcal{O}(3) \ .$$

Here the first term corresponds to externally applied potential fields. The second term describes particle interactions given by the pair potential, $U(\boldsymbol{r}_i, \boldsymbol{r}_j) = U(r_{ij})$, which depends on the inter-particle distance $\boldsymbol{r}_{ij} \equiv \boldsymbol{r}_i - \boldsymbol{r}_j$. By doing so, the N-body problem can be approximately solved via a paired potential [167].

On this work, in order to describe all the interactions involving colloidal particles we have used a modified Mie-like potential, whose general definition yields [170]

$$\phi(r) = \left(\frac{m}{m-n}\right)\left(\frac{m}{n}\right)^{n/(m-n)} \epsilon \left[\left(\frac{\sigma}{r}\right)^m - \left(\frac{\sigma}{r}\right)^n\right] \ . \tag{3.18}$$

---

[2] In order to optimise the code, the expression of these forces can be arranged by means of a clever idea. By means of defining the inverse of the distance as a variable, $r_i = 1/r$, and then calculating the square of it $r_i^2 = r_i \cdot r_i$, one can then multiply it until obtaining the desired power laws required,

$$r_i^{2n} = \prod^n r_i^2 \ ,$$

which leads, *e.g*, to that r_i^{24} is obtained by multiplying twelve times r_i^2. This method implies more lines of code and some extra definitions, but in the large scale of a complete Brownian dynamics simulations of hundreds of particles for thousands of time steps, the gain in time is substantial.

The exponents m and n can be varied depending on the nature of the particle and the interaction we want to describe, but the ratio between them has been kept constant, $m = 2n$. One of the most used forms of this potential correspond to the Lennard-Jones (LJ) potential, which was first introduced by Sir John Edward Lennard-Jones in 1924 [171]. This potential is defined by choosing the first exponent from Eq. (3.18) as $m = 2n$, being the most commonly used exponent $n = 6$,

$$\begin{aligned} U_{LJ}(r) &= 4\varepsilon \left[\left(\frac{\sigma}{r} \right)^{12} - \left(\frac{\sigma}{r} \right)^{6} \right] \\ &= \varepsilon \left[\left(\frac{r_m}{r} \right)^{12} - 2 \left(\frac{r_m}{r} \right)^{6} \right] , \end{aligned} \tag{3.19}$$

with ε is the potential depth, σ the distance at which the inter-particle potential is zero and $r_m = 2^{1/6}\sigma$, which corresponds at the distance at which the potential displays its minimum, *i.e.*, $-\varepsilon$. A common cutoff chosen for this potential is $r_c = 2.5\sigma$. Nevertheless, by choosing the cutoff radius as $r_c = 2^{1/6}\sigma$, or just r_m, the attractive part of the potential is cut off, leading to a purely repulsive potential, referred to as the Weeks-Chandler-Andersen (WCA) potential [172]. Finally, the value of C is always chosen such as the potential vanishes at the cutoff radius, r_c, in order to avoid discontinuities in the energies when two particles approach each other from beyond r_c. In the case of the full potential, $C = 0$, while for a purely repulsive potential (WCA), $C = \varepsilon$.

On this work, the steric, or excluded volume, effects between different colloidal particles are described by a generalised Lennard-Jones-type potential, Eq. (3.21), with $n = 24$. The interactions between fluid particles and colloids have been also modelled using the same potential as the steric effects with a general n exponent. Given the comparable sizes of the interacting fluid and colloidal particles, undesired depletion interactions between colloids can be induced [173, 174]. These depletion forces are entropic in origin, as first explained by the stablished Asakura-Oosawa model [175, 176]. The solvent particles act here as depletants and define the so-known depletion layer via their interaction with the bigger colloidal particles.

The depletion area is the overlap of the solvent-colloid interaction layers where two colloids are close to each other [177]. This depletion layer induces an attractive and osmotic depletion force between the colloids [173, 178], which acts on the outer surfaces of the colloids, promoting flocculation [179].

In the case of colloids, bare Mie potentials have large interaction layers, enhancing then depletion effects. The solution is then to increase the colloid size without varying the width of the interaction layer [180]. This can be achieved with displacements of the potential. This potential is then described by [108]

$$U(r) = \begin{cases} \infty \, , & r \leq \Delta \, , \\ 4\varepsilon \left[\left(\frac{\sigma}{r-\Delta} \right)^{2n} - \left(\frac{\sigma}{r-\Delta} \right)^{n} \right] + C \, , & \Delta < r < r_c \, , \\ 0 \, , & r_c \leq r \, , \end{cases} \tag{3.20}$$

where Δ enlarges the pairwise distance between colloids without modifying neither the shape of the pontential nor the effective size of the colloidal particle [181]. If this displacement is $\Delta > 0$, this effective radius is defined as $s = \sigma + \Delta$, leading to a parameter set $(s, \Delta, \varepsilon, n, r_c)$, where r_c depends on the chosen potential, *i.e.*, the thermophoretic nature [182]. Purely repulsive interactions between the colloid and the fluid particles are obtained by setting the cutoff radius as $r_c = 2^{1/n}\sigma + \Delta$, $n = 3$ and $C = \varepsilon$, and are proved to result in thermophilic nature [74, 110], and are shown as red lines in Fig. 3.4. For full potentials, with both the attractive and repulsive parts, $C = 0$ and the cutoff radius is set as the distance at which the value of the energy equals the corresponding of Eq. (3.20) with $\varepsilon = 1$, $n = 24$ and $r = 2.5\sigma$, thus

$$r_c = \Delta + \left[\frac{1}{2\varepsilon} \left(\varepsilon - \sqrt{\varepsilon \left(\varepsilon + U_{LJ,\varepsilon=1}(2.5\varepsilon) \right)} \right) \right]^{-1/n} \sigma \tag{3.21}$$

corresponds to the expression of the cutoff of the full potential. This potential leads then to the thermophobic behaviour [110, 74], and it is shown in Fig. 3.4 as blue lines.

The motion is achieved by means of a local temperature gradient applied to one of the swimmer's beads, known as the heated bead. The heating mechanism mimics the heating obtained by a laser source and illuminating a sample of partially gold-coated particles [81]. This has been implemented by rescaling the temperature of the fluid particles on a spherical short layer of $0.08 s_h$ around the heated particle up to a temperature of $T_h = 1.5$, while the overall fluid temperature is kept constant at $\overline{T} = 1.0$. The temperature rescaling has been achieved by a simple velocity rescaling [82, 108, 180, 182],

$$\boldsymbol{v}' = \sqrt{\frac{T_h}{T}} \boldsymbol{v} \, , \tag{3.22}$$

with T the current temperature, and $\boldsymbol{v}$ and $\boldsymbol{v}'$ the original and rescaled velocities of the fluid particles, respectively.

3.2.3 MPC-MD coupling

In order to simulate a colloidal suspension, a hybrid model considers MD to simulate the colloids and MPC-SRD to simulate the fluid. There is more than one

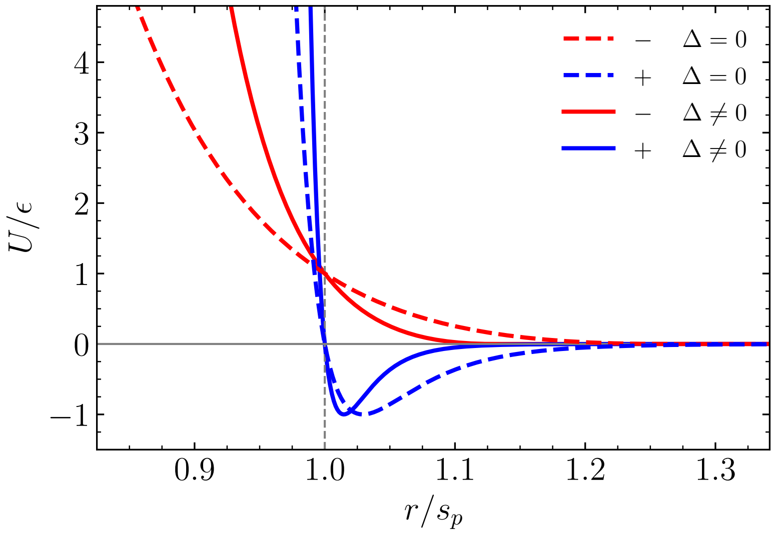

Figure 3.4: Representation of displaced (continuous lines) and non-displaced (dashed lines) Mie-like potentials for (red) thermophilic behaviour (WCA potential) and (blue) thermophobic nature (full potential).

method to couple MD with MPC to account for the colloid-solvent interactions. One straightforward way to implement this coupling is to consider the colloid as heavy fluid particles, such that they simply take part in the collision rule, contributing with a higher mass. This MPC-coupling has shown to be very efficient when applied to linear and star polymers or rods, among others [183]. Another way to approach this coupling is by describing the interacting between colloid and fluid through the introduction of pair-wise interaction potentials as done in MD simulations [143]. Although computationally more expensive, this method, known as MPC-MD coupling, has the advantage of allowing for a more precise and tunable description of the interaction properties between colloid and fluid, avoiding the penetration of the solvent in the colloid radius and enhancing the surface colloid-solvent interactions. This last approach is the one used in this work, as we need the molecular interactions between fluid and colloid to determine the response of the colloid to temperature gradients, thus describe the thermophoresis.

All hydrodynamic simulations, where the MPC-MD coupling for fluid and colloids has been used, are implemented in Lammps. This is a versatile, open-source framework for molecular simulations. Although it is, in its core, aimed at classic MD simulations, it is still very suitable for coarse-grained, mesoscale or continuous scenarios [184]. The main core of Lammps includes a parallel implementation of the MPC algorithm, in its SRD approach, with the implementation details discussed in [185]. This work is based on the study of the single and collective behaviour of active colloidal microswimmers, thus the systems range from small to large-scale simulation via the MPC-MD coupling. The packages Lammps offers are MPI-parallelised, highly optimised MD and a basic MPC algorithms, but not the coupling we require. Wagner [108] implemented an efficient coupling with a variety of other features, such as flow field measurements and specific thermostats, into Lammps. Extra modifications have been added in order to adapt the code to the trimer cases. More details on the implementation of such coupling can be found in [108].

3.3 Brownian Dynamics

Most of the biological systems contained in the soft matter field mentioned in the introduction are in aqueous solutions. Nonetheless, the effects of the fluid are not always required as precise as full-hydrodynamic simulations can offer, and the price for such methods is sometimes too high. Brownian dynamics, called after Robert Brown, is a simulation method that solves the Langevin equation for colloids in its overdamped regime, as described in section 2.1.

Brownian dynamics, or BD, assumes that the collisions between the fluid particles and the colloid induce a random displacement of the colloid positions, along a local friction proportional to its velocity [124]. Thus, all the fluid particles are omitted from the simulations. This method is nowadays very popular, and finds its uses in a broad variety of physical and biological systems [186, 187, 188, 189, 190], though it completely neglects momentum transport through the solvent, thus neglecting all hydrodynamic interactions. It is furthermore very interesting when used to compare with simulations with full hydrodynamic interactions, since the importance of those, large or small, can be clearly distinguished.

In the following, we introduce the Brownian dynamics algorithm based on the Langevin equation introduced in section 2.1, and specify in detail the parameters that have to be used for a fair comparison with the MPC-MD simulations employed in this dissertation.

3.3.1 Algorithm

The motion equation that describes the time evolution of the position, $\boldsymbol{r}_n$, of the particle n in a BD simulation is, as mentioned in section 2.1, the Langevin equation,

$$m\ddot{\boldsymbol{r}}_n = \boldsymbol{F}(\boldsymbol{r}_n) - \gamma\dot{\boldsymbol{r}}_n + \boldsymbol{\xi}^n(t) \ , \tag{3.23}$$

where γ is the friction coefficient, m is the mass of the particle, $\boldsymbol{F}(\boldsymbol{r})$ is the total sum of forces acting on particle n and $\boldsymbol{\xi}(t)$ is a delta-correlated Gaussian and

Markovian random force with zero-mean,

$$\langle \boldsymbol{\xi}^n(t) \rangle = 0,$$

and correlation

$$\langle \xi_i^n(t) \cdot \xi_j^m(t') \rangle = 2\gamma k_B T \; \delta(t - t') \; \delta_{ij} \; \delta_{nm} \; ,$$

with $i, j = x, y, z$ and $n, m \in [1, N]$ the particles under simulation.

For colloids at low Reynolds numbers, Eq. (3.23) reads

$$\dot{\boldsymbol{r}}_n(t) = \frac{\boldsymbol{F}_n(t) D}{k_B T} + \sqrt{2D} \; \boldsymbol{\xi}_n(t) \; . \tag{3.24}$$

In this description, the friction of the Einstein relation, γ, can be chosen to correspond to our MPC-MD model. This friction force then yields, in its general form,

$$\boldsymbol{F}_\gamma = -C_f \pi \eta \sigma_c \boldsymbol{v} \; , \tag{3.25}$$

with σ_c the radius of the bead, η the fluid viscosity and C_f a parameter set by the fluid and boundary conditions of the colloid. Pooley and Yeomans [158] used a kinetic theory approach to derive the heat conduction and continuum Navier-Stokes equations for an SRD fluid. With this, they obtained the expressions for the viscosity and thermal conductivity of the SRD fluid. Their model leads to Eq. (3.25) with $C_f = 3$ for a colloid with slip boundary conditions and with an SRD fluid without angular momentum conservation (AMC) as a solvent, instead of the $C_f = 6$ for a no-slip boundary condition, as the Stokes-Einstein equation describes. This result is proved by Yang *et al.* [191] by estimating the friction forces and friction coefficients for an SRD fluid without angular momentum conservation (MPC-SRD-a), obtaining $C_f = 2.91$. In the case of MPC-SRD+a, the friction force upon a colloid with slip boundary conditions yields to Eq. (3.25) with $C_f = 4$ [158, 192].

The algorithm used to integrate Eq. (3.24) is stochastic Euler's. This algorithm gives the position, $\boldsymbol{r}_n(t + \Delta t)$, and the velocity, $\boldsymbol{v}_n(t + \Delta t)$, of each bead at a time $t + \Delta t$ as

$$\begin{aligned} \boldsymbol{r}_n(t + \Delta t) &= \boldsymbol{r}_n(t) + \frac{\boldsymbol{F}_n(t) D}{k_B T} \Delta t + \sqrt{2D\Delta t} \; \boldsymbol{\xi}_n(t) \; , \\ \boldsymbol{v}_n(t + \Delta t) &= \frac{\boldsymbol{r}_n(t + \Delta t) - \boldsymbol{r}_n(t)}{\Delta t} \; . \end{aligned} \tag{3.26}$$

The total force applied to a colloidal bead in a BD simulation is the sum of intra- and inter-molecular interactions, and externally induced forces.

3.3.2 Thermophoretic Brownian Dynamics

When studying ensembles of thermophoretic swimmers, one needs to characterise the intermolecular interactions between beads of different swimmers. In this code, these interactions are the excluded volume effects (see 3.2.2.2) and the thermophoretic interactions. In MPC-MD simulations, phoresis appeared as a consequence of the solvent-colloid interactions in the presence of a temperature gradient. This is not the case for BD, where phoresis has to be specifically introduced.

In order to get a correct description of the thermophoretic force Eq. (2.33) is here applied. The force a phoretic bead experiences when near of a heated bead yields,

$$\boldsymbol{F}_T = -\alpha_T k_B \nabla_{\boldsymbol{r}} T \delta \boldsymbol{r} \ ,$$

where $\nabla_{\boldsymbol{r}} T$ is the gradient of temperature, α_T the thermodiffusion coefficient, k_B is the Boltzmann constant and $\delta \boldsymbol{r} = \Delta \boldsymbol{r} / |\Delta \boldsymbol{r}|$ the normalised distance between beads of different swimmers, *i.e.*, $\boldsymbol{r}_p - \boldsymbol{r}_h$. The temperature gradient has been calculated by solving the Laplace equation,

$$\nabla^2 T(\boldsymbol{r}) = 0 \ , \tag{3.27}$$

for the case of a point temperature point. In spherical coordinates, the Laplacian of the temperature reads,

$$\nabla^2_{\boldsymbol{r}} T(\boldsymbol{r}) = \frac{1}{r^2}\frac{\partial}{\partial r}\left(r^2 \frac{\partial T(\boldsymbol{r})}{\partial r}\right) + \frac{1}{r^2 \sin\theta}\frac{\partial}{\partial \theta}\left(\sin\theta \frac{\partial T(\boldsymbol{r})}{\partial \theta}\right) + \frac{1}{r^2 \sin^2\theta}\frac{\partial^2 T(\boldsymbol{r})}{\partial \phi^2} \ .$$

In this case, all angular terms vanish due to the symmetry of the system. This equation is easily solved analytically by imposing the boundary conditions $T(r = s_h) = T_h$ and $T(r \to \infty) = \overline{T}$, with T_h the temperature of the heated bead and $\overline{T}$ the average fluid temperature, taken as the reference unit. The solution of Eq. (3.27) reads then

$$T(r) = \left(\frac{T_h - \overline{T}}{r}\right) s_h + \overline{T} \ , \tag{3.28}$$

where $r = |\boldsymbol{r}_p - \boldsymbol{r}_h|$.

This temperature field is evaluated at the centre of the phoretic bead, instead of in its surface. In order to obtain a more physical value of the temperature gradient, Eq. (3.28) is integrated along the phoretic bead's diameter. For a phoretic and heated beads at distance r and of radii s_p and s_h, the integral limits are $R_i = r - s_p$

and $R_f = r + s_p$, and the integral results in

$$\begin{aligned}\langle \nabla T \rangle &= \frac{1}{R_f - R_i} \int_{R_i}^{R_f} \nabla T \mathrm{d}r \\ &= \frac{1}{2s_p} \int_{r-s_p}^{r+s_p} \left(\frac{\overline{T} - T_h}{r^2} \right) s_h \mathrm{d}r \\ &= \frac{(\overline{T} - T_h) s_h}{(r+s_p)(r-s_p)} \; . \end{aligned} \tag{3.29}$$

These are the necessary elements to determine adequate phoretic BD simulations, where the self-propulsion varies simultaneously with the intercolloid attraction or repulsion, whose sign and intensity are provided by the sign of α_T.

3.3.2.1 Estimation of α_T

Since one of the main goals of this phoretic BD simulations is to compare them with the corresponding hydrodynamic simulations, one important point is to determine the value of α_T that better fits these simulations. For this purpose, we aim at obtaining the measured self-propulsion velocity,

$$v_{sp} = \frac{\alpha_T k_B}{C \pi \eta (s_p + s_h)} \langle \nabla T \rangle \; , \tag{3.30}$$

from which we estimate the value of α_T, by fitting this equation with the obtained results, as shown in Fig. 3.5.

In order to estimate the value of α_T, we need the value of the temperature gradient that a phoretic bead feels while in contact with a heated bead. Thus, we need to use Eq. (3.29) with $r = s_p + s_h$, leading to

$$\begin{aligned}\langle \nabla T \rangle &= \frac{1}{R_f - R_i} \int_{R_i}^{R_f} \nabla T \mathrm{d}r \\ &= \frac{1}{2s_p} \int_{s_h}^{s_h+2s_p} \left(\frac{\overline{T} - T_h}{r^2} \right) s_h \mathrm{d}r \\ &= \frac{T_h - \overline{T}}{s_h + 2s_p} \; , \end{aligned} \tag{3.31}$$

where $R_i = s_h$ and $R_f = 2s_p + s_h$.

With the definition of the temperature gradient, $\langle \nabla T \rangle$, the thermodiffusion coefficient, α_T, and the friction of each bead, $\gamma = C_f \pi \eta (s_p + s_h)$, the self-propulsion velocity of the dimer has been obtained. Besides getting the same value of v_{sp}, it is also importart to adjust the Péclet number. The solution found to solve

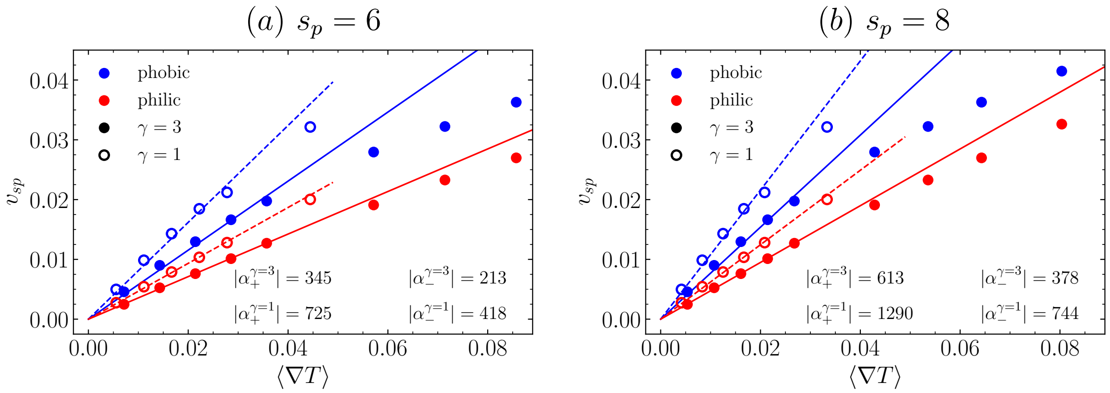

Figure 3.5: Self-propulsion velocity for a thermophobic (blue) and thermophilic (red) dimer ((*a*) for $s_p = 6$ and (*b*) for $s_p = 8$) as a function of the temperature gradient felt by the phoretic bead, $\langle \nabla T \rangle$. The linear regression has been done via Eq. (3.30), where $k_B = 1$. The friction values have been omitted from the legend of the regression, only the values of the thermodiffusion coefficient (α_+ and α_- for the phobic and philic respectively) are shown.

this issue is to interpret the spatial units of the BD model as a separate unit of measure than in MPC-MD. Hydrodynamic simulations have units of a, which is the collision cell size. These units do not need to correspond to the BD algorithm. Fig. 3.6 shows that the self-propulsion velocity does not change significantly while changing the size of the bead. This is due to the α_T being calculated with the definition of the self-propulsion velocity. Moreover, the size has a deep impact on the rotational diffusion coefficient, D_R of the dimers, and thus, on the Péclet number. The rotational effects come only from the thermal noise in the position update Eq. (3.26), where the size of the bead comes with the friction, and no effect of an increase of α_T is present.

Thus, the Péclet number is seen to match the results with hydrodynamics (dashed lines at 1 in Eq. (3.6)) when $s_p = 8$, which leads to the BD units to be $u_{bd} = \frac{3}{4}a$. All the BD simulations have thus been executed with this rescale.

By obtaining the self-propulsion velocity of dimers heated at different temperatures, *i.e.*, varying the value of $\langle \nabla T \rangle$, one can estimate the value of α_T by a simple linear regression. Nevertheless, this description no longer holds for high temperature gradients, where the linearity is broken. The results obtained by this approach differ by an order of magnitude. This result is coherent with the fact that for our swimmers, the gradient is not homogeneous in all space, due to the presence of a second (or third) bead, leading to an overestimation of α_T by solving the equations for an isolated bead.

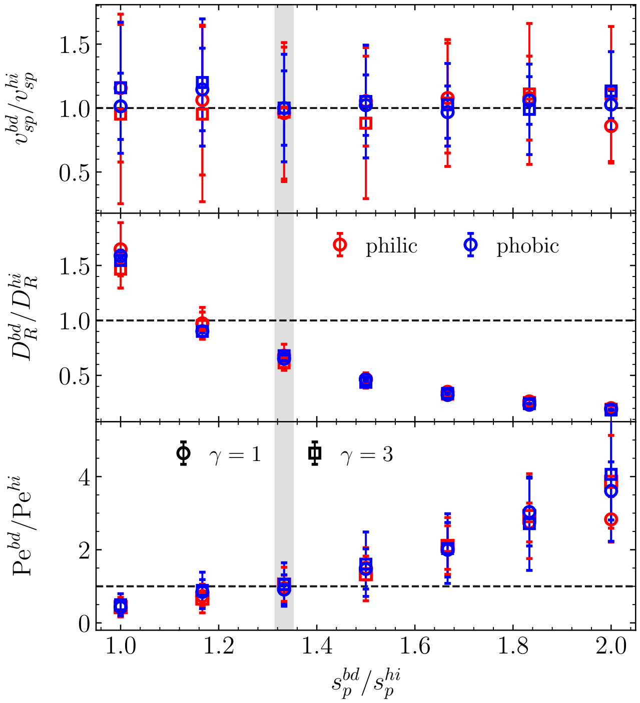

Figure 3.6: Values of the swimming properties of thermophoretic dimers without hydrodynamics (BD) rescaled by the values of the self-propulsion velocity, D_R and Pe from MPC-MD. Dashed black lines (at 1) correspond to the parameters with hydrodynamics. Thick, vertical, gray line corresponds to $s_p^{bd} = 8$, which leads to the best estimate of the Pe.

3.3.2.2 Self-propulsion force

Other models of active Brownian particles (ABPs) consider a different approach to the self-propulsion mechanism of the particles, which does not specify its phoretic origin. This approach imposes a constant velocity on the active particle, v_{sp} [193, 194]. These models are based on that, in the stationary state, the propulsion force of a colloid is equal to the viscous frictional force due to the fluid, as described by Stokes' law. In this description, $\boldsymbol{F}_{\text{drag}} = \gamma_f \boldsymbol{u}$, with $\boldsymbol{u}$ the fluid velocity relative to the colloid, which corresponds to the self-propulsion velocity v_{sp}, and γ_f the friction coefficient, which for a sphere of radius σ_c immersed in a fluid of viscosity η is $C_f \pi \eta \sigma_c$. Then, the propulsion force of a dimer results in

$$\boldsymbol{F}_{\text{prop}} = C_f \pi \eta (s_p + s_h) v_{sp} \hat{\boldsymbol{n}} \ ,$$

with s_p and s_h the radii of the phoretic and the heated beads, respectively, v_{sp} the self-propulsion velocity of the dimer obtained in the full hydrodynamic simulations, $\hat{\boldsymbol{n}}$ the direction orientation vector of the dimer, *i.e.*, $(\boldsymbol{r}_p - \boldsymbol{r}_h)/|\boldsymbol{r}_p - \boldsymbol{r}_h|$ and $C_f = 3$

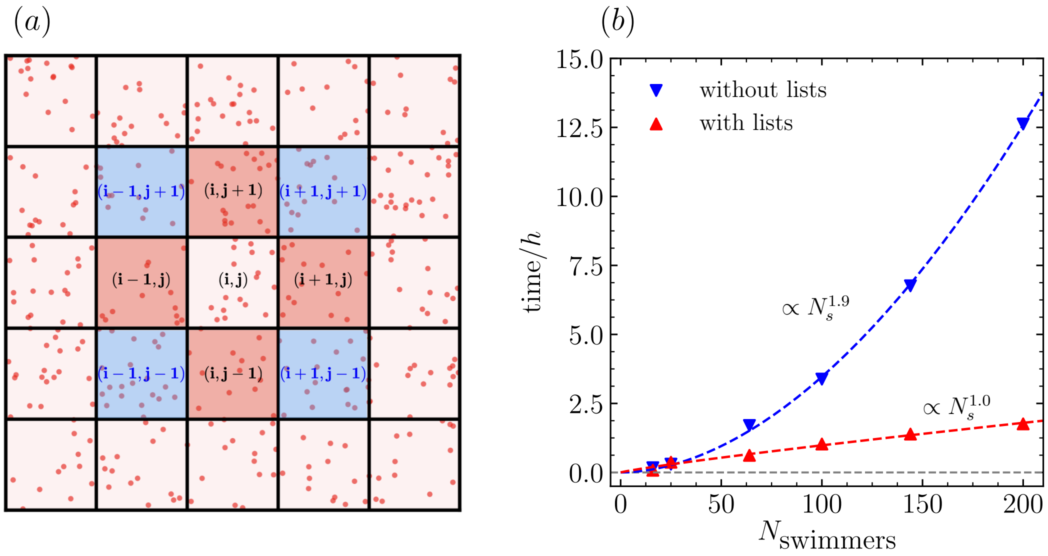

Figure 3.7: (*a*) Distribution of particles on cells inside the simulation box. (*b*) simulation time (in hours) as a function of the number of simulated dimers for a BD simulation without (blue data) and with (red data) cell lists. Only by using this method, it is seen that the simulation is significantly fast by using the cell list method.

for slip boundary conditions, or $C_f = 6$ for stick boundary conditions. In the case of the trimers, we used the same approach. In this case, the propulsion force has been applied for both thermophobic and thermophilic beads, with their corresponding dimer velocity.

We have used this method in order to compare it with the other approach, where the self-propulsion rises from the phoretic interactions between phoretic and heated particles of the same swimmer. This latter model is thus called BD-α, where the thermodiffusion coefficient is fixed, while the model presented in this section is called BD-v, accounting for the fixed self-propulsion velocity, v_{sp}.

3.3.3 Optimisation: cell lists

Large ensembles of particles can lead to a slowdown of the code. A computation of the pair-wise interactions grows quadratically with the number of particles, N^2, in a typical, serial BD code due to the nested loop. This bottleneck hugely limits the size of the studied system if no optimisation in the calculations is made.

Several ways to increase the efficiency of a BD code can be found in literature, but one in particularly is fit for our type of system due to its efficiency and sim-

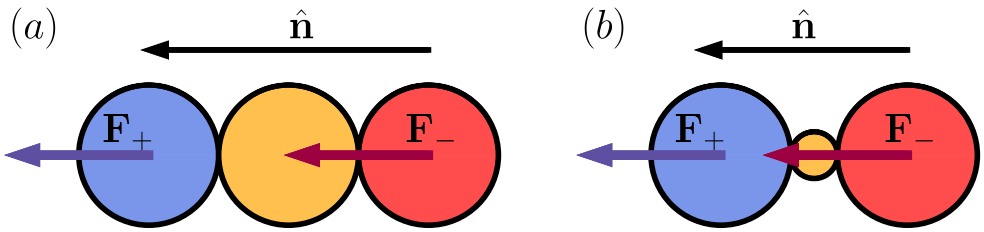

Figure 3.8: Sketch of a symmetric ($\gamma = 1$, (a)) and asymmetric ($\gamma = 3$, (b)) model trimer, where the blue and red beads correspond to the phobic and philic beads, respectively, and the yellow corresponds to the heated one. Blue and red arrows represent the thermophobic ($\boldsymbol{F}_{+}$) and thermophilic forces ($\boldsymbol{F}_{-}$), respectively. The black arrow is the orientation ($\hat{\boldsymbol{n}}$) and motion direction of the swimmer.

plicity to implement. This method is the so-called *cell lists*, where the system is divided in squared cells and all the particles in the system are sorted into them, as shown in Fig. 3.7a. The size of the cells has to be higher than the cutoff radius set for the thermophoretic forces, $r_c = 7s_p$. Then, the particles only interact with the particles within the same cell, and the neighbouring cells. Fig. 3.7a shows a cell (i, j) in a two dimensional system, and its neighbouring interacting cells, $(i \pm 1, j)$ and $(i, j \pm 1)$ as first neighbours (in deeper red), and $(i \pm 1, j \mp 1)$ as second neighbours (in blue), resulting in only 8 interacting cells. The nested loop does not include all the particles in the system, but only the neighbouring cells, reducing then the number of repetitions of the loop, leading to a much faster code. The speed comparison between a serial code and a code with cell lists implemented as a function of the number of dimeric swimmers is shown in Fig. 3.7b, where the time reduction is obvious. Note that given the quasi-two dimensional simulations in which we focus in this work, the cell list is enough to achieve the linear increase of the simulation time with the number of particles. For simulations in three dimensional systems, this typically needs to be combined with the Verlet list [167].

3.4 Swimmer model

The dimeric swimmers studied in this work have a characteristic radius s_h for the heated bead and s_p for the phoretic one. The two beads are bound together via a strong harmonic stretching potential, as described in Eq. (3.15). All interactions between the colloid and the fluid are accounted for via Eq. (3.20). The nature of thermophoresis arises from the choice of this potential. Lüsebrink *et al.* [110] found out that the bead behaves thermophobically for steep attractive potentials

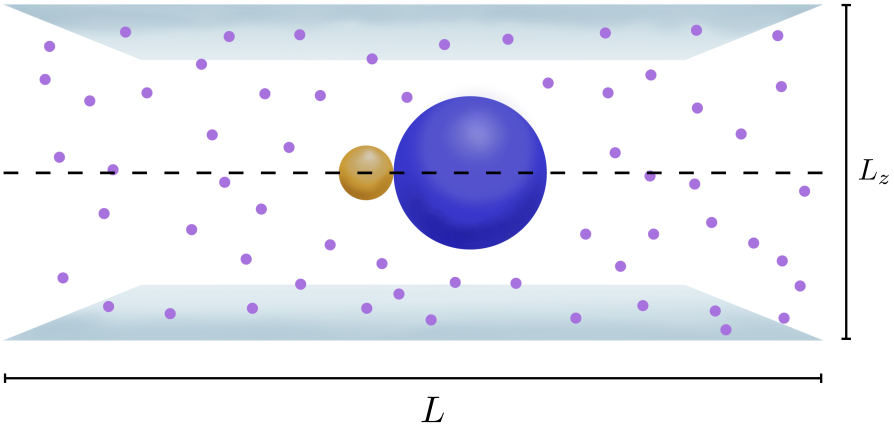

Figure 3.9: Sketch of the quasi-2d confinement of an asymmetric thermophoretic dimer. The blue sphere corresponds to the thermophobic bead, while the gold one corresponds to the heated bead. In blue are the two walls which confine the fluid. Purple dots are a non-scaled representation of the MPC fluid particles which can move in the 3d region enclosed in between.

(with $n = 24$, $\varepsilon = 1$ and $C = 0$), whereas for soft repulsive potentials it becomes thermophilic (with $n = 3$, $\varepsilon = 1$ and $C = 1$). The n exponents have been chosen as in [108], obtaining the faster swimmers for each phoretic nature, leading to more prominent flow fields, *i.e.*, stronger hydrodynamic interactions and less computationally expensive simulations.

The colloid-fluid interactions of the heated bead have no influence on the phoretic behaviour of the dimer, so in order to minimise computational effort a steep repulsive potential is chosen [108], with $n = 24$ and $\varepsilon = 1$. The temperature gradient on the swimmer is implemented by means of a local thermostat around the heated bead. This thermostatting is applied to all fluid particles in the range of $s_h < r < 1.08 s_h$ centred on the centre of the heated bead [82, 108] by a simple velocity rescale, as stated in Eq. (3.22). The heating achieves a temperature of T_h which, if not stated otherwise, is usually chosen to be $T_h = 1.5$.

The swimmers studied in this work have been confined in a quasi-2d slit system, with the simulation box sides $L_x = L_y = L$ and $L_z = \text{ceil}(1.67 l_s)$. In this scope, swimmers are unable to move in the z direction, having their movement confined to the xy plane. The fluid can freely move in all the 3d space between the walls, to which the fluid particles interact via a bounce-back rule. A sketch of the quasi-2d confinement is shown in Fig. 3.9, with the walls as blue planes, the swimmer in the centre and the purple dots as the fluid particles.

These swimmers also have two degrees of freedom in their geometrical construction. The first of them is the size of the beads, characterised by the radii ratio $\gamma = s_p/s_h$, while the second one is the bond length between the beads, δ_b. In this work we use $\delta_b = 0$, in order to keep all the beads of the swimmer in contact, following experimental setups by Valadares *et al.* [68].

In addition to the dimeric swimmer showed on previous works [82, 108, 180], a swimmer made of three beads of different nature is here investigated. Adding an extra thermophilic bead to a thermophobic dimer results in a trimeric swimmer with two engines creating a thrust in the same direction. These swimmers, sketched in Fig. 3.8a ($\gamma = 1$) and Fig. 3.8b ($\gamma = 3$), are called *linear trimers*. Note that, when the second phoretic bead is of the same phoretic nature as the first, the phoretic thrust has the same intensity but opposite direction, such that there is not propulsion, thus the linear construction does not work as a swimmer. A different construction is obtained if we impose that all the beads are in close contact with each other, obtaining a *triangular-shaped trimer*, with an angle between the phoretic beads as $\phi = 2 \arcsin\left[s_p/(s_p + s_h)\right]$. If both phoretic beads show the same thermophoretic behaviour, the phoretic forces add up, indeed leading to a swimmer. On the other hand, if one bead is thermophobic, and the other one thermophilic, the motion experiments a torque, leading to a rotor trimer. All the structures found in this dissertation are summarised in the sketches from Fig. 3.10, where the phoretic forces are omitted. The swimmers are placed sharing the same propulsion direction, except for the rotor trimers (Fig. 3.10k and Fig. 3.10l), given that the geometry of the forces leads to a torque on the motion, instead of a ballistic trajectory.

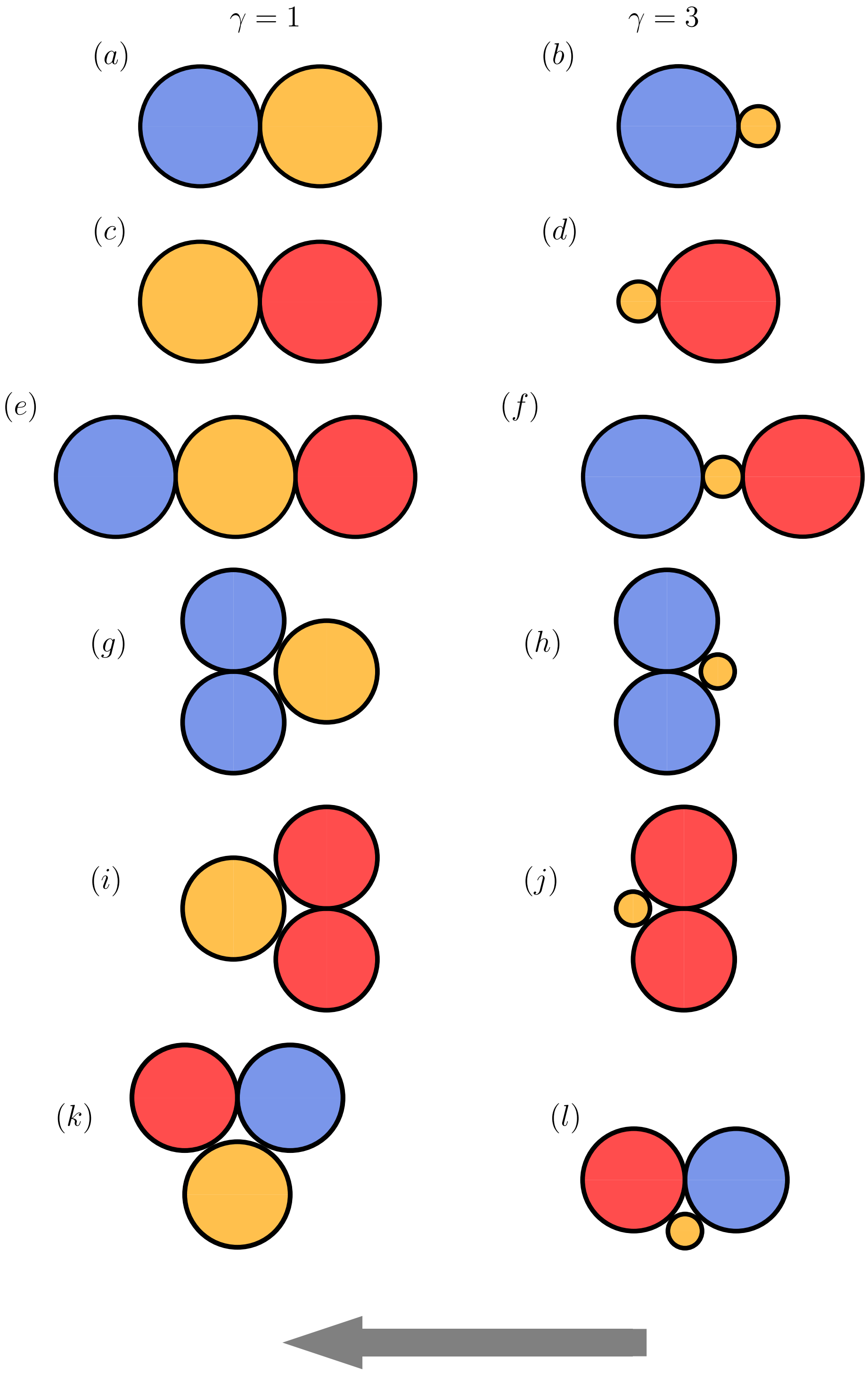

Figure 3.10: Sketches of all the multimeric swimmer structures studied in this dissertation. Blue and red beads correspond to thermophobic and thermophilic beads, respectively. Yellow beads stand for the heated beads. All swimmers, except for the rotors ((*k*) and (*l*)), are oriented in the same propulsion direction, represented by the grey arrow.

Chapter 4

Dynamics of single swimmers

In this chapter, the dynamics and hydrodynamics of single dimeric and trimeric swimmers are studied in detail.

In order to obtain self-propulsion in phoretic microswimmers, some symmetry breaking on the swimmer has to be achieved. The case under study, dimeric and trimeric microswimmers, achieve said symmetry breaking via the nature of the beads. One bead is simulated to mimic a higher thermal conductivity, thus absorbing energy faster and produce thereby a steady linear local temperature gradient around it. This bead is henceforth called *heated* bead. The other beads are the *phoretic* beads, either thermophilic or thermophobic. These beads are made of a material which does not absorb energy, but reacts to the local temperature gradient, experiencing then a phoretic thrust. By using this approach, dimers self-propel due to local gradients created by each individual microswimmers, so no external uniform gradient is considered, but only a heat source. For practical purposes, this implies that all effects due to the induced activity here discussed disappear when the external heat source is removed.

The first section presents the overall model of the swimmers. The swimming behaviour of single swimmers is characterised via the evaluation of the self-propulsion velocity, v_{sp}, the rotational diffusion coefficient, D_R, and the resulting Péclet number, Pe. The hydrodynamics is addressed by studying the velocity of the fluid around the swimmer. Effects of the confinement on the self-propulsion velocity and the rotational diffusion of thermophobic dimers are then showed by comparing existing simulations in 3-dimensional bulk, with new results in quasi-two dimensional confined conditions. Linear trimers are also investigated as a function of their beads' aspect ratio and of the overall size of the symmetric swimmer. Then, the results of the previous quantities are also shown for triangular-shaped trimers. The final section of this chapter studies the hydrodynamics of the swimming dimers and linear trimers. Their flow fields are shown and quantified as a function of the geometry of the swimmer.

4.1 Linear swimmers

4.1.1 Swimming velocity

The first quantity to study is the self-propulsion velocity of the swimmer. This velocity is calculated as the vectorial projection of the centre of mass velocity of the whole swimmer on the orientation axis along the bond of the swimmer (as seen in Fig. 3.8), $v_{sp} = \boldsymbol{v} \cdot \hat{\boldsymbol{n}}$, with $\boldsymbol{v}$ the vector velocity of the centre of mass of the swimmer, and $\hat{\boldsymbol{n}}$ the orientation vector of the swimmer. With this definition of the swimming velocity, the ballistic time of a thermophoretic swimmer is defined as $\tau_B = s_p/v_{sp}$, with s_p the radius of the thermophoretic bead. The direction and magnitude of the self-propulsion velocity is determined by the Soret coefficient of the swimmer, along with the value at which we heat the bead and the friction effects, as given by Eq. (3.30). At the stationary state, from which Eq. (3.30) is obtained, this velocity balances with the friction, thus being a constant value.

4.1.1.1 Quasi-2d confinement on swimmers

The confinement of thermophobic dimeric swimmers into the quasi-2d slit described before is here compared with the bulk free-swimming dimers presented by Wagner *et al.* [108, 180]. When studying the swimming behaviour of thermophoretic dimers, one must first face the asset of the geometry of the swimmer, similar to previous studies [108, 180]. In terms of geometry, there are two main quantities that need to be considered. First, one can change the aspect ratio between the radii of the phoretic and heated beads, *i.e.*, the ratio between the sizes of the beads of the swimmer, $\gamma = s_p/s_h$. When addressing this point, there are also two ways of changing the aspect ratio, say to keep the phoretic or the heated bead constant. If one decides to keep the phoretic bead at a fixed size, while changing the radius of the heated monomer, this parameter γ is a suitable tool to study the effects of the geometry while keeping a swimmer with an almost constant thermodiffusion coefficient, α_T, thus a constant thermophoretic response to the local ∇T. The second approach to study the geometry is to change the size of the whole swimmer, by increasing both s_p and s_h and keeping them at the same size, *i.e.*, $\gamma = 1$. The results are presented in Fig. 4.1, for dimeric (blue symbols) and trimeric (red symbols) swimmers in free 3d-bulk (empty square symbols) and in a quasi-2d confined system (full symbols). First, the effect of the quasi-2d confinement of dimers is discussed, followed by the comparison between dimeric and trimeric swimmers.

In Fig. 4.1a and Fig. 4.1b, the velocity is studied as a function of the aspect ratio with fixed phoretic radius s_p and varying s_h. Fig. 4.1c and Fig. 4.1d show the same study performed for symmetric swimmers, where the sizes of both beads have been changed simultaneously. Fig. 4.1a presents the propulsion velocity rescaled

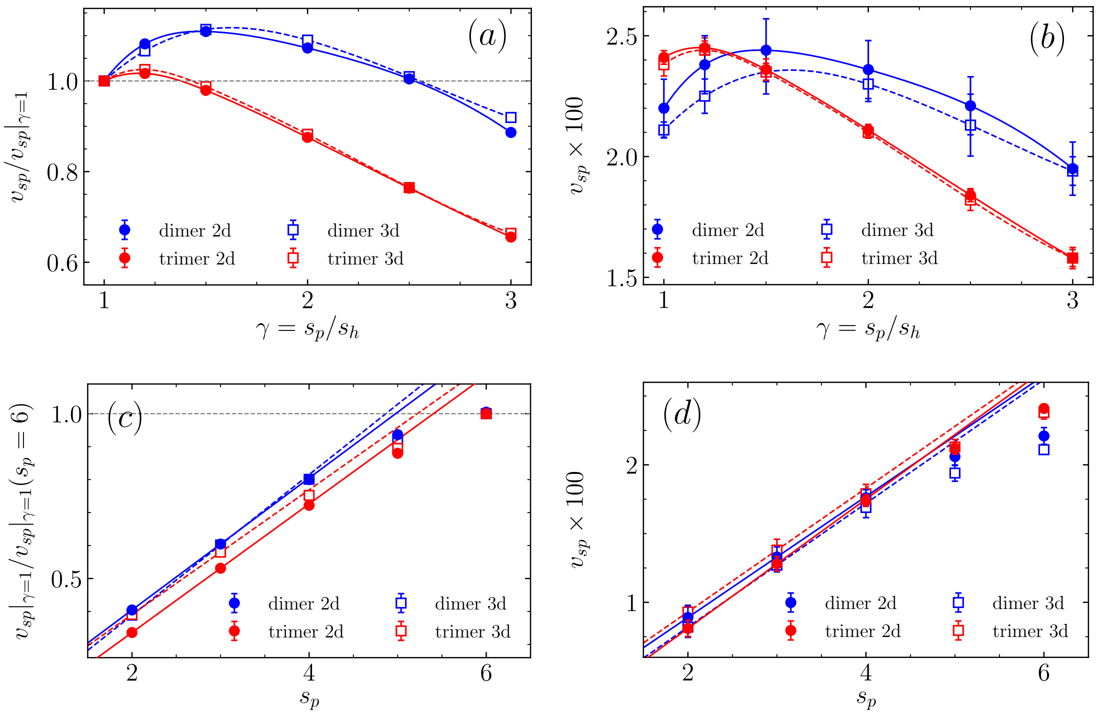

Figure 4.1: Self-propulsion velocity of dimers (blue) and linear trimers (red) as a function of the aspect ratio γ of the swimmers (top) and with respect to the size of the phoretic beads for symmetric swimmers (bottom) in 2d and 3d for a constant value of T_h, which corresponds to an almost constant value of ∇T. Figures depicting the velocity as a function of γ show a maximum due to the limits of the construction of swimmers, while for symmetric swimmers, the velocity shows no clear maxima. Lines correspond to the linear regressions fitting the data for the symmetric case, and the spline regression for the asymmetric case.

by the v_{sp} of the symmetric swimmer. In the limit $s_p \ll s_h$ ($\gamma \to 0$), the phoretic bead is very small, and the force exerted on it is too small in comparison to the friction force of the heated bead, such that the swimmer velocity vanishes. On the other hand, in the limit of large phoretic beads, $s_p \gg s_h$ ($\gamma \to \infty$), the phoretic surface that experiences a significant ∇T is very small relative to the total size of the thermophoretic bead, such that the self-propulsion velocity becomes negligible. For fixed phoretic beads, increasing the heated bead leads to a stronger temperature gradient, increasing the propulsion velocity. This effect also leads to an increase of the fluid friction, leading to a finite velocity. These two limits lead to a maximum of the velocity (as seen in Fig. 4.1a and Fig. 4.1b), corresponding to the most efficient geometry in terms of propulsion, which in turn leads to the most prominent flow fields. The first difference between free-swimming and confined swimmers is the location of the maximum. Wagner *et al.* [108, 180] showed that thermophobic dimers present the highest velocity at $\gamma \simeq 1.7$. When these same swimmers get confined in the quasi-2d slit, this maximum appears at $\gamma \simeq 1.5$. This change is enough to be perceived from Fig. 4.1a, but it is within the statistical error of the fitting equation. Moreover, in Fig. 4.1b the same velocities are shown but without the rescaling, from where it is clear that the confinement of thermophobic dimers leads to overall slightly faster swimmers for all the studied geometries. The same figure shows that, in terms of the absolute velocity, the maximum of the curve seems to be the same for both 2d and 3d systems. This means that the confinement of swimmers does not have a deep impact on the overall behaviour of v_{sp} respect γ.

Fig. 4.1c shows the self-propulsion velocity of the swimmers as a function of s_p rescaled with the velocity of the symmetric swimmer of phoretic radius $s_p = 6$. The velocity increases linearly with the size of the swimmer for small sizes, breaking this linearity for $s_p \geq 5$. The breaking of the linear dependency is due to increasingly big swimmer leaving the low Reynolds number regime. The biggest symmetric swimmers here presented have beads' radii of $s_p = 6$, which lead to a Reynolds number (Eq. (2.45) with $l_0 \equiv s_p$ and $u_0 \equiv v_{sp}$) of $\mathrm{Re} \simeq 0.15$, being on the Stokes limit approach [124].

The linear increase of the velocity with the size of the phoretic bead can be understood via the force and temperature gradient equation. The thermophoretic force has a linear dependency on the temperature gradient, ∇T, Eq. (2.33), and for a stationary system, this force equals to the drag force, leading to a self-propulsion velocity defined by Eq. (3.30). Then, the self-propulsion velocity takes the shape of

$$v_{sp} \propto \frac{\alpha_T \nabla T}{\gamma_T} \,, \tag{4.1}$$

in which the gradient of the temperature is defined by Eq. (3.31), which shows a dependency of $\nabla T \propto s_p^{-1}$. The translational friction coefficient, γ_T, is given by the Stokes-Einstein relation, thus $\gamma_T \propto s_p$. Finally, the thermodiffusion coefficient has been proven to decay as $\alpha_T \propto s_p^{-3}$ [108] for the parameters here employed, since $\Delta = \sigma_p$ in Eq. (3.20), such that $s_p = 2\sigma_p$. Putting everything together into Eq. (4.1) leads to the linear dependency of the velocity on the phoretic radius, $v_{sp} \propto s_p$, observed in Fig. 4.1c and Fig. 4.1d.

The absolute values of the self-propulsion velocities are presented in Fig. 4.1d. A comparison between this figure and Fig. 4.1b shows that the change of the overall size of the dimer has a deeper impact on its v_{sp} than the change of geometry, γ, due to the change on the phoretic response of the colloid, along with the variation of the strength of the thermal field. Moreover, symmetric dimers confined in the quasi-2d slit present a slight increase of their velocity compared to their free-swimming counterparts. These results agree with what one might expect for a quasi-2d confined system, where there is no possible motion in the z-coordinate. In this case, with the definition of $v_{sp} = \boldsymbol{v} \cdot \hat{\boldsymbol{n}}$, there is one degree of freedom less on $\boldsymbol{v}$, being the projection into $\hat{\boldsymbol{n}}$ closer to the direction of $\boldsymbol{v}$, leading to an increased the self-propulsion velocity.

Linear trimers have two active phoretic beads, one phobic and the other philic (see sketches from Fig. 3.10e and Fig. 3.10f), thus increasing the driving force, but also increasing its friction. Fig. 4.1a and Fig. 4.1b also give a comparison between thermophobic dimers and linear trimers in both dimensions, 2d and 3d. The major difference between the velocities shown in Fig. 4.1a and Fig. 4.1b of these new trimeric swimmers and the dimers is the position of the maximum of v_{sp}. Thermophobic dimers show the peak of their self-propulsion velocity around $\gamma \simeq 1.5$, while for these linear trimers, this maximum lies around $\gamma \simeq 1.2$. On the other hand, the gain in velocity at the peak is much smaller in the case of linear trimers, being almost a constant in the range $\gamma \in [1.0, 1.5]$. Higher γ, or smaller heated beads, leads to a significant decrease of the swimming velocity. Fig. 4.1b shows that linear trimers near the symmetric case, $\gamma \to 1$, present a higher self-propulsion velocity in both quasi-2d and 3d bulk cases compared to the dimers, whereas for increasing γ, thermophobic dimers become faster swimmers. This can be due the geometry of the linear trimers, where the friction on the thermophilic bead gets accentuated when γ increases, *i.e.*, the heated bead decreases. This can be seen in Fig. 3.10f, where the philic bead gets more exposed to the fluid, leading to a higher friction on the swimmer, thus slowing down the swimmer. This effect is not present on the thermophobic dimer, given that higher aspect ratios lead to lesser friction (see Fig. 3.10b). Nevertheless, smaller heated beads also lead to smaller temperature gradients, which results in a decrease of the velocity.

On the other hand, the results of the propulsion velocity of trimeric swimmers when $\gamma = 1$ are very interesting. Given that linear trimers can be thought of as thermophobic dimers with an extra thermophilic bead at the tail, two effects happen. First, there is an extra engine on the swimmer, namely the second phoretic bead, which increases the phoretic propulsion, thus supposedly leading to higher velocities. But the effect of the extra phoretic bead is balanced by an increase of the friction of the swimmer with the solvent. This is also studied in Fig. 4.1c and Fig. 4.1d, where the v_{sp} of trimers is calculated for different s_p values, and compared to the thermophobic dimer's velocities. This figure shows that the velocity increases linearly with the radius of the beads, with a slope near 1/6 for the linear trimers in 2d, *i.e.*, $v_{sp}/v_{sp}(s_p = 6) \propto s_p/6$. This is seen on the propulsion velocity of the $s_p = 2$, which is nearly a 35% of the velocity of the $s_p = 6$ swimmer, while also being a third in size. Fig. 4.1d shows the same velocities but in absolute value, where it is shown that all the velocities have approximately the same behaviour and the same values for the same s_p, independently of the swimmer or the confinement of the system. This means that the extra contribution to the phoretic force that is obtained by adding a second phoretic bead is balanced by the friction inherent to the presence of the second bead. The same linearity between the self-propulsion velocity and the phoretic bead's radius appear for the linear trimer case, as discussed in the previous section for dimers.

4.1.1.2 Finite size effects

The size of the simulation box, L, is of crucial importance when calculating the swimming velocity, and also deeply affects the hydrodynamics of the swimmer. The variation of the self-propulsion velocity with L is given by [108]

$$v_{sp} = v_\infty \left(\lambda_L \frac{l_s}{L} + 1 \right) , \tag{4.2}$$

with l_s the total swimmer length, *i.e.*, the sum of the diameters of all the beads, and L the length of the simulation box. Moreover, v_∞ is the self-propulsion velocity in an infinite simulation box, and λ_L is a parameter to quantify the effect of the finite size of the box. These effects encompass the hydrodynamic interaction of the swimmer with its images due to the periodic boundary conditions of the simulation box and the truncation of the wavelength spectrum. Fig. 4.2 shows the behaviour of the rescaled self-propulsion velocity as a function of the size ratio of the box for symmetric linear trimers of bead size $s_p = 2$ and $s_p = 4$. From the linear regressions, v_∞ and λ_L can be estimated for every geometry of swimmers, and thus characterise the effects of the box size. Interestingly, bigger swimmers show smaller values of λ_L, *i.e.*, smaller finite size effects, although they tend to swim faster than smaller swimmers. This can be understood as follows. Bigger swimmers have stronger phoretic thrusts due to bigger phoretic beads, *i.e.*, higher α_T, and therefore create stronger flow fields. Although smaller swimmers create weaker flow fields, their motion is more affected by fluid noise.

Big simulation boxes lead to estimates closer to the theoretical values of the swimming velocities, but the computational cost increases dramatically with the size of the simulation region. Given the influence of the size of the box is captured via a linear description, there is no need to study the effects of the finite size for all the swimmers. The compromise here is to find the smaller simulation box which in turn minimises the finite size effects. For single swimmers simulations discussed in this thesis, typically a box of $l_s/L = 0.2$ is chosen, leading to an overestimation of v_{sp} of $\sim 10\%$.

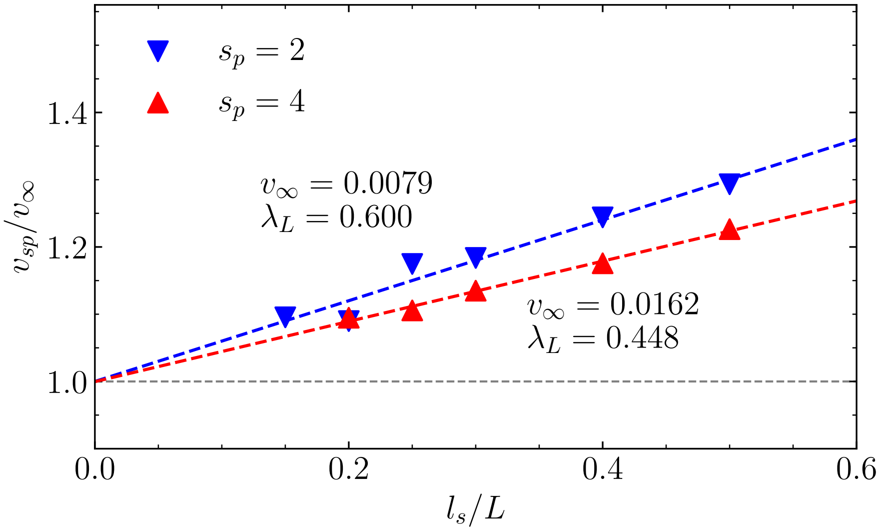

Figure 4.2: Values of the self-propulsion velocity of symmetric trimers ($s_p = 2$ and $s_p = 4$) rescaled by the theoretical velocity at infinitely large simulation box, v_∞, as a function of the ratio between the swimmer length, l_s, and the size of the simulation box, L. The linear regression (dashed line) is made with Eq. (4.2). The parameter λ_L quantifies the strength of the finite size effects.

4.1.2 MSD and MSAD

The characterisation of the mean square displacement (MSD), $\Delta \boldsymbol{r}^2$, and the mean square angular displacement (MSAD), $\Delta \boldsymbol{e}^2$, give more insight into the understanding of the swimmers' dynamical behaviour. For an active Brownian particle (ABP) the MSD takes the expression shown in Eq. (2.14). This definition has two main regimes, a short-time ballistic regime, where the MSD has a squared dependency with time, $\Delta \boldsymbol{r}^2 \propto t^2$, and a long-time ballistic regime, with a linear time-dependency, describing a diffusive motion.

The reorientation time $\tau_R = 1/D_R$ measures the characteristic time scale of the relaxation of the orientation of the swimmer. The mean square angular displacement, $\Delta \boldsymbol{e}^2$, describes the change of the orientation as a result of thermal fluctuations on the swimmer. Fig. 4.3a shows the comparison between thermophobic dimers (blue) and linear trimers (red) for symmetric and asymmetric swimmers. In overall, symmetric swimmers show a value of τ_R higher than the corresponding for the asymmetric ones. Asymmetric thermophobic dimers show a τ_R 22% smaller than symmetric ones, similar to the trimers, for which this difference is of 23%. Moreover, the characteristic time τ_R of trimers ($\simeq 10^5$) is of one order of magnitude higher than for dimers ($\simeq 10^4$). The simulations here performed consider 5×10^7 MD steps, which correspond to 5×10^5 MPC time units. Since the diffusive time

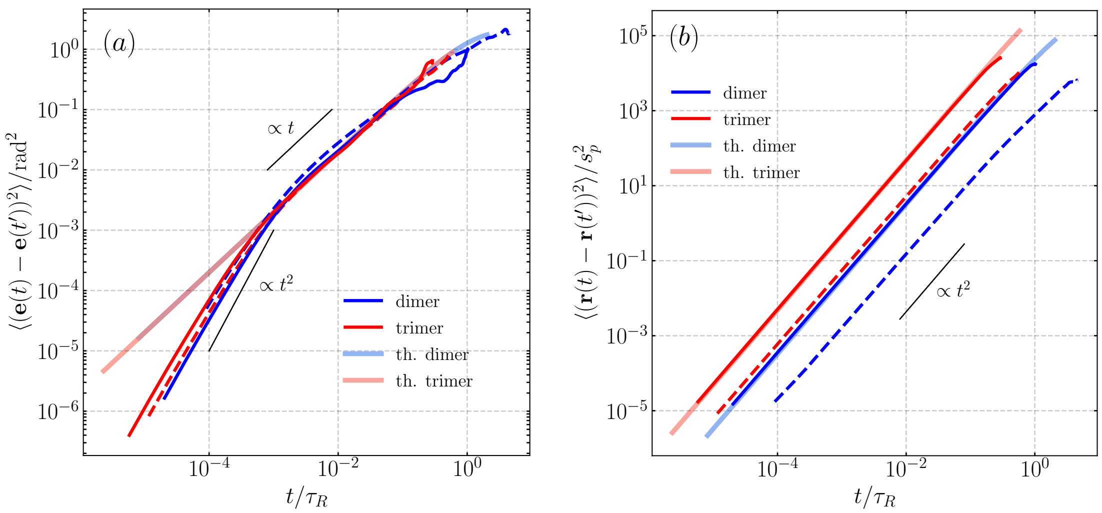

Figure 4.3: (*a*) Mean square angular displacement ($\Delta\boldsymbol{e}^2$) and (*b*) mean square displacement ($\Delta\boldsymbol{r}^2$) of phobic dimers (blue) and linear trimers (red) in quasi-2d confinement. Solid lines stand for symmetric swimmers ($\gamma = 1$) while dashed lines stand for asymmetric ones ($\gamma = 3$). Thicker lines correspond to the theoretical expression of the $\Delta\boldsymbol{r}^2$ and $\Delta\boldsymbol{e}^2$ from Eq. (2.14) and Eq. (2.8), respectively, with the parameters corresponding to the simulated symmetric swimmers. Both $\Delta\boldsymbol{r}^2$ and $\Delta\boldsymbol{r}^2$ are shown with the time rescaled by the rotational time τ_R.

starts for times around τ_R what we see in Fig. 4.3b, the $\Delta\boldsymbol{r}^2$ of both dimers and trimers in quasi-2d, is purely ballistic, independently of their geometry. The lack of the diffusive regime has prevented us from obtain the translational diffusion coefficient, D_T, from the fitting of the $\Delta\boldsymbol{r}^2$ with Eq. (2.14). Given the agreement between the $\Delta\boldsymbol{r}^2$ from simulations and Eq. (2.14), as seen in Fig. 4.3b, we can use the extended theoretical expression to estimate the mean square displacement at larger times. This estimation is shown in Fig. 4.4 for both phobic dimers and linear trimers. Note that the diffusion coefficient D_T used in the theoretical prediction of Fig. 4.3 and Fig. 4.4 is an underestimation of the ABP one (Eq. (2.5)), in order to ensure that the diffusion time scale is larger than the rotational, $\tau_D \gg \tau_R$. The observed regime corresponds to the ballistic motion, in the $\Delta\boldsymbol{r}^2$ from Fig. 4.3b, where $\Delta\boldsymbol{r}^2 \propto t^2$. At $t/\tau_R \simeq 1$, this behaviour changes, and the MSD enters the diffusive regime. By performing simulations over longer periods of time, this regime would also be reached by our swimmers, allowing for a good estimation of the D_T. Nonetheless, these simulations have not been performed because they would be too long to run and the extra insight on the system is not expected to be substantial.

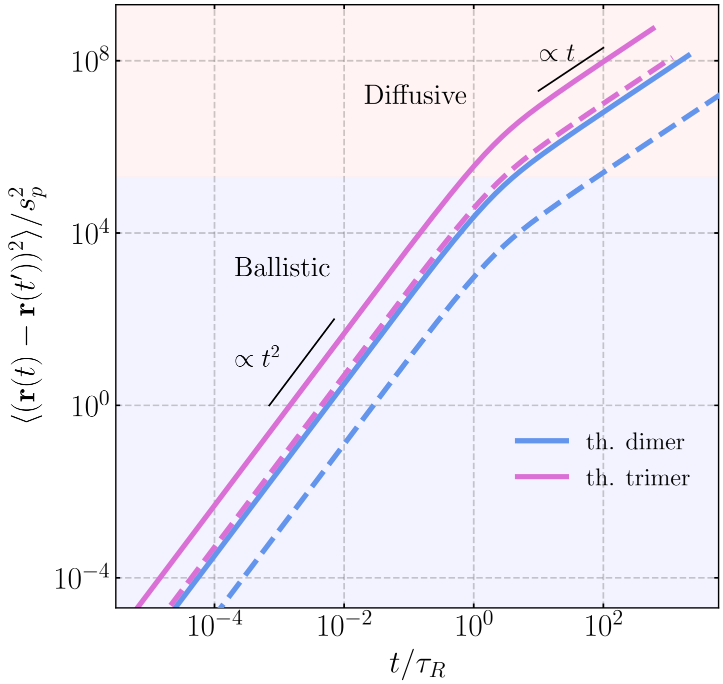

Figure 4.4: Theoretical mean square displacement ($\Delta \boldsymbol{r}^2$) of phobic dimers (blue) and linear trimers (purple) in quasi-2d confinement from Eq. (2.14) . Solid lines stand for symmetric swimmers ($\gamma = 1$) while dashed lines stand for asymmetric ones ($\gamma = 3$).

4.1.3 Rotational diffusion and Péclet number

The motion of such small self-propelled swimmers is highly affected by thermal fluctuations. Thus, the motion is stochastic, and the swimmers perform a persistent random walk as a result of the competition between the ballistic directed motion, characterised by their self-propulsion velocity, and an angular randomisation, due to the thermal rotational diffusion [31, 195, 196, 197]. The balance between translational and rotational diffusion of active colloids is characterised by the Péclet number, in Eq. (2.15). We choose the swimmer relevant length scale to be the phoretic bead radius, s_p, leading to $\mathrm{Pe} = v_{sp}/(D_R s_p)$. In this section, the study of the dependency of the rotational diffusion coefficient, D_R, and the Péclet number, Pe, with the geometry of the swimmer is presented for both thermophobic dimers and linear trimers.

The confinement effect on the swimming behaviour of the dimers is considered not only by the value of the propulsion velocity, but also by the influence of thermal fluctuations in the orientation of the swimmer's direction. This can be characterised by the rotational diffusion coefficient, D_R. The mean square angular

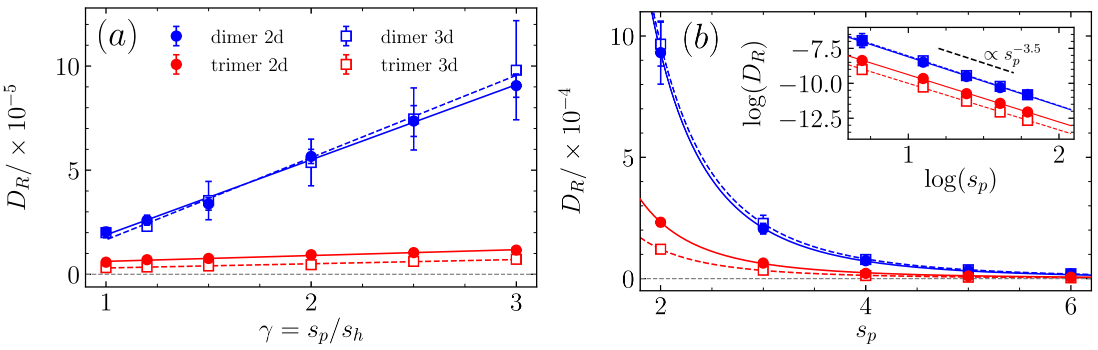

Figure 4.5: Rotational diffusion coefficient of (phobic) dimeric and trimeric swimmers in both 2d and 3d as a function of the aspect ratio of the swimmer, γ (a), and the size of the phoretic bead for symmetric swimmers (b). The inset in (b) corresponds to the log-log representation of the D_R, showing $D_R \propto s_p^{\alpha}$. Dashed lines correspond to the linear (a) and power law (b) regressions of the data.

displacement, $\Delta \boldsymbol{e}^2$ (from Fig. 4.3a), allows us to determine D_R in the simulations by using Eq. (2.8) to fit the simulation data, with $d = 2$ and 3, respectively for 2d and 3d systems. Fig. 4.5 shows the estimates of the D_R of thermophobic dimers and linear trimers in 2d and 3d systems, as a function of the geometry of the swimmer (aspect ratio between radii of beads, γ, Fig. 4.5a) and the overall size characterised by the phoretic bead's radius, s_p, for symmetric swimmers (Fig. 4.5b). From both Fig. 4.5a and Fig. 4.5b, the same behaviour is seen for the D_R, showing that the confining of such swimmers has no significant impact on the rotational dynamics. Fig. 4.5a shows a linear dependency of the D_R with the beads' aspect ratio. The rotational diffusion coefficient with the size of the phoretic bead s_p decays following a negative power law, as shown in the inset of Fig. 4.5b. This follows the theory of active Brownian particles (ABP), which suggests that for the D_R there is no further influence of hydrodynamic interactions. This equation is expressed as

$$D_R = m s_p^{\beta} \, , \tag{4.3}$$

where m is the slope, $m = k_B T / 8\pi\eta$ and β is the exponential decay. This dependency is shown in the inset of Fig. 4.5b to be $\beta \simeq -3.5$, which slightly differs from the theoretical ABP ($\beta = -3$) exponent shown in Eq. (2.6) for spherical colloids. This difference results in a lower D_R of the thermophoretic swimmers under study respect the common ABP, due to the non-spherical shape of our phoretic nanoswimmers. It is also seen to be independent of the confinement of the swimmers.

The quasi-2d confinement on dimers has been proved to have almost no impact on the swimming behaviour of thermophobic dimers. Nonetheless, this confine-

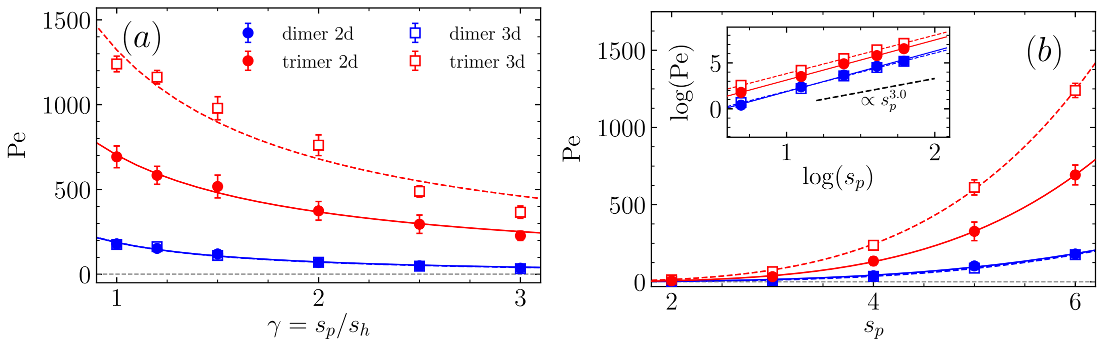

Figure 4.6: Representations of the Péclet number as a function of (a) the aspect ratio γ and (b) the size of the phoretic bead s_p for symmetric swimmers. Red symbols correspond to linear trimers, while blue symbols correspond to phobic dimers. Empty symbols stand for 3d systems, while full symbols stand for quasi-2d systems. Dashed (3d) and continuous (2d) lines correspond to the linear (a) and power law (b) regressions of the data.

ment plays a significant role on the re-orientation of the linear trimer's direction. The main result shows that linear trimers show less re-orientational effects than thermophobic dimers, *i.e.*, smaller D_R, as seen by comparing blue and red symbols from Fig. 4.5. This is due to the larger size and the linear construction of the trimer. The same figure shows that the quasi-2d confinement of trimers leads to a slightly higher D_R than 3d bulk trimers. Bigger swimmers are less subjected to the influence of thermal fluctuations in the re-orientation of the motion. From the inset of Fig. 4.5b, the D_R of linear trimers shows a similar power law decay on the size of the beads as for the phobic dimers, $D_R \propto s_p^{-3.5}$.

The effect of confinement is more evident for the resulting Péclet number, as shown in Fig. 4.6. Fig. 4.6a and Fig. 4.6b show Pe as a function of the aspect ratio and the radius of the phoretic bead for symmetric phobic dimers and linear trimers. Both figures show that the Pe displays the same behaviour for confined and free-swimming phobic dimers. The lines on Fig. 4.6 result from power-law regressions. Fig. 4.6a shows that the power law for thermophobic dimers is $\mathrm{Pe} \propto \gamma^{-1.4}$, whereas for the linear trimers is $\mathrm{Pe} \propto \gamma^{-1}$. On the other hand, the inset of Fig. 4.6b shows the log-log representation, leading to a power law dependency between the Péclet number and the size of the swimmer of $\mathrm{Pe} \propto s_p^3$, for both dimers and trimers.

Fig. 4.6a also shows that linear trimers have more ballistic trajectories compared to thermophobic dimers, characterised by higher Péclet numbers. Free-swimming linear trimers in 3d bulk present higher Pe than trimers in quasi-2d confinement, as a result of the increase of the D_R for 2d systems. Fig. 4.6b shows Pe as a function of the phoretic bead's radius, s_p, for symmetric swimmers, show-

Table 4.1: Values of the slope and exponents of the power law regressions of the size dependency of D_R (β) and the Péclet number (β') for symmetric ($\gamma = 1$) swimmers, as expressed in Eq. (4.3) and Eq. (4.4), respectively.

swimmer	β	β'	m $(\times 10^3)$
dimer 2d	-3.6 ± 0.1	2.9 ± 0.2	6.0 ± 1.0
dimer 3d	-3.6 ± 0.1	2.9 ± 0.1	11.5 ± 0.1
trimer 2d	-3.3 ± 0.1	3.3 ± 0.1	1.1 ± 0.4
trimer 3d	-3.3 ± 0.1	3.1 ± 0.1	1.1 ± 0.3

ing the same power law decay between the Péclet number and the size of the swimmer seen for the thermophobic dimers, Pe $\propto s_p^3$. Similarly to the D_R, the Péclet number also shows a power law decay with s_p,

$$\mathrm{Pe} \propto s_p^{\beta'} \ . \tag{4.4}$$

The exponent lies around Pe $\propto s_p^3$, as shown by the black dashed line in the inset of Fig. 4.6b. The precise values of the exponents of the power law regressions of both the rotational diffusion coefficient and the Péclet number are summarised in Tab. 4.1. These values show that there is no variation, within the accuracy of the measurements, when the swimmer is confined or free to swim in bulk, for both phobic dimers and linear trimers. The change of geometry from dimeric to trimeric swimmers shows a slightly higher difference between the exponents of the power law regression for both D_R and Pe. Nonetheless, these differences are still small and comparable to the theoretical value of the ABP. The theoretical value of the slope of the regression of D_R with s_p is $m = k_BT/8\pi\eta$, which if we take the viscosity of the MPC fluid as $\eta = 7.92$, for our simulation parameters, it results in a value of $m = 5 \times 10^{-3}$ for a spherical ABP. The results of m for our simulations are shown in Tab. 4.1. The slope obtained from the regressions of our simulations is of the same order of magnitude than the theoretical one, with small discrepancies due to the presence of hydrodynamic interactions and the shape of our swimmers, which modifies the prefactor of Eq. (2.6).

4.2 Triangular-shaped swimmers

A different trimeric construction is represented in the sketches Fig. 3.10g ($\gamma = 1$) and Fig. 3.10h ($\gamma = 3$), where both phoretic beads are of the same nature. We refer to this geometry as a *triangular* trimer. Due to the construction of the swimmer, the superposition of the two driving forces leads to a null displacement in the perpendicular direction of the swimmer, and a total force of self-propulsion in the

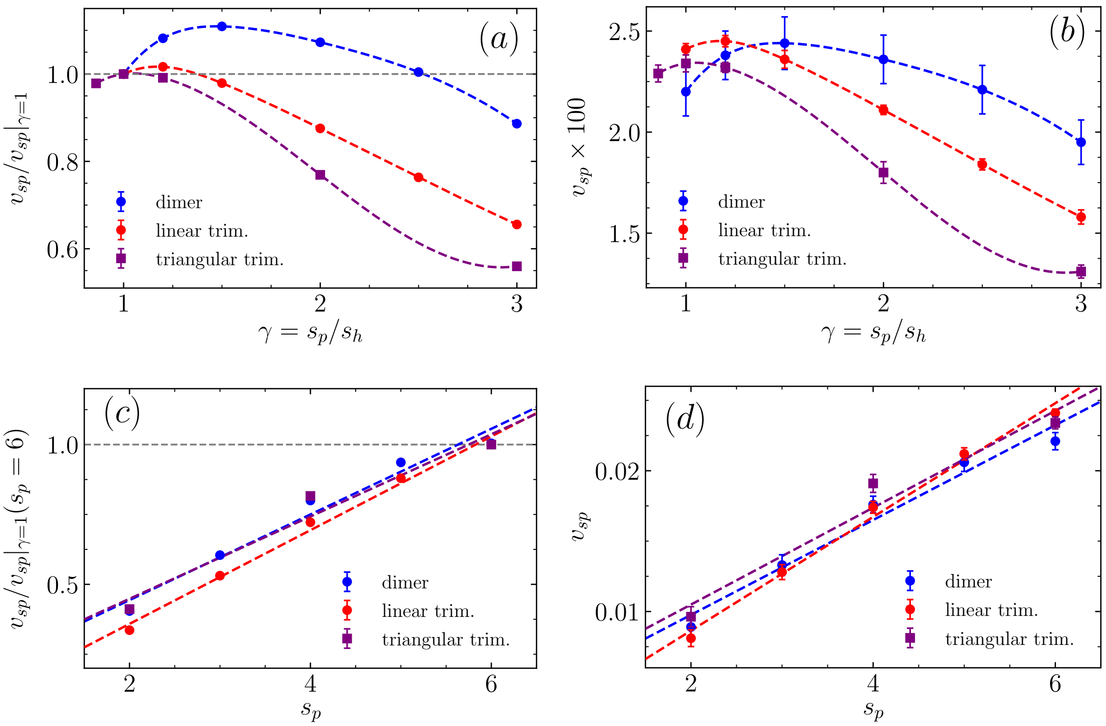

Figure 4.7: Self-propulsion velocity of the thermophobic triangular swimmers (purple) compared to the results of the thermophobic dimer (blue) and linear trimer (red), as a function of the aspect ratio γ ((*a*) and (*b*)) and the size of the phoretic bead for symmetric swimmers (*c*) and (*d*)). Figures (*a*) and (*c*) display the rescaled velocity of the swimmer as a function of symmetric swimmer's velocity ($s_p = 6$ for (*c*)), while in (*b*) and (*d*) the absolute velocity is shown. Dashed lines correspond to spline and linear regressions.

axial direction, as indicated in the sketches from Fig. 3.10g and Fig. 3.10h. This increased thermophoretic force is also accompanied by an increase of the friction force and steric effects different from those of the dimeric swimmers. In terms of experimental synthesis, the fact that only two material types are involved implies that this swimmer should be easier to synthesise than the already showed linear trimer.

In order to compare this geometry with the previous ones, the self-propulsion velocity of the swimmers is first studied for different bead size and bead ratios. The comparison is shown in Fig. 4.7. Triangular-like swimmers with smaller heated beads show smaller velocities than the corresponding dimers and than the linear trimers for all geometries, as seen in Fig. 4.7b. This indicates that the extra friction due to the second phoretic bead is higher than to the one corresponding to the

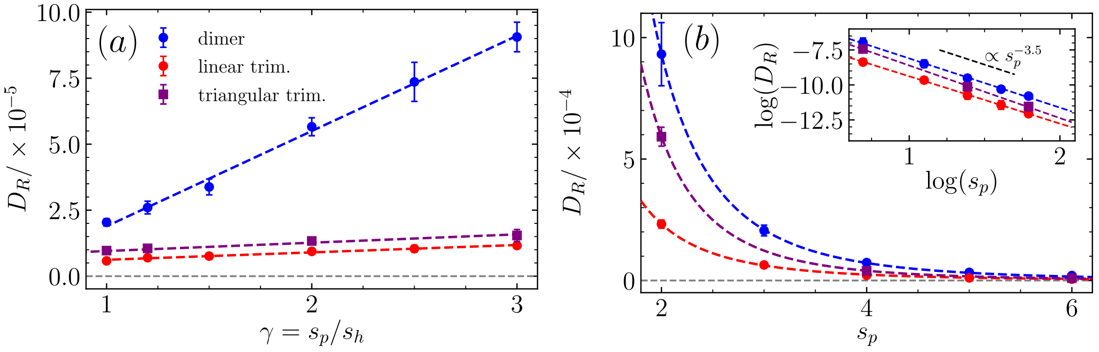

Figure 4.8: Rotational diffusion coefficient of the thermophobic triangle-like trimers (purple squares) compared to linear trimers (red) and thermophobic dimers (blue) as a function of the aspect ratio γ (a) and the size of the phoretic bead for symmetric swimmers, (b). Results show that the D_R of the triangular trimers is not strongly affected by the change of geometry of the swimmer, unlike the dimer. Nonetheless, the overall size of the swimmer has a considerable effect on this value. Dashed lines correspond to the linear (a) and power law (b) regressions of the data. Inset in (b) shows the D_R in log-log scale, with the linear regression of the data.

philic bead of the linear trimer. Fig. 4.7a shows v_{sp} as a function of the aspect ratio γ rescaled by the velocity of the symmetric geometry. Triangular-shaped swimmers have their faster geometry at the symmetric case $\gamma = 1$, differently from the other swimmers, where the maximum of the velocity is observed for asymmetric geometries, as seen in Fig. 4.7b for the absolute value of the swimming velocity. By decreasing the size of the heated bead (increasing γ), the decay of v_{sp} is faster than for the corresponding phobic dimers and linear trimers. Fig. 4.7c and Fig. 4.7d show the self-propulsion velocity of symmetric swimmers as a function of the bead radius. Swimmers with equally sized beads have approximately the same velocity, independently of whether the swimmers are dimers or any type of trimers, and show an approximate linear increase of the velocity with beads size, as already discussed for the thermophobic dimers. This velocity is rescaled by the self-propulsion velocity of the largest studied swimmer, $s_p = 6$, and showed in Fig. 4.7c.

The rotational diffusion coefficient of the triangular trimer as a function of the aspect ratio γ shows little difference with the D_R corresponding to the linear trimer, as shown in Fig. 4.8a. On the other hand, Fig. 4.8b shows that for symmetric geometries, a change in the phoretic radius has a larger effect on the D_R. The rotational diffusion coefficient of triangular trimers is substantially higher than the one of the linear trimers, but smaller than the dimeric swimmer ones for small swimmers ($s_p < 4$). Nonetheless, the inset of Fig. 4.8b shows that the triangular

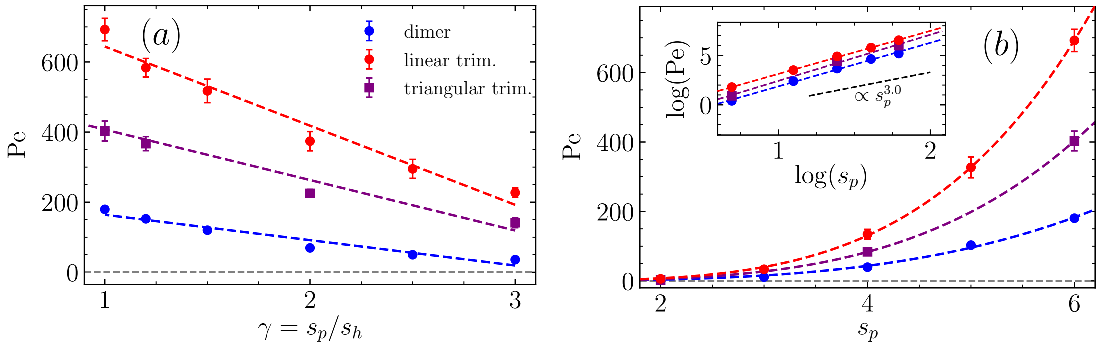

Figure 4.9: Péclet number for the thermophobic triangular trimers (purple) compared to the thermophobic dimers (blue) and linear trimers (red) as a function of the aspect ratio γ (a) and s_p for the symmetric case (b). Triangular trimers show that the extra phobic bead increases the Péclet number with respect to the dimers, but linear trimers remain more ballistic. Dashed lines correspond to the linear (a) and power law (b) regressions of the data. Inset in (b) shows the Péclet number in log-log scale, with the linear regression of the data, leading to Pe $\propto sp^{\beta}$.

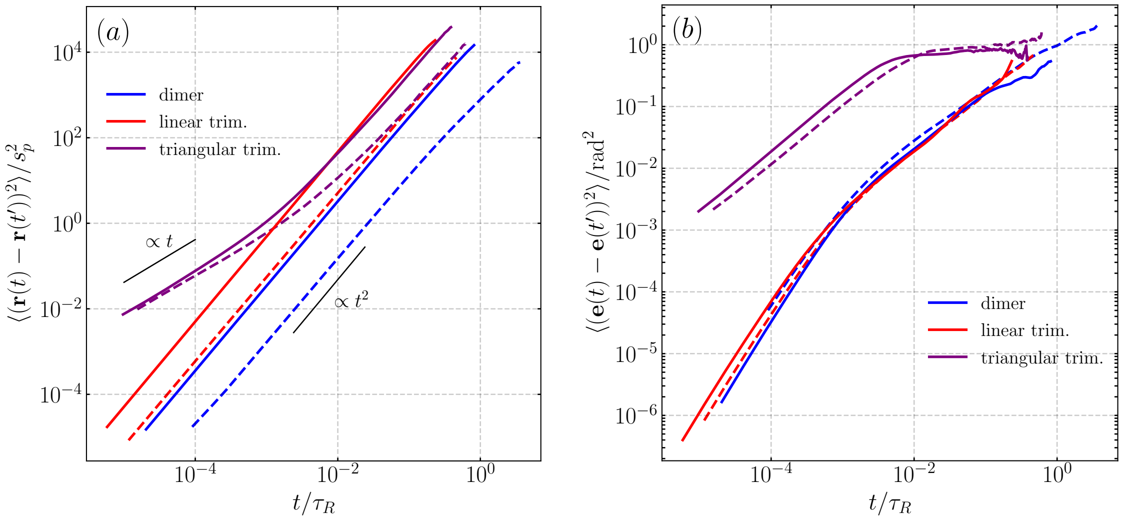

Figure 4.10: (a) Mean square displacement and (b) mean square angular displacement of thermophobic triangular trimers (purple) compared to thermophobic dimers (blue) and linear trimers (red) in quasi-2d confinement. Solid lines stand for symmetric swimmers ($\gamma = 1$) while dashed lines stand for asymmetric ones ($\gamma = 3$).

trimer's D_R displays the same power law behaviour as dimers and the linear trimers, with $\beta \simeq -3.5$. Fig. 4.9a shows the Péclet number of the phobic triangular trimers as a function of the aspect ratio between beads. The triangular trimer's Pe is shown to be smaller than the linear trimer's one, which derives from the difference in velocities, and larger than the phobic dimer's for all the studied values of the aspect ratio γ. Moreover, the Péclet number of these triangular-shaped swimmers show a clear linear decay with γ, as observed for the other swimmers studied here. Fig. 4.9b shows the Péclet number for symmetric swimmers as a function of the phoretic bead's radius, s_p. The inset in this figure shows that the Péclet number also follows the same power law as the other swimmers, $\mathrm{Pe} \propto s_p^3$.

Thermophobic dimers are more affected than both types of trimers by changes on their internal geometry, *i.e.*, the aspect ratio between the bead sizes. Given the triangular trimer construction, there is less available area of the phoretic bead to react to the temperature gradient than compared with the linear swimmers, leading to a lower phoretic propulsion force.

Triangular trimers show a diffusive regime for small time windows, reaching the ballistic regime characteristic of the active motion at larger times, shown in their $\Delta\boldsymbol{r}^2$ in Fig. 4.10a. This behaviour can be due to the geometry of the forces. For the triangular trimer case, the forces point from the centres of the phoretic beads outwards the swimmer. The forces are pulling in the same direction in the axis parallel to the motion, but in different directions in the axis perpendicular to the swimmer's orientation. This can lead to that, for short-ranged times, the triangular trimer propels in the $\hat{\boldsymbol{v}}$ direction, but with a substancial noise in the perpendicular direction due to the components of the two pulling forces, which yields to a diffusive-like behaviour of the trajectory. Nonetheless, for higher times, this short-time effects disappear and the motion is purely ballistic, as seen for its dimeric and linear trimeric counterparts. The ballistic time is shown in Tab. 4.2, compared to the rotational time τ_R between phobic dimers and linear and triangular (V-shaped) trimers. For completeness, and later reference, Tab. 4.2 also includes values obtained for thermophilic dimeric and triangular trimeric swimmers. The single properties of these thermophilic structures are not discussed here, but are, in general, similar to the thermophobic ones. It is seen that $\tau_B \ll \tau_R$ for all swimmers and geometries. This implies that the swimmer needs more time to reorient, leading to the ballistic trajectories seen in the $\Delta\boldsymbol{r}^2$ of Fig. 4.3b and Fig. 4.10. Note that the $\Delta\boldsymbol{r}^2$ of thermophobic triangular trimers show a diffusive regime at short time scales before reaching the ballistic regime, due to the propulsion forces which point in opposite directions, enhancing the short-scale diffusion due to thermal fluctuations.

Symmetric triangle-shaped trimers also display a linear dependency of v_{sp} with the size of the phoretic bead, as linear trimers and dimers (shown in the previ-

Table 4.2: Values of the ballistic (τ_B) and rotational (τ_R) times for the symmetric and asymmetric ($\gamma = 3$) phobic and philic dimers and triangular trimers, and linear trimers.

swimmer	$\tau_B(\gamma = 1)$	$\tau_B(\gamma = 3)$	$\tau_R(\gamma = 1)$	$\tau_R(\gamma = 3)$
phob. dimer	273 ± 2	308 ± 3	$(4.9 \pm 0.2) \times 10^4$	$(1.1 \pm 0.2) \times 10^4$
phil. dimer	469 ± 6	472 ± 6	$(2.4 \pm 0.1) \times 10^4$	$(3.9 \pm 0.2) \times 10^3$
lin. trimer	249 ± 2	380 ± 4	$(1.7 \pm 0.3) \times 10^5$	$(9.6 \pm 0.7) \times 10^4$
V phob. trimer	256 ± 2	458 ± 6	$(1.2 \pm 0.2) \times 10^5$	$(6.5 \pm 0.4) \times 10^4$
V phil. trimer	480 ± 6	833 ± 7	$(1.0 \pm 0.1) \times 10^5$	$(2.1 \pm 0.1) \times 10^4$

Table 4.3: Values of the slope and exponents of the power law regressions of the D_R (β) and the Péclet number (β') of the thermophobic symmetric ($\gamma = 1$) triangular trimer, as expressed in Eq. (4.3) and Eq. (4.4), respectively.

swimmer	m ($\times 10^3$)	β	β'
phobic	4.4 ± 0.5	-3.8 ± 0.1	3.3 ± 0.3

ous subsection). Moreover, the rotational diffusion coefficient D_R is a power law function with s_p (see Eq. (4.3)), as the Péclet number. Values of the exponents are shown in Tab. 4.3. Thermophobic triangular trimers show a lower exponent (or higher absolute value of β) than both thermophobic dimers and linear trimers. The effect of the increase in size has a more significant effect on the triangular swimmers than in the linear counterparts, due to their construction. Dimers are smaller than trimers, leading to a higher effect of the thermal noise, or fluid perturbations, on their motion. On the other hand, linear trimers have the same volume as triangle-shaped trimers, but the disposition of the beads leads to a swimmer more prone to suffer from fluid perturbations, due to the unique direction of both thermophoretic forces. Thermophobic triangular trimers move due to the superposition of the forces, which point forming a V shape, and in the direction away of the centre of mass of the swimmer. This construction leads to a swimmer in which the fluid perturbations have a smaller effect on the movement.

4.3 Hydrodynamics of linear swimmers

The interaction of two neighbouring swimmers is importantly affected by the interaction of their respective flow fields, which is going then to determine the collective swimming behaviour. We hereby present the flow fields of single 3d-bulk thermophobic and thermophilic dimers and linear trimers, with the quantification of said flow fields, comparing the two geometries. The geometry effects have been studied by varying the aspect ratio between beads, γ, while the propulsion mechanism is inherently different for all the three cases under study. In order to give a theoretical approach to the flow fields, two analytical models are here employed.

4.3.1 Stream lines and flow fields

The changes on the geometry of the swimmer do not only influence the swimming behaviour of the colloid, but more remarkably, the effect of the swimmer on the fluid surrounding it. Phoretic dimers have shown to produce flow fields of force-dipole-type for both catalytic [198, 199] and thermophoretic [108, 180] swimmers. These dipolar flow fields are characterised by their lateral hydrodynamic flow, falling in the pusher or puller categories [6]. In most biological swimmers, the nature of the flow field frequently relates with the propulsion mechanism. Puller swimmers usually have the propulsion on the head of the swimmer, as in the case of the flagellated green algae *Chlamydomonas reinhardtii* [200, 201, 202], while pusher swimmers have often the propulsion engine on the rear, such as *E. coli* bacteria [203, 204]. Puller swimmers push the fluid outwards in the lateral direction, *i.e.*, the direction perpendicular to the motion axis, resulting in a lateral hydrodynamic repulsion of any neighbouring swimmers. Pusher swimmers pull the fluid inwards in the lateral axis, leading to hydrodynamic attraction. One interesting example of pusher- and puller-like systems can be found in literature of squirmers with negative or positive squirmer parameter [88, 205].

The measurements of the flow fields of phobic/philic dimers with $\gamma = 1$, $\gamma = 2$ and $\gamma = 3$[1] in 3d are displayed in Fig. 4.11. For both thermophobic and thermophilic dimeric swimmers, the fluid is pushed away from the leading bead of the swimmer, returning to the rear of the swimmer due to the local circulation of the fluid. The main difference between thermophobic and thermophilic dimers lays in the position of the motor, which leads to an asymmetry of the surrounding flow fluid. Thermophobic beads are in the head of the swimmer, while thermophilic monomers are in the tail. This significant change is what leads the two different hydrodynamic behaviours. Thermophobic symmetric dimers (see Fig. 4.11a) display a flow field characteristic of the puller-type swimmers, pushing fluid outwards in the lateral direction of the swimmer, leading to a lateral hydrodynamic repulsion. The case of the thermophilic symmetric dimers is the opposite (see Fig. 4.11b), they show the flow field of a pusher-type swimmer, pulling the fluid inwards in the lateral direction, leading to a lateral hydrodynamic attraction towards the swimmer.

---

[1] Note that $\gamma = 3$ swimmers have been studied with $s_p = 6$ instead of $s_p = 4$ to avoid having $s_h < 2$, which can induce unphysical behaviours of the colloids due to the MPC-MD coupling between the colloid and the fluid. No significant differences are expected neither qualitatively nor quantitatively, if properly normalised.

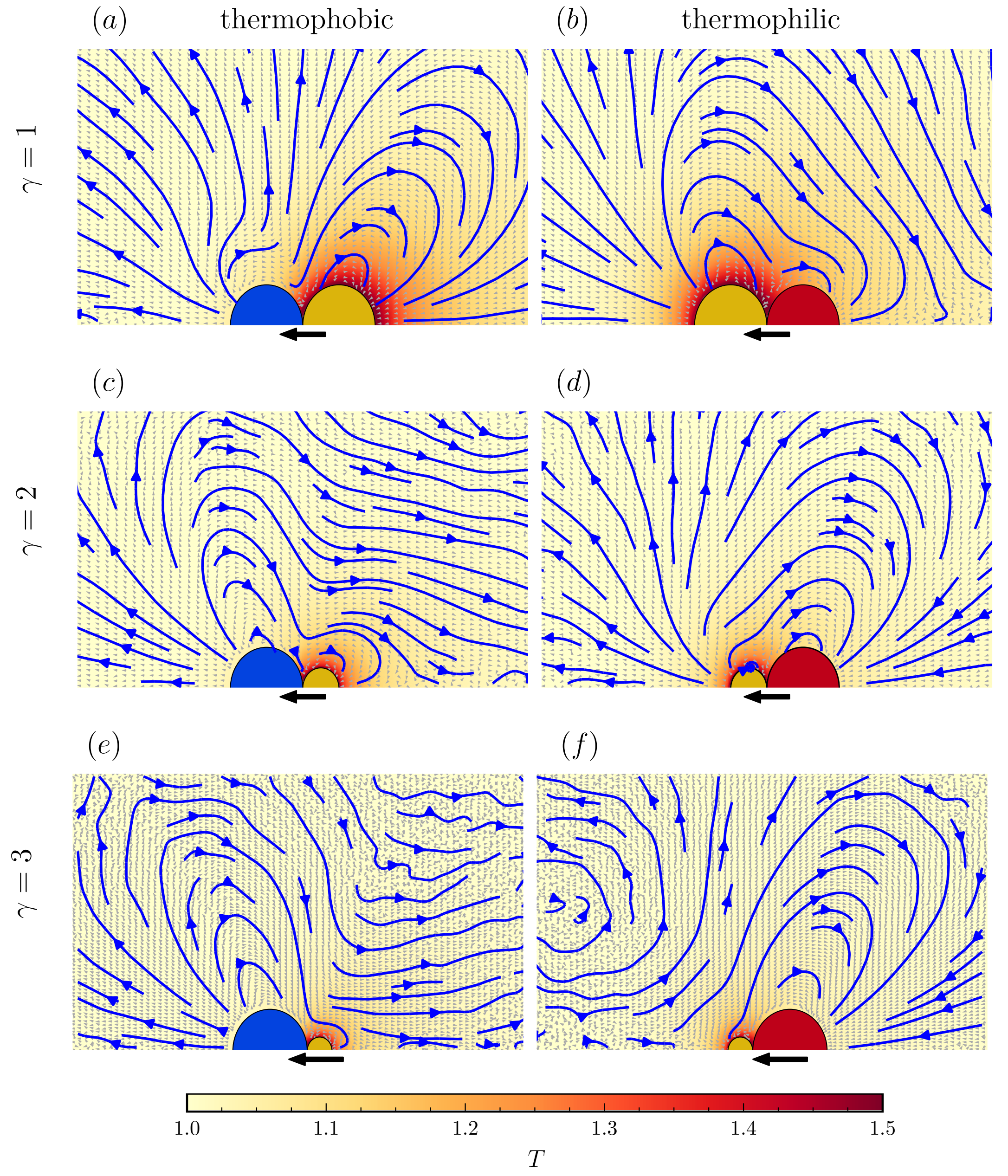

Figure 4.11: Characterisation of the fluid around phobic and philic dimeric swimmers with $\gamma = 1$, $\gamma = 2$ and $\gamma = 3$. All swimmers are depicted with the same propulsion direction. The colour map stands for the temperature gradient created by the heated particle, the small gray arrows stand for the velocity field, while the blue lines are the averaged stream lines.

Moreover, the flow field adapts to differences in the construction of the swimmer. Changing the relative size of the beads, γ, significantly modifies the hydrodynamic behaviour of the flow field. Considering Fig. 4.11a, Fig. 4.11c and Fig. 4.11e, when the value of γ increases, the lateral hydrodynamic interaction changes from repulsive to attractive, and viceversa if one considers the thermophilic case (Fig. 4.11b, Fig. 4.11d and Fig. 4.11f). The lobe formed by the stream lines around the phoretic bead of both swimmers increase as γ increases [108], being nearly inexistent for the case of the symmetric swimmers. Moreover, symmetric phobic and asymmetric philic dimers show a short-range change of the hydrodynamic lateral interaction.

The linear trimeric swimmer displays an interesting flow field, seen in Fig. 4.12, which, as a first approximation, can be understood as the superposition of the flow fields of the two dimeric swimmers of the same bead ratio. The main difference between the flow fields of the trimers with this simple superposition principle, are that for the case of the symmetric trimer, the behaviour of the single dimer flow field is lost, while the asymmetric trimer keeps both lobes of the flow fields. For the symmetric trimer case in Fig. 4.12a, we can see that the resulting stream lines resemble the superposition of the stream lines of the symmetric dimers, as shown in Fig. 4.12c. The hydrodynamic repulsion and the lobe-like shape of the stream lines seen in Fig. 4.11a are present in the trimer, with a small deviation due to the lobe of Fig. 4.11b. The differences for the asymmetric trimer are more noticeable. Comparing the stream lines of both asymmetric dimers with the linear trimer (Fig. 4.12b) we see that both the lobe-like shapes produced by the flow field are present on the stream lines of the asymmetric trimer. The direct superposition of the flow fields of the dimers that make the trimer are presented in Fig. 4.12c and Fig. 4.12d with black stream lines, for the symmetric and asymmetric case, respectively. For the symmetric trimer, this comparison leads to two very similar stream lines, although differences on the shape of the lobe around the philic bead can be observed, as well as the disappearance of the small attractive lobe in the proximity of the thermophobic bead. The direct superposition of the stream lines of the two asymmetric dimers Fig. 4.11c and Fig. 4.11d results in a very different flow field (see Fig. 4.12d). These differences can be considered higher order contributions since the fluid in proximity of the trimer feels simultaneously the presence of both phoretic beads.

Note that we do not characterise here the flow fields of the triangular trimers. For these structures, the cylindrical symmetry is lost, which importantly hampers the gathering of statistics. Furthermore, the differences that we expect with respect to the dimers are not really significant, especially considering the differences between $\gamma = 2$ and $\gamma = 3$ for the dimers in Fig. 4.11.

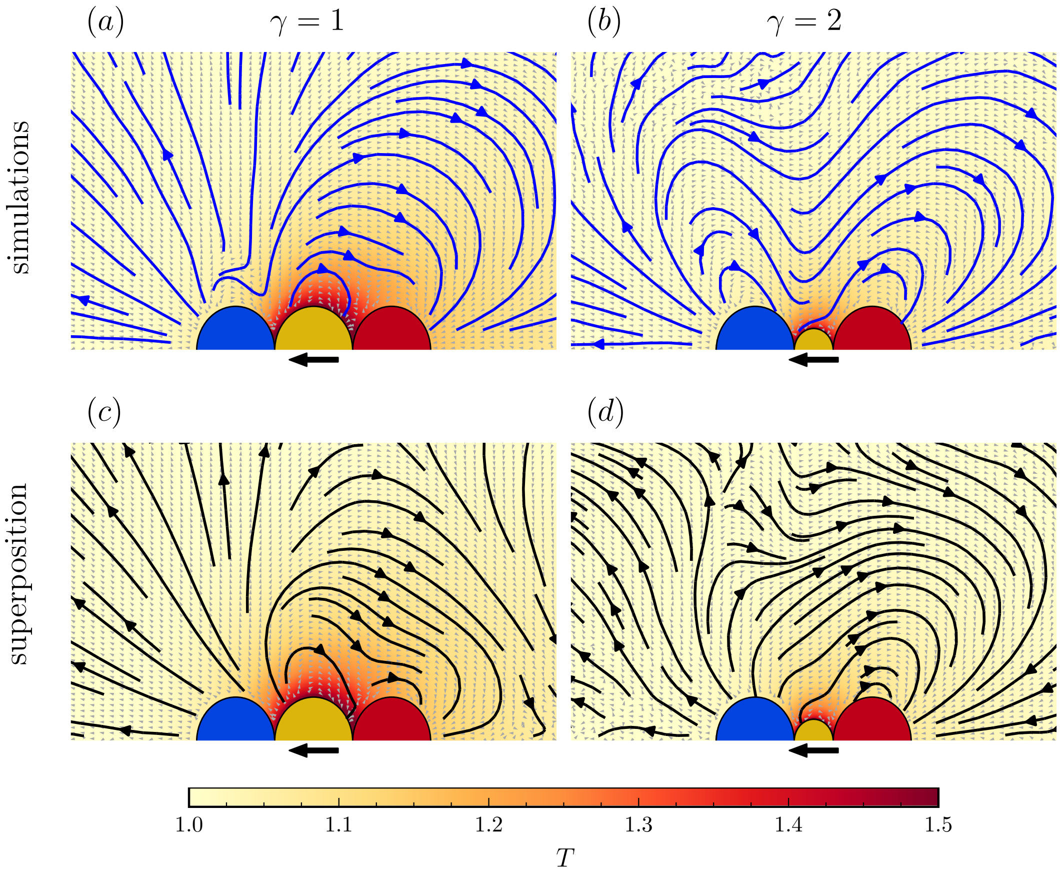

Figure 4.12: Characterisation of the fluid around the symmetric and asymmetric linear trimeric swimmers. All swimmers are depicted with the same propulsion direction. The colour map stands for the temperature gradient created by the heated particle, the small gray arrows stand for the velocity field. In (a) and (b), blue lines correspond to the flow field from the direct result from simulations. In (c) and (d), black lines are obtained as the superposition of the simulated dimeric velocity fields.

4.3.2 Quantification of the flow velocity

The fluid flow around the dimers and linear trimers is measured by a cylindrical average, and therefore characterised in cylindrical coordinates, yielding to two components, the radial component $\hat{\mathbf{r}}$, moving away from the swimmer, and the tangential component, $\hat{\mathbf{z}}$, along the swimmer direction, as depicted on the sketch from Fig. 4.13. The measured fluid velocities are compared with the fluid flow measured for phobic and philic dimers and linear trimers, which are performed with a similar cylindrical average [108, 180]. The fluid flow created by the motion

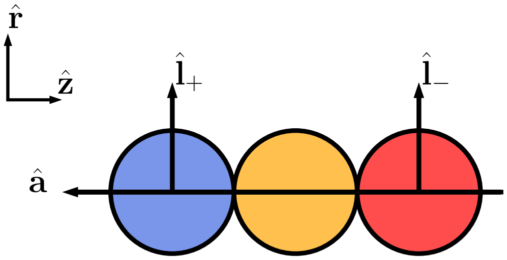

Figure 4.13: Scheme of the defined axis of the trimeric swimmer. The axial orientation corresponds to the swimming direction of the swimmer ($\hat{\mathbf{a}}$), while the lateral axis ($\hat{\mathbf{l}}_+$ and $\hat{\mathbf{l}}_-$ for the phobic and philic bead, respectively) corresponds to the perpendicular direction respect the swimming direction.

of the asymmetric dimer is both qualitative and quantitative different than the corresponding to the symmetric dimer, as seen when comparing the representation of u_l^z in Fig. 4.14a and Fig. 4.14b. The fluid flow created by the phobic bead in the case of the symmetric trimer strongly affects the flow created by the philic bead. On the other hand, the flow created by the phobic bead in the case of the asymmetric swimmer is too weak to influence the flow created by the thermophilic bead, conserving then a behaviour reminiscent of the original's dimer flow field. The flow field of the linear trimer resembles the flow fields of the corresponding dimers, as discussed in the previous section. The lobe-like shape that the fluid creates around the philic bead in the simulations for the symmetric trimer both decreases and changes its location in comparison with the overlapped flow fields. This lobe is located at a distance r_i from the thermophobic bead and at $r_j < r_i$ from the thermophilic bead, which has a small effect on the flow around the thermophobic bead, where the small lobe seen in Fig. 4.12a disappears. Moreover, it explains the significant changes between the flow fields obtained via simulations and direct addition of dimeric flow fields (also from the simulations). The same behaviour is observed for the asymmetric trimer, where the lobe around the thermophilic bead decreases for the case of the superimposed flow fields, due to the same effect. In this latter case, however, the lobe around the thermophobic bead, and thus the butterfly-like shape of the flow field, is completely lost. Moreover, the symmetric swimmers display a short-ranged change of the hydrodynamic behaviour. As mentioned before, thermophobic dimers are puller-type, with a lateral hydrodynamic repulsion, and viceversa for their philic counterparts. Nevertheless, as shown for the radial component of the lateral velocity of the fluid flow, u_l^r, displayed in both Fig. 4.14a and Fig. 4.14c, this interaction changes sign close to the phoretic bead (at distances $r < 2s_p$ from the phoretic bead).

In Fig. 4.14, the analytical approaches to the flow fields are also displayed. Dashed lines correspond to the approach presented by Yang *et al.* [74], in which the flow field of a thermophoretic dimer is treated as the superposition of the flow fields (solutions of the Stokes equation) produced by the heated bead, $\boldsymbol{u}_h(\boldsymbol{r})$, and phoretic bead, $\boldsymbol{u}_p(\boldsymbol{r})$,

$$\begin{aligned}
\boldsymbol{u}_h(\boldsymbol{r}) &= \frac{s_h}{2|\boldsymbol{r}-\boldsymbol{r}_h|}\left(\frac{(\boldsymbol{r}-\boldsymbol{r}_h)^2}{|\boldsymbol{r}-\boldsymbol{r}_h|^2}+\mathbb{I}\right)\cdot\boldsymbol{v}_s\ , \\
\boldsymbol{u}_p(\boldsymbol{r}) &= -\frac{s_p}{2|\boldsymbol{r}-\boldsymbol{r}_p|}\left(\frac{(\boldsymbol{r}-\boldsymbol{r}_p)^2}{|\boldsymbol{r}-\boldsymbol{r}_p|^2}+\mathbb{I}\right)\cdot\boldsymbol{v}_s \\
&\quad+\frac{s_p^3}{|\boldsymbol{r}-\boldsymbol{r}_p|^3}\left(3\frac{(\boldsymbol{r}-\boldsymbol{r}_p)|^2}{|\boldsymbol{r}-\boldsymbol{r}_p|^2}-\mathbb{I}\right)\cdot\boldsymbol{v}_s\ . \qquad (4.5)
\end{aligned}$$

Here $\boldsymbol{u}(\boldsymbol{r})=\boldsymbol{u}_h(\boldsymbol{r})+\boldsymbol{u}_p(\boldsymbol{r})$ is the velocity of the fluid, $\boldsymbol{v}_s$ the swimmer's velocity, and $\boldsymbol{r}_k$ the position of the bead. Thus, the far field around the dimer is estimated as the superposition of two Stokeslets, which lead to a Stokes dipole or stresslet, and $\boldsymbol{u}(\boldsymbol{r})\sim 1/r^2$ [74], the characteristic flow field of a microswimmer. This approach has the advantage of being independent on the propulsion mechanism of the swimmer. This prediction agrees with the simulation results for the radial component of flow velocity on the lateral axis, u^l, for both symmetric phobic (Fig. 4.14a) and philic (Fig. 4.14c) dimers at distances $r\geq 4s_p$. Nonetheless, at closer distances to the beads ($\boldsymbol{r}<4s_p$) the differences are important, as well as for the asymmetric dimers [108], where the short-ranged change of hydrodynamic interactions is not captured. In their comparison, Yang *et al.* considered a thermophoretic dimer whose beads were separated, which affects the flow fields of the dimers. For beads in contact, these two fields from Eq. (4.5) are no longer independent, thus breaking the assumption of the independent solutions of the Stokes equation. This approach also captures the behaviour of the fluid velocity u_r^l of the symmetric trimer around the phobic bead, given the resemblance with the phobic dimer, but fails on the philic axis or once again on the asymmetric geometry.

Another approach to the prediction of these flow fields was addressed by Reigh and Kapral [199] for a catalytic dimer using a bispherical coordinate system, and considering slightly separated beads. This approach can be tuned and adapted to thermophoretic dimers by changing the slip boundary condition on the velocity [108]. This velocity is given by

$$v_B=-\frac{\rho}{\mu_d T}\nabla_{\boldsymbol{r}}T\int_0^B \mathrm{d}r'\ r'\ U(r')\exp\left[-\frac{U(r')}{k_B T}\right]\ ,$$

with ρ the density of fluid around the swimmer, μ_d the fluid's dynamic viscosity, T the temperature of the fluid and $U(r)$ the interaction potential between the fluid and the colloids. This velocity can be approximated for small temperature gradients to

$$v_B=-\kappa_T\nabla_{\boldsymbol{r}}T\ ,$$

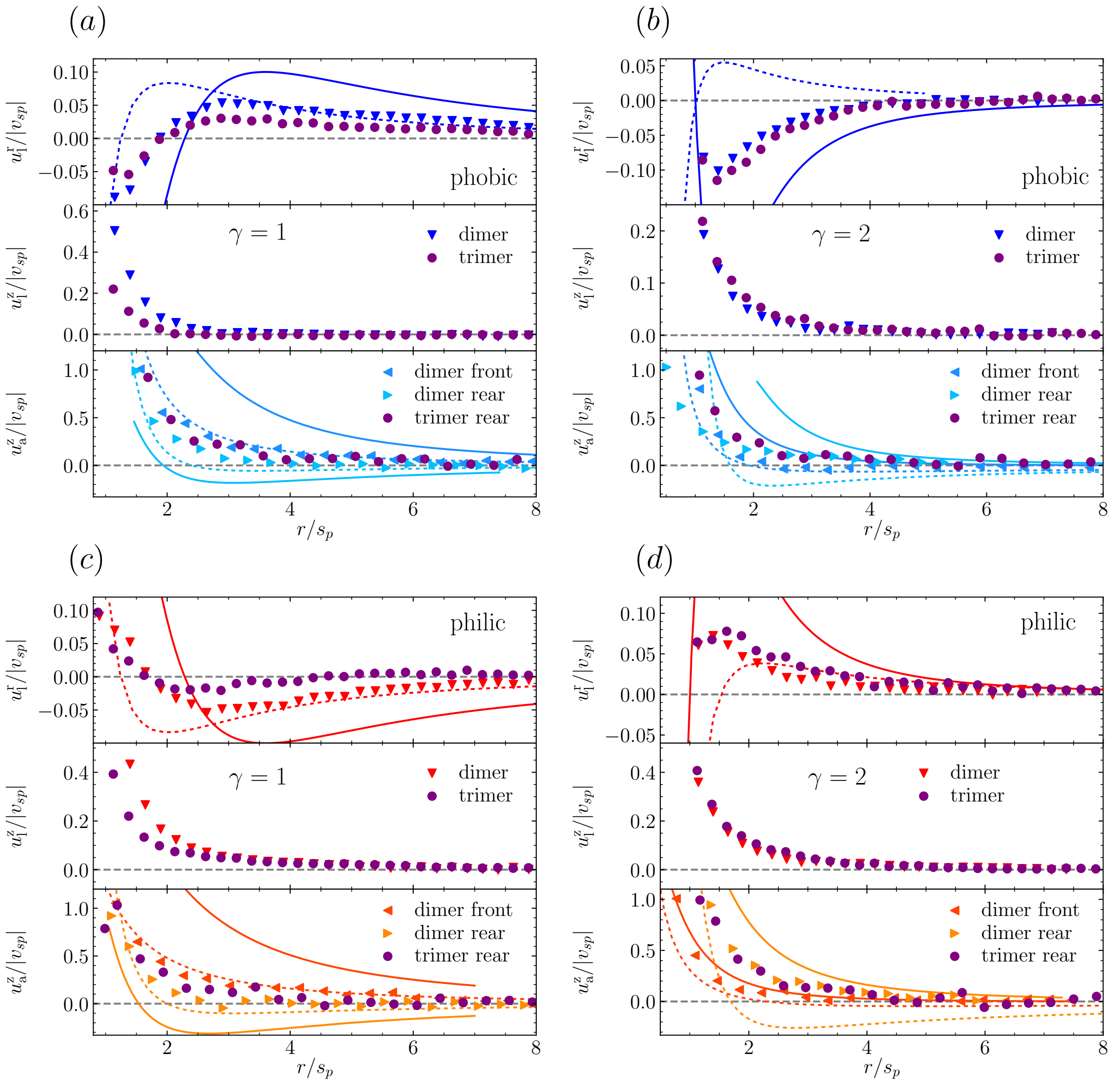

Figure 4.14: Quantification of the swimmers flow velocity measured around both main axes, the lateral axis l and the axial one a, as sketched in Fig. 4.13. The thermophobic dimer's and trimer's bead analysis is shown in (a) for $\gamma = 1$ and (b) for $\gamma = 2$, while the thermophilic case is shown in (c) for $\gamma = 1$ and (d) for $\gamma = 2$. The axial flow velocity, u_a^z, is measured in the moving direction, z, to the front (dark blue dots) and the rear direction (light blue dots) for the dimer, and in purple and pink for the trimer . Measurements have been done with the phoretic bead as a reference. The lateral velocity, u_l is calculated in both coordinates, the moving direction z and the radial direction r, perpendicular to the swimmer motion. Velocities are rescaled by the swimmer's velocity, v_{sp}, and the distance r is rescaled by the radius of the phoretic bead s_p. Dashed lines correspond to the theoretical approach of Yang *et al.* [74] and solid lines represent the thermophoretic variant of the framework of Reigh and Kapral [199], with $\delta_b = 0.5$.

where κ_T is the thermal conductivity (see section 2.4.3)

$$\kappa_T = \frac{\overline{\rho}}{\mu_d \overline{T}} \Lambda ,$$

and

$$\Lambda = \int_0^B \mathrm{d}r \; r \; U(r) \exp\left[-\frac{U(r)}{k_B T} \right] .$$

This expression of the slip velocity along with suitable boundary conditions allow the translation of Reigh and Kapral's prediction to thermophoresis. The boundary condition used in Ref. [199] has to be substituted by a heat flux, $(\nabla T \cdot \tilde{\eta})_{\eta=\eta_1} = q/k_T$, with k_T the thermal conductivity. The heat flux at a distance r is

$$q(r) = \left(T(r) - \overline{T} \right) \frac{r}{s_h^2} k_T ,$$

which at the surface of the heated bead becomes $q(s_h) = (T_h - \overline{T}) k_T / s_h^2$. For a full derivation of this theoretical approach, see [108]. This thermophoretic variant of the approach of Reigh and Kapral [199] (solid lines in Fig. 4.14) results in a qualitatively better prediction of the flow fields, both phobic and philic, and symmetric and asymmetric geometries, since it captures the changes of hydrodynamic lateral interactions for all the swimmers studied. The discrepancies on the quantitative descriptions may lie on the strong approximations used for the derivation of the boundary conditions of the theoretical model applied to the thermophoretic dimer [108]. Furthermore, although this approach allows us to get the beads closer, the state in which beads are in contact can not be reached. On the theoretical predictions in Fig. 4.14 (solid lines), a small distance δ has been set in between the beads to avoid the singularity.

4.3.3 Fixed swimmers

Hydrodynamic interactions do not only appear for suspended moving objects, but also in some cases for fixed particles, due to the interactions between the fluid and the colloid's surface, as in the case of the osmotic flows. This flow field is very relevant in various situations, and of particular interest for our work when there is aggregation in the system, given that the swimmers trapped in clusters are still able to create a hydrodynamic field, altering the mechanism involved in the aggregation process. This section shows the flow fields of fixed thermophobic Fig. 4.15 and thermophilic Fig. 4.16, symmetric and asymmetric dimers, where the phoretic bead has been measured as $s_p = 6$ for all cases. All the flow fields are taken in the dimer reference frame. The linear trimer flow fields are not presented for

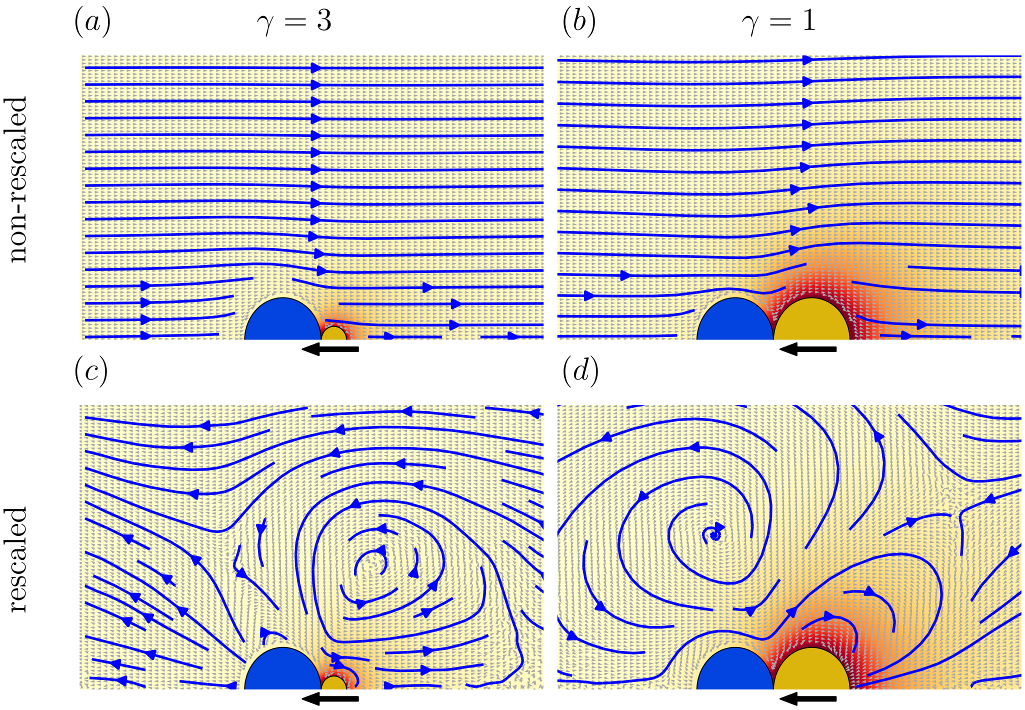

Figure 4.15: Flow fields of (*a*) asymmetric ($\gamma = 3$) and symmetric (*b*) phobic dimers when fixed (upper) and subtracting the flow velocity at the edges of the simulation box (bottom).

the fixed case, given that the dynamics of the ensembles does not show aggregated structures where these flow fields are relevant. The phobic and philic dimers' flow fields in Fig. 4.15 and Fig. 4.16 show that there is always a hydrodynamic attraction towards the head of the swimmer for a fixed swimmer, whereas the back shows a hydrodynamic repulsion, independently of the geometry and of phoretic nature of the dimer. This is of the uttermost importance, given that the structure of the surface of the cluster determines the overall hydrodynamic interaction of the aggregate. Fig. 4.15a and Fig. 4.15b show the flow fields of fixed thermophobic dimers, for $\gamma = 3$ and $\gamma = 1$, respectively.

In order to better understand these flows, we show in Fig. 4.15c and Fig. 4.15d the flow field of the same dimer with the fluid velocity at the edge of the simulation box subtracted from all the fluid velocities. Similarly, Fig. 4.16a and Fig. 4.16b show the flow fields of the fixed philic dimer, and Fig. 4.16c and Fig. 4.16d show the same flow fields rescaled by the fluid velocity at the limit of the box. In general, these rescaled flows show a certain degree of resemblance with the flows of the corresponding swimming structures, although the parallelism is not the same for all of them. The obtained rescaled flow field of the asymmetric phobic dimer does

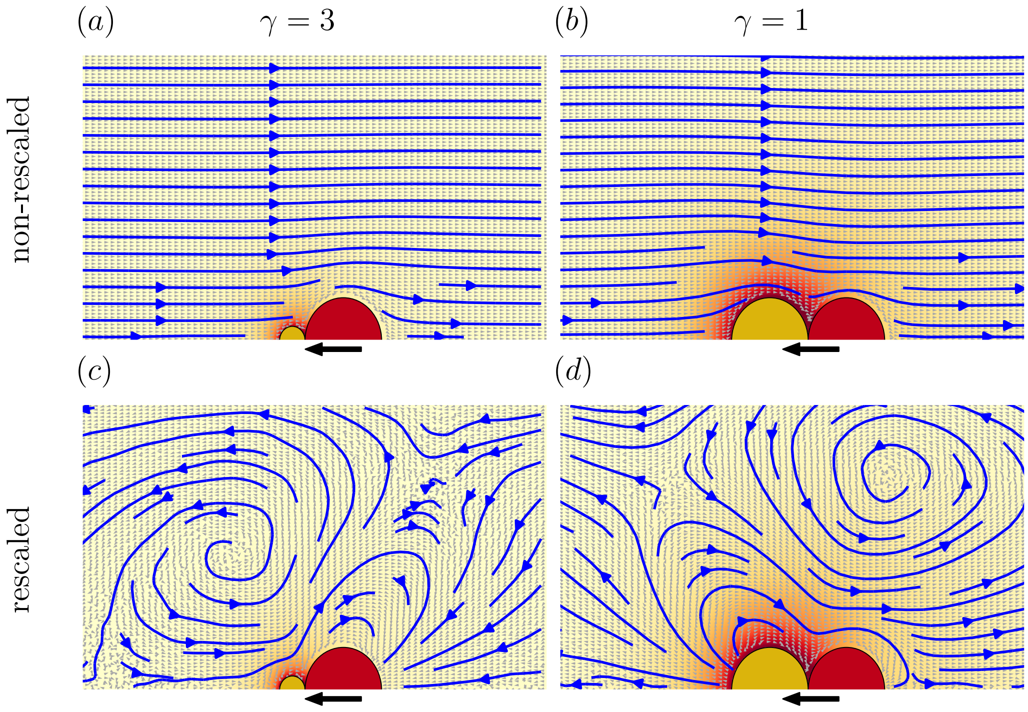

Figure 4.16: Flow fields of (*a*) asymmetric ($\gamma = 3$) and symmetric (*b*) philic dimers when fixed (upper) and subtracting the flow velocity at the edges of the simulation box (bottom).

not resemble too strongly the one corresponding to the freely swimming one. The symmetric one still holds some resemblance of the lobe around the heated bead, but the presence of the fluid vortex in the front of the dimer is not observed for free swimming dimers. Moreover, the flow field of the asymmetric philic dimer when fixed resembles the corresponding to the unbound dimer. Similarly to the symmetric phobic dimer, the symmetric philic dimer shows a vortex not present when swimming, and a decrease of the lobe around the heated bead.

Fig. 4.17 shows the quantification of the flow fields of the asymmetric and symmetric thermophilic dimer, following the same procedure showed on the previous section. The radial component of the lateral fluid velocity, u_l^r, does not change significantly by restraining the dimer from moving. As expected, the z component of both lateral and axial fluid velocities is deeply affected by fixing the dimer. Nevertheless, by rescaling these velocities, as done for the flow field, the u_a^z and u_l^z from the swimming dimer are recovered.

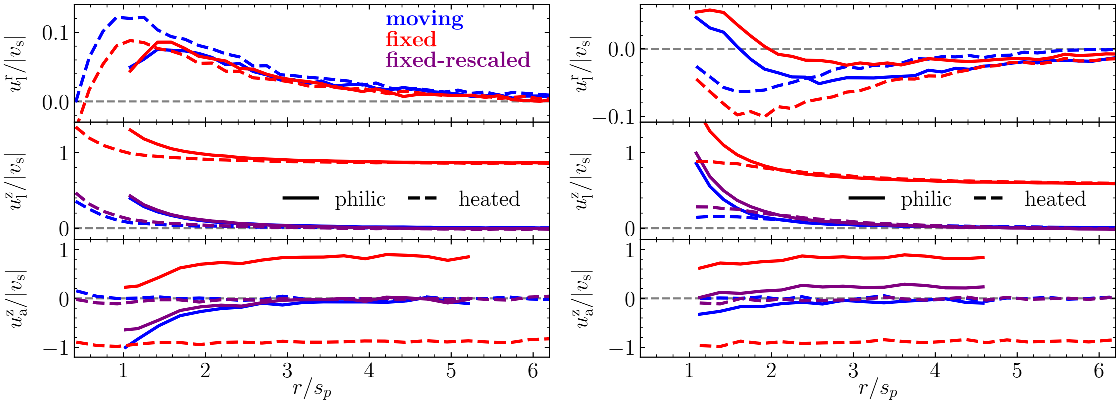

Figure 4.17: Quantification of the flow field of the (*a*) asymmetric $\gamma = 3$ and (*b*) symmetric thermophilic dimer. Blue lines stand for a freely swimming dimer, while red stands for a fixed dimer. Purple lines result from the rescale of velocities using the $u_l^z|_\infty = 0.87v_{sp}$ for the asymmetric and $u_l^z|_\infty = 0.60v_{sp}$ for the symmetric dimer. Solid lines correspond to the phoretic bead reference, while dashed lines correspond to the reference of the heated bead.

4.4 Summary

The characterisation of the swimming behaviour of single thermally driven dimers and linear trimers has been discussed in terms of the propulsion velocities and rotational diffusion. All the quantities studied change due to the geometric construction and the overall size of the swimmer, while the heating temperature has been kept constant. Moreover, the effect of the quasi-2d confinement has been considered via simulations on a quasi-2d slit.

Thermophobic dimers show a slight increase of their self-propulsion velocity when confined in a quasi-2d slit. On the other hand, this confinement shows no large impact on the rotational noise of the swimmers, as seen from very similar results of the rotational diffusion coefficient. This leads to very similar Péclet numbers for thermophobic dimers swimming in 3d-bulk and quasi-2d systems. The effects of the quasi-2d confinement on the self-propulsion velocity of linear trimers is less noticeable than in the case of dimers. This velocity seems not to change with the confinement. For the symmetric swimmer case, the velocity of the linear trimers is also seen to be very close to the dimer's, given that the extra thrust due to the second phoretic bead is balanced by friction. On the other hand, the rotational diffusion coefficient increases for confined linear trimers, which leads to a significant decrease of the Péclet numbers for quasi-2d systems.

Homogeneous thermophobic triangular-shaped trimers show that the swimming velocity decreases significantly with the beads' aspect ratio, as seen for the other swimmers, although their fastest velocity lies around that of $\gamma = 1$. These swimmers show a rotational diffusion coefficient with values between the thermophobic dimer and the linear trimer, leading also to values of the Péclet number between the values of those two swimmers.

This chapter has also investigated the hydrodynamics of a self-propelled moving swimmer. The propulsion mechanism shows to strongly influence the shape of the flow field around the microswimmer, similar to biological organisms. Moreover, the geometry of the swimmer has also a high impact on the shape of the hydrodynamic field, allowing us to tune the hydrodynamic interactions with the aspect ratio, from attractive to repulsive, and viceversa. From the quantification, it is also seen that asymmetric swimmer seems to create stronger fluid perturbations, leading to higher fluid velocities. The flow fields of linear trimers can be understood as the superposition of the flow fields of the corresponding dimers only in first order approximation. This assumption has only moderate differences with the flow field of the symmetric linear trimer, but does not account for the asymmetric swimmer. Moreover, symmetric swimmers, both phobic/philic dimers and linear trimers, show a short-range change on their hydrodynamic interactions, which have a very important role on their collective behaviour, influencing the clustering mechanism.

Chapter 5

Collective behaviour of dimers

Biological and artificial active systems display a variety of collective behaviour such as vortices, motility-induced phase separation or swarming.

Motility-induced phase separation (MIPS) describes the phase separation of a system due to particle aggregation induced by their propulsion [206]. MIPS occurs when more than two active particles collide heads-on and block their motion. It takes some time for the propulsion direction to reorient and resume their motion, which might eventually dissolve this transient structure. During this reorientation time, more particles can collide with such aggregates, forming bigger structures. Then, the system may phase-separate into a gas-like phase of the free self-propelled particles and a dynamic crystalline structure of particles with its propulsion hindered. This aggregation mechanism does not require any alignment mechanism [88]. Moreover, MIPS is observed in both 2d and 3d systems. In 3d bulk systems, the two observed phases are liquid- and gas-like, while 2d systems display crystalline and gas-like phases [17]. The phase behaviour further changes when inter-particle interactions are present. Theurkauff *et al.* [207] reported an experimental observation of what is called a *living crystal*, a dynamic clustering where small clusters form and dissolve constantly, exchanging particles with each other, usually with non-vanishing propulsion velocity.

This chapter addresses the behaviour of thermophobic and thermophilic dimers when found in ensembles of 200 swimmers on simulations at three different densities and two geometries. Static properties, such as the radial distribution function, along with dynamic properties are hereby presented to give an understanding on the different collective behaviour of dimers due to their phoresis and hydrodynamics. Moreover, this chapter also includes the comparison with similar systems without hydrodynamics, via BD simulations following the method from chapter 3, section 3.3, which provides us with the possibility of identifying the effects due to hydrodynamic interactions. The thermophoretic nature of the swimmers under study determines the motion of the swimmers in large ensembles which is a function not only of the geometry but also of the system density. Different mechanisms such as alignment or aggregation are observed in simulations and are subsequently analysed. Thermophobic dimers combine hydrodynamic interactions with phoretic repulsion, leading to swimming aligned clusters. Occasional static aggregates are formed by collisions between the aforementioned clusters, but none of these clusters show long-term stability. On the other hand, thermophilic dimers combine also the hydrodynamic interactions (as seen in Fig. 4.1) but with full phoretic attraction. This leads to the formation of large, static aggregates which can turn into one single big cluster which engulfs nearly all dimers of the system, independently of the aspect ratio of the dimers. This huge clusters do not swim due to the non mutual alignment of the swimmers, and the homogenisation of the temperature gradient on the inside of the aggregate, which suppresses the thermophoretic forces. Aggregates such as these lead to large bodies performing a Brownian motion.

The main goal of this chapter lies in the comparison between thermophoretic dimers swimming at 3d bulk and quasi-2d systems and the effects of both the density, ϕ, and the presence of hydrodynamic interactions.

5.1 Cluster and swimming analysis

In order to identify the structural features, the steady-state radial distribution function (RDF, $g(r)$ or pair correlation function) is here studied. This function is a description of how the density of particles in a system varies as a function of the distance from a reference particle. The RDF is given as [208]

$$g(r) = \frac{1}{\rho}\left\langle \sum_{j<i=1}^{N_s} \delta(|\boldsymbol{r}_i - \boldsymbol{r}_j| - r) \right\rangle , \tag{5.1}$$

where $\rho = N_s/V$ is the number density of swimmers in the system, N_s is the number of swimmers under study, $r_{ij} = |\boldsymbol{r}_i - \boldsymbol{r}_j|$ is the relative distance between particles i and j, and the brackets indicate an average over time and realisations. This function shows the distribution of particles on the system via peaks on the distribution function, and the position of the peak indicates the configuration of the aggregates. The higher the peaks, the more probable of finding particles at a certain distance is, and due to the temporal average, more persistent this configurations are.

The RDF (Eq. (5.1)) can be studied considering phoretic-phoretic and heated-heated distances or the distance between phoretic and heated beads for all the swimmers, independently if they are a member of a cluster or not. The simultaneous consideration of these three functions allows us to identify some relevant swimmer arrangements. More information about the ordering of a large-scale aggregate can be obtained from the structure factor, $S(q)$, with q being the scattering vector. This is a property of interest, given that it can be directly measured in experimental observations [209], and it can be obtained via the Fourier transform of the radial distribution function,

$$S(q) = 1 + 2\pi \frac{N_s}{L^2} \int \Big[g(r) - 1\Big] \frac{\sin(qr)}{q} \mathrm{d}r \ , \tag{5.2}$$

with L the length of the simulation box.

Another structural property to study in these systems is the orientation ordering, or angular alignment, characterised by the spatial distribution of the average orientation angle $\Theta(r)$ between pairs of dimers separated by a centre of mass distance r [180, 208],

$$\Theta(r) = \left\langle \sum_{j<i=1}^{N_s} \arccos \Big[\hat{\boldsymbol{n}}_i(\boldsymbol{r}_i^{\mathrm{cm}}) \cdot \hat{\boldsymbol{n}}_j(\boldsymbol{r}_j^{\mathrm{cm}})\Big] \, \delta(r_{ij}^{\mathrm{cm}} - r) \right\rangle \ , \tag{5.3}$$

where $\boldsymbol{r}_i^{\mathrm{cm}}$ and $\boldsymbol{r}_j^{\mathrm{cm}}$ are the positions of the centre of masses of dimers i and j respectively, thus $r_{ij}^{\mathrm{cm}} = |\boldsymbol{r}_i^{\mathrm{cm}} - \boldsymbol{r}_j^{\mathrm{cm}}|$, and $\hat{\boldsymbol{n}}_i$ is the orientation of said dimer. From this definition follows that $\Theta = 0$ and π correspond to parallel and antiparallel alignment of dimers, while perpendicular orientation or uncorrelated distributed orientations correspond to $\Theta = \pi/2$.

The swimming of the ensembles of dimers can be further characterised by three properties studied as a function of the cluster size. First the probability P of finding a swimmer in a cluster of size N_c is studied by counting the number of free-swimming dimers or swimmers conforming the cluster. Secondly, the average propulsion velocity of the clusters is quantified as a function of the cluster size. This velocity is defined as

$$v_{sp}(N_c) = \frac{1}{N_c} \sum_{k \in C} \boldsymbol{v}^k \sum_{k \in C} \boldsymbol{n}^k \ , \tag{5.4}$$

which is then normalised by the self-propulsion velocity of a single dimer, or $N_c = 1$, and where C is the cluster of size N_c. The two summations stand for the total velocity of the cluster projected on the average main orientation of the aggregate, to obtain a good estimation of the self-propulsion velocity of such clusters. The correlation between orientations of all the members of a cluster of size N_c is described as

$$\langle \boldsymbol{n}(\boldsymbol{r}_i) \cdot \boldsymbol{n}(\boldsymbol{r}_j) \rangle (N_c) = \frac{1}{N_c} \sum_{i \in C} \sum_{j \in C} \boldsymbol{n}(\boldsymbol{r}_i) \cdot \boldsymbol{n}(\boldsymbol{r}_j) \ , \tag{5.5}$$

where $\boldsymbol{n}(r)$ is the orientation of the swimmer in its propulsion axis.

For systems displaying a trend to form stable aggregates, some cluster characterisation quantities, and their evolution with time, are analysed. First, the sizes of the clusters are studied by quantifying the size of the bigger cluster, N_{max}, the average size of all the clusters (excluding single free-swimming dimers), N_{av}, the number of single dimers on the system, N_{sing}, and the total number of clusters (with more than one swimmer on them) in the system, N_c.

The average time a swimmer spends in a cluster, or bounding time, $\langle\tau_c\rangle$, is also calculated. This quantity gives an insight of the aggregation of clusters in the system. A steadily increasing $\langle\tau_c\rangle$ means that the swimmers spend more and more time within a cluster, implying then that the aggregates are stable. In contrast, if this time reaches a plateau, then the swimmers only spend a certain amount of time on a cluster, breaking free after it, thus leading to non-stable aggregates.

5.2 Quasi-2d confinement of ensembles

5.2.1 Thermophobic dimers

Thermophobicity leads to repulsive interactions between phoretic and heated beads. The phoretic bead of each dimer tries to move away from the heated bead, but due to the bond between them this leads to the phoretic bead pulling the heated bead, thus yielding the propulsion of the dimer. Moreover, this phoretic bead feels a repulsive interaction towards the heated beads of all the other swimmers around it.

The hydrodynamic behaviour of a swimming dimer has a strong dependency on the geometry of the swimmer, as shown in Fig. 4.1. Symmetric dimers display a hydrodynamic repulsion on the axis perpendicular to the motion orientation (lateral axis). Nonetheless, at short ranges this interaction changes to attractive, which could lead to unstable linear or front-like clusters, enhanced by steric effects. Two symmetric swimmers swimming closely together can be attracted by hydrodynamics, which competes with the thermophoretic mutual repulsion. When this repulsion and/or thermal and fluid fluctuations brings them far apart, the hydrodynamic interactions also become repulsive and the pair dissolves, thus leading to the instability of the clusters. On the other hand, asymmetric dimers ($\gamma = 3$) display a lateral hydrodynamic attraction in all the spatial range. Two asymmetric thermophobic dimers placed parallel to each other are attracted by hydrodynamics but repelled by thermophoresis. This points to the formation of linear clusters, or groups of oriented dimers swimming in the same direction. Nonetheless, this clusters are unstable due to thermal fluctuations and to collisions with

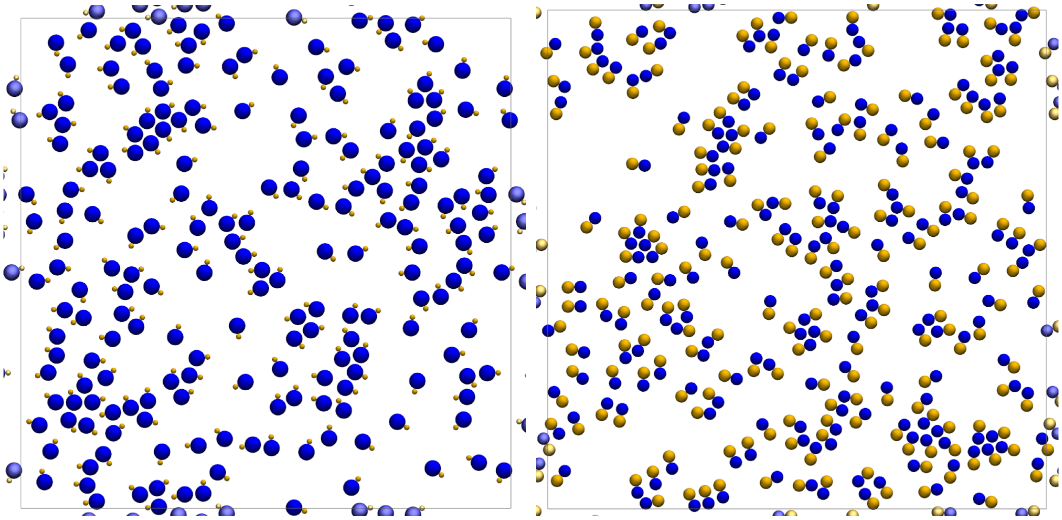

Figure 5.1: Snapshots of (a) asymmetric $\gamma = 3$ and (b) symmetric hydrodynamic thermophobic dimers at an area fraction $\phi = 0.2$.

other clusters or free swimming dimers. The same principle has been observed in 3d simulations of thermophobic dimers to form planar structures [180].

Fig. 5.1 shows two snapshots of 200 thermophobic dimers at an area fraction of $\phi = 0.2$ of geometries $\gamma = 3$ (Fig. 5.1a) and $\gamma = 1$ (Fig. 5.1b). In Fig. 5.1a the aggregates that can be identified are small linearly oriented pairs or trios. In Fig. 5.1b, some oriented clusters are also present, and in this case, these aggregates are easier to identify from the snapshot. This is a result of the combination of the high density, which leads to dimers getting closer to their counterparts, and the short-ranged hydrodynamic attraction that thermophobic symmetric dimers show, as seen in Fig. 4.14a. The simulations show that these constructions are composed mostly of three dimers, which meet at the same time in the same direction. The swimmer in the middle is stuck between the other two, while the other two get close enough to get trapped by hydrodynamics. These trios get dissolved by both frontal collisions with other swimmers and reorientations due to fluctuations, which allow the dimers to exit the range of hydrodynamic attraction and leave the cluster.

The structural characteristics are investigated by the pair correlation function and the orientation distribution function, as shown in Fig. 5.2 for ensembles of thermophobic dimers in 2d (purple lines) and 3d (orange lines) systems. Fig. 5.2a and Fig. 5.2b show the radial distribution function between phoretic beads for $\gamma = 3$ and $\gamma = 1$, respectively. Both systems and geometries show a pronounced peak at bead contact, *i.e.*, $r \simeq 2.2 s_p$, which is shown in the sketch from Fig. 5.3. This value is slightly higher than just the sum of the beads' radii due to the

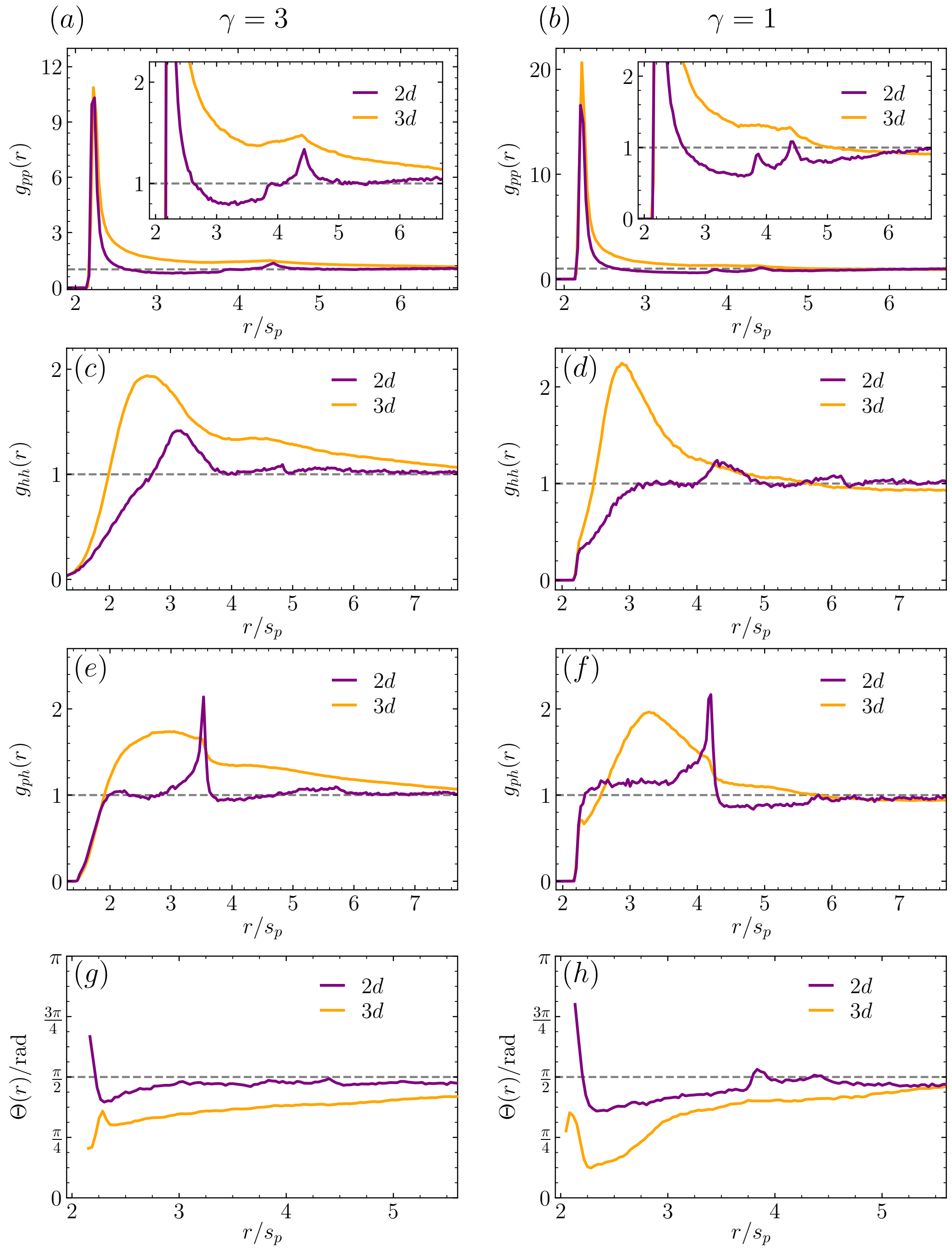

Figure 5.2: RDF of phoretic-phoretic (*a*) and (*b*), heated-heated (*c*) and (*d*), and phoretic-heated (*e*) and (*f*) beads of an ensemble of $\gamma = 3$ (left) and $\gamma = 1$ (right) phobic dimers. Purple lines correspond to 2d systems at $\phi = 0.2$, while orange lines correspond to the 3d simulations from [108] at $\phi_v = 0.005$. Figures (*g*) and (*h*) correspond to the angular distribution $\Theta(r)$, Eq. (5.3).

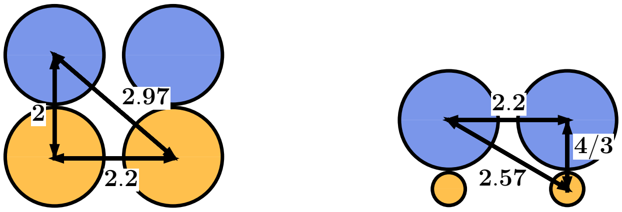

Figure 5.3: Schemes of dimers in a perfectly aligned configuration with their phoretic beads in contact for symmetric ($\gamma = 1$) and asymmetric ($\gamma = 3$) swimmers. The relevant distances, corresponding to the expected peaks of the radial distribution functions, are shown. All distances are in units of the phoretic bead's radius, s_p.

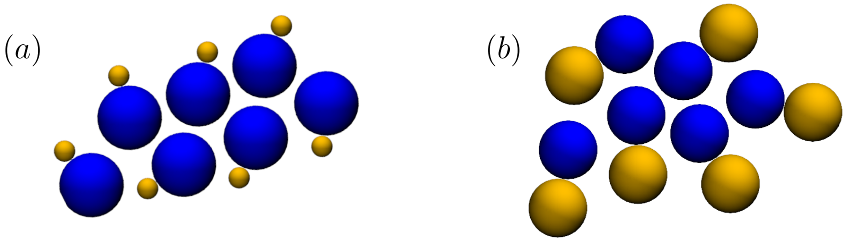

Figure 5.4: Snapshots depicting collisions between small clusters of asymemtric ($\gamma = 3$, (a)) and symmetric ($\gamma = 1$, (b)) thermophobic dimers.

extra separation δ imposed in the excluded volume's potential between beads, as described in section 3.2.2.3. The minimum distance between phoretic beads in both geometric cases is then $2s_p + \delta$. Nonetheless, for the quasi-2d simulations of both asymmetric and symmetric dimers at $\phi = 0.2$, the $g_{pp}(r)$ shows peaks at around $\sim 4s_p$, which points to an ordering at second neighbours distances. This ordering is not really present in the 3d-bulk case as in the 2d, as seen from the orange lines in both Fig. 5.2a and Fig. 5.2b, due to the broader possibility of small structures formed in 3d bulk. The radial distribution function shown in Fig. 5.2c and Fig. 5.2d corresponds to the $g(r)$ between heated-heated beads where the most visible difference is that the peaks of the $g(r)$ corresponding to the quasi-2d confinement are smaller and displaced at larger distances with respect to the ones of the 3d-bulk systems. This displacement on the position of the peaks is also observed for the phoretic-heated radial distribution function shown in Fig. 5.2e and Fig. 5.2f, showing that the structures formed in 3d-bulk systems are more compact than the ones on a quasi-2d confined system. Moreover, this figure also shows that the peaks corresponding to quasi-2d systems are narrower than the 3d-bulk ones, increasing the probability of finding a second bead at a certain distance r, thus also narrowing the number of possible structures formed in the system. Quasi-2d confinement seems to break the orientation of the dimers, compared to their free-3d bulk counterparts, which also means that the larger possible number of arrangements in 3d configurations contributes to form more packed and ordered structures. Moreover, symmetric swimmers seem to show higher ordering at larger distances compared to asymmetric dimers for both 2d and 3d systems. This can be caused by steric effects due to their larger size, while the correlation between orientations of asymmetric dimers, being smaller, tends to decay faster. The angle distribution function in Fig. 5.2g and Fig. 5.2h shows that swimmers in 3d-bulk have parallel alignment at short distances ($\Theta \ll \pi/2$), while in quasi-2d confinement $\Theta \to \pi$, indicating an antiparallel alignment, which results from frontal collisions between dimers.

Fig. 5.3 shows a sketch of two perfectly aligned symmetric and asymmetric dimers with the distances between beads in units of s_p. In order to have these configurations, both the phoretic-phoretic and heated-heated $g(r)$ should show narrow peaks at contact, *i.e.*, $2.2s_p$. This is not seen in the heated-heated RDFs, where in neither Fig. 5.2c for the quasi-2d confined ensembles, nor in Fig. 5.2d, seem that the peaks indicate structures resulting from the frontal collision between dimers, not from swimming clustering. Structures such as these can be identified in Fig. 5.1. Fig. 5.4 shows simulation snapshots with examples for these structures. Fig. 5.4a corresponds to two quasi-aligned swimming clusters, showing that the structure yields far from the ideal configuration shown in Fig. 5.3. Fig. 5.4b shows a collision between several symmetric swimmers, with all their phoretic beads in contact, corresponding to the peak at $2.2s_p$ of $g_{pp}(r)$.

5.2.2 Thermophilic dimers

The phoretic bead pushes the heated bead, thus inducing the motion. Attractive phoresis, thermophilicity, leads to the formation of static aggregates of dimers, independently of the density or geometry of the swimmers in the system, as can be seen in two typical snapshots in Fig. 5.5a and Fig. 5.5b. These aggregates only move due to thermal fluctuations, thus performing a Brownian motion, and tend to slowly grow and form large clusters, encompassing nearly all the swimmers in the system at $t \to \infty$.

The main difference between the radial distribution functions of thermophobic and thermophilic dimers lies in the shape and abundance of peaks. Thermophobic dimers display a main and a secondary peak, implying the lack of stable aggregation on these types of systems. On the other hand, thermophilic dimers display RDFs with more sharpened peaks, characteristic of crystalline-like structures such as the aggregates shown in Fig. 5.5. These same figures show the RDF between phoretic-phoretic, phoretic-heated and heated-heated beads for a 3d-bulk (orange)

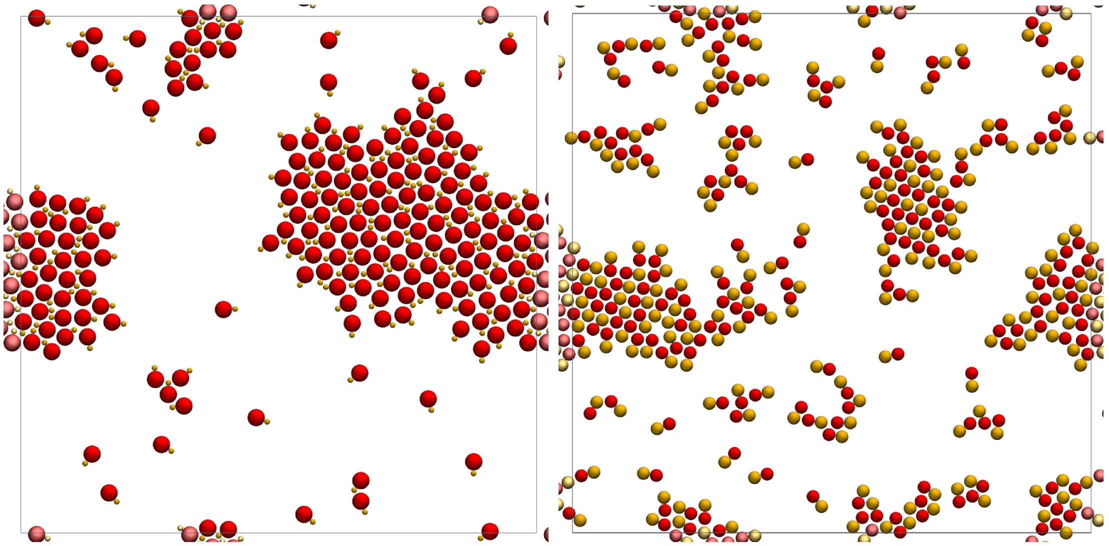

Figure 5.5: Snapshots of (a) asymmetric $\gamma = 3$ and (b) symmetric hydrodynamic thermophilic dimers at an area fraction $\phi = 0.2$.

and quasi-2d confined system (purple). In overall, it is seen that most of the peaks are at the same position independently of the dimensionality of the system, implying that the clustering mechanism is the same on both systems. Nevertheless, it is also seen that the quasi-2d systems show higher peaks on nearly all the $g(r)$. This means that the quasi-2d confinement, or deletion of one degree of freedom on the motion, yields more aggregation of the dimers, forming more crystalline ordered clusters.

5.3 Hydrodynamic simulations *vs* active Brownian swimmers

Hydrodynamic interactions play a crucial role in a very large number of both biological or artificial systems. Analytical or computer simulations studies of these systems do not always account for them, although it is well known that the consideration of these hydrodynamic interactions can change drastically the properties of ensembles of microswimmers. Studies showed that hydrodynamics change the aggregation mechanism of spherical particles [19, 210, 211]. In chapter 4, the hydrodynamics of the swimming dimers have been treated, showing that the flow fields can lead to either attractive or repulsive interactions, which is crucial on the formation of aggregates. This section gives a comparison between full hydrodynamic simulations (+HI) with the MPC-MD method, and active Brownian

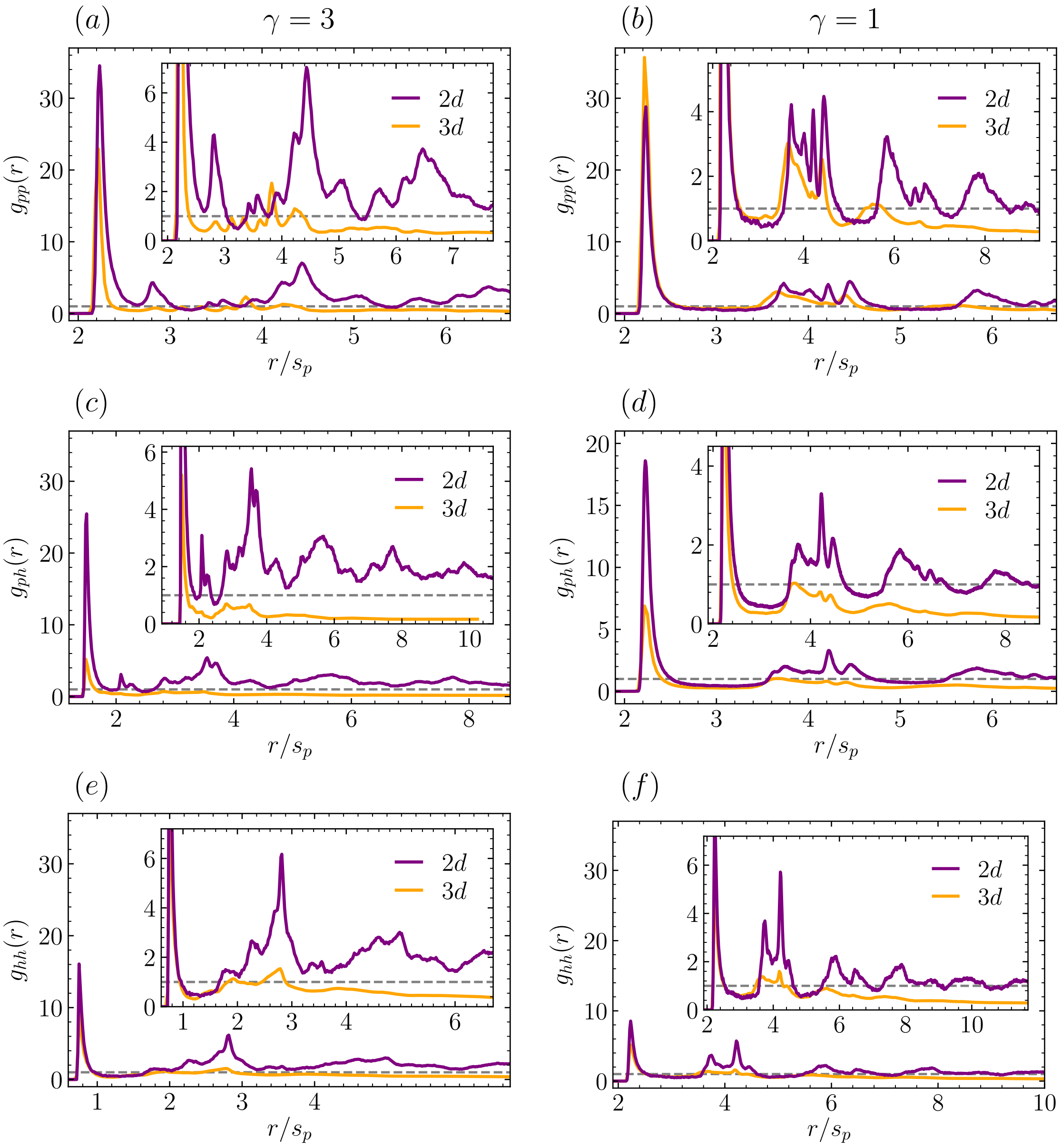

Figure 5.6: Radial distribution function between phoretic-phoretic ((a) and (b)), phoretic-heated ((c) and (d)) and heated-heated ((e) and (f)) beads of an ensemble of asymmetric ($\gamma = 3$) and symmetric ($\gamma = 1$) thermophilic dimers in quasi-2d confinement with $\phi = 0.2$ (purple lines) and 3d-bulk with $\phi_v = 0.05$ (orange lines) systems. The distance has been rescaled by the radius of the phoretic bead ($s_p = 6$ in all systems).

particles (−HI) with the phoretic BD method, which allows us for a very precise quantification of the importance of hydrodynamic interactions in the different systems.

5.3.1 Thermophobic dimers

Recent studies showed that hydrodynamic interactions play a very important role on the collective behaviour of thermophobic dimers in 3d bulk [180, 212]. Thus, a further comparison between quasi-2d confined dimers with and without hydrodynamics is in order. A visual inspection of the resulting simulations does not show very obvious differences, such that the snapshots of Fig. 5.1 continue being a reasonable reference. A more precise comparison can be performed by calculating the RDF as shown in Fig. 5.7f. In all the following RDF figures, blue lines correspond to +HI and red lines to −HI simulations, and all distances have been rescaled by s_p. Fig. 5.7a and Fig. 5.7b show the RDF of the phoretic-phoretic beads for asymmetric and symmetric dimers, respectively, showing a well defined peak for beads at contact for both HI and BD models. Asymmetric dimers show another clear but smaller peak at around the distance of the second neighbour, $r \sim 4s_p$, independently of the presence of hydrodynamics, but it is missing for BD simulations of symmetric swimmers, as seen in Fig. 5.7b. Furthermore, symmetric +HI swimmers show this second peak divided in two smaller peaks, $r^{+/-} \simeq 4s_p \pm 2\delta$, with $\delta = 0.2(s_p + s_p)$. The r^+ corresponds to the swimming, quasi aligned trio, whereas r^- describes short-time unstable aggregates formed mostly due to motility induced clustering (MIC). Perfectly aligned clusters should show the peaks at the shortest allowed distances as shown in Fig. 5.3. From the heated-heated RDFs of the asymmetric swimmer, Fig. 5.7c, it is seen that this peak is not found at $2.2s_p$, as expected for an aligned pair, but displaced for both ±HI systems. Moreover, the first peak of Fig. 5.7c +HI is narrower than the BD one, implying −HI simulations show more pair configurations than +HI systems. On the other hand, no relevant peak is seen for this RDF in the symmetric case of Fig. 5.7d, which indicates that there is no predominant inherent ordering in the system for the heated-heated bead case. Finally, Fig. 5.7e and Fig. 5.7f show the phoretic-heated radial distribution function. Aligned pairs should show peaks at $\sim 2.5s_p$ for $\gamma = 3$ and $\sim 3s_p$ for $\gamma = 1$. BD simulations show this peak very clearly on Fig. 5.7e, whereas HI simulations show a very small peak also at this distance, but a higher one displaced. For symmetric geometries, BD simulations show again this peak, but HI simulations do not.

Asymmetric swimmers seem to show higher alignment than the symmetric ones, but taking a look at the simulation movies for the $\gamma = 1$, aligned clusters are also seen for $\gamma = 1$. Examples of these front-like aggregates are shown in Fig. 5.8a ($\gamma = 3$) and Fig. 5.8b ($\gamma = 1$) as snapshots directly extracted from simulations.

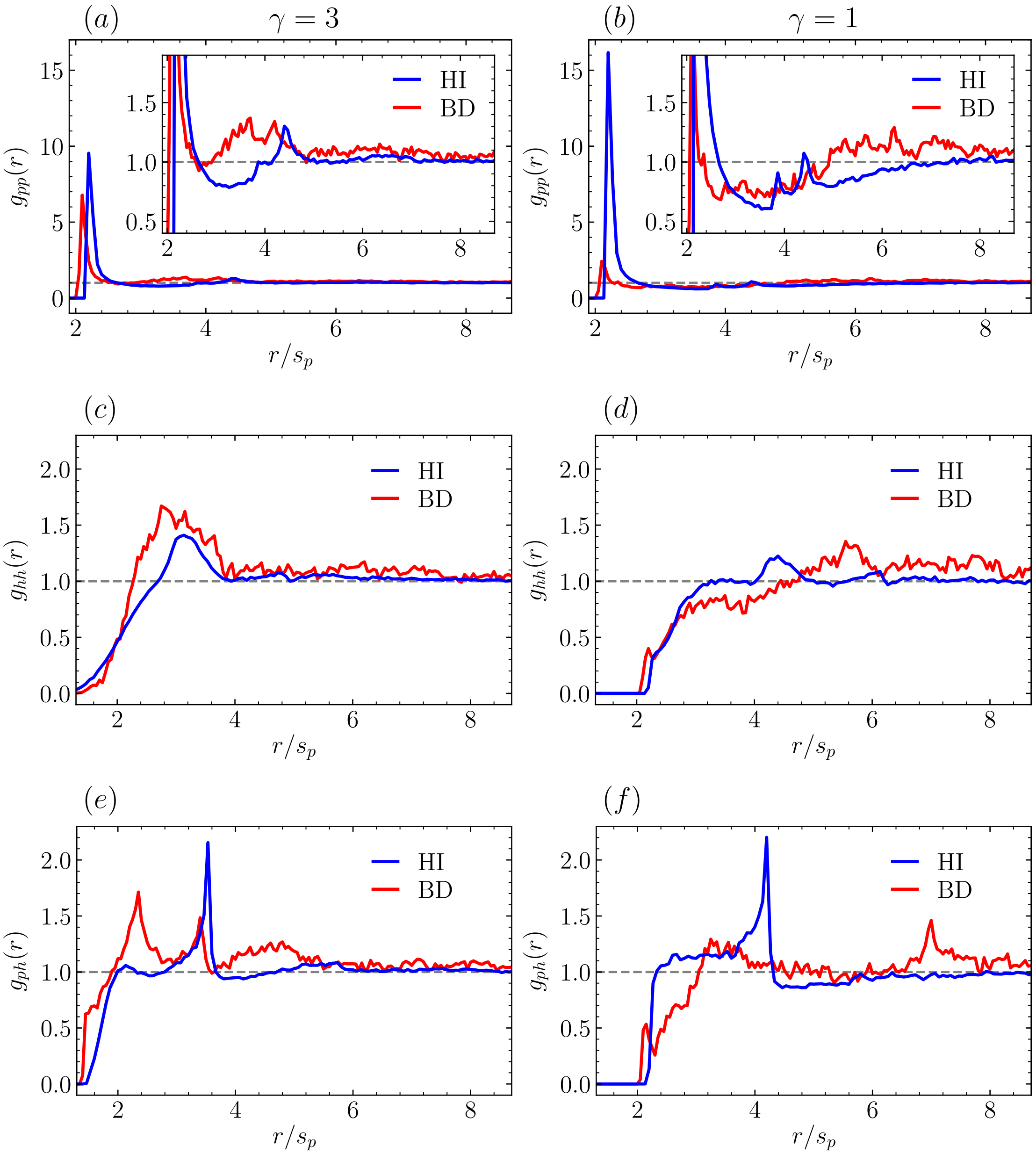

Figure 5.7: Radial distribution function of phoretic-phoretic (a) and (b), heated-heated (c) and (d), and phoretic-heated (e) and (f) beads of an ensemble of asymmetric (left figures) and symmetric (right figures) thermophobic dimers. The distance has been rescaled by the phoretic bead radius, s_p. Blue lines correspond to full hydrodynamic simulations (MPC+MD), while red lines correspond to BD simulations.

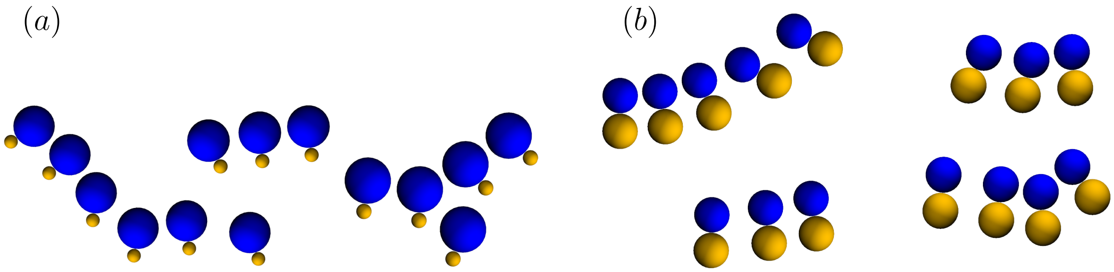

Figure 5.8: Snapshots depicting aligned swimming clusters of asymmetric ($\gamma = 3$, (a)) and symmetric ($\gamma = 1$, (b)) thermophobic dimers obtained with HI at $\phi = 0.2$.

The reason the RDF does not display the peaks of these structures for symmetric swimmers is because such systems are very dynamic, implying that a combination of collisions and swimming alignment leads to a very small contribution of such structures due to the performed time average. Further quantification on the collective behaviour of thermophobic dimers can be seen in Fig. 5.9 with the cluster probability, the average propulsion velocity of the cluster (rescaled by the single swimmer velocity), Eq. (5.4), and the average orientation correlation, Eq. (5.5), as a function of the cluster size. Fig. 5.9a shows these values for $\gamma = 3$ dimers, while Fig. 5.9b for the symmetric ones. From Fig. 5.9a, we can see that higher densities lead to bigger clusters, with and without hydrodynamic interactions. Nonetheless, +HI systems show slightly smaller clusters, while −HI systems show faster and very much more oriented clusters. Full hydrodynamic systems show that big clusters loose all the orientation correlation fast, whereas the orientation correlation of −HI systems reaches a plateau at high cluster sizes. This is also seen for the symmetric case from Fig. 5.9b.

The aligned clusters form as a result of both steric interactions and hydrodynamic attractive interactions, displayed by asymmetric thermophobic dimers and the symmetric dimers at short ranges. Hydrodynamics shows a considerable impact on the formation of aligned clusters in 3d bulk systems of thermophobic dimers, as seen by Wagner *et al.* [180, 212], but the confinement of these swimmers in a quasi-2d slit suppresses the effect of these interactions. The shape of the flow field of such dimers, shown in Fig. 4.11a and Fig. 4.11e, shows that the lobe-like shape can ultimately induce a torque to a neighbouring dimer due to the contribution u_l^z shown in Fig. 4.14a and Fig. 4.14b, pushing it to its rear. This extra contribution can also play a major role on the unalignment of the clusters. This result is also presented by Theers *et al.* [19], where they showed that hydrodynamics breaks up clustering by comparing ensembles of spherical ABPs (no hydrodynamics) with squirmer (with hydrodynamics) ensembles in a narrow slit system, similar to our quasi-2d slit. Phoretic Brownian asymmetric phobic di-

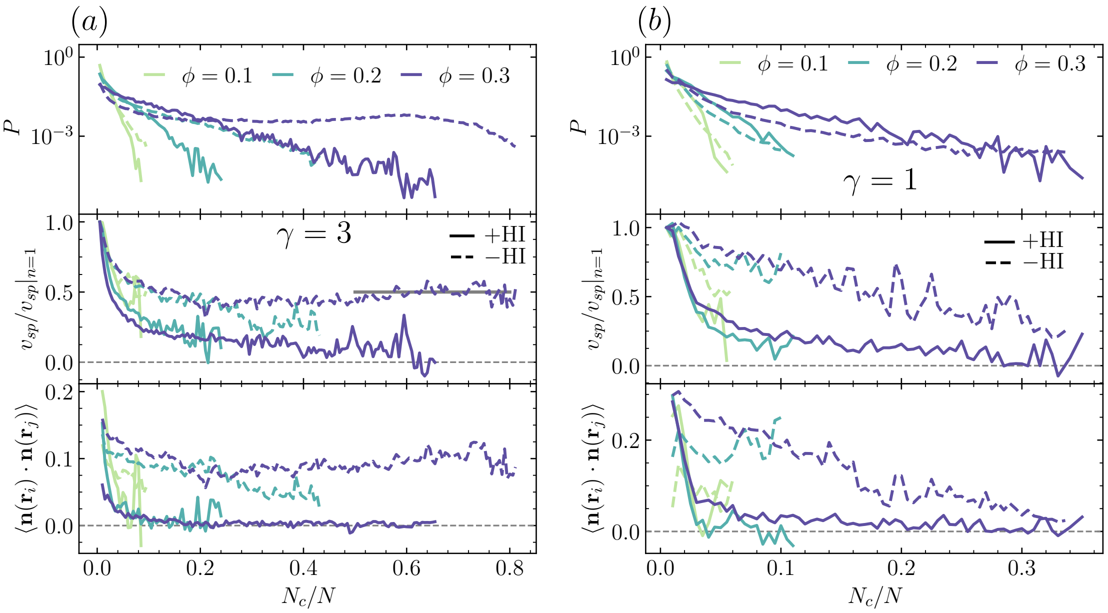

Figure 5.9: Cluster analysis of ensembles of 200 thermophobic $\gamma = 3$ and $\gamma = 1$ dimers in quasi-2d confinement for densities of $\phi = 0.1$, $\phi = 0.2$ and $\phi = 0.3$ in a quasi-2d systems. Continuous lines correspond to +HI simulations, while dashed lines correspond to −HI (BDα) simulations.

mers show swarming behaviour of large clusters, given that swarms of between a 20% and an 80% of the system show a nearly constant velocity, of a 50% of the total velocity of the single dimer. Moreover, these swarms also show non-vanishing orientations, which lead to lane formation of the swarms on the system.

5.3.2 Thermophilic dimers

The investigation of the collective behaviour of thermophilic dimers has been divided in two parts. The first one is to study the static properties of the system, *i.e.*, the structural configuration of the aggregates and the swimming properties. Then, the dynamic or time-dependent properties have been studied in order to characterise the dynamics of the aggregation process, which is also compared with the thermophobic case.

5.3.2.1 Asymmetric dimers

The simulation results from MPC-MD and BD systems show that ensembles of asymmetric $\gamma = 3$ thermophilic dimers show aggregation regardless of the presence

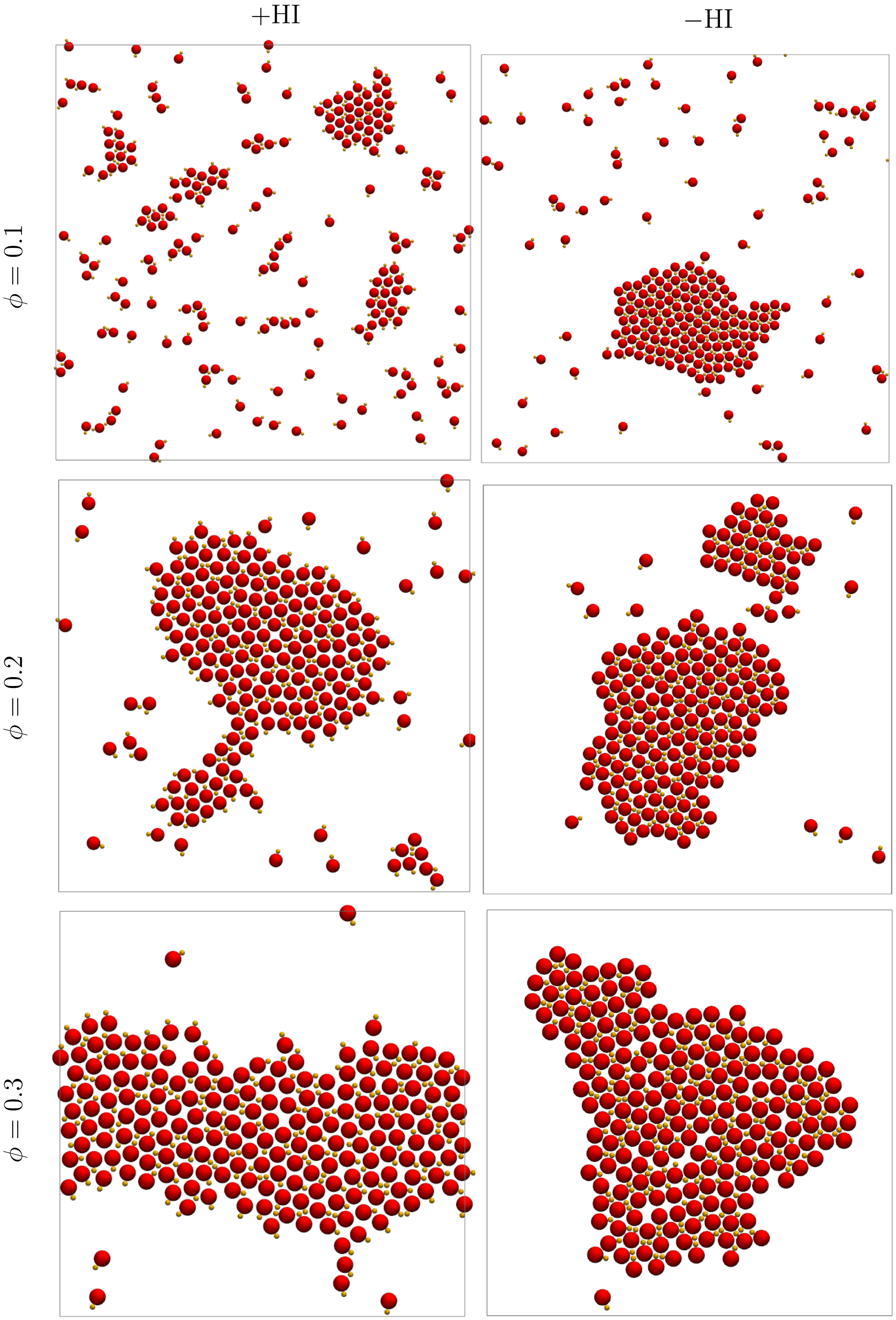

Figure 5.10: Snapshots of ensembles of $\gamma = 3$ dimers +HI (left) and −HI (right) at $\phi = 0.1$, 0.2 and 0.3 at times around $300\tau_B$.

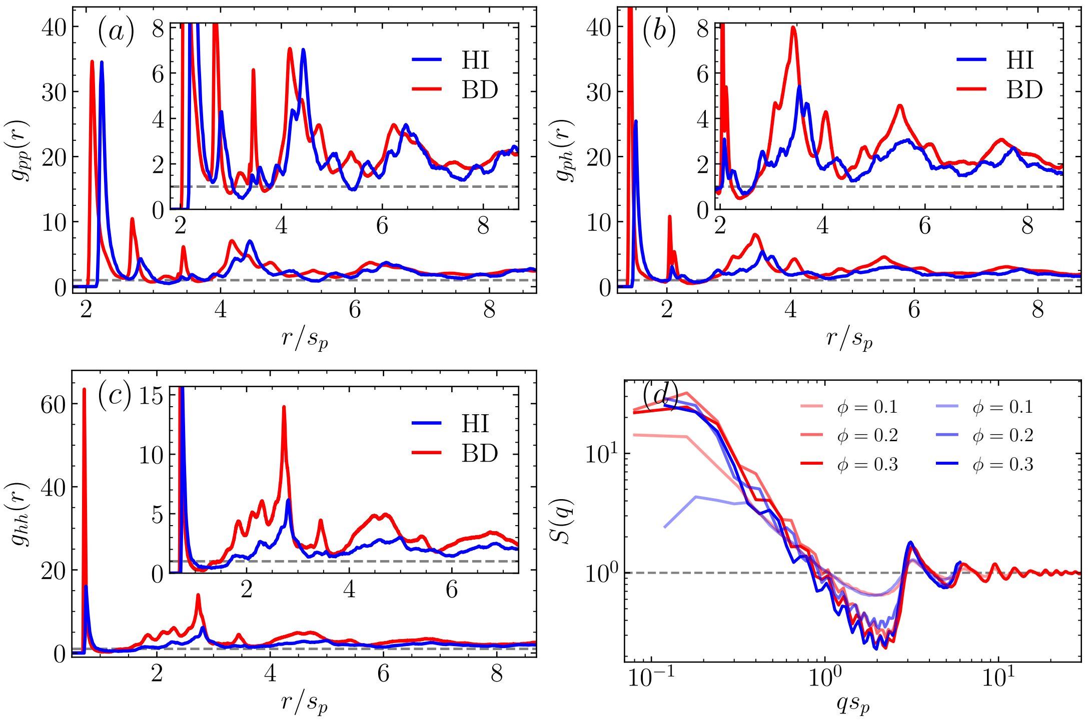

Figure 5.11: Radial distribution function between phoretic-phoretic (*a*), phoretic-heated (*b*) and heated-heated (*c*) beads of an ensemble of symmetric and asymmetric thermophilic (red colours) dimers, and (*d*) structure factor of the phoretic-phoretic beads. The distance has been rescaled by the phoretic bead radius for all the cases. Blue lines correspond to full hydrodynamic simulations (MPC+MD), while red lines correspond to BD simulations. The insets are a zoom in on the secondary peaks of the functions.

of hydrodynamics simulations. Snapshots of late stages of the simulations are shown in Fig. 5.10 for three values of the density. The main difference between both models is the aggregation mechanism, which leads to different aggregate configurations.

This aggregation leads to a crystalline-like structure, with very defined peaks, as seen from the multiple peaks on all the RDFs of Fig. 5.11. The first peak in all figures represents the beads in contact, being around $1.2(s_i + s_j)$, with i and j standing for phoretic or heated. The following peaks arise from second, third and further order neighbours within the aggregates, such that the peak heights importantly decrease with increasing the separation. Fig. 5.11a shows the phoretic-phoretic bead's radial distribution function, from where it is clearly seen that there is inherent ordering at large distances within the aggregates. Distant peaks are broader, due to more possible configurations of phoretic beads, implying the loss of ordering at large distances. Moreover, BD simulations seem to show their peaks slightly closer than +HI, implying more compact structures, which can also be seen from the snapshots in Fig. 5.10. Also, the peaks of −HI systems are higher than +HI systems for phoretic-heated (Fig. 5.11b) and heated-heated (Fig. 5.11c) beads, but approximately the same for the phoretic-phoretic (Fig. 5.11a) bead. This indicates that the difference between aggregates yields in the internal structure, resulting from the aggregation mechanism.

The main difference between both +HI and −HI asymmetric $\gamma = 3$ dimers systems is the aggregation mechanism. The aggregates of dimers with hydrodynamic interactions present configurations where the heated bead of the dimers on the surface of the aggregate is pointing outwards the main body of the aggregate, creating rough surfaces. This configuration is not observed in the absence of hydrodynamic interactions, where the heated beads of the dimers on the perimeter of the cluster tend to point towards the centre of the aggregate, leading to more faceted clusters. This leads to the surface dimer's heated beads to be outwards the cluster, alone or in pairs, which is seen in the radial distribution function between heated beads, $g_{hh}(r)$ on Fig. 5.11c. In this figure, hydrodynamic simulations show lower peaks than the Brownian dynamics simulations, accounting for the fewer heated bead pairs and trios found in such aggregates when fluid-mediated interactions are present. Moreover, the BD peaks seen in all the $g(r)$ from Fig. 5.11 are at closer distances than the HI ones, implying that systems without HI lead to more compact structures. HI structures form with a triangular lattice, which can be seen from the simulation snapshots of Fig. 5.10. The structure factor from Fig. 5.11d (Eq. (5.2)) shows that increasing the density of swimmers, more ordered aggregates are present. The $S(q)$ with and without hydrodynamic interactions are very similar, resulting from the formation of a large-scale connected aggregate for both systems. This is characterised by the peak at $q \to 0$, and the absence of larger peaks at higher distances.

The process that yields the heads-out or heads-in configurations of the philic aggregates arise directly from the hydrodynamic interaction within the system. Hydrodynamics are understood by means of the flow field created by the swimming dimers, but it has also been observed that the flow field of a dimer trapped in the cluster is of uttermost relevancy on this process. Fig. 4.11f, shows the flow field (in the reference system of the swimmer) of a $\gamma = 3$ swimming dimer. From the stream lines, it is seen that when the dimer approaches the cluster it feels a slightly repulsive hydrodynamic interaction due to the front vortex of the moving dimer, which in turn creates a torque on the motion. This torque, plus the rear hydrodynamic attraction, leads to what we call *backwards parking*, *i.e.*, the swimmer swims in the direction opposite to the propulsion when it gets close enough to the

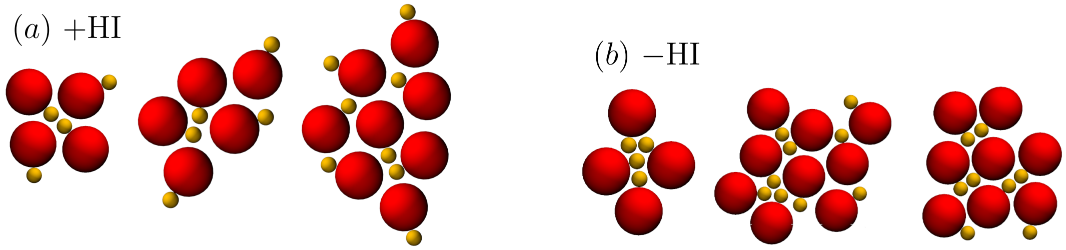

Figure 5.12: Early nucleation for +HI (*a*) and −HI (*b*). (*a*) shows the first step (left) of the early nucleation due to hydrodynamic interactions, and increasingly bigger aggregates showing heads-out configurations (from left to right). (*b*) shows heads-in configurations of asymmetric dimers.

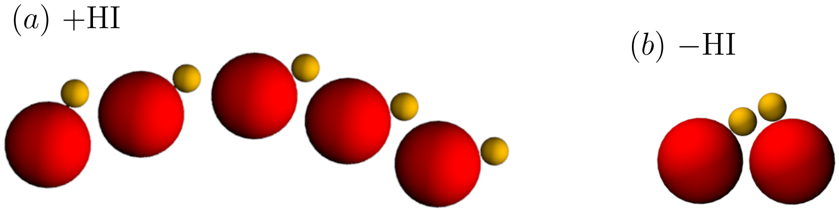

Figure 5.13: Snapshots from simulations of (*a*) asymmetric philic dimers swimming with the flow due to HI and (*b*) the same swimmers from BD simulations, swimming with the heat.

surface of the cluster. This effect is enhanced due to the heads-out configuration of the aggregate's surface. Fig. 4.16a shows that a fixed dimer, such as one of the dimers at the surface of the cluster, creates a strong hydrodynamical attraction at the heated bead, implying then the importance of the near-field hydrodynamic in such systems. The combination of the heads-out configuration along with the attractive flow field in front of the heated beads leads to philic aggregates with a net osmotic attractive field around them. Examples on the early nucleation and growth of aggregates showing heads-out structures are in Fig. 5.12a. On the other hand, systems lacking the presence of hydrodynamics (BD simulations) lead to the heads-in configurations of aggregates, as seen for the first steps of nucleation shown in Fig. 5.12b. This is what one can initially expect, given that the philic dimer swims with the heated bead on the front, colliding then with the aggregate and getting stuck there from both its propulsion and phoretic interactions. Moreover, the swimming behaviour is shown to be different from both +HI and −HI. Simulations with full hydrodynamic interactions show the dimers swimming on the back of another dimer, as shown in Fig. 5.13a. This is due to the strong rear attractive flow field of the swimming dimers, which allows the dimers to get into the strong attraction and swimming *with the flow*, as seen in the two examples

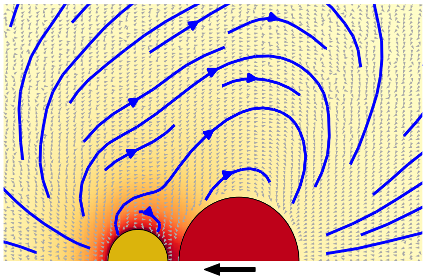

Figure 5.14: Flow field of a thermophoretic asymmetric $\gamma = 2$ dimer with an extra bond distance between the beads, following the dimer construction from [199].

in Fig. 5.13a. In the absence of flow, philic dimers swim together only due to the phoretic attraction, or swimming *with the heat*, as seen in Fig. 5.13b, forming small, aligned clusters. Nevertheless, the swimming behaviour in the presence of hydrodynamics is not stable. As mentioned, the rear flow created by the motion eventually induces a torque on the dimer behind, leading to a pair of dimers united by both phoresis and the osmotic field, as already seen in Fig. 5.12a. This is the seed to small aggregates, which already form in a *heads-out* way. Brownian dimers collide frontwards and get stuck due to collisions, leading to the early nucleation of *heads-in* aggregates, as seen in Fig. 5.12b.

Chemically-propelled dimeric microswimmers have been investigated by Colberg and Kapral [213] with an MPC simulation model strongly related to the one employed here for the thermophoretic dimers. These chemical dimers are immersed in a binary fluid, with particles of types A and B which interact differently with the colloid surface, but not between them. One bead catalyses the reaction $A \to B$, and is therefore known as the catalytic (C) bead, which creates a concentration gradient. The other bead is non-catalytic (N), and is characterised by having different interactions with the A and B molecules, determined by different values of the ϵ from their potential, which in their case is a standard WCA, this is Eq. (3.20) with $n = 6$ and $C = \varepsilon$. This asymmetry on the interactions is what drives the motion of the catalytic dimers. The aspect ratio of their dimer is $\gamma = 2$, and they added an extra bond distance between the C and N beads of $\delta_{\mathrm{CN}} = (2^{1/6}/2 - 1)(\sigma_{\mathrm{C}} + \sigma_{\mathrm{N}})$, with σ_k the radius of the C and N beads, respectively. The phoretic mechanism is not inherently different for thermophoresis and diffusiophoresis, given that the equation governing the phenomenology is the same with gradients of different nature, such that very similar dynamic behaviours could be expected. However, in their work, they reported the formation of aggregates to be heads-in, which differs from the results we report here. In order to understand this different behaviour, we have studied the flow fields of a thermophoretic dimer with a similar geometry as that employed in Ref. [199], namely $\gamma = 2$ philic di-

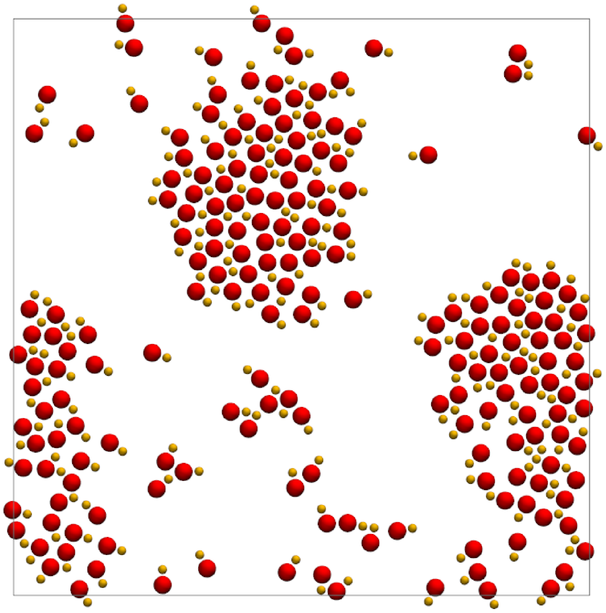

Figure 5.15: Simulation snapshot of hydrodynamic $\gamma = 2$ thermophoretic dimers with an extra bond distance between the beads.

mers, with an extra separation between the beads of $\delta = 0.735a$. The flow field shown in Fig. 5.14 resembles quite significantly the one for the $\gamma = 2$ dimer with beads at contact in Fig. 4.11d, implying that the effect of an extra separation between beads has no deep impact on the hydrodynamics. From the comparison between our results, see Fig. 5.14, and the flow fields reported in Ref. [199], we already see a qualitatively difference between the resulting hydrodynamics. Our flow field shows a repulsion around the head of the swimmer, which induces the hydrodynamic torque when a dimmer approaches an aggregate. The catalytic dimer from Ref. [199] shows an attractive hydrodynamic interaction on the head of the swimmer, enhancing the heads-in configuration of their clusters. Remarkably, the lateral torques are not present in their case. We have further studied the collective behaviour of the thermophoretic dimer shown in Fig. 5.14 for our typical system size and temperature. We have obtained similar heads-out aggregation as the thermophoretic non-displaced, $\gamma = 3$ philic dimer (as seen in Fig. 5.15), instead of the heads-out shown by the catalytic dimers from Ref. [213]. We attribute this discrepancy to the different choice of the boundary conditions of the particle which creates the gradient, due to the different potentials chosen to describe the fluid-heated bead interactions. We chose a WCA potential with $n = 24$, whereas they used a $n = 6$ (Lennard-Jones). This remains a matter of further research.

5.3.2.2 Symmetric dimers

Ensembles of symmetric $\gamma = 1$ philic dimers are hereby studied with a comparison in the absence of HI. Snapshots from Fig. 5.16 show the aggregates formed at late stages of the simulation, for three different densities, with and without hydrodynamic interactions, proving that no stable aggregation is present in such systems. The +HI aggregates also display triangular lattices, with the heated beads pointing outwards the centre of the cluster, or *heads-out*, although steric effects decrease this configuration with respect to the asymmetric case. On the other hand, systems where the hydrodynamic interactions have not been included, −HI, the results change drastically. Dimers with hydrodynamic interactions swim following other dimers due to the attractive flow on the back of the phoretic bead (as seen from the symmetric philic dimer flow fields in Fig. 4.11b), forming pairs as the one depicted in Fig. 5.17a (upper), and due to the lobe-like stream lines a torque is induced on the motion, forming T-like structures (also depicted in Fig. 5.17a, lower) and inducing triplets or quadruplets which constitute the first steps of the nucleation.

Ensembles in the absence of hydrodynamic interactions show that the dimers swim well oriented and parallel (see Fig. 5.17b), or what we call to swim *with the heat*, given that this configuration results from the propulsion and the alignment due to the phoretic interactions. In these systems, no aggregation is shown. Instead, these large and oriented swimming clusters form and dissolve due to thermal fluctuations and collisions with other swimmers.

The non-aggregation of symmetric philic dimers is also seen on the RDFs in Fig. 5.18, which show the comparison between +HI and −HI simulations. Fig. 5.18a presents the phoretic-phoretic RDF, showing that systems with full hydrodynamics display several peaks, as in the $\gamma = 3$ case. The first is placed at beads at contact, and the following stand for pairs, triplets, quadruplets, *etc.* The second main peak is seen to be composed of several peaks around $4s_p$, given the inner structure of the cluster, seen as to be a triangular lattice-like. This peak is also observed in Fig. 5.18b for the phoretic-heated RDF. Finally, Fig. 5.18c shows that the second peak shows two maxima, implying two defined structural configurations for +HI. In all the RDFs for the −HI system, only the first and second peaks are visible, being also lower than those of +HI systems. Therefore, there is no large aggregated structures of symmetric philic dimers in the absence of hydrodynamics, but only small clusters. The non-aggregation of Brownian symmetric dimers is further proven with the $S(q)$ shown in Fig. 5.18d. The lack of the peak in hydrodynamic simulations stresses the lack of the formation of large, ordered aggregates in the case of the absence of hydrodynamic interactions. The smaller, displaced peak observed for BD stands for the smaller aggregates seen in Fig. 5.16.

Further relevant quantification of these thermophilic dimers, both asymmetric

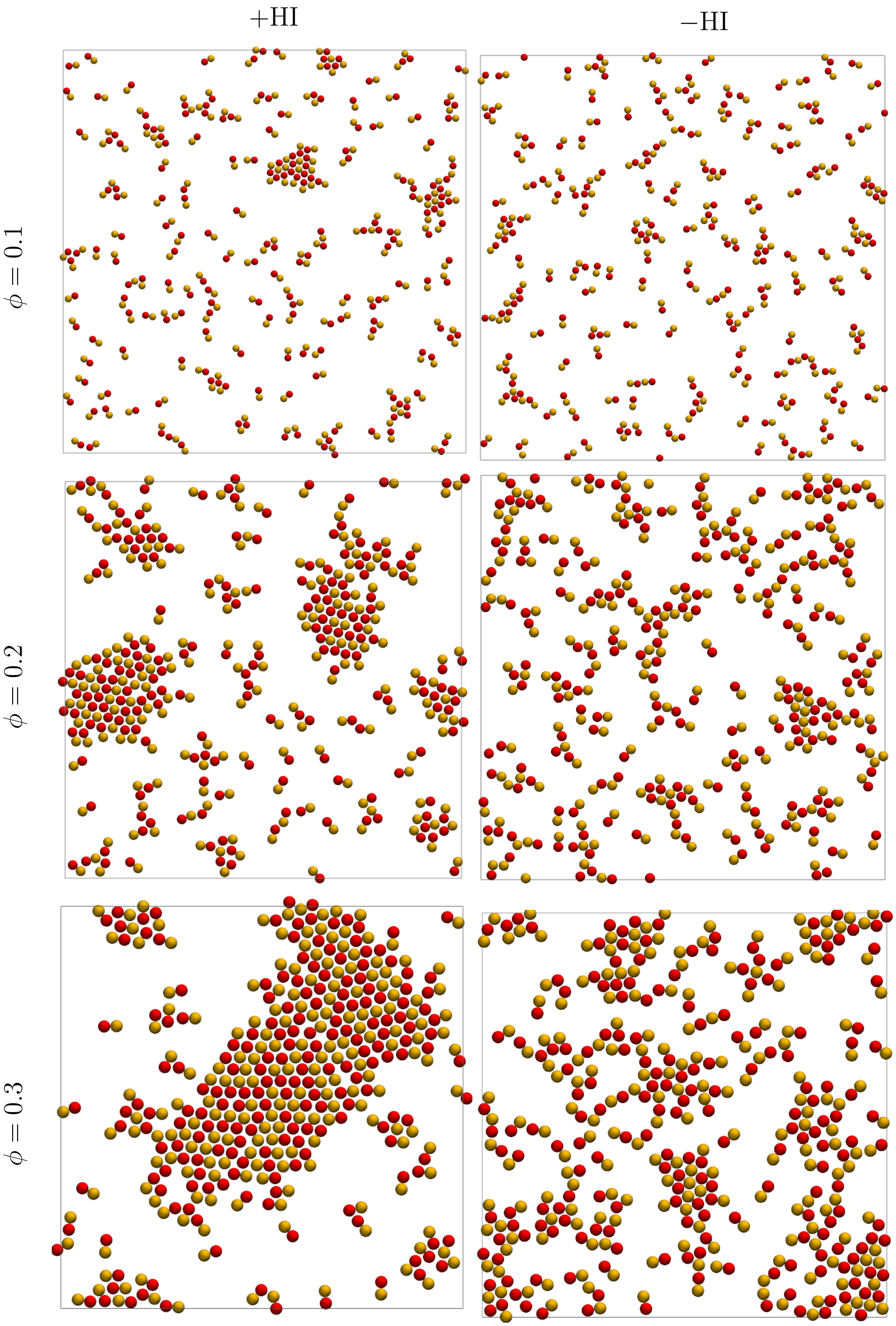

Figure 5.16: Snapshots of ensembles of $\gamma = 1$ dimers +HI (above) and −HI (below) at $\phi = 0.1$, 0.2 and 0.3 and a time around $340\tau_B$.

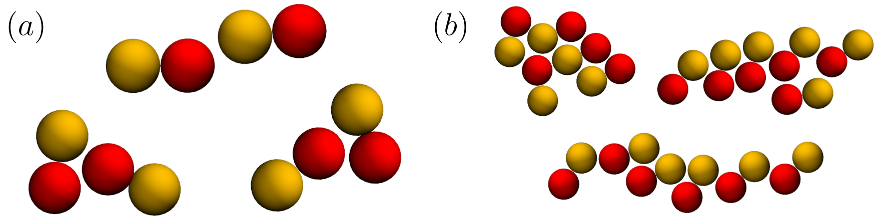

Figure 5.17: Snapshots from simulations showing swimming clusters for +HI (*a*) and −HI (*b*). (*a*) shows two dimers swimming with the flow (upper) and forming the T structure due to the hydrodynamic torque (bottom). (*b*) shows symmetric philic dimers swimming with the heat.

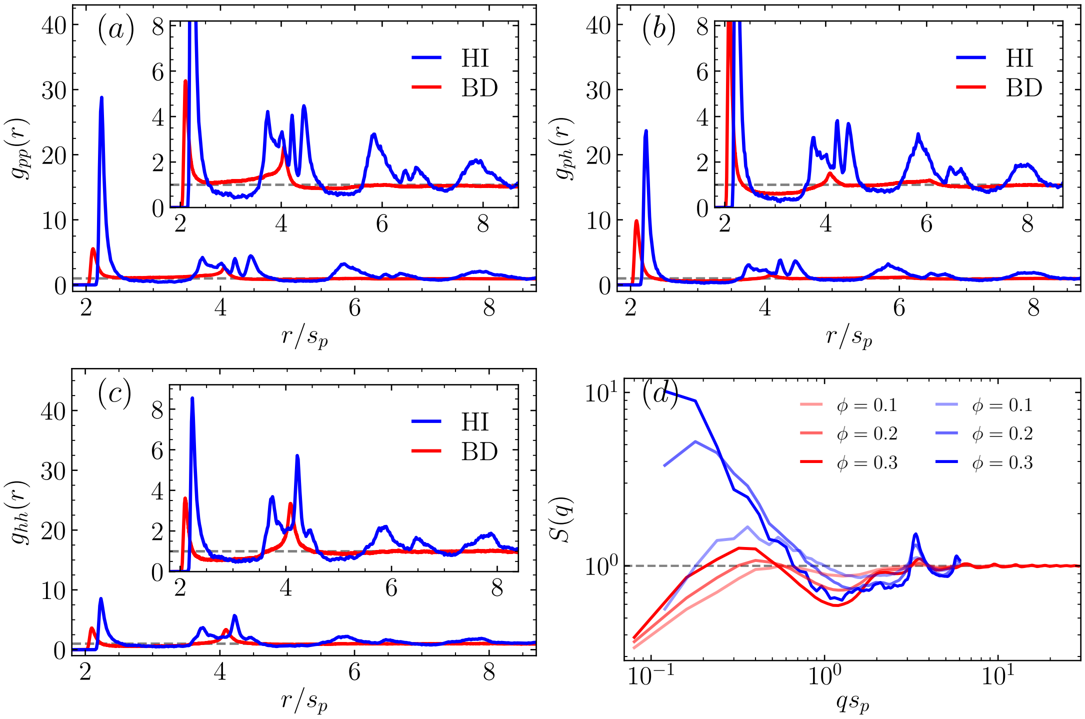

Figure 5.18: Radial distribution function between phoretic-phoretic (a), phoretic-heated (*b*) and heated-heated (*c*) beads of an ensemble of symmetric and asymmetric thermophilic (red colours) dimers at $\phi = 0.2$, and (*d*) structure factor of the phoretic-phoretic beads at three different densities. The distance has been rescaled by the phoretic bead radius for all the cases. Blue lines correspond to full hydrodynamic simulations (MPC+MD), while red lines correspond to BD simulations.

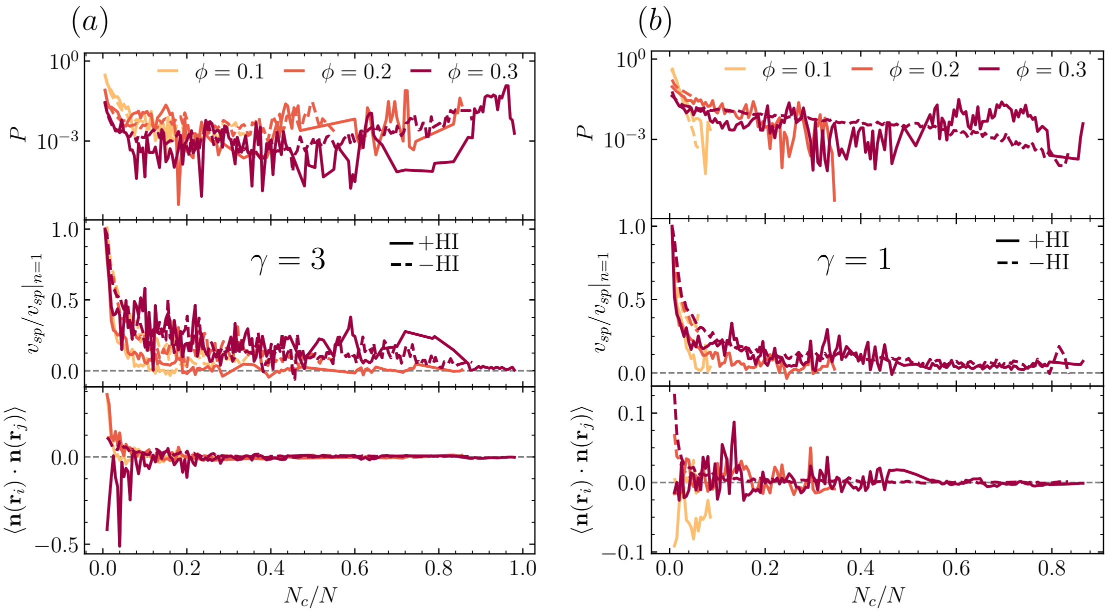

Figure 5.19: Cluster analysis of ensembles of 200 thermophilic $\gamma = 3$ and $\gamma = 1$ dimers in quasi-2d confinement, for densities of $\phi = 0.1$, $\phi = 0.2$ and $\phi = 0.3$ with and without HI, as indicated in the labels.

and symmetric, is obtained in Fig. 5.19, which displays the cluster probability, the average propulsion velocity of a cluster, Eq. (5.4), and the average orientation, Eq. (5.5). Big aggregates present in the snapshots in Fig. 5.16 imply that the average propulsion velocity is $v_{sp} \to 0$, along with the average orientation of the clusters. These big clusters only perform a Brownian motion due to thermal fluctuations, and the orientation of the swimmers is randomised within the aggregate. This is observed in both Fig. 5.19a ($\gamma = 3$) and Fig. 5.19b ($\gamma = 1$) for the +HI systems (continuous lines), where velocities decay to nearly zero for increasing cluster sizes, along with the average orientation of the aggregates.

On the other hand, only $\gamma = 3$ swimmers show aggregation without hydrodynamic interactions. Fig. 5.19b shows that symmetric −HI aggregates (dashed lines) also have nearly vanishing velocities due to the collisions of the clusters, creating big aggregates which dissolve when the dimers reorient and continue swimming. Given that the average orientation does indeed decay to zero, these are just results of collisions due to steric effects of a crowded system, and do not constitute aligned swimming clusters as in the thermophobic case.

5.3.2.3 Time-dependent properties

To complete the study on the aggregation process of thermophilic dimers, the time-dependent properties are important to study, and are also interesting to compare with the thermophobic case. One of these properties is the evolution of the aggregates of thermophilic dimers. We start from a dilute configuration without the presence of any temperature gradient, and we characterise the time evolution with the presence of a temperature gradient towards the corresponding non-equilibrium steady state (NESS). In particular, we quantify the size of the bigger cluster present in the system (N_{max}), the average size of all clusters (N_{av}), the number of single swimmers (N_{sing}) and the total number of clusters (N_c), as shown in Fig. 5.20a and Fig. 5.20b for $\gamma = 3$ and $\gamma = 1$, respectively. All the quantities except the total number of clusters have been rescaled by the number of swimmers, *i.e.*, $n_k = N_k/N_s$, with $N_s = 200$. Results for $\gamma = 3$ show very similar behaviours between the full-hydrodynamic and the Brownian dynamics simulations. The difference is evident in the symmetric case, where hydrodynamics favours the collapse and formation of aggregates. In the absence of hydrodynamic interactions, symmetric swimmers show that the biggest formed aggregates are made of around a 25% of the total number of swimmers, while in +HI systems, the biggest cluster is around 75% of the total size of the system for a density of $\phi = 0.3$ at the studied times, although it shows a growing tendency with time, which leads to a single big cluster engulfing nearly all dimers at $t \to \infty$. Both geometries and systems show that higher densities lead to faster aggregation, as expected for these dimers. Fig. 5.20a and Fig. 5.20b also show the lack of large aggregation of symmetric dimers without HI, whereas asymmetric dimers show slightly larger clusters, as seen from the average size of the clusters. This agrees with the total number of clusters, which is larger for symmetric dimers, implying more but smaller clusters than for asymmetric dimers.

Another quantity that provides more insight into the problem is the average time that a dimer stays inside a cluster, or bounding time, $\langle \tau_c \rangle$. This quantity is a time average calculated as a function of time, such that it is expected to increase with time for systems with aggregation. Fig. 5.21a and Fig. 5.21b show this average time for $\gamma = 3$ and $\gamma = 1$ systems, respectively, at densities $\phi = 0.1$, 0.2 and 0.3, where $\langle \tau_c \rangle$ and the time have been rescaled by the ballistic time of the corresponding dimer, $\tau_B = s_p/v_{sp}$. Fig. 5.21a shows that for short times, +HI systems yield faster aggregation, which implies that hydrodynamic interactions speed up the early nucleation. The $\langle \tau_c \rangle$ increases with time as expected for both +HI and −HI, showing the aggregation on these systems. The increase of $\langle \tau_c \rangle$ as a function of time indicates that dimers stay within the aggregates on average, indicating that these are long-time stable.

Ensembles of symmetric dimers show a much more important difference due to

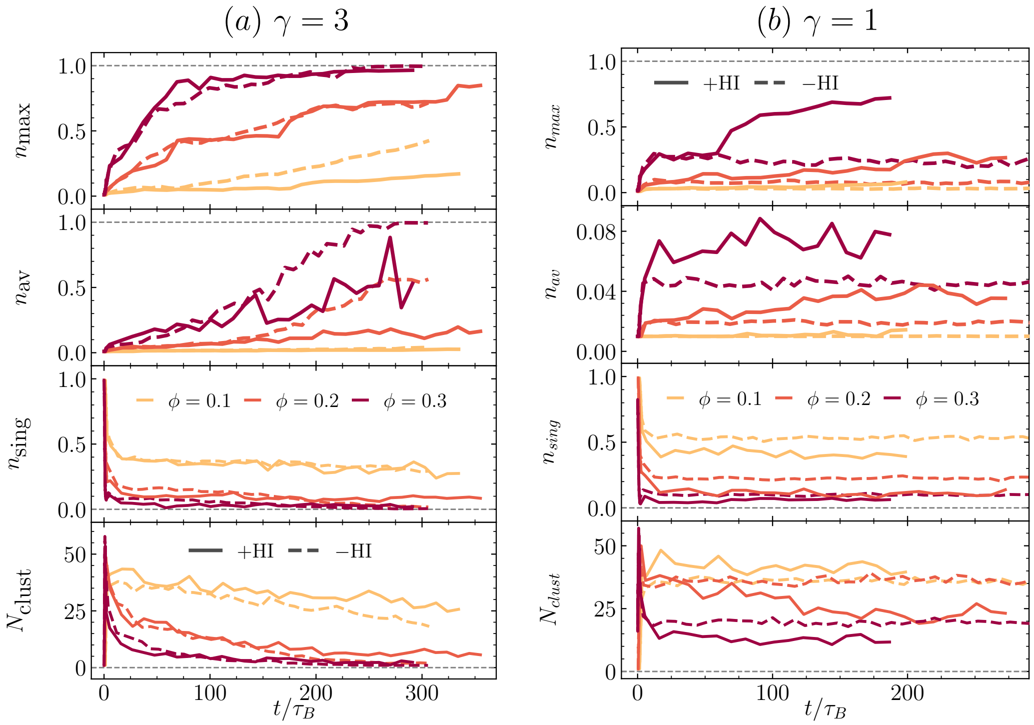

Figure 5.20: Time evolution of the sizes of clusters of (a) $\gamma = 3$ and (b) $\gamma = 1$ thermophilic dimers.

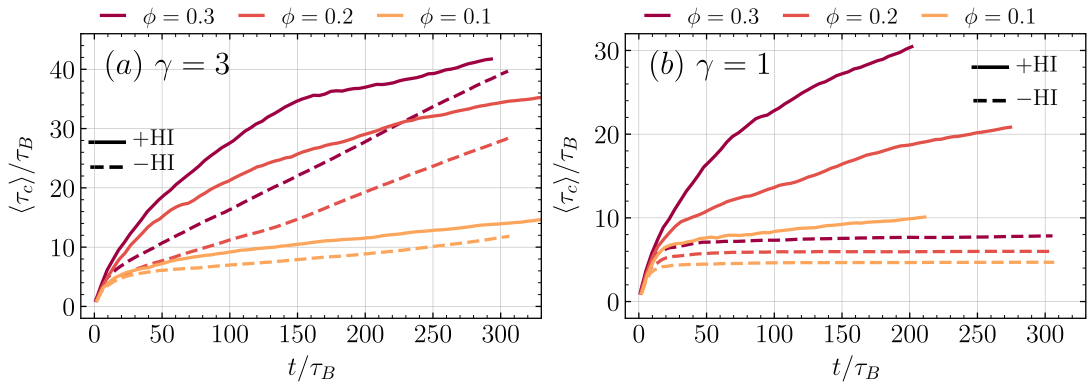

Figure 5.21: Bounding time of (a) asymmetric ($\gamma = 3$) and (b) symmetric ($\gamma = 1$) thermophilic dimers.

the presence of hydrodynamic interactions. Fig. 5.21b shows that hydrodynamic systems indeed aggregate, *i.e.*, $\langle \tau_c \rangle$ steadily increases with time, while Brownian dimers reach a stationary state at an earlier time, leading to a plateau of $\langle \tau_c \rangle$.

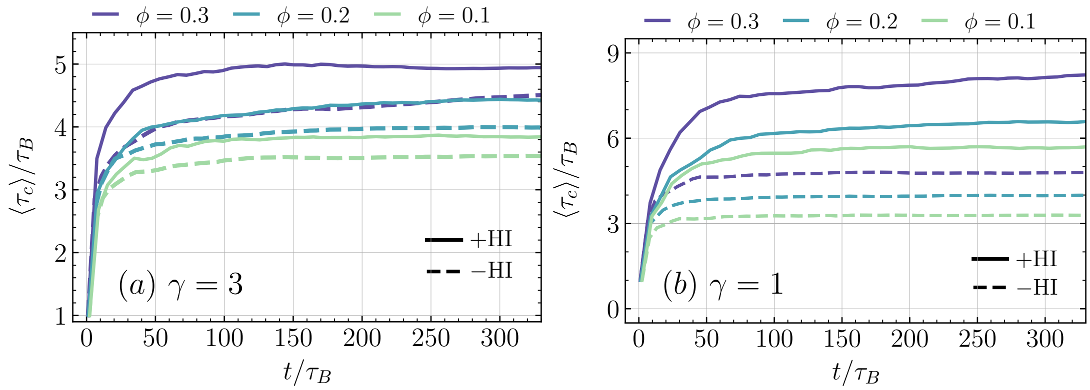

Figure 5.22: Bounding time of (a) asymmetric ($\gamma = 3$) and (b) symmetric ($\gamma = 1$) thermophobic dimers.

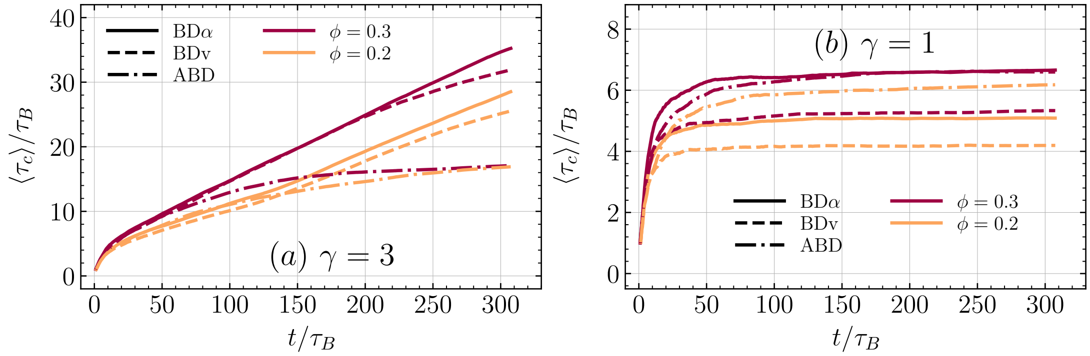

Figure 5.23: Comparison of bounding time of thermophilic dimers for the three different BD models at (a) $\gamma = 3$ and (b) $\gamma = 1$.

The plateaus are density dependent, where for increasing ϕ also increases the probability of two dimers interacting. This means that dimers spend an average constant amount of time bounded to other dimers, before detaching and possibly getting stuck again in another aggregate. This leads to fast moving and dissolving, head-aligned clusters. For this symmetric geometry, as also seen in Fig. 5.16, hydrodynamics has proven to enhance phase separation. This difference is obtained due to the hydrodynamically induced torques from the flow fields of symmetric dimers (see Fig. 4.11b), which favours the bounding between pairs of dimers.

The bounding time $\langle\tau_c\rangle$ presented in Fig. 5.21 can now be compared with the one for ensembles of thermophobic dimers (section 5.3.1). These times are shown in Fig. 5.22. The bounding time for phobic dimers reaches the plateau at short times for both $\gamma = 3$ (Fig. 5.22a) and $\gamma = 1$ (Fig. 5.22b) dimers, reflecting the lack of stable aggregation on such systems. Moreover, BD simulations show that the $\langle\tau_c\rangle$ without hydrodynamic interactions decrease significantly. Interestingly, the bounding time is higher for symmetric thermophobic dimers, despite their hydrodynamic lateral interactions (see flow field from Fig. 4.11a) being repulsive, instead of the attractive ones of the $\gamma = 3$. This is also accentuated by the fact that the differences between bounding times of +HI and −HI are more pronounced on the case of $\gamma = 1$ swimmers. This demonstrates that most of the alignment on these systems is not induced by hydrodynamics, oppositely to the 3d case [180, 212], but from pure steric and phoretic effects.

A comparison between the different Brownian models as presented in section 3.3 is also shown here for the average cluster time, $\langle\tau_c\rangle$. Fig. 5.23a presents systems of asymmetric $\gamma = 3$ dimers, and shows that the two phoretic methods, BDα and BDv, yield similar results. This is interesting given that the velocity-fixed BD, dimers within the aggregate do not have their velocities screened by the homogeneous temperature gradient created by their neighbours. Then, their propulsion is not hindered, which could induce instability to the aggregate. From Fig. 5.23a it is seen that inter-swimmer phoresis and geometry hinder the effect of a constant propulsion. The opposite is observed in Fig. 5.23b, where the constant self-propulsion velocity of the BDv decreases the bounding time on the stationary state. Active Brownian dimers (ABD), due to the lack of phoretic attraction, do not accomplish aggregation in neither any of the two studied densities nor the two geometries of dimers. Nevertheless, deleting the inter-swimmer phoresis of the BDv model increases the $\langle\tau_c\rangle$.

5.3.3 MSD and MSAD of crowded systems

Additional valuable information on the collective behaviour of such swimmers can be obtained by comparing the swimming behaviour of swimmers while isolated and in ensembles. This can be done by studying the mean square displacement ($\Delta\boldsymbol{r}^2$ Eq. (2.14)) and mean square angular displacement ($\Delta\boldsymbol{e}^2$ Eq. (2.8)), as presented in Fig. 5.24, where, as it was discussed for single dimers, the mean square displacement shows a ballistic behaviour ($\Delta\boldsymbol{r}^2 \propto t^2$) for over all the studied time window, implying that the direction of the phoretic motion is long persistent since the total simulated time is comparable to τ_R. Given that our simulations do not quite reach the stationary state for the thermophilic dimers, their mean square displacement does not provide relevant information. Longer simulations would be required to capture the aggregation in the $\Delta\boldsymbol{r}^2$ and $\Delta\boldsymbol{e}^2$.

For small times, this is also observed for the dimers in ensembles. For higher times, the ballistic behaviour is lost, as seen in Fig. 5.24a in the plateau around τ_R. This change in the behaviour with respect to the isolated swimmers is caused by the caging effect for dense systems. Swimmers try to move through the simulation

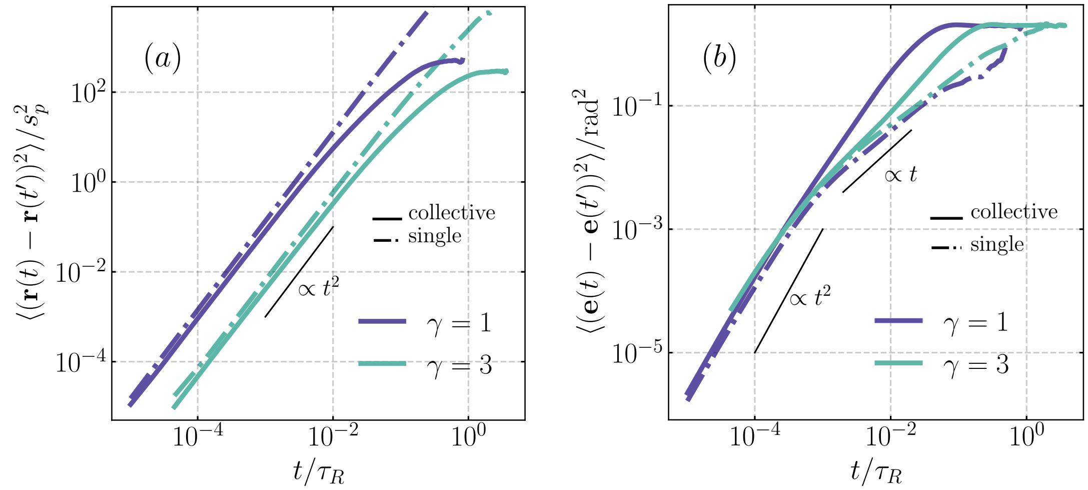

Figure 5.24: (*a*) Mean square displacement and (*b*) mean square angular displacement of thermophobic dimers, respect the rescaled time. Solid lines correspond to the ensembles at $\phi = 0.2$, while dashed lines correspond to single swimmer .

box, but they find other swimmers and interact with them, either by colliding or swimming together. This limits their speed during the reorientation time, as seen from the cluster analysis from Fig. 5.9, thus losing the pure ballistic motion which isolated swimmers show. For larger simulation times, the $\Delta\boldsymbol{r}^2$ is expected to recover the diffusive behaviour, after the characteristic reorientation time of inter-swimmer interactions.

The mean square angular displacement, $\Delta\boldsymbol{e}^2$, quantifies the correlations between the orientations as a function of the elapsed time. In Fig. 5.24b, the $\Delta\boldsymbol{e}^2$ shows no difference between the isolated and ensemble systems for small times since at these times dimers have not yet interacted with their neighbours. Higher times show a discrepancy between these functions, showing the influence of other swimmers when $\Delta\boldsymbol{e}^2 \propto t$ for isolated dimers while $\Delta\boldsymbol{e}^2 \propto t^2$ for dimers in ensembles of thermophobic dimers. Thermophobic dimers in ensembles tend to reorient more often than isolated dimers, leading to higher $\Delta\boldsymbol{e}^2$. This is due to the amount of collisions between particles in crowded systems, such that the ballistic and directed motion observed for isolated dimers is lost for more crowded systems. This can also be seen in the $\Delta\boldsymbol{r}^2$, since symmetric swimmers, due to their size, show smaller $\Delta\boldsymbol{e}^2$ compared to their asymmetric ($\gamma = 3$) counterparts, which tend to reorient more often.

5.3.4 Hydrodynamic stability of aligned clusters

Here we place 20 asymmetric ($\gamma = 3$) thermophobic dimers in a linear initial configuration in order to study the persistence of this forcedly aligned cluster in the presence and absence of hydrodynamics. Fig. 5.25 shows the trajectories of the CM of such dimers, starting from the left and moving to the right of each figure, at three different heating temperatures, $T_h = 1.8$, 1.5 and 1.2. Swimmers heated at higher T_h propel faster, thus displaying longer trajectories in both MPC-MD and BD simulations.

Comparing the sets of simulations at the same temperature, we see that the presence of hydrodynamics destabilises the initially aligned structure, while BD simulations show less dispersion of the trajectories. This implies that the front-like clustering observed in thermophobic dimers in quasi-2d confinement are mostly occurring due to a certain degree from the combination of steric and phoretic effects, contrarily to the 3d-bulk case [180, 212], where the presence of HI has shown the formation of these aligned structures.

The quantification of the trajectories of these clusters is presented in Fig. 5.26 with the orientation correlation function (Eq. (5.5)), Fig. 5.26a, and the average

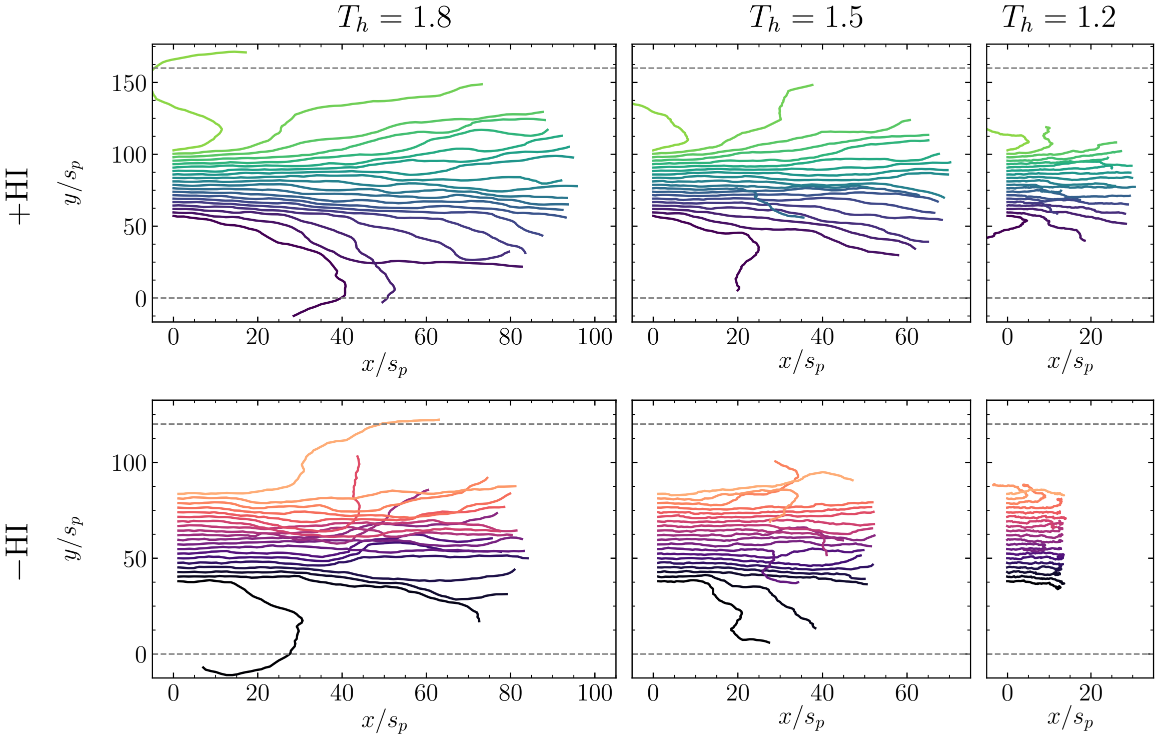

Figure 5.25: Trajectories of 20 forcedly aligned thermophobic $\gamma = 3$ dimers with hydrodynamic interactions (top figures) and without (bottom figures).

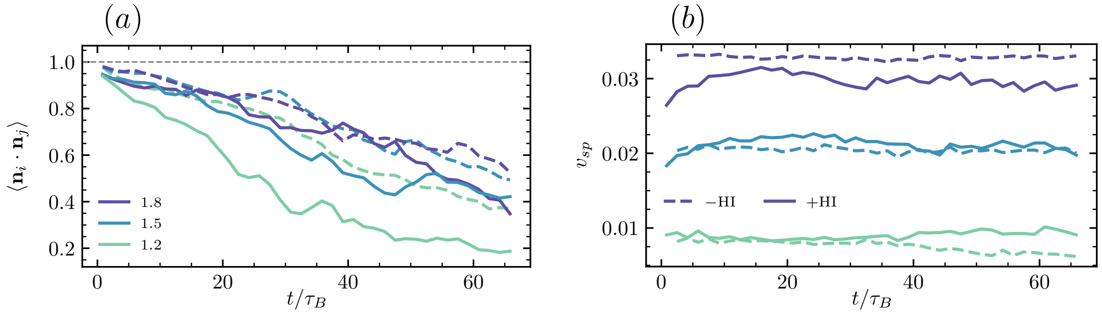

Figure 5.26: Orientation correlation function (*a*) and self-propulsion velocity (*b*) of 20 +HI (solid lines) and BD (dashed lines) thermophobic $\gamma = 3$ dimers for a initially aligned state cluster as a function of the time rescaled by the +HI swimmer's ballistic time (at $T_h = 1.5$) for systems at four heating temperatures, $T_h = 1.2$, 1.5 and 1.8.

propulsion velocity of the cluster (Eq. (5.4)), Fig. 5.26b, for both +HI and −HI.

Fig. 5.26a shows that, in overall, BD simulations display a higher orientation correlation over time, leading to a more aligned cluster, as seen from the trajectories from Fig. 5.25 while hydrodynamic interactions seem to destabilise the alignment. Moreover, both systems display a very similar velocity, very close to the self-propulsion velocity of the single swimmer with the corresponding heating temperature, T_h.

With these results, we see that the formation of aligned, front-like clusters in quasi-2d is mostly cause by motility-induced clustering (MIC), or the balance between steric and phoretic effects. Thermophobicity induces alignment, especially for dimers with neighbours in both sides, so this effect is larger for 3d simulations. Hydrodynamics, although being laterally attractive flow field towards the neighbouring swimmer, favours the dissolution of the linear cluster, leading to the results from Fig. 5.9, and agreeing with the results for spherical particles from [19, 214], but in contrast for the elongated squirmer (pusher, puller and neutral) swimmers shown also in [19].

5.4 Summary

The dimensionality of the system and the presence of hydrodynamic interactions are proven to be key elements on the aggregation and clustering mechanism of thermophoretic self-propelled dimeric swimmers. The quasi-2d confinement presented in this work allows the MPC-SRD fluid to move in a narrow slit but forces the colloids to move on the xy plane. This largely restricts the number of dimers with direct interaction, which drastically changes the effect on the clustering mechanism.

By confining thermophobic swimmers, their hydrodynamic interactions, instead of favouring the clustering as in 3d, destabilise the motion of aligned swimmers. Thus, phoretic Brownian dynamics simulations have proven that the alignment and cluster formation on quasi-2d systems of thermophobic dimers is due to MIC and pure collisions between clusters. Moreover, these BD simulations show that in the absense of hydrodynamics, the system shows larger, faster and more oriented swarming clusters for asymmetric and symmetric phobic dimers, which are considered as swarms due to their non-vanishing self-propulsion velocity and orientational correlation.

The aggregation process of thermophilic dimers gets in contrast favoured by the quasi-2d confinement. The lack of one degree of freedom forces the aggregates to form following a cristalline-like, triangular lattice, much more ordered than in 3d bulk. This aggregation process shows also a deep dependency on the presence of the hydrodynamic interactions. Hydrodynamic simulations have shown that the aggregation of thermophilic dimers is due to the effects of the short-range flow field. These fluid-mediated interactions act as a hydrodynamic torque to the dimer when two swimmers get closer together. Moreover, it has been seen that a non-moving dimer also shows an attractive hydrodynamic field to its head, and repulsive on its rear. Thus, a philic dimer swimming towards a cluster will be under the effect of the hydrodynamic torque created by its own motion when approaching the aggregate, which will make it turn direction, and it will get caught by the attractive hydrodynamic field of the aggregate. This leads to aggregates displaying heads-out configurations. Brownian asymmetric dimers aggregate only due to their propulsion, colliding with other swimmers, and then getting stuck due to their geometry, propulsion and phoresis. The aggregates formed in the absence of HI show then heads-in configurations, given that no torque is present to change the swimming direction of the dimers. More remarkable is the difference in the symmetric case, where aggregation only appears in the case +HI due to the lateral hydrodynamic attraction between philic symmetric dimers.

Chapter 6

Collective behaviour of trimers

This chapter addresses the collective phenomena of ensembles of trimeric swimmers confined in a quasi-2d slit. We make a distinction between the triangular-shaped homogeneous trimers, and the rod-like heterogeneous trimers, both swimmers already introduced in chapter 4. Ensembles of 200 trimers are studied, at area fractions of $\phi = 0.1$ and 0.2 and geometries of $\gamma = 3$ and 1, as in the dimer case. Moreover, a comparison with the same systems in the absence of hydrodynamic interactions is presented by means of Brownian dynamics simulations, using the method presented in section 3.3.

The structure of both types of trimers presented here perform translational motions when isolated, similar to the dimeric swimmers, although, interestingly, the collective dynamics is significantly different. In chapter 4 we already showed that the velocities are very similar for all the swimmers under study, but the Péclet number highly depends on the geometry of the swimmer, which affects the aggregation mechanism. The effect of the beads' aspect ratio are further studied, and are proved to have a deep impact on the collective behaviour of the trimers. Moreover, hydrodynamics are also seen to provide differences in the systems, making the collective behaviour of the trimers a subtle interplay of phoresis, steric interactions and hydrodynamics.

6.1 Homophoretic triangular trimers

The main characteristics of the triangular-shaped trimer construction are that both phoretic beads display the same phoretic response, thus being homophoretic trimers, and that the three beads are at contact, forming a triangular or V-shaped structure. Sketches of this structure are depicted in Fig. 3.10g and Fig. 3.10h for the phobic, and Fig. 3.10i and Fig. 3.10j for the philic, for both symmetric and asymmetric trimers. Phoretic beads are chosen to have the same size for all geometries, thus displaying a similar thermophoretic force in modulus. This leads to a directed, translational motion, where the force components perpendicular to the swimmer axis balance each other, only persisting the parallel component. The motion resembles, thus, the dimeric one, but with an extra bead and a reduced rotational diffusion. Although the change of geometry has an influence on the flow field of the swimmer, these changes are expected to be a slight variation of the dimer's one, as already discussed in chapter 4, and are not here presented.

6.1.1 Thermophobic trimers

Thermophobic triangular-like trimers with hydrodynamic interactions show, to some degree, aggregation in both geometries and densities under study, as seen in both Fig. 6.1 and Fig. 6.2 for $\gamma = 3$ and $\gamma = 1$, respectively. These aggregates are small, mostly isolated pairs or trios, as seen for both geometries and densities. When two trimers propelling in opposite directions collide, they form a stable structure. Due to their geometry, thermal fluctuations are too weak to make them leave this hooked pair configuration. Moreover, this configuration is reinforced due to the attractive hydrodynamic attraction due to the flow field of a non-propelling swimmers, as seen in the flow fields of the phobic dimers in Fig. 4.11. Given that the trimer flow field is assumed to be a variation of the dimer one, we use this one in our discussion. These flow fields are shown in Fig. 4.11 for both geometries (Fig. 4.11a and Fig. 4.11b for the symmetric case, and Fig. 4.11e and Fig. 4.11f for the asymmetric case) and propelling/fixed states. Pairs like that rotate due to the asymmetry of the configuration, as seen from Fig. 6.3. When a third particle gets attached, the aggregate swims or rotates, depending on the configuration of the trio, as represented in Fig. 6.4. Larger aggregations are also seen for HI simulations, forming two layer lines of swimmers. Moreover, Fig. 6.1 and Fig. 6.2 also show the comparison of similar systems in the absence of hydrodynamic interactions. From these snapshots, we can infere that hydrodynamic interactions penalise the formation of the bigger aggregates present in BD systems. Brownian simulations show asymmetric aggregates resembling more the thermophilic dimer aggregates than the phobic systems. On the other hand, symmetric BD ensembles show smaller aggregates than $\gamma = 3$. Note that all snapshots have been taken at a time already in the stationary state, in order to obtain a fair comparison between HI and BD simulations. Brownian swimmers also show the same pair formation as the hydrodynamic swimmers, implying that the effect of the attractive flow field is not as relevant as the pure propulsion and steric effects on the formation of such structures, but can help on the stabilisation of hydrodynamic pairs.

The radial distribution function between the different kinds of beads for both geometries is shown in Fig. 6.5. The first result is that, as in the philic dimer's case, BD aggregates are more compact than HI, displaying peaks slightly displaced towards closer distances. Fig. 6.5a shows the phoretic-phoretic RDF of $\gamma = 3$ trimers. Brownian simulations show higher peaks at bead contact, $\sim 2s_p$, and at second neighbours, $\sim 4s_p$, than systems with HI. Moreover, BD systems also display a peak at third neighbours, $\sim 6s_p$, which HI simulations do not, confirming the presence of bigger aggregates when hydrodynamics are not present in the system, as already seen in the snapshots in Fig. 6.1 and Fig. 6.2. Fig. 6.5b shows the same RDF for symmetric swimmers, with the first peaks similar in height. BD simulations also show the third neighbour peak, whereas HI simulations do not. Systems without hydrodynamics also show the presence of extra peaks for the phoretic-bead RDF of trimers from Fig. 6.5c and Fig. 6.5d, together with the heated-heated one from Fig. 6.5e and Fig. 6.5f. Fig. 6.5c shows that, for asymmetric trimers, a phoretic and heated beads at contact are highly penalised on systems with hydrodynamic simulations, given that only BD simulations show the peak at the corresponding distance, $s_p + s_h \simeq 1.3s_p$. Phoretic-heated beads at contact show a peak corresponding to structures such as the ones shown in snapshots Fig. 6.6a and Fig. 6.6b, both taken from Brownian simulations. These structures are prohibited in the presence of hydrodynamics due to the rear repulsive flow of asymmetric swimming and fixed trimers (see the corresponding flow fields of the dimer, Fig. 4.11e and Fig. 4.15a), and non-moving symmetric trimers (see the fixed phobic dimer flow field in Fig. 4.15b). The peak of the phoretic-heated bead at contact is not as high as the next ones for BD $\gamma = 3$ simulations, implying that these configurations are not very common. The flow field of the swimming symmetric dimer, Fig. 4.11a, suggests that swimming structures such as Fig. 6.6b could form in HI systems due to the rear attractive flow of the phobic symmetric trimer. Nevertheless, given that the formation of pairs due to frontal collisions is a very fast process, most trimers are already stuck and not swimming, thus displaying rear repulsive hydrodynamic interactions, which do not allow other swimmers to approach them. Nonetheless, the symmetric swimmers indeed show contact between phoretic and heated beads, both for HI and BD simulations, as seen in Fig. 6.5d. This peak is thus attributed to the propulsion mechanism and geometry effects instead of the hydrodynamics of the swimmers, which lead to the formation of structures corresponding to the snapshot Fig. 6.6c instead of the swimming, aligned lines from BD simulations (Fig. 6.6b). Figures Fig. 6.5e and Fig. 6.5f also show that pairs of heated beads are highly uncommon, being almost inexistent for $\gamma = 1$ systems. In both asymmetric (Fig. 6.5e) and symmetric (Fig. 6.5f) systems, the most probable position of two heated beads is slightly smaller than $4s_p + 2s_h$, which corresponds to the distance between the heated beads of a stable pair of oppositely oriented trimers, as shown in Fig. 6.3, implying that these configurations are the most common in such systems. Nevertheless, BD simulations show a closer peak on the $g_{hh}(r)$ for both asymmetric and symmetric swimmers, corresponding

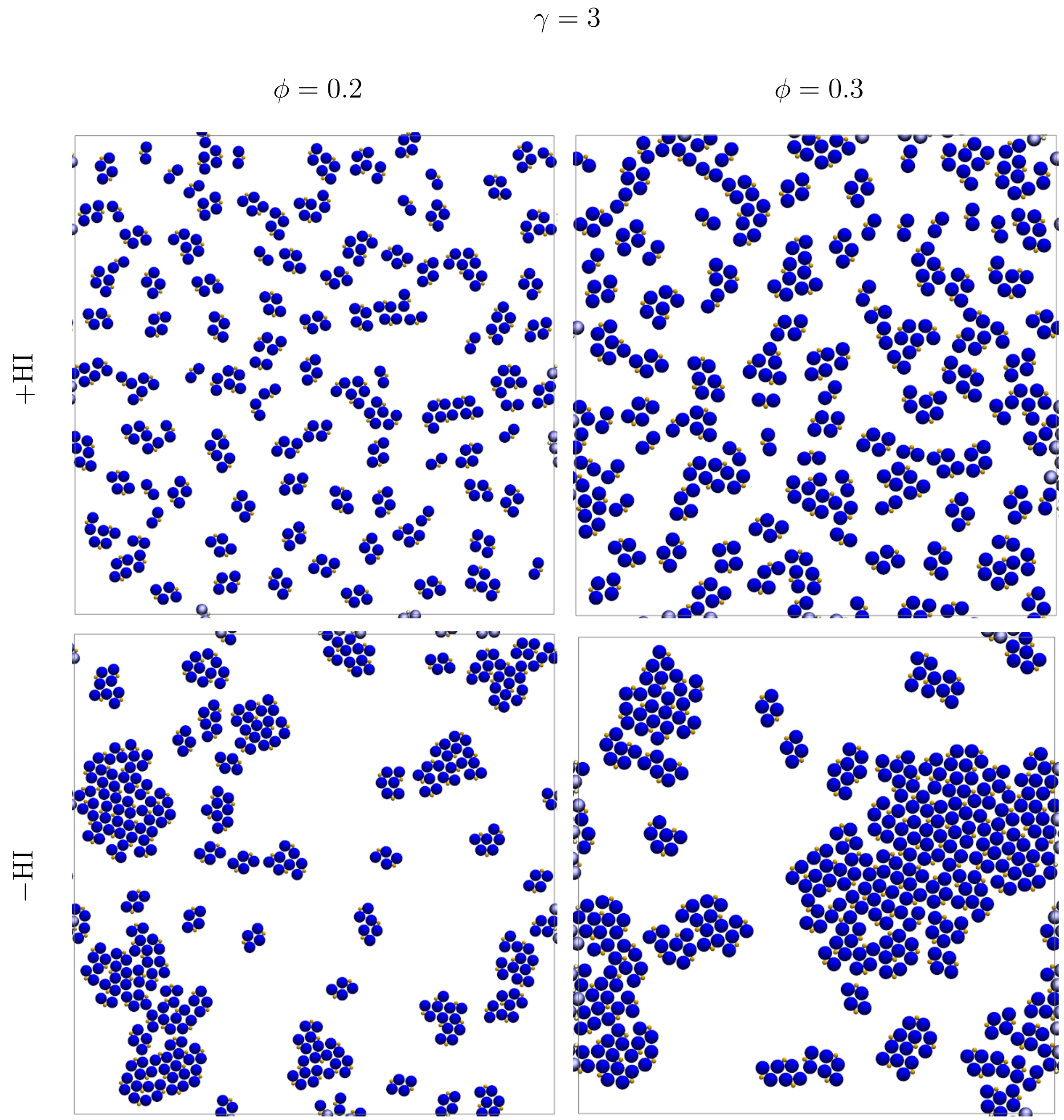

Figure 6.1: Snapshots of $\gamma = 3$ thermophobic triangular trimers at an area fractions $\phi = 0.2$ and $\phi = 0.3$ for $t/\tau_B \sim 100$. Upper figures are from HI simulations, while figures on the bottom correspond to BD simulations.

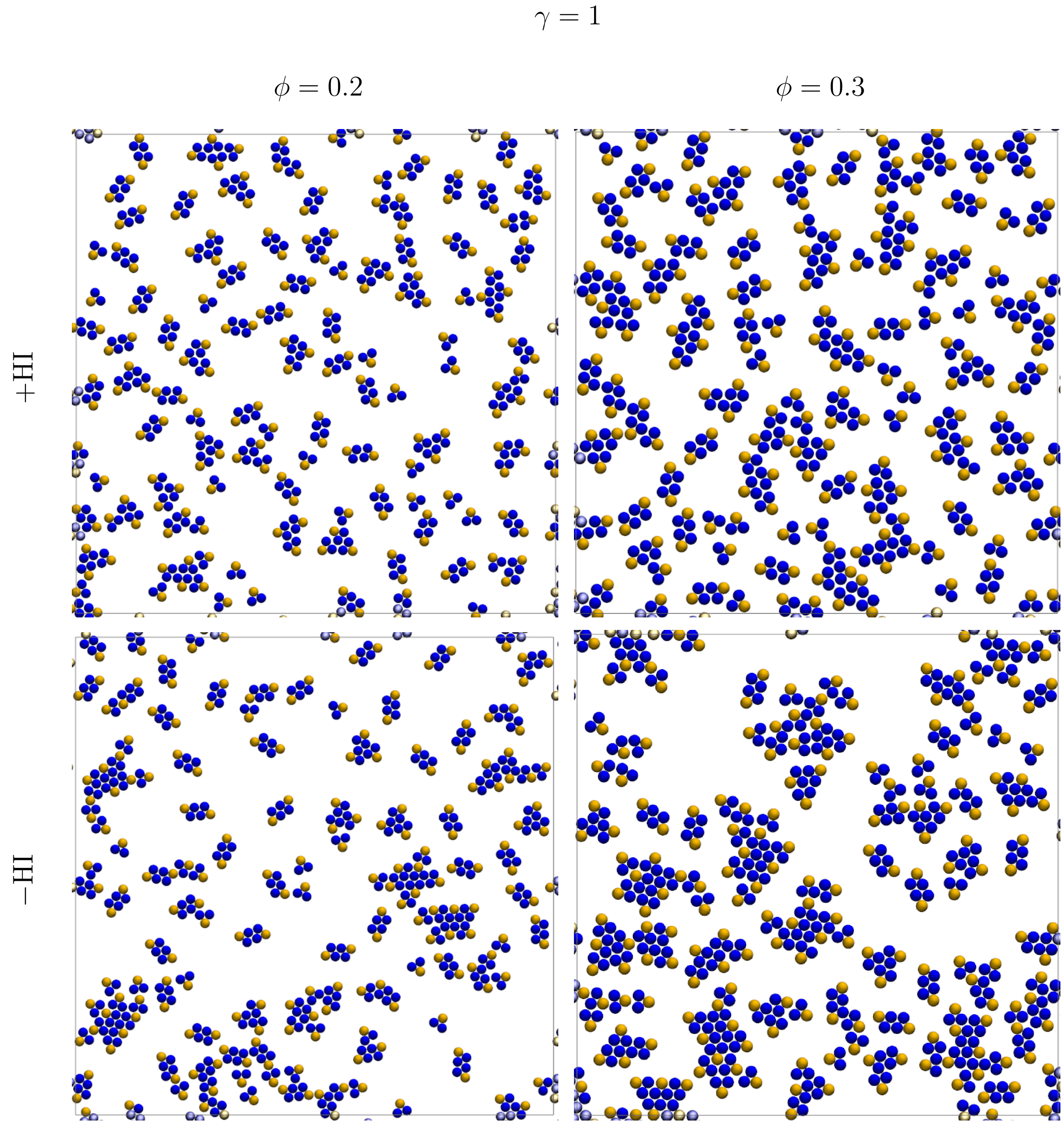

Figure 6.2: Snapshots of $\gamma = 1$ thermophobic triangular trimers at an area fractions $\phi = 0.2$ and $\phi = 0.3$ for $t/\tau_B \sim 150$. Upper figures are from HI simulations, while figures on the bottom correspond to BD simulations.

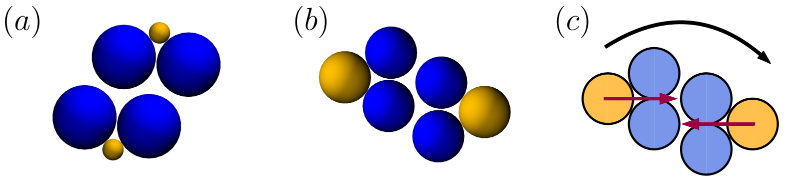

Figure 6.3: Pair of thermophobic triangular trimers, (a) asymmetric pair and (b) symmetric from simulations, and (c) a sketch of a symmetric pair. The construction of these pairs is a result of the shape of the swimmers, getting stuck together like two gears. The propulsion forces (purple arrows in c) are parallel but not perfectly aligned, which induces a torque (black arrow from c) on the pair, making this construction to rotate.

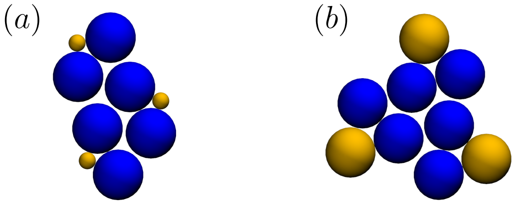

Figure 6.4: Trios of thermophobic triangular trimers, (a) asymmetric and (b) symmetric from simulations. The configuration of the trio dictates the motion of the structure. The asymmetric example leads to a propelling trio, whereas the symmetric structure is a rotating trio.

to configurations such as the ones in Fig. 6.6a and Fig. 6.6b. The argument of the prohibition of these structures on HI systems is reinforced by the absence of the corresponding peaks on the heated-heated RDFs. This is also seen for the small aggregates shown in Fig. 6.7, where the rear flow repulsion leads to two layered clusters (Fig. 6.7a and Fig. 6.7b), instead of the more circular aggregates of BD systems (Fig. 6.7c). Moreover, BD ensembles show shorter peaks at higher distances due to the presence of more beads on bigger and ordered aggregates.

The stability of such structures is studied following the same procedure as for the dimeric swimmers from section 5.3.2.3. Fig. 6.8 shows the size of the biggest cluster present in the system, n_{max}, the average size of the clusters, n_{av}, the number of single swimmers, n_{sing}, pairs, n_{pair}, and trios, n_{trio}, and the total number of clusters present in the system, N_{max}, as a function of time. Fig. 6.8a shows the results of asymmetric swimmers, while Fig. 6.8b shows the symmetric ones. Asymmetric triangular trimers show bigger clusters when hydrodynamic interactions are not present (dashed lines) for both geometries. Moreover, the difference between BD and HI is more pronounced for asymmetric swimmers. Both

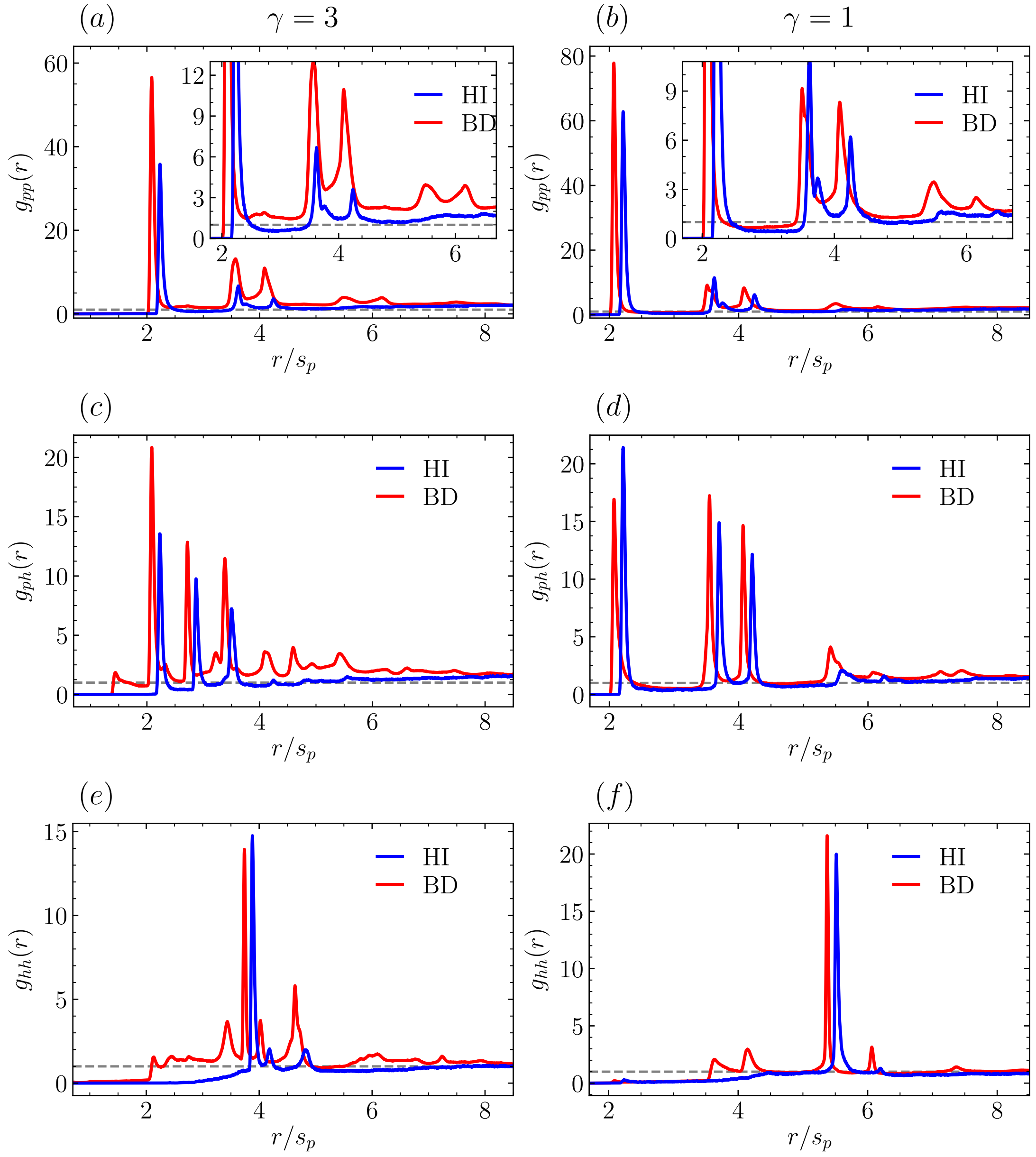

Figure 6.5: Radial distribution function of tiangular trimers at area density $\phi = 0.2$ between (a) and (b) phoretic-phoretic, (c) and (d) phoretic-heated and (e) and (f) heated-heated beads. Blue lines stand for hydrodynamic simulations, while red stand for Brownian simulations.

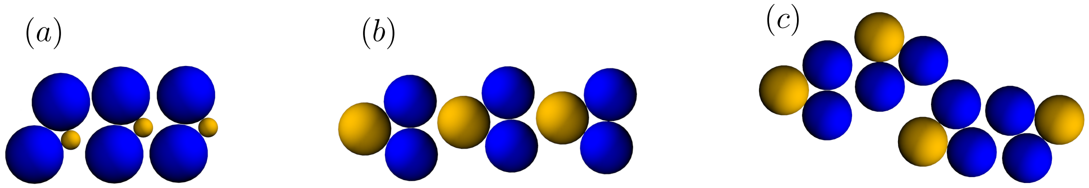

Figure 6.6: Swimming clusters of aligned thermophobic (a) asymmetric and (b) symmetric trimers in the absence of hydrodynamic interactions (BD simulations), and (c) small structure of hydrodynamic symmetric trimers showing close proximity between phoretic and heated beads.

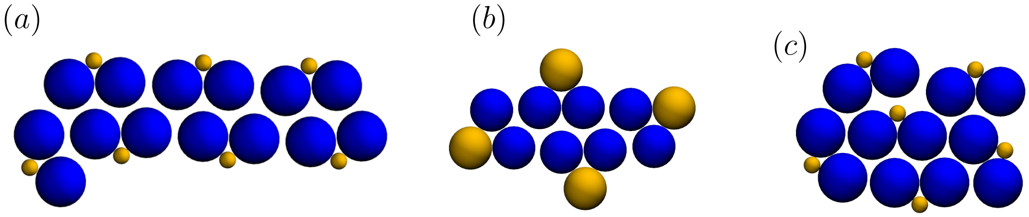

Figure 6.7: Linear clusters of hydrodynamic (a) asymmetric and (b) symmetric triangular phobic trimers, and (c) small aggregate of BD asymmetric phobic trimers.

geometries in the presence of hydrodynamic interactions (continuous lines) also show that there are practically no isolated swimming trimers, implying that nearly all of them are trapped in clusters. These clusters are small, given that the biggest cluster does not encompass the majority of swimmers in neither geometry, and the total number of clusters is significantly high. These small clusters are mostly pairs and trios, as seen from the snapshots Fig. 6.1 and Fig. 6.2, and confirmed from both Fig. 6.8a and Fig. 6.8b, where the number of trimeric pairs and trios is, in overall, higher in the presence of hydrodynamics. The number of these trimeric pairs and trios decreases with density, due to bigger aggregates being formed. At large times, the pairs constitute around a 20% of the system for an area fraction of $\phi = 0.2$, both for HI asymmetric and symmetric, while the trios constitute around a 10% of the system, nearly the same as the isolated trimers. This implies that, when hydrodynamic interactions are present, nearly a 40% of the system is composed of very small aggregates and isolated swimmers. These numbers are reduced to nearly half in the Brownian case, together with larger values of the biggest cluster in the system, as seen from the larger aggregation from the simulation snapshots. The aggregates forming in the presence of hydrodynamic interactions also appear to be more unstable, compared to their Brownian counterparts. Fig. 6.9a and

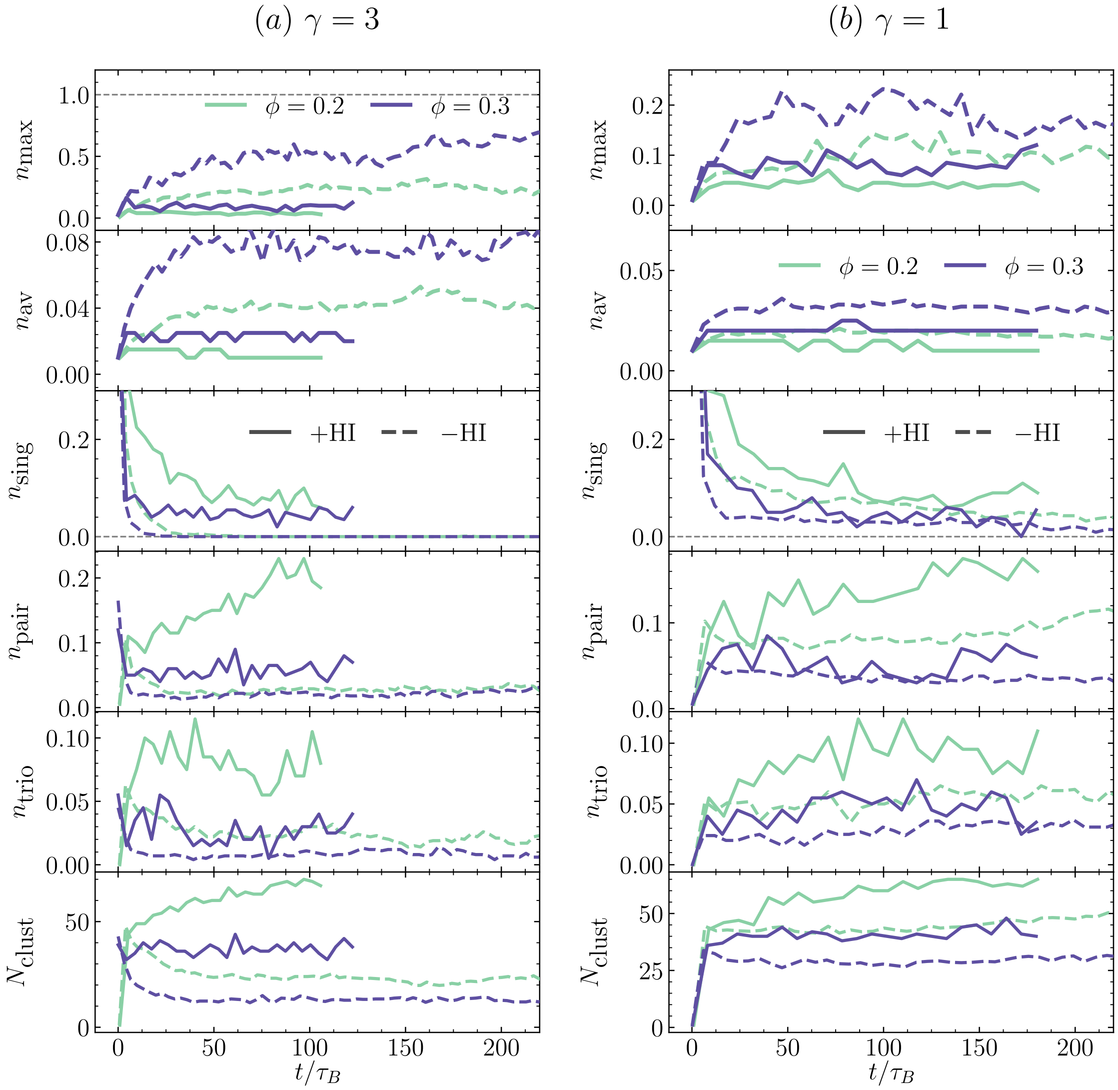

Figure 6.8: Time dependency of the cluster sizes of (a) $\gamma = 3$ and (b) $\gamma = 1$ thermophobic v-shaped trimers. The n labels stand for the normalisation with the total number of swimmers, $n_k \equiv N_k/N_s$. The size of the biggest cluster in the system is $n_{\max}$, the average size of clusters is n_{av}, the number of single swimmers, pairs and trios are n_{sing}, n_{pair} and n_{trio}, respectively, and the total number of clusters present is N_{clust}. Dark colour is for $\phi = 0.3$, while lighter colour corresponds to $\phi = 0.2$. Continuous lines correspond to full hydrodynamic simulations (MPC+MD), while dashed lines correspond to BD simulations.

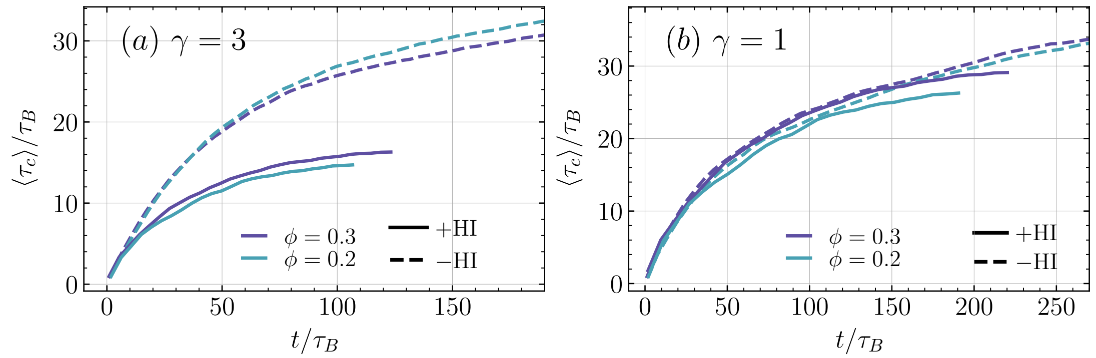

Figure 6.9: Bounding time of (*a*) asymmetric ($\gamma = 3$) and (*b*) symmetric ($\gamma = 1$) thermophobic v-shaped trimers.

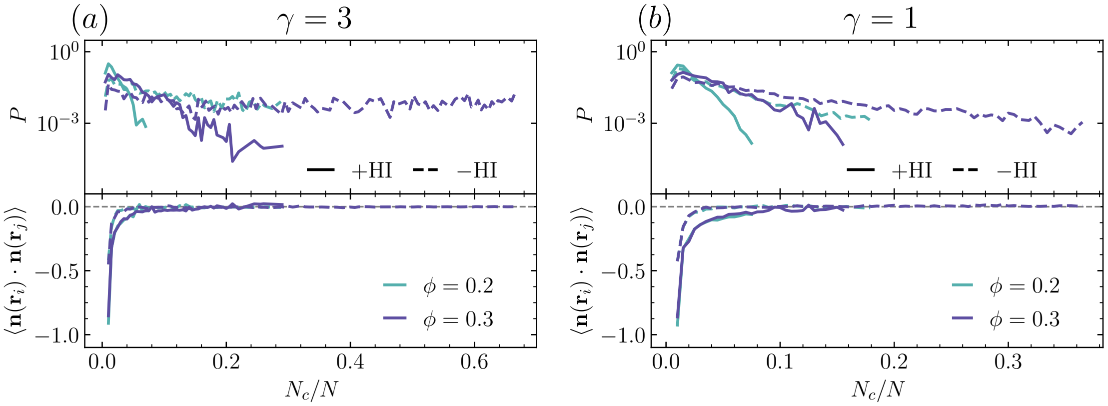

Figure 6.10: Cluster analysis of ensembles of 200 thermophobic $\gamma = 3$ and $\gamma = 1$ triangular trimers in quasi-2d confinement for densities of $\phi = 0.2$ and $\phi = 0.3$ in quasi-2d systems.

Fig. 6.9b show the average time a swimmer spends in a cluster (or bounding time), $\langle\tau_c\rangle$, for $\gamma = 3$ and $\gamma = 1$ trimers, respectively. Asymmetric swimmers show that the $\langle\tau_c\rangle$ for BD simulations are considerably higher than the corresponding one of HI. Thus, BD aggregates are more stable, *i.e.*, the swimmers spend more time being members of an aggregate, although none of these clusters will grow in time to occupy the whole system, as seen for the case of the thermophilic dimers. Thus, hydrodynamics seems to destabilise these larger structures. On the other hand, symmetric ones show very similar $\langle\tau_c\rangle$ with and without the presence of hydrodynamic interactions, and even for different values of the area fraction ϕ.

Fig. 6.10 shows that the probability of finding a swimmer in a big cluster increases with density, thus also the formation of big aggregates, which is consistent with the results shown for N_{clust} in Fig. 6.8. Agreeing with the previous figures, hydrodynamic systems show far smaller clusters than BD systems. Moreover, from the same figure, the orientation correlation function is shown as a function of the cluster size. The first datapoint corresponds to pairs, and for both geometries in the presence of hydrodynamics, it is seen that the correlation is negative, and close to the unit. This quantifies that pairs indeed form mostly due to two trimers colliding face to face, as already mentioned, and that further swimmers collide in a similar manner. Brownian pairs, on the other hand, do not show the correlation of orientations to reach the value corresponding to frontal collisions. This value is closer to -0.5, due to the presence of the linear swimming pairs, showed in Fig. 6.6a and Fig. 6.6b, which are less common but present enough in the system to have an effect on the orientation correlations. This indicates that the front-to-front hydrodynamic attraction induced by the non-propelling self-phoretic trimers is strong enough to stabilise these pairs (see Fig. 4.15a and Fig. 4.15b).

The results presented in this section are very interesting, provided that these homophoretic phobic trimers come from a dimer with an extra bead. Section 5.3.1 showed that these phobic dimers do not form large aggregates, and the clusters formed are highly unstable. By adding the second phobic bead, the swimming behaviour of the phobic dimers is lost, and steric effects predominate by keeping the small clusters together over time, leading to stable aggregates.

A final remark on these trimers is a further comparison with the dimers. Phobic dimers have a lower Péclet number than phobic homophoretic trimers, which can play a role in the dynamics of ensembles. Asymmetric $\gamma = 3$ trimers are slower than $\gamma = 3$ phobic dimers and show smaller D_R. Further research can address the study of phobic homophoretic trimers with a similar Péclet of the phobic dimers by means of decreasing the ∇T of the trimers. A decrease on the thermal gradient leads to a decrease in velocity, which in turn leads to two trimers taking more time to find each other, collide, and get stuck in the studied pairs and trios. The dynamics of the ensembles would be slower, but the prediction is that, at the steady state, trimers with a similar Péclet number as phobic dimers will behave as the phobic trimers showed in this section.

6.1.2 Thermophilic trimers

Thermophilic triangular-like trimers are here investigated. Although we could expect a very similar aggregation mechanism as the philic dimers, the opposite is seen. Triangular-like trimers have higher Péclet numbers than dimers, and their flow field is assumed to be a modification of the dimeric one, which leads to think that the aggregation mechanism of such swimmers would be similar. Thermophilic dimers have shown to aggregate *heads-out*, being affected by the hydrodynamic torque of their flow fields before reaching the cluster and are later attracted by hy-

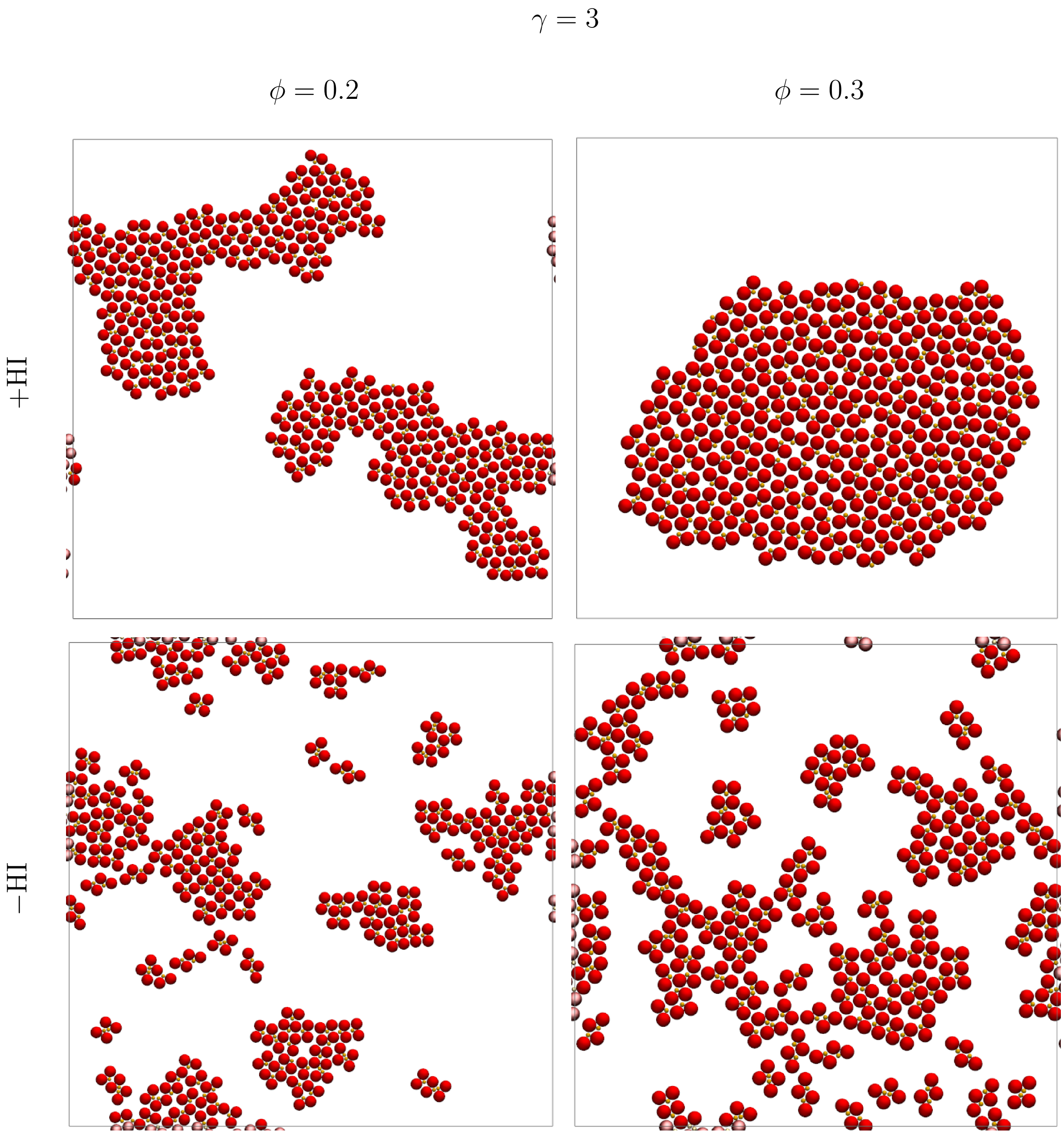

Figure 6.11: Snapshots of $\gamma = 3$ thermophilic triangular trimers at an area fractions $\phi = 0.2$ and $\phi = 0.3$ for $t/\tau_b \sim 160$. Upper figures are from HI simulations, while figures on the bottom correspond to BD simulations.

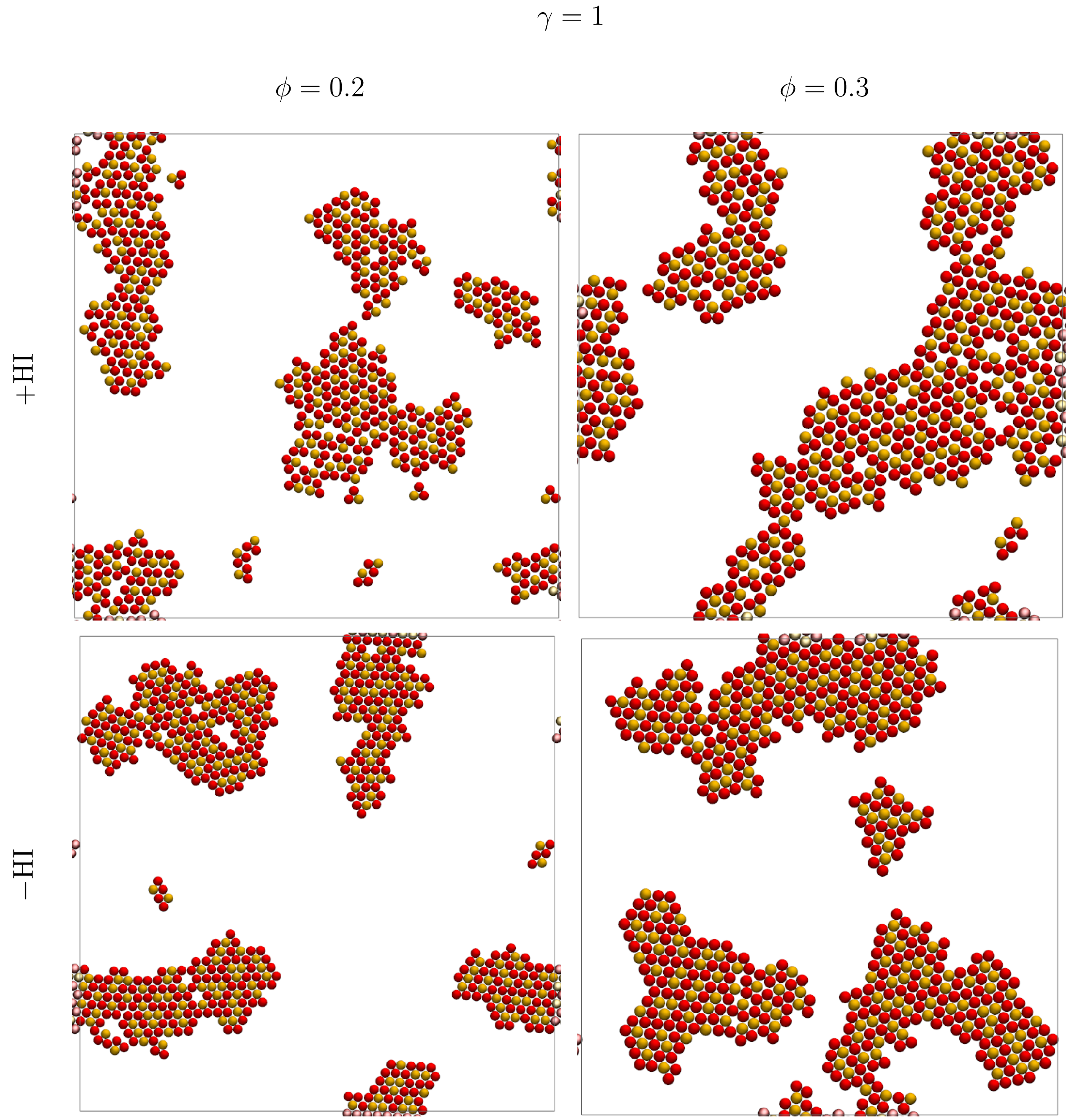

Figure 6.12: Snapshots of $\gamma = 1$ thermophilic triangular trimers at an area fractions $\phi = 0.2$ and $\phi = 0.3$ for $t/\tau_b \sim 110$. Upper figures are from HI simulations, while figures on the bottom correspond to BD simulations.

drodynamic interactions towards the main aggregate. Although the hydrodynamics of these philic homophoretic trimers are expected to be very similar to the philic dimers', the effect of HI on the clustering mechanism seen for the dimers is not present on the aggregation of these trimers. This implies the presence of extra effects with a deeper impact on the clustering of trimers. Fig. 6.11 and Fig. 6.12 show snapshots of $\gamma = 3$ and $\gamma = 1$ trimers at area fractions $\phi = 0.2$ and 0.3. From these snapshots, it is seen that the aggregates show *heads-in* configurations, contrarily to what would be expected from the previous argument. This implies that swimmers join the aggregate face forward, only due to propulsion, and get stuck by phoresis and propulsion, more resembling MIPS. Aggregates of asymmetric trimers (+HI) collapse faster to stable, compact structures, that rearrange and form spherical-like clusters with time, as observed in Fig. 6.11 for $\gamma = 3$ at $\phi = 0.3$, which eventually engulf mostly all swimmers in the system. On the other hand, symmetric swimmers show a fast collapse into more faceted aggregates, not reaching the circular shape of their asymmetric counterparts, and with all the beads forming a nearly perfect triangular lattice. The lower figures from Fig. 6.11 and Fig. 6.12 correspond to BD simulations. From these snapshots, it is seen that the asymmetric case shows a huge difference with and without hydrodynamics, where much smaller aggregates are formed. Aggregates of hydrodynamic asymmetric trimers are compact clusters, while BD aggregates are looser, moving small structures that tend to largely persist over time. Oppositely, symmetric BD systems are very similar to the HI ones, being even more compact and ordered. Note that, as in the phobic case, all snapshots have been taken at a time already in the stationary state, in order to obtain a fair comparison between HI and BD simulations.

Fig. 6.13 shows the radial distribution function, which gives an idea of the internal structure of big aggregates. The main difference between $\gamma = 3$ and $\gamma = 1$ geometries is that symmetric aggregates show a much more crystalline structure and more internal ordering than asymmetric clusters, shown by the presence of more defined peaks. This can also be seen from the snapshots in Fig. 6.12, where the triangular lattice is clear for the beads of $\gamma = 1$ aggregates, whereas asymmetric aggregates show less structural ordering within the main cluster body. Symmetric BD aggregates show even a more compact crystalline structure than HI aggregates, as seen from the snapshots and all the $\gamma = 1$ RDFs from Fig. 6.13, where the BD (red) peaks are higher and narrower than HI, implying a more precise ordering within the cluster. Hydrodynamic aggregates show small voids in the middle of the aggregates, which are not present in dry aggregates, which further increases the compactness of BD aggregates. Moreover, Brownian aggregates show more flat aggregate surfaces than the hydrodynamic aggregates.

The first steps of nucleation of the philic trimers resemble the early nucleation of the phobic case. Firstly, two trimers collide due to propulsion and get trapped

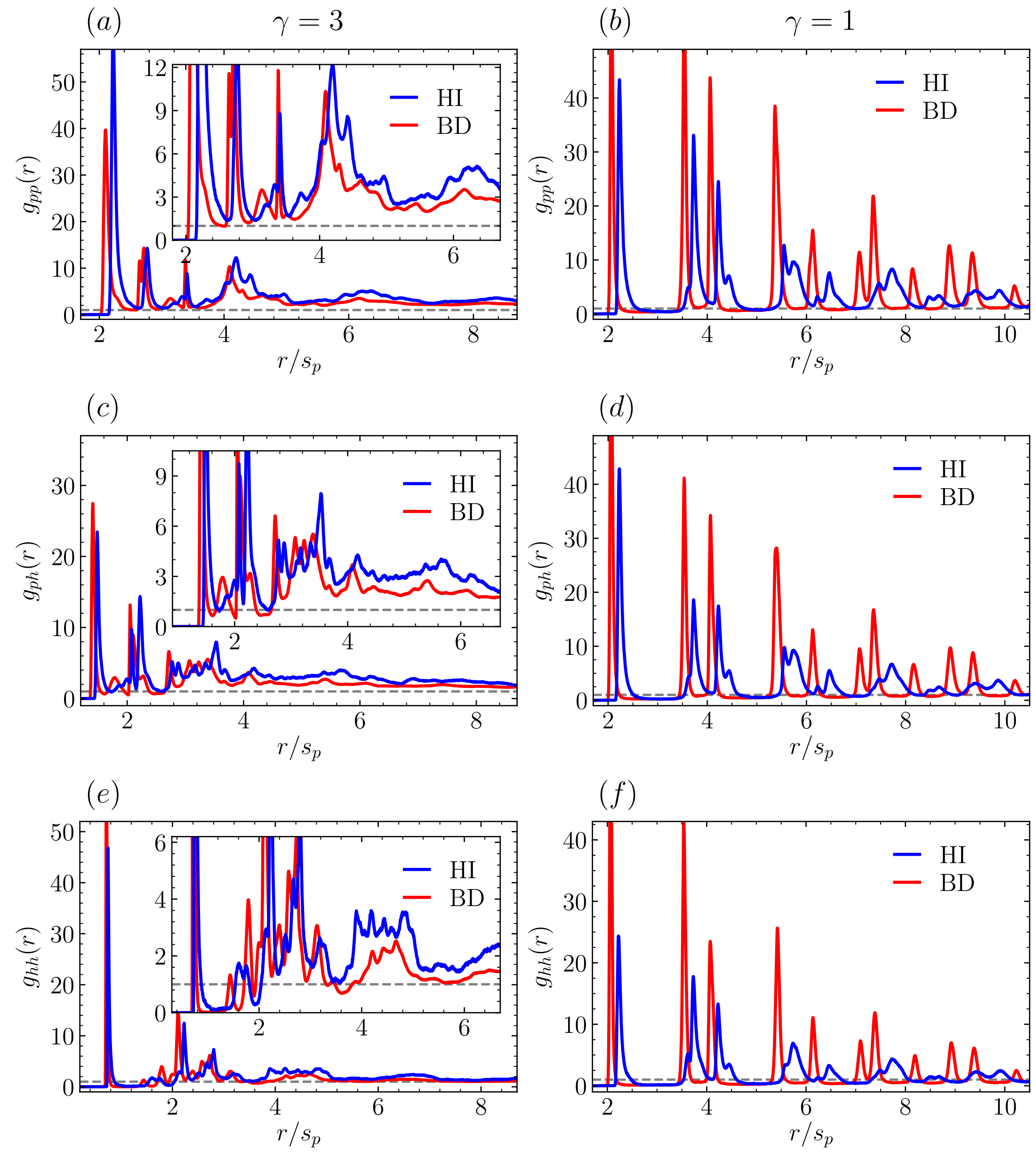

Figure 6.13: Radial distribution function of triangular trimers at area density $\phi = 0.2$ between (*a*) and (*b*) phoretic-phoretic, (*c*) and (*d*) phoretic-heated and (*e*) and (*f*) heated-heated beads. Blue lines stand for hydrodynamic simulations, while red stand for Brownian simulations.

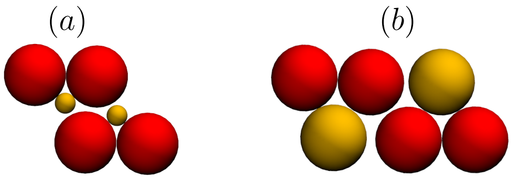

Figure 6.14: Thermophilic triangular trimer (*a*) asymmetric and (*b*) symmetric rotating pairs from simulations, and asymmetric (*c*) and symmetric (*d*) translating pairs. Figure (*d*) combines both translation with a rotational component.

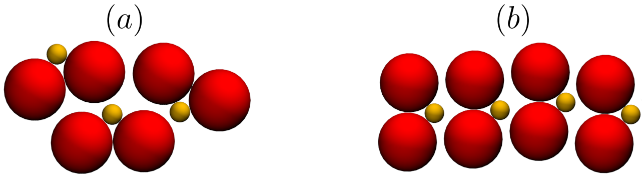

Figure 6.15: Small aggregates of asymmetric ($\gamma = 3$) philic trimers with a configuration that leads to a (*a*) rotational and a (*b*) net translational motion. The difference in motions comes from the structure of the aggregate and the superposition of the propulsion forces.

by geometry, forming pairs, as depicted in Fig. 6.14. Depending on how they get hooked, these pairs can show rotational (Fig. 6.14a and Fig. 6.14b) or translational (Fig. 6.14c or Fig. 6.14d) motions. All these pairs are observed in both HI and BD systems. In the case of the hydrodynamic triangular trimers, the swimmers swim both *with the flow* and *with the heat*. Moreover, the process for which two trimers get trapped is the responsible of the heads-in configuration of the aggregates. Asymmetric hydrodynamic pairs are already formed heads-in, and when more swimmers further collide with these structures, they form small aggregates that can further swim, as seen from trios similar to the phobic case (see Fig. 6.15a) or asymmetric line clusters (Fig. 6.15b) that act as mechanical pushers. Symmetric HI swimmers do not show that clearly the heads-in configuration, due to the geometry effects having a deeper effect on the aggregation than the pure propulsion.

The lack of formation of big aggregates for asymmetric BD systems is also characterised by means of the study of the sizes of the clusters with time. This is shown in Fig. 6.16, where the size of the biggest cluster, the average size of all clusters, the total number of single isolated swimmers and total number of clusters are displayed as a function of the simulation time. Due to the relevance of big aggregates, the study of the number of pairs and trios has been neglected for the philic trimer case. Both Fig. 6.16a ($\gamma = 3$) and Fig. 6.16b ($\gamma = 1$) show that hydrodynamics leads, in overall, to bigger aggregates. This is more relevant

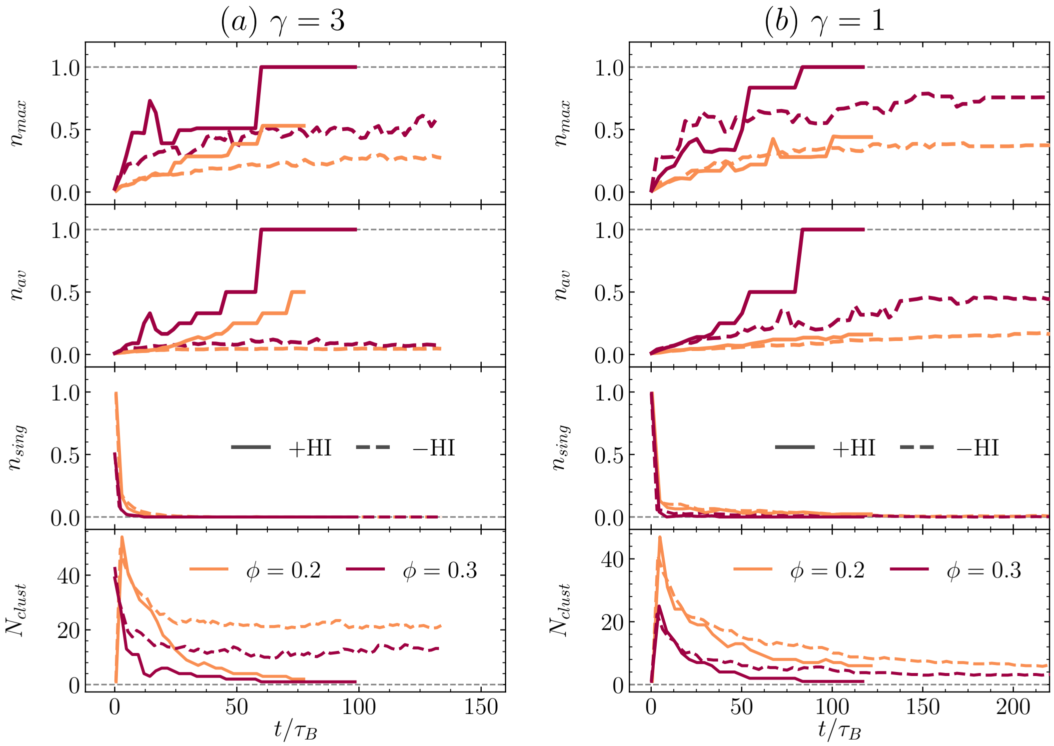

Figure 6.16: Time dependency of the sizes of clusters of (a) $\gamma = 3$ and (b) $\gamma = 1$ thermophilic homophoretic v-shaped trimers. The n labels stand for the normalisation with the total number of swimmers, $n_k \equiv N_k/N_s$. Displayed in both figures are the size of the biggest cluster in the system, the average size of clusters, the number of single swimmers, pairs and trios, and the total number of clusters present. Dark colour is for $\phi = 0.3$, while lighter colour corresponds to $\phi = 0.2$. Continuous lines correspond to full hydrodynamic simulations (MPC+MD), while dashed lines correspond to BD simulations.

for the asymmetric case, in which hydrodynamics seems to play a major role on the aggregation process, leading to bigger and much fewer clusters, as seen from the total number of clusters, N_{clust}. Symmetric trimers show qualitatively the same results with and without hydrodynamics. The pairs showed to form for philic homophoretic trimers are not seen to form for the philic dimer case. The trimeric pairs are formed by phoresis, hydrodynamics and steric effects, whereas philic dimers lack the required geometry to get stuck and form similar pairs, thus requiring extra dimers to start the nucleation process.

The bounding time $\langle\tau_c\rangle$ of the triangular-like trimers is shown in both Fig. 6.17a ($\gamma = 3$) and Fig. 6.17b ($\gamma = 1$), with (continuous lines) and without (dashed lines)

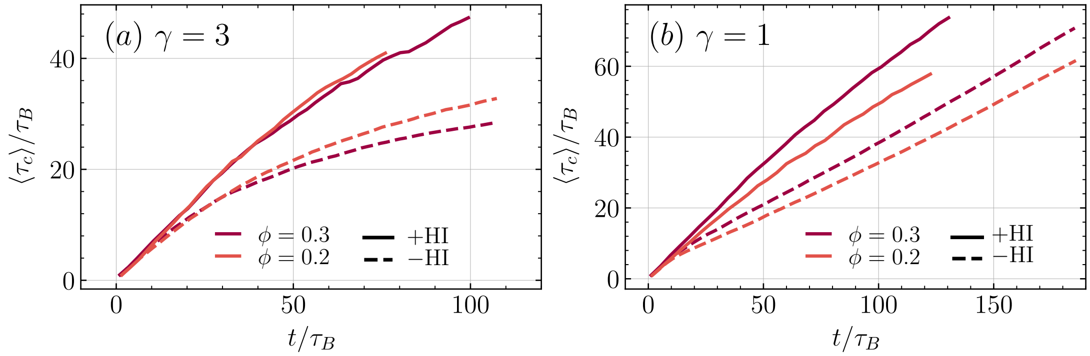

Figure 6.17: Bounding time of (a) asymmetric ($\gamma = 3$) and (b) symmetric ($\gamma = 1$) thermophilic v-shaped trimers.

hydrodynamic interactions. Asymmetric hydrodynamic swimmers show larger $\langle\tau_c\rangle$ than BD swimmers, given that in the absence of hydrodynamic interactions, the swimmers do not form such large aggregates, and are more prone to change and rearrange pairs. On the other hand, symmetric swimmers with hydrodynamics show larger $\langle\tau_c\rangle$ at short times, as a result of the fast collapse of the clusters. Nevertheless, both HI and BD show the same tendency at larger times. This implies that the aggregates are very similar in the steady state, as already discussed.

6.2 Heterophoretic linear trimers

Linear thermophoretic trimeric swimmers combine both natures of phoresis on the same swimmer, as already introduced in chapter 4 (see sketches from Fig. 3.10e and Fig. 3.10f). As in the case of the triangular trimer, both phoretic beads are kept at the same size, $s_p = 6$, while $s_h = 2$ for $\gamma = 3$ or $s_h = 6$ for the symmetric case. Fig. 6.18 and Fig. 6.19 show ensembles of 200 linear asymmetric and symmetric trimers, respectively, with a comparison with Brownian phoretic linear trimers. Both snapshots have been taken at the steady state of the simulation, giving a fair comparison between both systems. The simulations and snapshots show that both geometries of linear trimers, with and without hydrodynamics, lead to the formation of unstable, small and aligned clusters, instead of the steady aggregates seen for the case of the homophoretic triangular trimers. These small swarms are unstable groups of two to five trimers, which propel for some time in a determined direction before being destabilised by thermal fluctuations and collisions with other swimmers. Larger densities lead to these small swarms to collide with other swarms or isolated swimming trimers, forming then unstable, bigger aggregates, a behaviour very much resemblant to the case of the thermophobic dimers discussed in section 5.3.1. The main reason for the presence of small swarming clusters in both HI and phoretic BD is due to the combination of attractive and repulsive phoretic interactions in the two axial sides of the linear trimers. The small differences observed between hydrodynamic and dry systems are explained by the hydrodynamic flow field of the trimers, in Fig. 4.12, which do not introduce large torques in the neighbouring particles. This translates into an effective small additional lateral repulsion, not significantly strong, thus leading to the similarities between MPC+MD and phoretic BD simulations.

The quantification of such clusters is shown in Fig. 6.20, where the probability, the velocity and the orientation of a cluster of size N_c are presented following the same analysis from section 5.1. The comparison between both figures shows that, for both geometries and in the presence and absence of hydrodynamics, higher densities lead to larger clusters. Asymmetric linear trimers form indeed larger aggregates for both HI and BD simulations, compared to their symmetric counterparts. This is then only due to the geometry of the trimer, being a pair of $\gamma = 3$ trimers more prone to get stuck after a collision, constituting the seed of a small swarm. Fig. 6.20a shows that the aggregates formed for $\gamma = 3$ trimers are similar in size in the presence and absence of hydrodynamics. Moreover, both HI and BD $\gamma = 3$ systems show that large aggregates, bigger than a 30% of the total number of swimmers, show a constant self-propulsion velocity, of around a 25% of the isolated linear trimer, thus displaying swarming behaviour. The most significant difference between hydrodynamic and Brownian simulations is the average orientation of the cluster. Simulations show that hydrodynamics leads to more aligned clusters. This is attributed to the balance between the phoretic interactions and the flow field of the linear trimers, which is expected not to be significantly different from that of $\gamma = 2$ showed in Fig. 4.12b. The flow field is attractive around the phobic bead, whereas phoresis is repulsive. The philic bead shows the opposite, a repulsive flow field and an attractive phoretic interaction. These interactions balance, leading to aligned, swimming clusters. Smaller clusters indeed show an alignment, along with a non-vanishing velocity, which corresponds to the small swarms seen in the snapshots from Fig. 6.18.

The same analysis is performed for symmetric swimmers, and shown in Fig. 6.20b. In this case, all the aggregates are proven to be smaller than the $\gamma = 3$ case. Moreover, hydrodynamics penalises the formation of larger aggregates, leading to bigger and faster Brownian aggregates. The flow field of the symmetric linear trimer is shown, for $s_p = 4$, in Fig. 4.12a, and quantified in Fig. 4.14a and Fig. 4.14c. Fig. 4.14a shows a short-ranged hydrodynamic attraction of the flow fields of symmetric trimers around the thermophobic bead, which explains that small clusters in the presence of hydrodynamics are more aligned than Brownian ones, whereas bigger aggregates show more alignment in the absence of hydro-

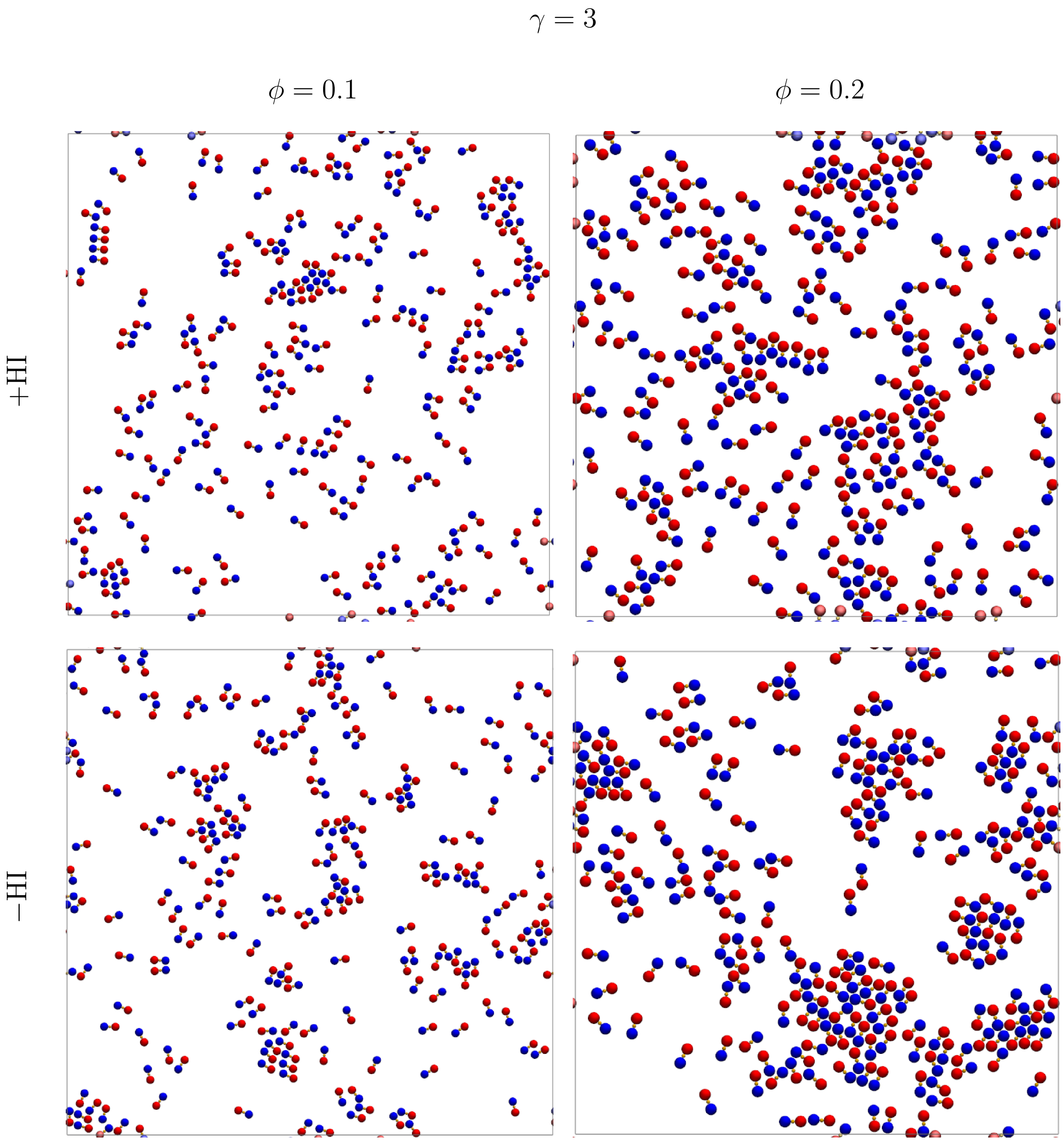

Figure 6.18: Snapshots of 200 asymmetric ($\gamma = 3$) linear trimers for $\phi = 0.1$ and $\phi = 0.2$ in quasi-2d confinement taken around $t/\tau_B \sim 200$.

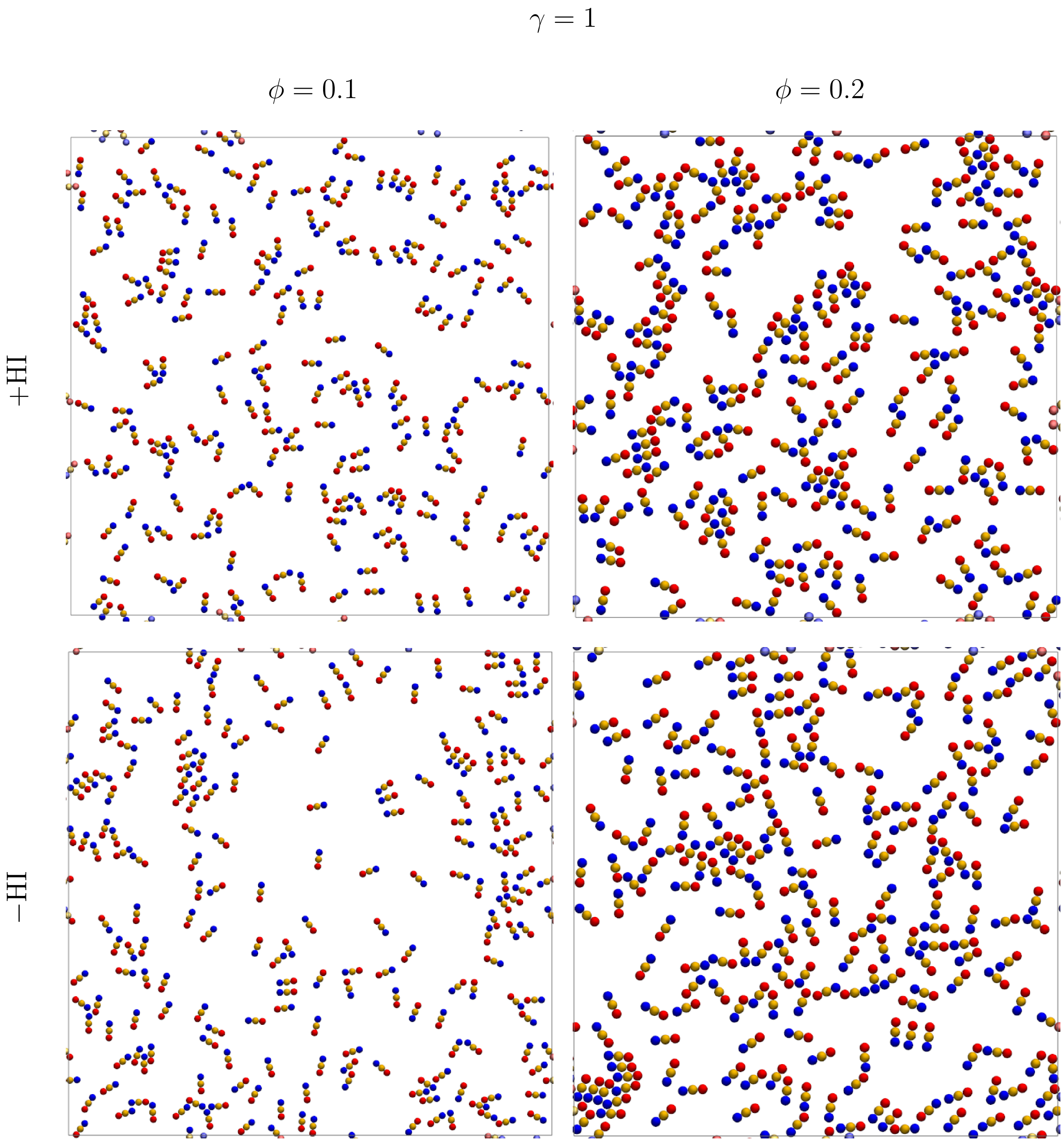

Figure 6.19: Snapshots of 200 symmetric linear trimers for $\phi = 0.1$ and $\phi = 0.2$ in quasi-2d confinement taken around $t/\tau_B \sim 300$.

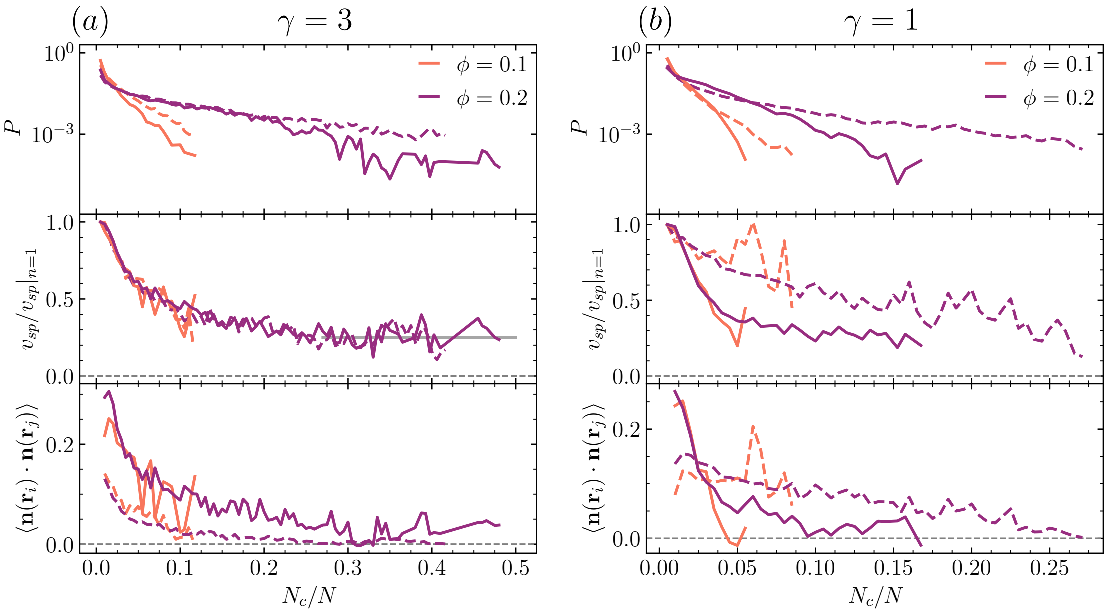

Figure 6.20: Cluster analysis of ensembles of 200 $\gamma = 3$ and $\gamma = 1$ linear trimers in quasi-2d confinement for densities of $\phi = 0.1$ and $\phi = 0.2$ in a quasi-2d systems. The gray line in (a) shows the constant value of the self-propulsion velocity of larger clusters, at around a 25% of the single $\gamma = 3$ trimer velocity.

dynamics, as seen in Fig. 6.20b. As seen by comparing the average orientation correlation of Fig. 6.20a and Fig. 6.20b with hydrodynamics, asymmetric aggregates are slightly more aligned than symmetric ones.

These results are further understood by studying the radial distribution function, Eq. (5.1), between the different beads, as can be seen in Fig. 6.21. Fig. 6.21a and Fig. 6.21b show the RDF between phobic-phobic and philic-philic (inset) beads for asymmetric and symmetric trimers, respectively. A common characteristic in all cases is that, at first approximation, similar peak structures can be observed with and without hydrodynamic interactions, although all peaks for the phoretic BD systems are displaced to smaller distances with respect to the peaks with HI. This displacement is roughly $0.2s_p$, and indicates that hydrodynamic interactions induce an effective additional repulsive layer around the swimmers. All figures show the peak corresponding to bead contact, which, for the asymmetric linear trimers, is higher for phoretic Brownian systems, indicating that the contact configurations occur more frequently than in the case of hydrodynamic simulations. For symmetric linear swimmers this is different, since contact between philic-philic and phobic-phobic beads are both clearly more likely for simulations including hydrodynamic interactions. The asymmetric case clearly shows the presence of second

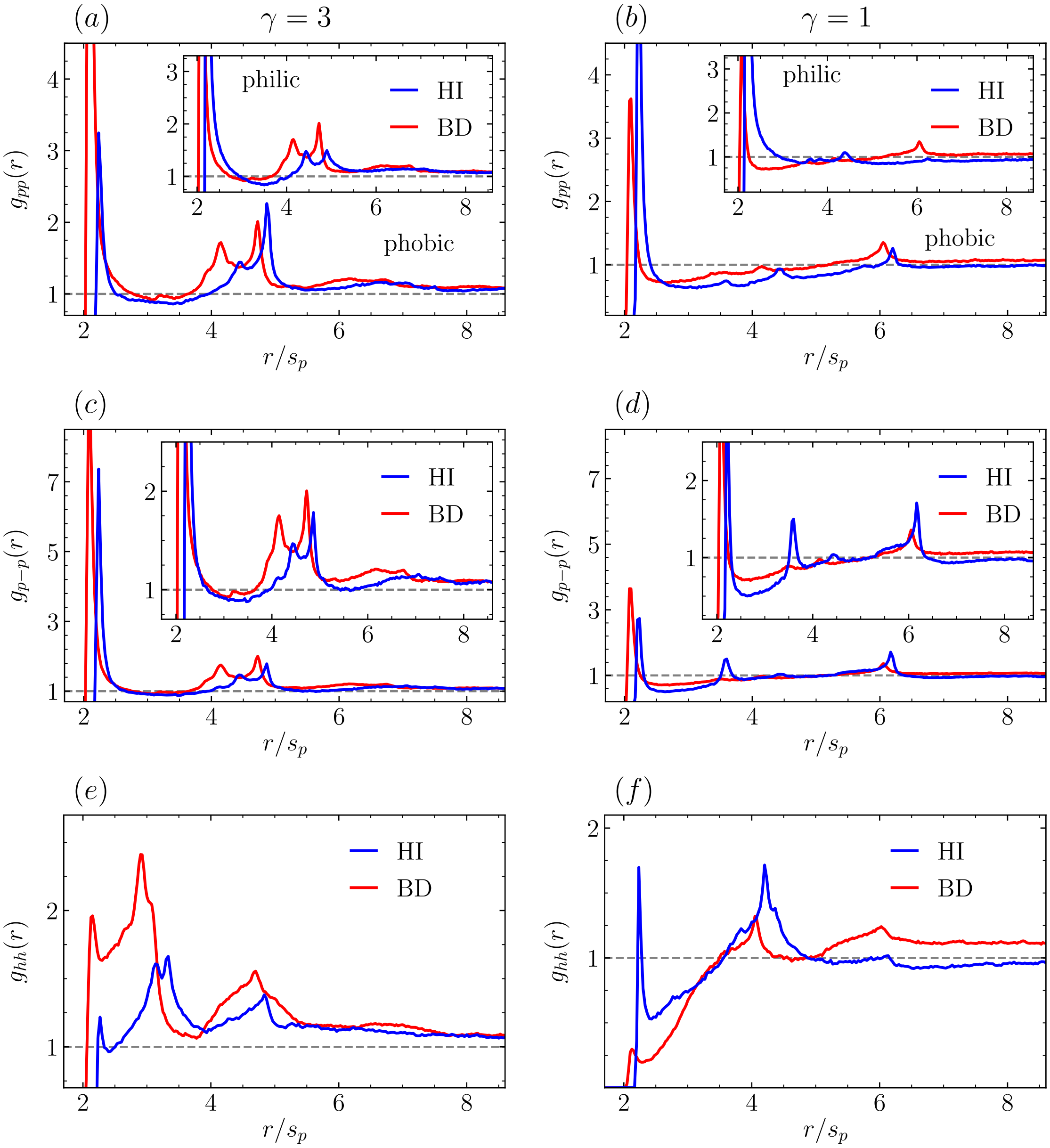

Figure 6.21: Radial distribution function between (a) and (b) phobic-phobic and philic-philic (insets), (c) and (d) phobic-philic (zoom of peaks in insets) and (e) and (f) heated-heated beads of an ensemble of symmetric and asymmetric thermophoretic linear trimers at an area fraction $\phi = 0.2$. The distance has been rescaled by the phoretic radius. Blue lines correspond to full hydrodynamic simulations (MPC+MD), while red lines correspond to BD simulations.

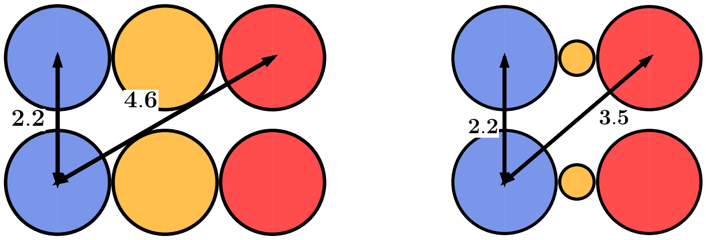

Figure 6.22: Schemes of dimers in a perfectly aligned configuration with their phoretic beads in contact for symmetric ($\gamma = 1$) and asymmetric ($\gamma = 3$) swimmers. The relevant distances, corresponding to the expected peaks of the radial distribution functions, are shown. All distances are in units of the phoretic bead's radius, s_p.

bead neighbours, *i.e.*, the two peaks around $\simeq 4.4s_p$ and $\simeq 5s_p$, for both phobic and philic, and HI and BD simulations. The peaks observed for the philic-philic RDF are slightly smaller than the phobic ones. This is explained by the presence of extra phobic beads as second neighbours as a result of the frontal collision and formation of larger aggregates, instead of trios of aligned trimers. Some hints of these second neighbour peaks are also observed for $\gamma = 1$, but with much less probability, as expected from the results from Fig. 6.20a. Fig. 6.21c shows the phobic-philic (or $p - p$) RDF for asymmetric trimers, with the peaks corresponding to aligned pairs and trios, between $4s_p$ and $5s_p$. These peaks also account for aggregates such as the swarms observed in the simulation snapshots. Fig. 6.21d corresponds to the symmetric case, which also shows the peaks of pairs and trios. The Brownian peaks are far smaller than the HI ones, which indicates larger alignment in the presence of hydrodynamic interactions, in agreement with the results from Fig. 6.20b, that small $\gamma = 1$ aggregates are more aligned in the presence of hydrodynamics. Fig. 6.21e and Fig. 6.21f show the heated-heated radial distribution function, showing that alignment with higher order neighbours is more present in asymmetric linear trimer systems.

The stability of swarms can be further quantified with the bounding time, $\langle \tau_c \rangle$, namely the average time that two swimmers remain together after an eventual encounter. This was introduced in section 5.1 and previously analysed for other swimmers. Fig. 6.23a and Fig. 6.23b show the bounding time for $\gamma = 3$ and $\gamma = 1$ linear trimers, respectively, displaying a similar behaviour as the thermophobic dimer case, seen in Fig. 5.22, in which $\langle \tau_c \rangle$ shows a plateau. This indicates that the clusters are unstable, and separate after a certain amount of time equal to $\langle \tau_c \rangle$ at the plateau. Simulations at $\phi = 0.1$ are too short to reach a perfectly constant plateau, but the results strongly suggest that the bounding time reaches a constant value, given that no stable aggregate will be present at $t/\tau_B \to \infty$. The

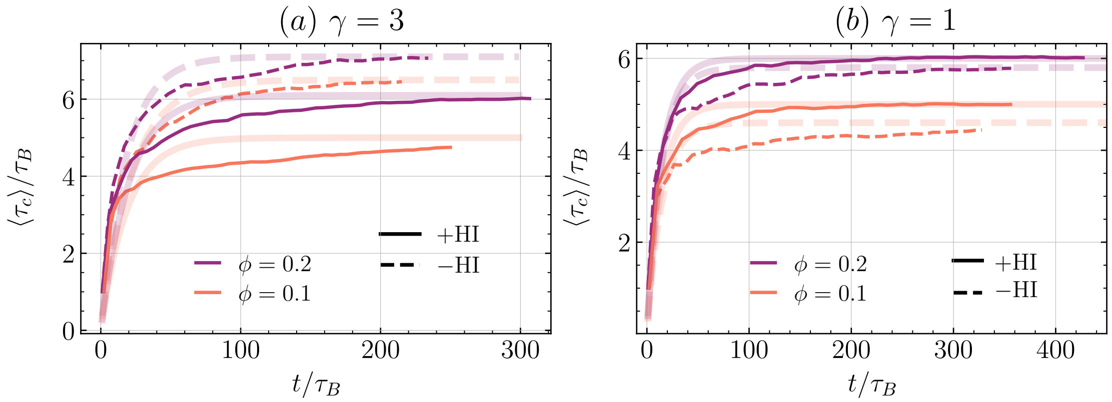

Figure 6.23: Bounding times, $\langle\tau_c\rangle$, of (a) $\gamma = 3$ and (b) $\gamma = 1$ heterophoretic linear trimers at area fractions $\phi = 0.1$ and 0.2. Thicker lines stand for the fitting of the bounding time via Eq. (6.1).

value of the $\langle\tau_c\rangle$ at the plateau, $\overline{\tau}_c$ refers then to the average time a swimmer is bound to another swimmer. Both $\gamma = 3$ and $\gamma = 1$ trimers show this constant value for $\phi = 0.2$ being around 6, whereas for the $\gamma = 3$ phobic dimers is shown to be ~ 4.5, and for $\gamma = 1$ is ~ 6.5. The increase of $\langle\tau_c\rangle$ for the asymmetric trimers is due to the steric effects, which favours a swimmer to get stuck with another trimer. Symmetric dimers and trimers show qualitatively the same behaviour, given that their flow fields are similar, and in neither case stuck structures appear. Lastly, Brownian simulations showed that hydrodynamic interactions destabilise the aggregates of $\gamma = 3$ linear trimers, given that the time two swimmers spent together, $\langle\tau_c\rangle$, is higher in dry systems compared to hydrodynamic swimmers. For symmetric linear trimers, hydrodynamic interactions seem to have the opposite effect of stabilising the bounded pairs, although the difference is not really significant, implying that hydrodynamics does not play a major role in the breaking of symmetric aggregates. This result of the bounding time, in combination with the results from Fig. 6.20, implies that the larger BD aggregates of these symmetric swimmers are very unstable, dissolving fast after forming, as the Brownian $\langle\tau_c\rangle$ should be higher than the HI one otherwise. The bounding time of systems with unstable clusters can be fitted via

$$\langle\tau_c\rangle = \overline{\tau}_c\left(1 - e^{-t/\tau_c'}\right) \ , \tag{6.1}$$

with τ_c' is related with the time that $\langle\tau_c\rangle$ needs to reach the constant value, $\overline{\tau}_c$. This equation also applies to the thermophobic dimers presented in section 5.3.1. The bounding times of thermophobic dimers and linear trimers has been fitted via Eq. (6.1), and the results are shown in Tab. 6.1. The higher the density, the larger

Table 6.1: Values of the fitting of the bounding time of non-aggregated systems via Eq. (6.1) for $\gamma = 3$ and $\gamma = 1$ phobic dimers and linear trimers, both with and without hydrodynamics.

(a) HI phobic dimers

ϕ	γ	$\overline{\tau}_c/\tau_B$	τ_c'/τ_B
0.1	3	4.0 ± 0.2	8 ± 1
0.1	1	5.6 ± 0.1	15 ± 1
0.2	3	4.5 ± 0.3	10 ± 1
0.2	1	6.5 ± 0.2	20 ± 1

(b) HI linear trimers

ϕ	γ	$\overline{\tau}_c/\tau_B$	τ_c'/τ_B
0.1	3	5.0 ± 0.2	19 ± 1
0.1	1	5.0 ± 0.2	15 ± 1
0.2	3	6.1 ± 0.2	20 ± 1
0.2	1	6.0 ± 0.1	14 ± 1

(c) BD phobic dimers

ϕ	γ	$\overline{\tau}_c/\tau_B$	τ_c'/τ_B
0.1	3	3.5 ± 0.2	7 ± 1
0.1	1	3.3 ± 0.3	6 ± 1
0.2	3	3.9 ± 0.1	7 ± 1
0.2	1	4.0 ± 0.1	7 ± 1

(d) BD linear trimers

ϕ	γ	$\overline{\tau}_c/\tau_B$	τ_c'/τ_B
0.1	3	6.2 ± 0.3	22 ± 1
0.1	1	4.6 ± 0.1	15 ± 1
0.2	3	7.1 ± 0.3	18 ± 1
0.2	1	5.8 ± 0.2	16 ± 1

$\overline{\tau}_c$ is, as expected, given that the swimmers have a higher probability of finding a neighbour and get bound to it. The change of the beads' aspect ratio shows a larger impact on the $\overline{\tau}_c$ of thermophobic dimers. Curiously, despite the repulsive flow field of symmetric dimers (see Fig. 4.11a), $\overline{\tau}_c$ increases for smaller γ. This is most probably due to the hydrodynamic drag force induced the flow field of a $\gamma = 3$ dimer (see Fig. 4.11e), which destabilises a bound $\gamma = 3$ dimeric pair. Linear trimers, on the other hand, show the same asymptotic value of the bounding time for both symmetric and asymmetric swimmers. The opposite behaviour is seen for Brownian systems, in which γ has a deeper impact on the $\overline{\tau}_c$ of the linear trimers. Moreover, the Brownian $\overline{\tau}_c$ is smaller than for HI systems, for both asymmetric and symmetric phobic dimers, although these BD swimmers form larger clusters, as seen in Fig. 5.9. This proves that although BD forms larger clusters, these are more unstable and dissolve faster than those formed in the presence of hydrodynamic interactions. The asymptotic value of the bounding time, $\overline{\tau}_c$ is larger for symmetric phobic dimers than for symmetric linear trimers, but this changes for the asymmetric case, in which $\gamma = 3$ linear trimers show larger values of $\overline{\tau}_c$, at both studied densities. These results lead to that asymmetric linear trimers form more persistent clusters than asymmetric dimers both with and without hydrodynamic interactions, most probably due to two $\gamma = 3$ linear trimers being more prone to get stuck due to steric effects. Moreover, increasing ϕ has no significant effect on the τ_c' of phobic dimers and linear trimers, compared to the effect of changing γ. Increasing the beads' aspect ratio leads to an increase of τ_c' of the linear trimers (HI and BD), along with the BD phobic dimers, but a higher γ leads to a decrease of τ_c' for HI phobic dimers. Larger values of τ_c' imply that the system takes more time to reach the steady state of the collective behaviour.

6.3 Summary

In this chapter, the swimming behaviour of trimeric swimmers has been studied. It has been proven that the steric, or geometry, effects play a major role on the aggregation and swimming behaviour of trimeric structures, alongside phoresis and hydrodynamics. Thermophobic triangular trimers are shown to form larger clusters only in the absence of hydrodynamic interactions. This behaviour is due to the rear flow field of two hooked pairs in the presence of hydrodynamic interactions, which highly penalises the formation of larger, two-layered aligned structures for both asymmetric and symmetric swimmers. Hydrodynamic asymmetric phobic triangular trimers mostly aggregate in pairs or trios, leading to smaller and less stable clusters than dry systems. Symmetric hydrodynamic phobic trimers form slightly larger clusters due to geometry effects, which are able to partially overcome the hydrodynamic repulsion, being the differences with the phoretic Brownian case therefore less important.

The opposite has been seen in ensembles of asymmetric thermophilic triangular trimers, where hydrodynamics is very relevant for the aggregation. Hydrodynamic asymmetric philic trimers form ordered clusters, resembling the ones observed for the philic dimer case. Nevertheless, these clusters show mostly heads-in configurations, instead of the heads-out seen on the dimeric case. Hydrodynamics stabilises the aggregates of asymmetric philic trimers. Symmetric philic trimers show very similar results with or without hydrodynamic interactions. Phoretic Brownian philic $\gamma = 1$ trimers form a nearly perfect triangular lattice. Hydrodynamic interactions, in this case, tend to reorient some of the symmetric trimers when approaching the cluster, such that more heads-out configurations are present in the hydrodynamic configurations compared to the Brownian ones. Furthermore, the structures are less compact with hydrodynamics, such that HI slightly destabilises the clusters, opposite to the asymmetric trimers.

Finally, the collective behaviour of linear trimers has been studied. No stable aggregation has been present in any system, and the results resemble the behaviour obtained for the phobic dimer rather than the previously studied triangular trimers, with some differences in the swimming behaviour of the clusters. Asymmetric linear trimers show small, aligned and swarming clusters with HI, due to the balance of the flow fields and the phoresis between swimmers. The clusters formed in the presence of hydrodynamics are smaller than the ones seen in the phobic dimer case. On the other hand, these larger clusters of linear trimers show constant non-vanishing velocities, implying that there is a net motion of the swarm, whereas larger aggregates of hydrodynamic phobic dimers showed nearly zero propulsion velocities. Dry asymmetric linear trimers form slightly larger swarms than their hydrodynamic counterparts, but with less alignment. Symmetric linear trimers form smaller clusters than the asymmetric ones, both for the presence and absence of hydrodynamic interactions. Phoretic Brownian systems show larger orientations for larger aggregates, but smaller aggregates get more aligned in the presence of hydrodynamics.

The trimers presented in this chapter are very interesting, since the different described behaviours for different swimmer structures can have diverse practical applications. Moreover, the results remarkably show that a small change in the structure of the swimmer can lead to very deep changes in the dynamics, as how adding an extra bead to a dimer can lead to a trimer which instead of the unstable, swimming clustering can form stable, non-moving and small aggregates or by increasing the size of a rod-like structure by adding an extra phoretic bead can lead to non-vanishing velocity of larger aggregates.

Chapter 7

Thermophoretic rotors

Micro and nanorotors are observed for both artificial and biological swimmers. An example in biology is the spherical *Volvox* algae [215]. When two nearby *Volvox* colonies swim close to a surface, they get attracted between one another, forming a stable spinning bound state. Examples of artificial microrotors are superparamagnetic colloidal particles in a rotating magnetic field [216, 217, 218, 219], dipolar colloids in a rotating electric field [220] or colloidal dimers rotated by laser tweezers [221]. One advantage of these artificial spinning or rotating colloids is their possible application as micropumps in microfluidic devices [218, 219, 221].

This chapter investigates a triangular trimer, where one phoretic bead is thermophobic, and the other one, thermophilic, as shown in the sketches Fig. 3.10k and Fig. 3.10l. This choice leads to a rotor swimmer, due to the inherent torque imposed by the phoretic forces, as shown in Fig. 7.1. Interestingly, the rotors presented here do not require any external oscillatory field or flow, given that the rotation is achieved by the direction of the phoretic forces, similarly to the Quincke rollers [222, 223, 224], which achieve spontaneous electro-rotation while exposed to a static electric field. Rotor swimmers can also be easily constructed from other trimeric structures. Any deviation from the linearity of the rod-like trimer treated in the previous chapter, or a small change in the size of one of the phoretic beads of the triangular trimer leads to a rotor instead of a ballistic swimmer. Such swimmers are easy to synthesise as variations of the already studied swimmers, which can also be generated during the synthesis of the ballistic trimers due to the polydispersity of the sizes of the phoretic beads or the structure of the swimmers.

7.1 Dynamics of thermophoretic rotors

The dynamics of the quasi-2d confined swimmer from Fig. 7.1 leads to a 2d rotation of the fluid surrounding the swimmer, which is the predominant flow field

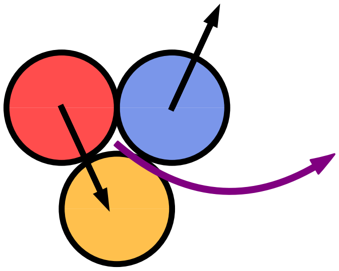

Figure 7.1: Sketch of a symmetric rotor, with the phoretic forces represented with black lines. The trajectory resulting from these forces is shown in purple.

[225]. As already discussed in section 3.1.3, MPC-SRD does not, in its original formulation, account for the conservation of angular momentum (AMC), which can ultimately induce unphysical results for systems where there is an inherent rotation of fluid. Section 3.1.3 presented a method to implement the AMC to a 2d rotation, which has been implemented in our code in order to be able to account for the angular momentum of our fluid. This chapter studies the behaviour of single phoretic rotors as a function of their geometry in the presence of a hydrodynamic solvent, and also analises the effect of the conservation of angular momentum on the swimming behaviour of these thermophoretic rotors. This understanding of the single structures constitutes then a necessary step for the study of ensembles of rotors.

The motion of these phoretic microtors can be decomposed in two motions; an inherent rotation of the swimmer around its centre of mass, and an overall displacement of the swimmer, or the motion of its centre of mass (CM). The swimmer's inner rotation is characterised by the frequency, ω, which is here calculated by Fourier transforming the relative positions of the phoretic beads as a function of time, $\Delta x^{\mu}(t) = x^{\mu}(t) - x^{\mu}_{cm}(t)$, with $\mu \in [x, y]$. Fig. 7.2 shows the relative x position of the thermophobic bead for symmetric and asymmetric rotors, along with the comparison without AMC. The relative positions of the beads with respect to the centre of mass display a sinusoidal function with time with a frequency depending on the temperature generated by the heated bead and amplitudes equal to the sum of radii. The frequency of these functions is presented in Fig. 7.3 as a function of the heating temperature, for three geometries, with and without AMC. The first result to notice is that all frequencies increase linearly with the applied temperature gradient, which is a reasonable trend since the motion is due to phoresis and the related force increases linearly with ∇T, as seen in Eq. (2.33). Furthermore, similar to the study of single dimers and trimers, the frequency also shows a non-linear dependency with the geometry. Asymmetric $\gamma = 2$ rotors display the higher frequency of rotation, whereas symmetric and asymmetric $\gamma = 3$ show very similar ω. Moreover, the absence of the AMC in the fluid slightly decreases the frequency

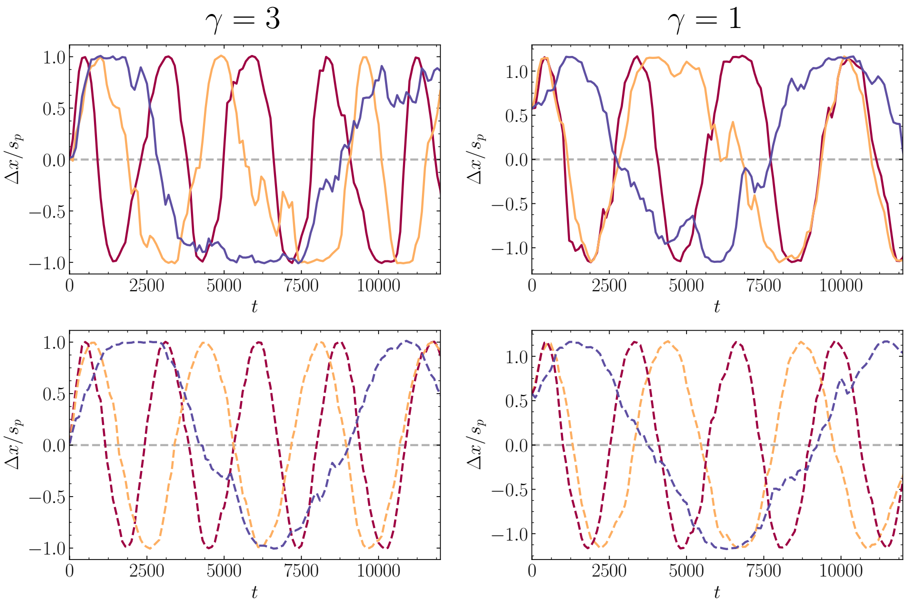

Figure 7.2: Relative x positions of the thermophobic bead with respect to the centre of mass of the swimmer at $T_h = 1.2$ (blue), $T_h = 1.5$ (orange) and $T_h = 1.8$ (red). They show a sinusoidal trajectory over time corresponding to the first rotation. Continuous lines correspond to MPC-SRD+a, whereas dashed lines correspond to MPC-SRD−a simulations.

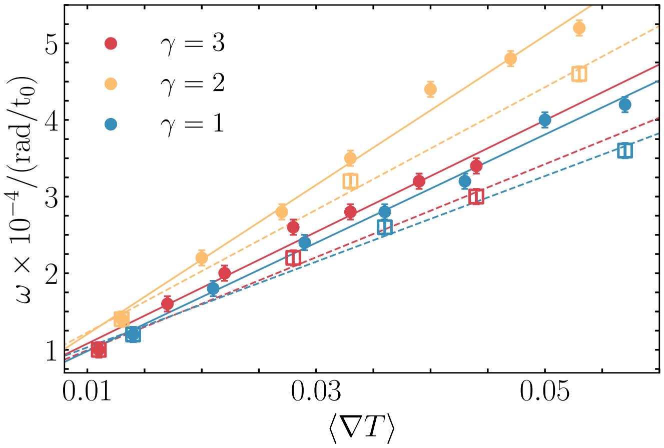

Figure 7.3: Primary rotation frequency at different geometries of phoretic rotors, $\gamma = 3,\ 2,\ 1$, with $s_p = 6$. Full symbols (and continuous lines) correspond to MPC-SRD+a simulations, while empty symbols (and dashed lines) correspond to MPC-SRD−a simulations.

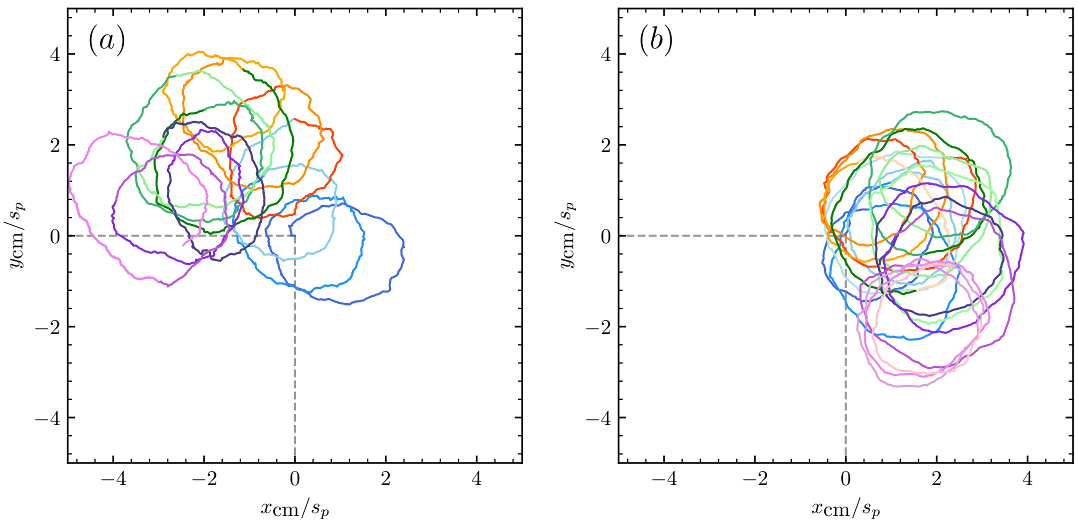

Figure 7.4: Trajectories of the centre of mass for a $\gamma = 3$ rotor at temperatures of (a) $T_h = 1.5$, which corresponds to $\langle \nabla T \rangle \sim 0.04$ and (b) $T_h = 1.8$, which corresponds to $\langle \nabla T \rangle \sim 0.06$, without angular momentum conservation. Colours correspond to the trajectories cut in sections, to enhance the visibility of the trochoidal segments.

of rotation, showing an increasing deviation from the MPC-SRD+a for increasing T_h. The second part of the dynamics of the rotors is given by the motion of the centre of mass of the swimmer, which is determined by the torque and the resulting propelling force on the swimmer. The requisite for the conversion of rotational into translational motion is a symmetry breaking in the system. The phoretic rotor swimmer from Fig. 7.1 already presents an inherent symmetry breaking on the actuation point of the thermophoretic forces. This asymmetry leads to the rotation around its centre of mass, but also induces the translational and rotational motion of the CM. Fig. 7.4 shows the trajectories of the CM of an MPC-SRD−a asymmetric, $\gamma = 3$, rotor at $T_h = 1.5$ (Fig. 7.4a) and $T_h = 1.8$ (Fig. 7.4b). These figures show helicoidal trajectories, with radii slightly bigger for higher temperatures. Furthermore, these helicoidal trajectories have been individually studied as a function of the geometry and the heating temperature and shown in Fig. 7.4a and Fig. 7.4b as different coloured sections of the whole trajectories. A set of examples of trochoidal trajectories are shown in Fig. 7.5 for $\gamma = 3$ rotors, which have been fitted via the trochoid parametric equations, which describe the motion of a point

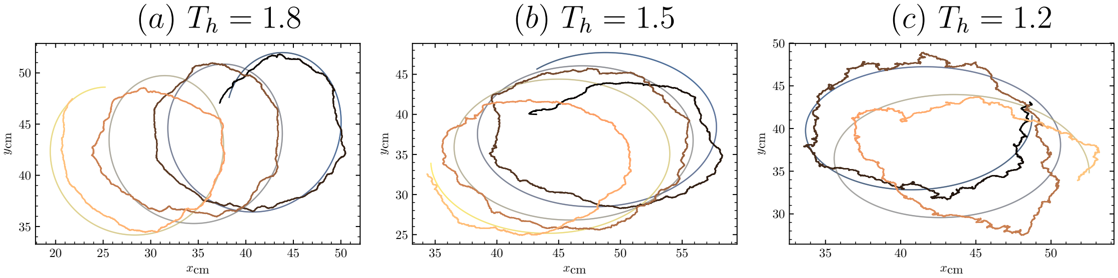

(a) $T_h = 1.8$ (b) $T_h = 1.5$ (c) $T_h = 1.2$

Figure 7.5: Sections of the trajectories of asymmetric $\gamma = 3$ thermophoretic rotors, for three different temperatures. These trajectories correspond to simulations without angular momentum conservation. Colours remark the fit of the trochoidal sections of the trajectories with Eq. (7.1).

P in the rotating plane of a circle of radius a sliding along the t direction,

$$\begin{aligned} x(t) &= at - b\sin(t) \ , \\ y(t) &= a - b\cos(t) \ , \end{aligned} \tag{7.1}$$

which is also shown in Fig. 7.5, with t the simulation time and b the distance between the circle centre and the position of P. Thus, b/a characterise the radius and the pitch of the trochoid. In the case of the −a rotors shown in Fig. 7.5, $b/a \gg 1$, which implies that the rotational motion of the centre of mass of the rotor dominates over the translational motion, leading to the more circular trajectories seen in Fig. 7.4. This ratio for the trochoidal fit of Fig. 7.5 is $b/a \simeq 7.5$ for Fig. 7.5a, $b/a \simeq 23$ for Fig. 7.5b and $b/a \simeq 13$ for Fig. 7.5c. Fig. 7.6 shows the trajectories of the centre of mass of MPC-SRD+a $\gamma = 3$ and $\gamma = 1$ phoretic rotors, at three different temperatures. A fast comparison with Fig. 7.4 evidences the accountance for the angular momentum conservation highly diminishes the trochoidal trajectory of the motion, which in turn also leads to larger displacements over time.

7.2 Effects of the angular momentum conservation on the motion

The effect of the angular momentum conservation on the rotor motion can be further investigated through the mean square displacement with and without AMC, showed in Fig. 7.7 along with the mean square angular displacement, $\Delta\boldsymbol{e}^2$, of rotors with three different beads' aspect ratios. Fickian diffusion is assumed to satisfy Gaussian statistics, *i.e.*, the thermal noise follows a Gaussian distribution, as taken for most Langevin models, Eq. (2.2). Nevertheless, in the presence of activity, the $\Delta\boldsymbol{r}^2$ shows a quadratic (ballistic) dependency with time and the Fickian diffusion

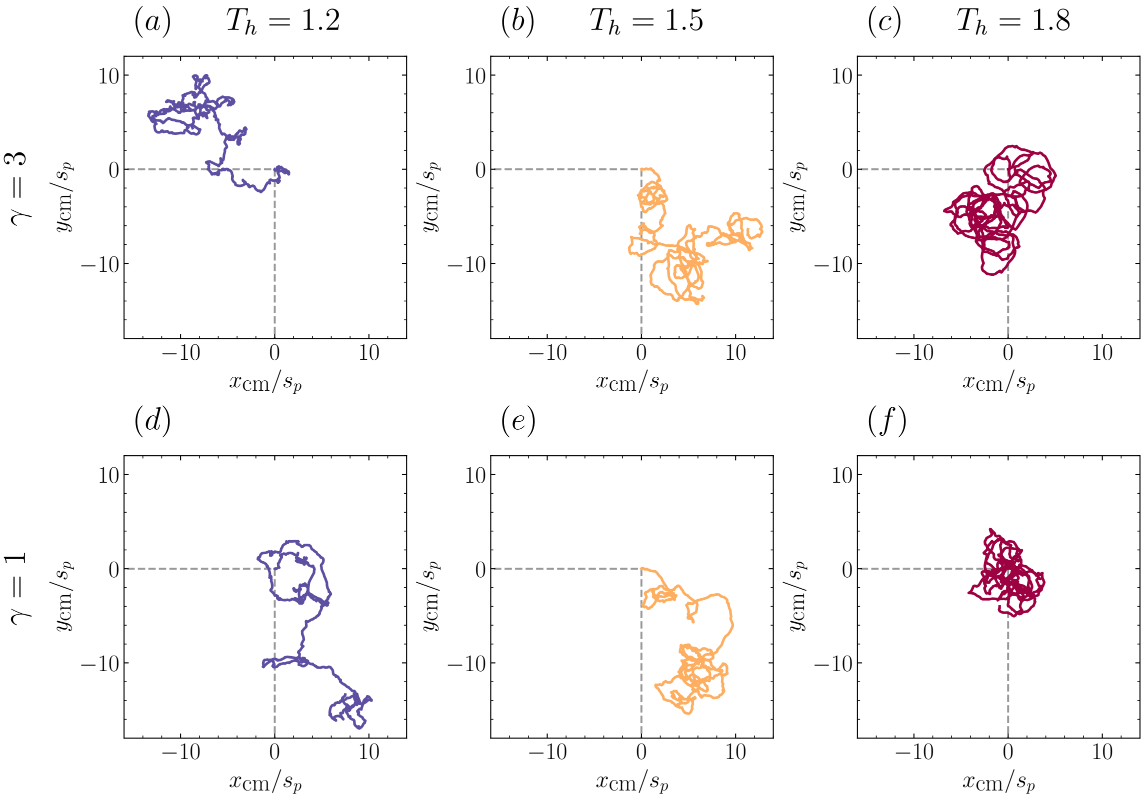

Figure 7.6: Trajectories of the centre of mass of asymmetric ($\gamma = 3$) and symmetric heterophoretic triangular trimers with angular momentum conservation for three different temperatures, from left to right, $T_h = 1.2,\ 1.5$ and 1.8. The colours of the trajectories correspond to the same legend of Fig. 7.2, and the gray line is the corresponding fit.

is only expected at much longer time scales. This has been already discussed in this dissertation for all $\Delta \boldsymbol{r}^2$, and this mechanism has been proven to dominate the dynamics also for rotors. Simulations of phoretic rotors have been performed for same simulation times as linear trimers and dimers, but given that rotors show larger D_R, thus smaller τ_R, for both +a and −a models, our simulations reach the diffusive part of their $\Delta \boldsymbol{r}^2$, as seen in Fig. 7.7, contrarily to the ballistic swimmers from chapter 4. The most interesting part is the comparison of the $\Delta \boldsymbol{r}^2$ of +a and −a rotors at and after $t/\tau_R = 1$. Rotors without AMC show a damped oscillatory behaviour of their $\Delta \boldsymbol{r}^2$ at the diffusive regime, which in average leads to subdiffusion. An oscillatory $\Delta \boldsymbol{r}^2$ implies that the radial (translation) and orthoradial (rotation) movements are not independent [226]. This behaviour has been predicted for granular materials [226] and observed in the context of both

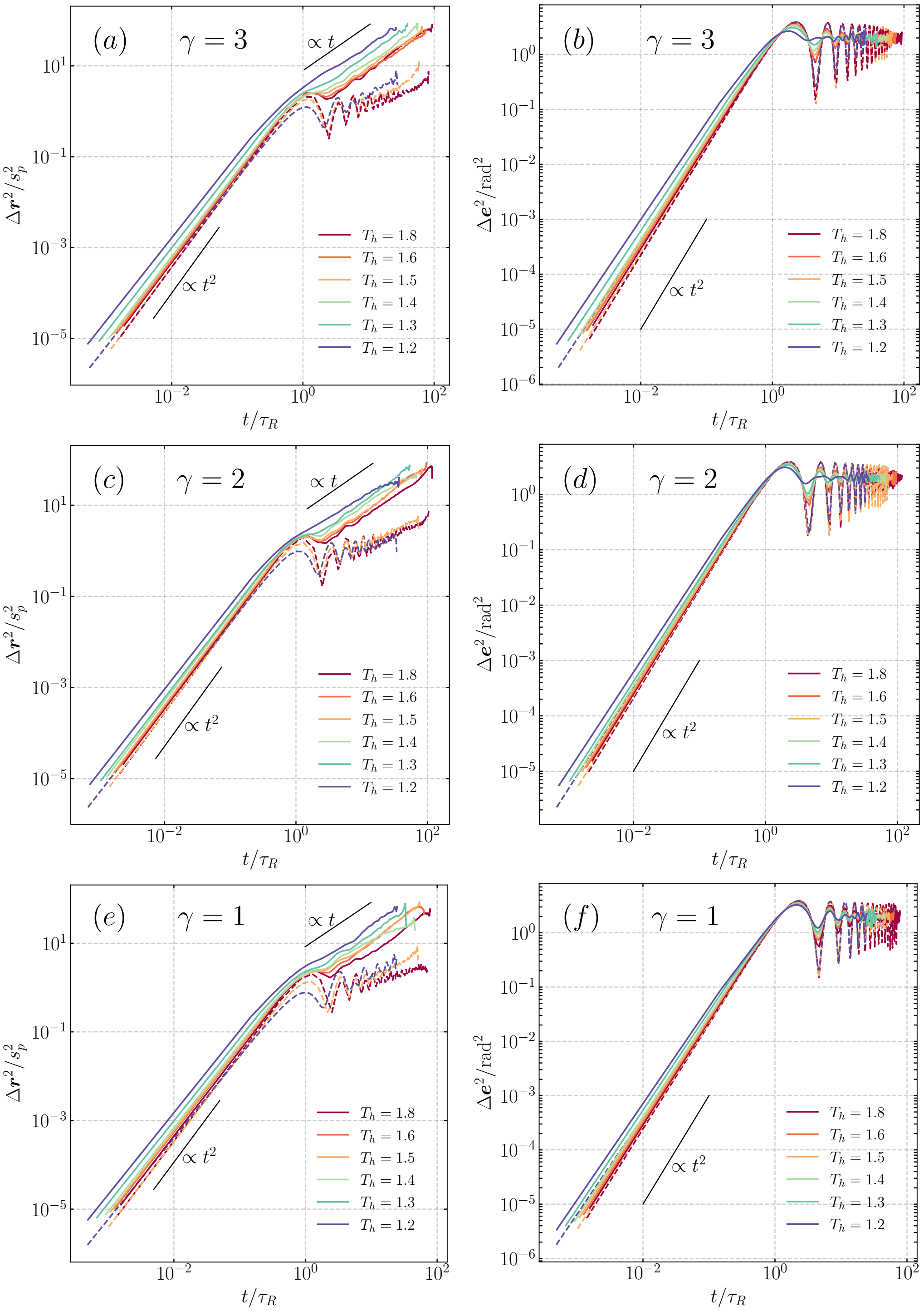

Figure 7.7: Mean square displacement ($\Delta \boldsymbol{r}^2$) and mean square angular displacement ($\Delta \boldsymbol{e}^2$) for, from top to bottom, $\gamma = 3$, 2 and 1, with $s_p = 6$. Continuous lines stand for MPC-SRD+a, while dashed lines correspond to MPC-SRD−a simulations. Times have been rescaled by the corresponding rotational time of the rotors.

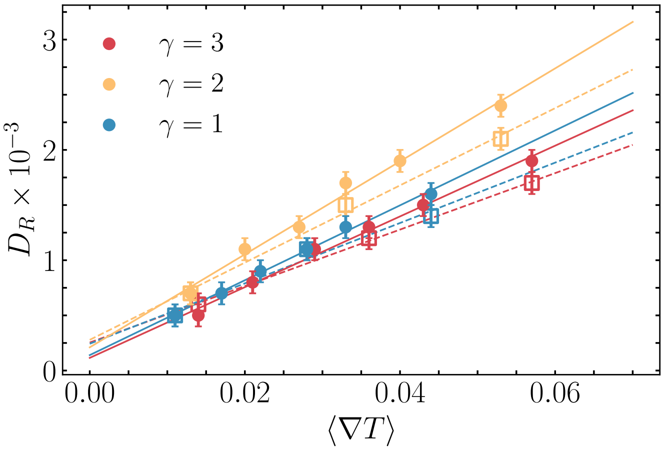

Figure 7.8: Rotational diffusion coefficient of phoretic rotors at different temperatures, for three geometries, from the fitting of $\Delta \boldsymbol{e}^2$ via Eq. (2.8). Full symbols (and continuous lines) correspond to MPC-SRD+a simulations, while empty symbols (and dashed lines) correspond to MPC-SRD−a simulations.

charged balls constrained to move in a circular channel [227] and in the movement of territorial animals [228]. Rotors that conserve the angular momentum show the transition to the diffusive behaviour without an evident oscillatory behaviour of their $\Delta \boldsymbol{r}^2$, implying that the AMC decouples the radial and orthoradial movements on these rotors, leading to the noisier trajectories seen in Fig. 7.6. It has been seen from Couette flow studies [191], in which a fluid is contained between two concentric cylinders, one rotating and the other one fixed, that the fluid velocity in the absence of AMC loses the linear dependency with the distance to the inner cylinder. This can induce spurious rotations on the fluid, which in the case here investigated can be the cause of the coupling of the rotational and translational motions for the MPC-SRD−a rotors. Similar results are seen for the mean square angular displacement, where the rotors without AMC show larger oscillations at $t/\tau_0 = 1$ compared to the +a ones. All figures in Fig. 7.7 also prove that this effect is independent of the geometry, γ, of the rotor. Nevertheless, higher temperature yields more helicoidal trajectories for both +a and −a, as the $\Delta \boldsymbol{r}^2$ decreases more for higher temperatures at $t/\tau_0 \sim 1$. For the case of −a, the peaks are deeper at higher temperatures, where for rotors with AMC, there is the presence of a minimum of the $\Delta \boldsymbol{r}^2$ at $t/\tau_0 \geq 1$.

As done for the single swimmers in chapter 4, the rotational diffusion coefficient corresponding to the motion of the centre of mass of the phoretic rotors has been obtained by fitting the $\Delta \boldsymbol{e}^2$ from Fig. 7.7 with Eq. (2.8). The results of the effective D_R for the three geometries shown in Fig. 7.7 are given in Fig. 7.8 as a function of the heating temperature and with and without AMC. The first observation is that the D_R depends linearly with the heating temperature, increasing with increasing T_h. This result implies the higher the heating temperature is, the more oscillatory, or helicoidal, the trajectory is, for both +a and −a. In other words, the translation and rotation motions are more coupled for increasing temperatures, as seen from the $\Delta \boldsymbol{r}^2$, where higher temperatures show a deeper minimum of this parameter compared to an AMC rotor. For lower T_h, the mean square displacement becomes diffusive without showing the presence of this minimum. Moreover, AMC leads to overall higher D_R, due to the more oscillatory behaviour of these trajectories, as already discussed.

7.3 Non-Gaussian parameter

Ideal Gaussian diffusion must satisfy that the self-part of the van Hove correlation function, *i.e.*, the particle's self-displacement, follows a Gaussian distribution,

$$G(\boldsymbol{r}, t) = \frac{1}{(4\pi D_T t)^{d/2}} \exp\left(-\frac{\boldsymbol{r}^2}{4D_T t}\right) ,$$

with $G(\boldsymbol{r}, t)\mathrm{d}\boldsymbol{r}$ being the probability for a particle to be found at $\boldsymbol{r}(t)$ starting from $\boldsymbol{r}(0) = \boldsymbol{r}_0$, being $\boldsymbol{r}_0$ the origin [192, 229]. The non-Gaussian parameter (NGP) [230] quantifies the deviation of the diffusion of a colloid from pure Gaussian diffusion. For a 2d system, the NGP is given by [231, 232]

$$\alpha_2(t) = \frac{1}{2} \frac{\langle |\Delta \boldsymbol{r}(t)|^4 \rangle}{\langle |\Delta \boldsymbol{r}(t)|^2 \rangle^2} - 1 , \tag{7.2}$$

where the moments correspond to $\langle |\Delta \boldsymbol{r}(t)|^n \rangle = \langle |\boldsymbol{r}(t) - \boldsymbol{r}(t')|^n \rangle$. Values of $\alpha_2 = 0$ correspond to diffusions following a Gaussian distribution, and larger values indicate a non-homogeneous motion. The subfigures in Fig. 7.9 show the NGP for +a and −a rotors, and geometries $\gamma = 1,\ 2$ and 3, at different temperatures. Systems with AMC show larger deviations from the Gaussian diffusion, while −a rotors have smaller NGP, and interestingly, this parameter also decreases for increasing temperatures. This result may seem contradictory, given that lower temperature leads to less activity, thus should also lead to a closer Gaussian diffusion. Comparing the trajectories of the CM of the −a rotors from Fig. 7.4 with the +a rotors from Fig. 7.6 and for the different heating temperatures, we observe that the absence of AMC also leads to more localised trajectories than +a rotors, leading to smaller α_2 values. Moreover, higher temperatures also lead to more localised motions, thus smaller α_2 and more Gaussian diffusion. This result is also observed from the mean displacement, $|\Delta \boldsymbol{r}|$, shown in Fig. 7.7 and further emphasised in Fig. 7.10a, which shows that for $t/\tau_R = 0.1$ (in the ballistic regime) the $|\Delta \boldsymbol{r}|$ increases for

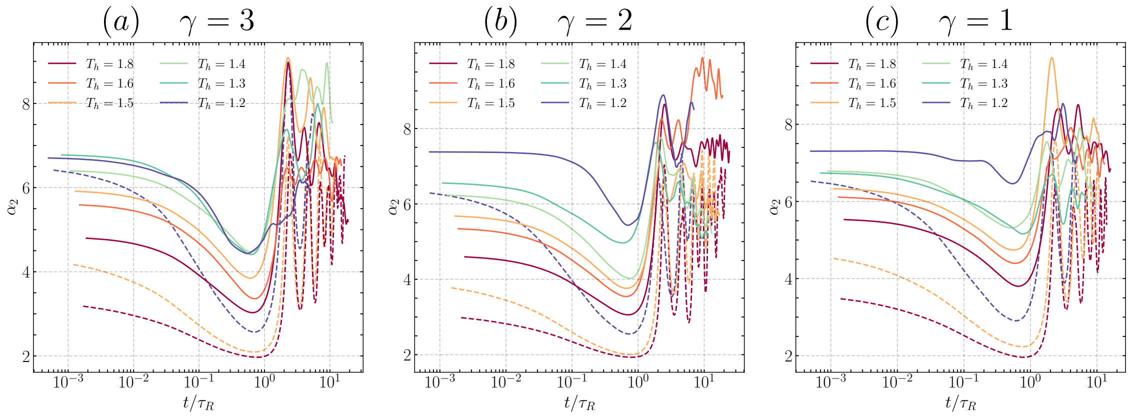

Figure 7.9: Non-Gaussian parameter, Eq. (7.2), of phoretic rotors of geometries, from left to right, $\gamma = 3$, 2 and 1, with $s_p = 6$. Continuous lines stand for MPC-SRD+a, while dashed lines correspond to MPC-SRD−a simulations.

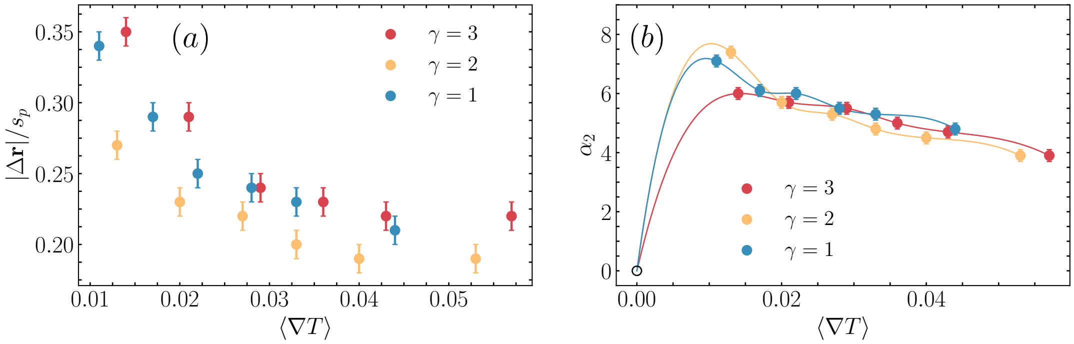

Figure 7.10: Values of (a) the mean displacement and (b) non-Gaussian parameter of a +a thermophoretic rotor as a function of the heating temperature for three rotor geometries, and at a fixed time of $t/\tau_R = 0.1$, which corresponds to the ballistic regime of the $\Delta \boldsymbol{r}^2$. The empty symbol on (b) corresponds to the theoretical value at zero activity ($\alpha_2 = 0$), and the lines stand for the spline regression of the data to show the non-monotonic behaviour of α_2.

lower temperatures, which in turn leads to the increase of the non-Gaussian parameter, as seen in Fig. 7.10b, also for $t/\tau_R = 0.1$. Then, higher temperatures lead to more localised motions, or smaller mean displacements, thus smaller α_2, or more Gaussian diffusions. Note that the behaviour of the NGP with the temperature should not be monotonic. At zero activity, or $T_h = \overline{T}$, the non-Gaussian parameter has to decay to zero for an equilibrium system, as shown in the spline regression in Fig. 7.10b. This implies that the $|\Delta \boldsymbol{r}|$ should also decrease when $\langle \nabla T \rangle \to 0$, showing a maximum as seen for α_2. Further research is required to have a deeper understanding of this behaviour.

The three subfigures in Fig. 7.9 show nearly constant values of α_2 for +a rotors at small times, which correspond to the ballistic regime. Higher temperatures show an enhancement of the initial plateau of the NGP due to the higher Péclet numbers. This plateau is not as present in the absence of AMC due to the more rotational behaviour of −a rotors. The NGP decreases with time and approaches a minimum at around $t \to \tau_R$, at the same time as $\Delta \boldsymbol{r}^2$ reaches the diffusion regime. The rotational behaviour of the trajectories is then observed for $t/\tau_R > 1$ in the form of oscillations of α_2 as a function of time. Rotors without AMC show more defined oscillations with larger amplitudes than +a rotors. This relates again to the helicoidal nature of the CM trajectory of rotors without AMC, as already discussed. Angular momentum conservation breaks this helicoidal trajectory, thus diminishing the oscillatory behaviour of the NGP.

7.4 Summary

Thermophoretic rotors induce hydrodynamic fields that require for a correct conservation of the angular momentum in order to provide the correct physical description of the phenomenon. In its original form, MPC-SRD does not account for angular momentum conservation, an aspect that needs to be addressed and corrected in order to study rotational swimmers. In this chapter, the AMC has been applied using the method presented in section 3.1.3, and the effects of it have been studied on their swimming dynamics for different geometries and heating temperatures.

The total motion of rotors is composed of two parts. The first one corresponds to the inner rotation of the trimer, *i.e.*, the rotation of the beads with respect to the centre of mass of the swimmer. This has been quantified by studying the relative positions of the beads with respect to the centre of mass position. These functions show a sinusoidal behaviour, from which we have obtained the rotation frequency. AMC has proved to enhance this rotation, leading to higher rotation frequencies, ω, for all temperatures and beads' aspect ratios. These frequencies also show a maximum as a function of the beads' aspect ratio, similarly to the self-propulsion velocity results shown in section 4.1.1. In this chapter, three different beads' aspect ratios have been studied, with $\gamma = 2$ showing a significant increase of the rotation frequency.

The second part is the motion of the centre of mass of the rotor as a result of the asymmetry on the direction of the phoretic forces. Rotors without angular momentum conservation move following clear helicoidal trajectories. Phoretic rotors with AMC do not show these oscillatory motions. Rotors simulated with MPC-

SRD+a show smaller rotational diffusion coefficients, given their more ballistic trajectories, also being a result from less helicoidal motions. On the other hand, the absence of AMC is proven to enhance the trochoidal motion, thus leading to larger D_R due to the rotational nature of the trajectory.

The mean square displacement shows that all rotors show the characteristic ballistic motion at small times. Moreover, −a rotors show an oscillatory behaviour of the $\Delta \boldsymbol{r}^2$ at $t/\tau_R > 1$, implying that there is an inherent coupling between the translational and rotational motion of the centre of mass. AMC has proven to decouple both motions given the disappearance of the oscillations of the $\Delta \boldsymbol{r}^2$. This result is reinforced via the mean square angular displacement, which shows larger oscillations in the absence of AMC.

Finally, the non-Gaussian parameter is presented, showing that both +a and −a rotors are far from Gaussian diffusion, and for times larger than τ_R, the oscillations of this parameter manifest the helicoidal behaviour of the CM motion of −a rotors.

Chapter 8

Concluding summary and outlook

The dynamic behaviour of dimeric and trimeric microswimmers driven by thermophoresis is investigated in this dissertation. Modifying the overall geometry of the phoretic multimers results in microswimmers with different propulsion and steric properties, and, very interestingly, with different phoretic and hydrodynamic interparticle properties, which translates into different collective behaviours for the different multimeric swimmers. The work here presented studies up to twelve of these structures, characterising their collective behaviour in relation to their single particle properties.

The interplay of phoresis, geometry and hydrodynamics has been studied by means of two simulation approaches. Hydrodynamic simulations have been performed with a mesoscale approach, MPC-MD, which also includes thermal transport. In order to study dry systems, we introduce a thermophoretic Brownian model, in which hydrodynamic interactions are, by construction, neglected and where the self-propulsion and inter-colloidal phoresis are coupled interactions mimicking the behaviour of real systems.

All investigated swimmers have one heated bead, which creates a thermal gradient. Dimers have a second bead, of phoretic nature, which interacts to this temperature gradient, thus driving the motion of the swimmer. Trimers have an extra second phoretic bead, which can be either of the same phoretic nature as the first one, or show the opposite phoretic response. Trimers with the two phoretic beads either philic or phobic (homophoretic trimers) are built forming a triangle, a construction that allows them to self-propel. Two cases are studied for trimers with different phoretic responses. Rod-like, or linear, heterophoretic trimers have the hot bead in the centre and two beads with different phoretic responses. This configuration leads to ballistic swimmers, given that both forces point in the same direction, thus driving the motion. Triangular-shaped trimers with one phobic and one philic bead are inherently different from ballistic swimmers. Given their construction, the actuation of the force leads to a torque in the swimmer, which results in a rotational motion.

The dynamics of swimming dimers and trimers has been discussed in chapter 4 in terms of their propulsion velocities, their rotational diffusion, characterised by the rotational diffusion coefficient and Péclet number, and their hydrodynamics. Firstly, the effects of quasi-2d confinement have been studied for thermophobic dimers and both linear and phobic triangular trimers by confining the swimmers in a two-wall slit, where the swimmers can only move in the 2d plane, whereas the fluid particles are allowed to move in the bulk space between the two walls. Results from quasi-2d confined swimmers have been then compared with simulations of 3d bulk. Simulation results suggest that the thermophobic dimers show similar dynamics in both quasi-2d and 3d systems, with a slight increase of their self-propulsion velocity due to the 2d confinement. Confinement leads to an increase of the rotational diffusion of linear trimers, but has no significant effect on their self-propulsion velocity. This leads to a decrease of the Péclet number of confined linear trimers. Moreover, the linear trimer does not show a significant difference on its self-propulsion velocity compared to the thermophobic dimer, implying that the extra thermophoretic thrust of the second phoretic bead balances with the increase of fluid friction on the swimmer. Homogeneous thermophobic triangular trimers also show a very similar self-propulsion velocity as both the phobic dimer and linear trimer. As in for the linear trimer, the extra phoretic thrust on this swimmer is balanced by the increase of friction due to the second bead. Nonetheless, this construction shows an enhanced rotational diffusion compared to the linear trimers, but a lower D_R compared to the thermophobic dimers, which lead to Péclet numbers between the ones from the linear trimers and phobic dimers.

The relative size of the beads plays a major role on the dynamics, and especially also on the hydrodynamics, of the swimmers. The phoretic beads are always kept at the same size in order to maintain the same phoretic behaviour, whereas the heated bead has been decreased. The fluid friction also changes with the beads sizes aspect ratio $\gamma = s_p/s_h$, thus varying the propulsion velocity of swimmers. Phobic dimers and linear trimers show that the fastest geometry lies in an asymmetric construction, close to $\gamma = 1.5$, whereas triangular phobic trimers are faster for the symmetric case. Given their construction, a decrease of the heated bead has not an influence on the friction of triangular trimers as deep as in the dimer or linear timer case, but it rather reduces the phoretic thrust. The effect of the geometry on the hydrodynamics is shown to be crucial. Changes on the beads' aspect ratio lead to both quantitative and qualitative changes on the flow field of the swimmers, *e.g.*, phobic symmetric dimers show a lateral repulsion hydrodynamic interaction, whereas asymmetric ones show an attraction. These flow field changes are the origin of the enhancement or diminishment of interactions that lead to hydrodynamic-induced torques on the motion of pairs of swimmers, such as in the case of thermophilic dimers or linear trimers. These interactions are very relevant for inter-swimmer interactions, which intervene in the collective behaviour of swimmers, resulting in systems with different dynamic behaviours.

The interplay of hydrodynamics, phoresis and steric effects has been studied for ensembles of both phobic and philic dimers in chapter 5 and of linear and triangular trimers in chapter 6. Asymmetric thermophobic dimers show thermophoretic repulsion to other swimmers combined with lateral hydrodynamic attraction. In 3d, these swimmers form aligned front-like clusters [180, 212] as a result of the balance between hydrodynamics and phoresis. When confined, these dimers see a destabilisation of such aligned clustering, which is attributed to the loss of one degree of freedom on the attractive hydrodynamic interactions, leading to smaller number of potential neighbours, thus less fluid-mediated attractive interactions. Phoretic Brownian simulations show an increase of alignment of these asymmetric phobic dimers due to motility induced clustering, a combination between phoresis and steric effects, along with the absence of the repulsive hydrodynamics. Symmetric thermophobic dimers, on the other hand, have repulsive lateral hydrodynamic interactions, which completely destroys any alignment in clusters. Brownian simulations of these symmetric dimers show that phoresis and steric effects balance leading to only collision clusters with a non-zero velocity and alignment. Hydrodynamics is then proven to penalise the formation of aligned swimming clusters, or swarms, for both asymmetric and symmetric thermophobic dimers, which in this case does not qualitatively change the system behaviour.

The aggregation mechanism of thermophilic dimers is proven to be highly dominated by the presence of hydrodynamic interactions. The flow fields of asymmetric dimers show lateral hydrodynamic repulsion combined with hydrodynamic attraction in both the front and rear of the dimer. Moreover, the flow field forms a fluid vortex in the front of the swimmer, which shows to play an importat role on the aggregation mechanism. Hydrodynamic simulations show that the philic dimers on the surface of the aggregate are pointing outwards the cluster, in the same direction of their propulsion, opposite to the aggregate structure that simply propelling particles form. This occurs due to a hydrodynamic-induced torque when a dimer is approaching an aggregate, changing their trajectory, and then getting trapped again by the hydrodynamic attractive field of the clustered particles. Moreover, static asymmetric philic dimers show a strong attractive flow field to their heads, *i.e.*, heated bead, which produces an attractive field around all the aggregate, enhancing clustering. Brownian simulations show otherwise, that asymmetric philic dimer aggregates are formed due to MIPS, dimers colliding due to propulsion, and then getting stuck in an aggregate by both phoresis and propulsion. This is seen given that all the philic dimers on the surface of the cluster have their head, the heated beads, pointing inwards the cluster. On the case of symmetric philic dimers, aggregation is dominated by hydrodynamics, with phoretic Brownian systems lacking the formation of larger aggregates. Symmetric hydrodynamic philic dimers have lateral hydrodynamic attraction, which greatly helps for hydrodynamic symmetric dimers to start to form aggregates.

Ensembles of homophoretic triangular trimers show aggregation, to some degree, for both phobic and philic trimers. Thermophobic trimers aggregate usually due to MIPS, pairs of swimmers colliding and getting stuck by steric effects. Phobic asymmetric trimers show that the clusters are mostly pairs or trios, and that hydrodynamics and phoretic repulsion prohibit the formation of larger structures. Symmetric hydrodynamic phobic trimers are able to partially overcome the effect of hydrodynamic repulsion due to steric effects, forming slightly bigger aggregates. Both thermophilic asymmetric and symmetric trimers show the formation of large aggregates with hydrodynamics, nearly engulfing all the swimmers in the system. Contrarily to the asymmetric philic dimer case, propulsion dominates over the fluid-mediated torque on homophoretic philic trimers, leading to heads-in aggregates. Brownian simulations prove that asymmetric trimers form these large aggregates due to hydrodynamics, whereas dry aggregates show smaller clusters. No significant difference has been found between hydrodynamic and dry systems of symmetric philic triangular trimers. Smaller differences between hydrodynamic and non-hydrodynamic systems are that Brownian homophilic symmetric trimers form more compact aggregates, lacking the empty voids that are observed for the hydrodynamic case.

The collective behaviour of linear heterophoretic trimers shows similarities with the thermophobic dimers, with the formation of swimming aligned clusters. Linear trimers form smaller aggregates than phobic dimers, but the resulting swarms show higher average self-propulsion velocities and are more aligned than the swarms of thermophobic dimers. Hydrodynamic interactions have a relatively small influence in this case, showing some enhancement in the alignment of asymmetric heterophoretic linear trimers, but decrease it for symmetric linear trimers. Dry systems also show that symmetric linear trimers form slightly faster and bigger swarms, due to the mostly repulsive flow fields of such symmetric trimers.

The last studied swimmer structures are microrotors with a heterophoretic triangular trimer geometry. This construction has the same shape as the homophoretic trimers, but each phoretic bead shows a different phoretic response, thus the motion is not ballistic, but rotational, as a result of the phoretic torque. MPC does not conserve, in its original formulation, angular momentum, which can be crucial for the correct physical description of the dynamics of such swimmers, due to their inherent rotation, although the effect on different systems has proven to be different. Thus, the effects of angular momentum conservation have been studied on the dynamics of thermophoretic rotors. The motion of such rotors can be understood as two coupled motions. The first motion is the inner rotation of the swimmer, or the rotation of the beads around the centre of mass of the rotor. This behaviour is characterised by a rotation frequency, which can be obtained from the Fourier transform of the sinusoidal behaviour of the beads' relative positions with respect to the centre of mass. Swimmers that conserve angular momentum show slightly higher frequencies of rotation than non-conserving rotors. The relative size of the beads of the rotor also plays a major role on the frequency. Three beads' aspect ratio have been studied, proving that rotors with an intermediate bead size ratio display the highest rotation frequency. The second part of the motion describes the trajectory of the centre of mass, and is driven due to the asymmetry on the phoretic thrust of the inner rotation. The absence of the AMC is proven to couple the rotational and translational motion of the centre of mass of the rotor, as seen by the oscillatory behaviour of the $\Delta \boldsymbol{r}^2$ at $t/\tau_R > 1$. This also enhances a trochoidal shape of the trajectory of the centre of mass of the swimmer, thus also increasing the rotational diffusion coefficient.

Several other projects can be envisioned to be of interest as a continuation of the work presented in this dissertation. One clear example is the study of the collective behaviour of heterothermophoretic rotors, and the effect of the angular momentum conservation on such systems. The flow field of such swimmers is of interest in order to have a broader understanding on the effects of the conservation of the angular momentum, and to help the understanding of the inter-rotor interactions. In the case of phoretic rotors, hydrodynamics can lead to synchronisation effects, which can also be compared with dry systems using the thermophoretic Brownian method we have proposed applied to the rotors. Other geometries of trimeric swimmers can also lead to rotations similar to the trimeric rotors shown in chapter 7. Homophoretic triangular trimers with an asymmetry on the sizes of the phoretic beads, *i.e.*, having one phoretic bead bigger than the other, will lead to rotational motions. Such homophoretic rotors are very interesting from an experimental point of view given that their synthesis only involves one species of phoretic beads. The study of these two types of rotors can be taken into 3d-bulk systems, in which non-confinement of the motion can lead to more defined helicoidal trajectories.

It is also interesting to study the effects of increasing densities for systems in which swarming has been present. Future work can focus on the phase transition of thermophobic dimers or linear trimers, and study whether for higher densities, the swarming behaviour is enhanced or jammed states take over the dynamics. Moreover, mixtures of different swimmers can be analysed, *e.g.*, asymmetric phobic dimers and some linear trimers, as dimers do not show swarming, whereas clusters of rod-like trimers do. Different fractions of trimer and dimers can be studied, in order to obtain asymmetric phobic dimeric swarming assisted by linear trimers.

The aggregation of philic dimers and triangular trimers can be easily controlled by turning off the illumination. The study of the formation and desintegration of aggregates of philic swimmers is also of interest due to the promising applications in medical procedures to block or free channels due to the bio-compatible and controllable temperature gradients used.

All this dissertation has treated the case in which the heated beads of the swimmers is equal or smaller than the phoretic beads. Heated beads larger than the thermophoretic ones will change both the swimming and the hydrodynamic behaviour of the swimmers, which is expected to have a large impact on their collective behaviour, making their future investigation also of interest.

Bibliography

[1] P.-G. De Gennes, “Soft matter,” *Rev. Mod. Phys.*, vol. 64, 1992.

[2] S. C. Glotzer, “Editorial: Soft matters,” *Phys. Rev. Lett.*, vol. 114, no. 050001, 2015.

[3] R. A. L. Jones, *Soft Condensed Matter.* Oxford Master Series in Physics, Oxford University Press, 2002.

[4] S. Ramaswamy, “The mechanics and statistics of active matter,” *Annu. Rev. Condens. Matter Phys.*, vol. 1, 2010.

[5] M. C. Marchetti, J.-F. Joanny, S. Ramaswamy, T. B. Liverpool, J. Prost, M. Rao, and A. S. Simha, “Hydrodynamics of soft active matter,” *Rev. Mod. Phys.*, vol. 85, 2013.

[6] J. Elgeti, R. G. Winkler, and G. Gompper, “Physics of microswimmers–single particle motion and collective behavior: A review,” *Rep. Prog. Phys.*, vol. 78, no. 056601, 2015.

[7] C. Bechinger, R. Di Leonardo, H. Löwen, C. Reichhardt, and G. Volpe, “Active particles in complex and crowded environments,” *Rev. Mod. Phys.*, vol. 88, 2016.

[8] P. Romanczuk, M. Bär, W. Ebeling, and B. Lindner, “Active Brownian particles: From individual to collective stochastic dynamics,” *Eur. Phys. J. Special Topics*, vol. 202, 2012.

[9] G. De Magistris and D. Marenduzzo, “An introduction to the physics of active matter,” *Physica A*, vol. 418, 2015.

[10] E. Lauga and T. R. Powers, “The hydrodynamics of swimming microorganisms,” *Rep. Prog. Phys.*, vol. 72, no. 9, p. 096601, 2009.

[11] E. M. Purcell, “Life at low reynolds number,” *Am. J. Phys.*, vol. 45, no. 3, 1977.

[12] L. Turner, W. S. Ryu, and H. C. Berg, “Real-time imaging of fluoroscent flagellar filaments,” *J. Bacteriol.*, vol. 182, no. 2793, 2000.

[13] J. Cosson, P. Huitorel, and C. Gagnon, “How spermatozoa come to be confined to surfaces,” *Cell Motil. Cytoskeleton*, vol. 54, no. 56, 2003.

[14] H. Machemer, “Cilliary activity and the origin of metachrony in *paramecium*: Effects of increased viscosity,” *J. Exp. Biol.*, vol. 57, 1972.

[15] T. Vicsek and A. Zafeiris, “Collective motion,” *Phys. Rep.*, vol. 517, no. 3, pp. 71 – 140, 2012. Collective motion.

[16] C. J. Ingham and E. Ben Jacob, “Swarming and complex pattern formation in paenibacillus vortex studied by imaging and tracking cells,” *BMC microbiology*, vol. 8, pp. 36–36, 2008.

[17] A. Wysocki, R. G. Winkler, and G. Gompper, “Cooperative motion of active Brownian spheres in three-dimensional dense suspensions,” *EPL*, vol. 105, no. 4, p. 48004, 2014.

[18] I. Buttinoni, J. Bialké, F. Kümmel, H. Löwen, C. Bechinger, and T. Speck, “Dynamical clustering and phase separation in suspensions of self-propelled colloidal particles,” *Phys. Rev. Lett.*, vol. 110, p. 238301, 2013.

[19] M. Theers, E. Westphal, K. Qi, R. G. Winkler, and G. Gompper, “Clustering of microswimmers: interplay of shape and hydrodynamics,” *Soft Matter*, vol. 14, no. 8590, 2018.

[20] K. F. Jarrell and M. J. McBride, “The surprisingly diverse ways that prokaryotes move,” *Nat. Rev. Microbiol.*, vol. 6, 2008.

[21] J. P. Armitage and R. M. Berry, “Assembly and dynamics of the bacterial flagellum,” *Annu. Rev. Microbiol.*, vol. 74, 2020.

[22] K. Drescher, R. E. Goldstein, N. Michel, M. Polin, and I. Tuval, “Direct measurement of the flow field around swimming microorganisms,” *Phys. Rev. Lett.*, vol. 105, no. 168101, 2010.

[23] O. S. Pak and E. Lauga, *Theoretical models in low-Reynolds-number locomotion*, ch. 1. Royal Society of Chemistry, 2015.

[24] H. Jiang and T. Kiørboe, “Propulsion efficiency and imposed flow fields of a copepod jump,” *J. Exp. Biol.*, vol. 214, no. 3, 2011.

[25] T. Kiørboe, H. Jiang, R. J. Gonçalves, L. T. Nielsen, and N. Wadhwa, "Flow disturbances generated by feeding and swimming zooplankton," *Prog. Natl. Acad. Sci.*, vol. 111, no. 32, 2014.

[26] G. I. Taylor, "Analysis of the swimming of microscopic organisms," *Proc. R. Soc. Lond. A*, vol. 209, no. 447, 1951.

[27] M. J. Lighthill, "On the squirming motion of nearly spherical defomable bodies through liquids at very small Reynolds numbers," *Commun. Pure Apply. Math.*, vol. 5, 1952.

[28] J. R. Blake, "A spherical envelope approach to ciliary propulsion," *J. Fluid. Mech.*, vol. 46, 1971.

[29] M. Theers, E. Westphal, G. Gompper, and R. G. Winkler, "Modeling a spheroidal microswimmer and cooperative swimming in a narrow slit," *Soft Matter*, vol. 12, no. 7372, 2016.

[30] R. Dreyfus, J. Baudry, M. L. Roper, M. Fermigier, H. A. Stone, and J. Bibette, "Microscopic artificial swimmers," *Nature*, vol. 437, 2005.

[31] J. Palacci, C. Cottin-Bizonne, C. Ybert, and L. Bocquet, "Sedimentation and effective temperature of active colloidal suspensions," *Phys. Rev. Lett.*, vol. 105, p. 088304, 2010.

[32] W. F. Paxton, K. C. Kistler, C. C. Olmeda, A. Sen, S. K. St. Angelo, Y. Cao, T. E. Mallouk, P. E. Lammert, and V. H. Crespi, "Catalytic nanomotors: Autonomous movement of striped nanorods," *J. Am. Chem. Soc.*, vol. 126, 2004.

[33] S. Sanchez, A. N. Ananth, V. M. Fomin, M. Viehrig, and O. G. Schmidt, "Superfast motion of catalytic microjet engines at physiological temperature," *J. Am. Chem. Soc.*, vol. 133, no. 38, 2011.

[34] W. Gao, S. Sattayasamitsathit, J. Orozco, and J. Wang, "Highly efficient catalytic microengines: Template electrosynthesis of polyaniline/platinum microtubes," *J. Am. Chem. Soc.*, vol. 133, no. 31, 2011.

[35] 20th Century Fox, "Fantastic voyage." Film, 1966.

[36] S. Gonzalez and R. Soto, "Directed assembly of active colloidal molecules," *New J. Phys.*, vol. 21, no. 033041, 2019.

[37] M. Vilfan, A. Potočnik, B. Kavčič, N. Osterman, I. Poberaj, A. Vilfan, and D. Babič, "Self-assembled artificial cilia," *Proc. Natl. Acad. Sci.*, vol. 107, no. 5, pp. 1844–1847, 2010.

[38] H. R. Vutukuri, A. F. Demirörs, B. Peng, P. D. J. van Oostrum, A. Imhof, and A. van Blaaderen, “Inside back cover: Colloidal analogues of charged and uncharged polymer chains with tunable stiffness (angew. chem. int. ed. 45/2012),” *Angewandte Chemie International Edition*, vol. 51, no. 45, pp. 11389–11389, 2012.

[39] H. R. Vutukuri, B. Bet, R. van Roij, M. Dijkstra, and W. T. S. Huck, “Rational design and dynamics of self-propelled colloidal bead chains: from rotators to flagella,” *Sci. Rep.*, vol. 7, no. 1, p. 16758, 2017.

[40] F. Schmidt, B. Liebchen, H. Löwen, and G. Volpe, “Light-controlled assembly of active colloidal molecules,” *J. Chem. Phys.*, vol. 150, no. 9, p. 094905, 2019.

[41] H. Xing, Z. Wang, Z. Xu, N. Y. Wong, Y. Xiang, G. L. Liu, and Y. Lu, “DNA-directed assembly of asymmetric nanoclusters using Janus nanoparticles,” *ACS Nano*, vol. 6, no. 1, pp. 802–809, 2012.

[42] Y. Wang, Y. Wang, D. R. Breed, V. N. Manoharan, L. Feng, A. D. Hollingsworth, M. Weck, and D. J. Pine, “Colloids with valence and specific directional bonding,” *Nature*, vol. 491, no. 7422, pp. 51–55, 2012.

[43] Z. Zeravcic and M. P. Brenner, “Self-replicating colloidal clusters,” *Proc. Natl. Acad. Sci.*, vol. 111, no. 5, pp. 1748–1753, 2014.

[44] Z. Zeravcic, V. N. Manoharan, and M. P. Brenner, “Size limits of self-assembled colloidal structures made using specific interactions,” *Proc. Natl. Acad. Sci.*, vol. 111, no. 45, pp. 15918–15923, 2014.

[45] J. Zhang and S. Granick, “Natural selection in the colloid world: active chiral spirals,” *Faraday Discussions*, vol. 191, no. 0, pp. 35–46, 2016.

[46] R. Niu, T. Palberg, and T. Speck, “Self-assembly of colloidal molecules due to self-generated flow,” *Phys. Rev. Lett.*, vol. 119, p. 028001, 2017.

[47] J. Zhang, J. Yan, and S. Granick, “Directed self-assembly pathways of active colloidal clusters,” *Angewandte Chemie International Edition*, vol. 55, no. 17, pp. 5166–5169, 2016.

[48] C. Casagrande, P. Fabre, E. Raphaël, and M. Veyssié, ““Janus beads”: Realization and behaviour at water/oil interfaces,” *EPL*, vol. 9, no. 251, 1989.

[49] J. R. Howse, R. A. L. Jones, A. J. Ryan, T. Gough, R. Vafabakhsh, and R. Golestanian, “Self-motile colloidal particles: From directed propulsion to random walk,” *Phys. Rev. Lett.*, vol. 99, 2007.

[50] R. Golestanian, T. B. Liverpool, and A. Ajdari, "Propulsion of a molecular machine by asymmetric distribution of reaction products," *Phys. Rev. Lett.*, vol. 94, no. 220801, 2005.

[51] M. A. Houck and B. M. OConnor, "Ecological and evolutionary significance of phoresy in the astigmata," *Annu. Rev. Entomol.*, vol. 36, 1991.

[52] P. S. White, L. Morran, and J. Roode, "Phoresy," *Curr Biol.*, vol. 27, no. 12, 2017.

[53] R. Kapral, "Perspective: Nanomotors without moving parts that propel themselves in solution," *J. Chem. Phys.*, vol. 138, no. 020901, 2013.

[54] S. Saha, R. Golestanian, and S. Ramaswamy, "Clusters, asters, and collective oscillations in chemotactic colloids," *Phys. Rev. E*, vol. 89, no. 6, pp. 062316–, 2014.

[55] J. Burelbach, M. Zupkauskas, R. Lamboll, Y. Lan, and E. Eiser, "Colloidal motion under the action of a thermophoretic force," *J. Chem. Phys.*, vol. 147, no. 9, p. 094906, 2017.

[56] R. Piazza and A. Parola, "Thermophoresis in colloidal suspensions," *J. Phys.: Condens. Matter*, vol. 20, no. 15, 2008.

[57] A. Würger, "Thermal non-equilibrium transport in colloids," *Rep. Prog. Phys.*, vol. 73, 2010.

[58] C. Lozano, B. ten Hagen, H. Löwen, and C. Bechinger, "Phototaxis of synthetic microswimmers in optical landscapes," *Nat. Commun.*, vol. 7, no. 1, p. 12828, 2016.

[59] F. A. Morrison, "Electrophoresis of a particle of arbitrary shape," *J. Colloid Interface Sci.*, vol. 34, no. 2, pp. 210 – 214, 1970.

[60] K. Makino and H. Ohshima, "Electrophoretic mobility of a colloidal particle with constant surface charge density," *Langmuir*, vol. 26, no. 23, pp. 18016–18019, 2010.

[61] M. M. Hatlo, D. Panja, and R. van Roij, "Translocation of dna molecules through nanopores with salt gradients: The role of osmotic flow," *Phys. Rev. Lett.*, vol. 107, p. 068101, 2011.

[62] B. Sabass and U. Seifert, "Dynamics and efficiency of a self-propelled, diffusiophoretic swimmer," *J. Chem. Phys.*, vol. 136, no. 6, p. 064508, 2012.

[63] S. Samin and R. van Roij, "Solvo-osmotic flow in electrolytic mixtures," *J. Fluid. Mech.*, vol. 819, p. R1, 2017.

[64] M. Suwa and H. Watarai, "Magnetoanalysis of micro/nanoparticles: A review," *Anal. Chim. Acta*, vol. 690, no. 2, pp. 137–147, 2011.

[65] M. Benelmekki, L. M. Martinez, J. S. Andreu, J. Camacho, and J. Faraudo, "Magnetophoresis of colloidal particles in a dispersion of superparamagnetic nanoparticles: theory and experiments," *Soft Matter*, vol. 8, no. 22, pp. 6039–6047, 2012.

[66] Z. M. Sherman, J. L. Pallone, R. M. Erb, and J. W. Swan, "Enhanced diffusion and magnetophoresis of paramagnetic colloidal particles in rotating magnetic fields," *Soft Matter*, vol. 15, no. 33, pp. 6677–6689, 2019.

[67] G. Rückner and R. Kapral, "Chemically powered nanodimers," *Phys. Rev. Lett.*, vol. 98, no. 150603, 2007.

[68] L. F. Valadares, Y.-G. Tao, N. S. Zacharia, V. Kitaev, F. Galembeck, R. Kapral, and G. A. Ozin, "Catalytic nanomotors: Self-propelled sphere dimers," *Small*, vol. 6, no. 4, pp. 565–572, 2010.

[69] Y. Lu, H. Xiong, X. Jiang, Y. Xia, M. Prentiss, and G. M. Whitesides, "Asymmetric dimers can be formed by dewetting half-shells of gold deposited on the surfaces of spherical oxide colloids," *J. Am. Chem. Soc.*, vol. 125, no. 42, pp. 12724–12725, 2003.

[70] S. Wang, F. Ma, H. Zhao, and N. Wu, "Bulk synthesis of metal–organic hybrid dimers and their propulsion under electric fields," *ACS Appl. Mater. Interfaces*, vol. 6, no. 6, pp. 4560–4569, 2014.

[71] Z. Wang, Z. Wang, J. Li, S. T. H. Cheung, C. Tian, S.-H. Kim, G.-R. Yi, E. Ducrot, and Y. Wang, "Active patchy colloids with shape-tunable dynamics," *J. Am. Chem. Soc.*, vol. 141, no. 37, pp. 14853–14863, 2019.

[72] S.-M. Yang, S.-H. Kim, J.-M. Lim, and G.-R. Yi, "Synthesis and assembly of structured colloidal particles," *J. Mater. Chem.*, vol. 18, no. 19, pp. 2177–2190, 2008.

[73] S.-H. Kim, A. D. Hollingsworth, S. Sacanna, S.-J. Chang, G. Lee, D. J. Pine, and G.-R. Yi, "Synthesis and assembly of colloidal particles with sticky dimples," *J. Am. Chem. Soc.*, vol. 134, no. 39, pp. 16115–16118, 2012.

[74] M. Yang, A. Wysocki, and M. Ripoll, "Hydrodynamic simulations of self-phoretic microswimmers," *Soft Matter*, vol. 10, pp. 6208–6218, 2014.

[75] C. Ludwig, *Diffusion zwischen ungleich erwärmten Orten gleich zusammengesetzter Lösungen*, vol. 65. Sitzungsbericht. Kaiser. Akad. Wiss. (Mathem.-Naturwiss. Cl.), Wien, 1856.

[76] C. Soret, *Sur l'état d'équilibre que prend, du point de vue de sa concentration, une dissolution saline primitivement homogène, dont deux parties sont portées à des températures différentes*, vol. tomme II. Archives de Genève, 3e période, 1879.

[77] L. Talbot, R. K. Cheng, R. W. Schefer, and D. R. Willis, "Thermophoresis of particles in a heated boundary layer," *J. Fluid. Mech.*, vol. 101, no. 4, pp. 737–758, 1980.

[78] S. Wiegand, "Thermal diffusion in liquid mixtures and polymer solutions," *J. Phys.: Condens. Matter*, vol. 16, no. 10, pp. R357–R379, 2004.

[79] S. Duhr and D. Braun, "Why molecules move along a temperature gradient," *Proc. Natl. Acad. Sci.*, vol. 103, no. 52, 2006.

[80] P. Reineck, C. J. Wienken, and D. Braun, "Thermophoresis of single stranded DNA," *Electrophoresis*, vol. 31, 2010.

[81] H. R. Jiang, N. Yoshinaga, and M. Sano, "Active motion of a Janus particle by self-thermophoresis in a defocused laser beam," *Phys. Rev. Lett.*, vol. 105, no. 268302, 2010.

[82] M. Yang and M. Ripoll, "Simulations of thermophoretic nanoswimmers," *Phys. Rev. E*, vol. 84, no. 061401, 2011.

[83] W. Humphrey, A. Dalke, and K. Schulten, "VMD – Visual Molecular Dynamics," *J. Mol. Graph.*, vol. 14, pp. 33–38, 1996.

[84] J. D. Hunter, "Matplotlib: A 2d graphics environment," *Comput. Sci. Eng.*, vol. 9, no. 3, pp. 90–95, 2007.

[85] J. K. G. Dhont, *An Introduction to Dynamics of Colloids.* Elsevier Science B. V., 1996.

[86] S. Kondrat, *Physics of Life - Lecture Notes of the 49th IFF Spring School*, ch. D1 - Physics and modelling of intracellular diffusion. Forschungszentrum Jülich, 2018.

[87] R. G. Winkler, *Physics of Life - Lecture Notes of the 49th IFF Spring School*, ch. E3 - Principles of Active Matter. Forschungszentrum Jülich, 2018.

[88] A. Zöttl and H. Stark, "Emergent behavior in active colloids," *J. Phys.: Condens. Matter*, vol. 28, no. 25, p. 253001, 2016.

[89] S. Das, G. Gompper, and R. G. Winkler, "Confined active brownian particles: theoretical description of propulsion-induced accumulation," *New J. Phys.*, vol. 20, 2018.

[90] K. Franke and H. Gruler, "Galvanotaxis of human granulocytes: electric field jump studies," *Eur. Biophys. J.*, vol. 18, pp. 335–346, 1990.

[91] S. Michelin and E. Lauga, "Phoretic self-propulsion at finite Péclet numbers," *J. Fluid. Mech.*, vol. 747, pp. 572–604, 2014.

[92] N. G. van Kampen, "Diffusion in inhomogeneous media," *J. Phys. Chem. Solids*, vol. 49, no. 6, pp. 673 – 677, 1988.

[93] I. Goldhirsch and D. Ronis, "Theory of thermophoresis. i. general considerations and mode-coupling analysis," *Phys. Rev. A*, vol. 27, no. 3, 1981.

[94] A. W. C. Lau and T. C. Lubensky, "State-dependent diffusion: Thermodynamic consistency and its path integral formulation," *Phys. Rev. E*, vol. 76, p. 011123, 2007.

[95] R. E. Mortensen, "Mathematical problems of modeling stochastic nonlinear dynamic systems," *J. Stat. Phys.*, vol. 1, no. 2, pp. 271–296, 1969.

[96] N. G. van Kampen, "Itô versus stratonovich," *J. Stat. Phys.*, vol. 24, no. 1, pp. 175–187, 1981.

[97] M. Widder and U. Titulaer, "Brownian motion in a medium with inhomogeneous temperature," *Physica A*, vol. 154, no. 3, pp. 452 – 466, 1989.

[98] U. M. Titulaer, "A systematic solution procedure for the Fokker-Planck equation of a Brownian particle in the high-friction case," *Physica A*, vol. 91, no. 3, pp. 321 – 344, 1978.

[99] N. G. van Kampen, "Relative stability in nonuniform temperature," *IBM J. Res. Dev.*, vol. 32, no. 1, pp. 107–111, 1988.

[100] M. Yang and M. Ripoll, "Brownian motion in inhomogeneous suspensions," *Phys. Rev. E*, vol. 87, p. 062110, 2013.

[101] J. K. G. Dhont, "Thermodiffusion of interacting colloids. ii. a microscopic approach," *J. Chem. Phys.*, vol. 120, 2004.

[102] M. Yang and M. Ripoll, “Driving forces and polymer hydrodynamics in the Soret effect,” *J. Phys.: Condens. Matter*, vol. 24, no. 19, p. 195101, 2012.

[103] F. Jülicher and J. Prost, “Generic theory of colloidal transport,” *Eur. Phys. J. E*, vol. 29, no. 1, pp. 27–36, 2009.

[104] A. Fick, “V. on liquid diffusion,” *Philos. Mag.*, vol. 10, no. 63, pp. 30–39, 1855.

[105] S. R. de Groot and P. Mazur, *Non-Equilibrium Thermodynamics.* Dover, 1962.

[106] M. Yang and M. Ripoll, “Drift velocity in non-isothermal inhomogeneous systems,” *J. Chem. Phys.*, vol. 136, no. 20, p. 204508, 2012.

[107] G. Jacucci and I. R. McDonald, “Structure and diffusion in mixtures of rare-gas liquids,” *Physica A*, vol. 80, no. 6, pp. 607 – 625, 1975.

[108] M. Wagner, *Colloidal Microswimmers driven by Thermophoresis.* PhD thesis, Mathematisch-Naturwissenschaftlichen Fakultät, Universität zu Köln, 2017.

[109] E. Bringuier, “On the notion of thermophoretic velocity,” *Philos. Mag.*, vol. 87, no. 6, pp. 873–883, 2007.

[110] D. Lüsebrink, M. Yang, and M. Ripoll, “Thermophoresis of colloids by mesoscale simulations,” *J. Phys.: Condens. Matter*, vol. 24, no. 28, 2012.

[111] M. Theers, *Mesoscale hydrodynamic simulations – From a single colloid to the collective dynamics of microswimmers.* PhD thesis, Fakultät für Mathematik, Informatik und Naturwissenschaften der RWTH Aachen Universität, 2017.

[112] P. Kundu, I. Cohen, and D. Dowling, *Fluid Mechanics.* Academic Press, 6th ed., 2015.

[113] G. G. Stokes, “On the effect of the internal friction of fluids on the motion of pendulums,” *Trans. Cambridge Philos. Soc.*, vol. 9, pp. 8–106, 1851.

[114] G. K. Batchelor, *An Introduction to Fluid Dynamics.* Cambridge: Cambridge University Press, 1967.

[115] J. Lighthill, *Mathematical Biofluiddynamics.* SIAM, Philadelphia, 1975.

[116] C. Brennen and H. Winet, “Fluid mechanics of propulsion by cilia and flagella,” *Annu. Rev. Fluid Mech.*, vol. 9, pp. 339–398, 1977.

[117] L. J. Fauci and R. Dillon, "Biofluidmechanics of reproduction," *Annu. Rev. Fluid Mech.*, vol. 38, pp. 371–394, 2006.

[118] A. J. Chorin and J. E. Marsden, *A Mathematical Introduction to Fluid Mechanics*. Springer-Verlag New York Inc., 2000.

[119] A. Sommerfeld, "A contribution to hydrodynamic explanation of turbulent fluid motions," *International Congress of Mathematicians*, vol. 3, pp. 116–124, 1908.

[120] O. Reynolds, "XXIX. an experimental investigation of the circumstances which determine whether the motion of water shall be direct or sinuous, and of the law of resistance in parallel channels," *Philos. Trans. R. Soc.*, vol. 174, pp. 935–982, 1883.

[121] N. Rott, "Note on the history of the reynolds number," *Annu. Rev. Fluid Mech.*, vol. 22, no. 1, pp. 1–12, 1990.

[122] M. Ripoll, K. Mussawisade, R. G. Winkler, and G. Gompper, "Dynamic regimes of fluids simulated by multiparticle-collision dynamics," *Phys. Rev. E*, vol. 72, p. 016701, 2005.

[123] J. C. Dixon, *The Shock Absorber Handbook*. John Wiley & Sons, Ltd, 2nd edition ed., 2007.

[124] J. T. Padding and A. A. Louis, "Hydrodynamic interactions and Brownian forces in colloidal suspensions: Coarse-graining over time and length scales," *Phys. Rev. E*, vol. 72, p. 031402, 2006.

[125] Y. Zhang, R. Qin, and D. R. Emerson, "Lattice Boltzmann simulation of rarefied gas flows in microchannels," *Phys. Rev. E*, vol. 71, p. 047702, 2005.

[126] T. M. Squires and S. R. Quake, "Microfluidics: Fluid physics at the nanoliter scale," *Rev. Mod. Phys.*, vol. 77, pp. 977–1026, 2005.

[127] M. Yang and M. Ripoll, "Thermophoretically induced flow field around a colloidal particle," *Soft Matter*, vol. 9, pp. 4661–4671, 2013.

[128] A. Malevanets and R. Kapral, "Mesoscopic model for solvent dynamics," *J. Chem. Phys.*, vol. 110, pp. 8605–8613, 1999.

[129] S. Chen and G. D. Doolen, "Lattice Boltzmann method for fluid flows," *Annu. Rev. Fluid Mech.*, vol. 30, no. 1, pp. 329–364, 1998.

[130] R. R. Nourgaliev, T. N. Dinh, T. G. Theofanous, and D. Joseph, "The Lattice Boltzmann equation method: theoretical interpretation, numerics and implications," *Int. J. Multiph. Flow*, vol. 29, no. 1, pp. 117–169, 2003.

[131] U. D. Schiller, T. Krüger, and O. Henrich, "Mesoscopic modelling and simulation of soft matter," *Soft Matter*, vol. 14, pp. 9–26, 2018.

[132] G. R. McNamara and G. Zanetti, "Use of the Boltzmann equation to simulate Lattice-Gas Automata," *Phys. Rev. Lett.*, vol. 61, pp. 2332–2335, 1988.

[133] J. Hardy, Y. Pomeau, and O. de Pazzis, "Time evolution of a two-dimensional classical lattice system," *Phys. Rev. Lett.*, vol. 31, pp. 276–279, 1973.

[134] J. Hardy, Y. Pomeau, and O. de Pazzis, "Time evolution of a two-dimensional model system. i. invariant states and time correlation functions," *J. Math. Phys.*, vol. 14, no. 12, pp. 1746–1759, 1973.

[135] U. Frisch, B. Hasslacher, and Y. Pomeau, "Lattice-Gas Automata for the Navier-Stokes equation," *Phys. Rev. Lett.*, vol. 56, no. 14, pp. 1505–1508, 1986.

[136] J. P. Boon, *Lattice Gas Automaton Methods*, pp. 2805–2809. Dordrecht: Springer Netherlands, 2005.

[137] X. He and L.-S. Luo, "Theory of the Lattice Boltzmann method: From the Boltzmann equation to the lattice Boltzmann equation," *Phys. Rev. E*, vol. 56, pp. 6811–6817, 1997.

[138] P. J. Hoogerbrugge and J. M. V. A. Koelman, "Simulating microscopic hydrodynamic phenomena with dissipative particle dynamics," *EPL*, vol. 19, no. 3, pp. 155–160, 1992.

[139] P. Español and P. Warren, "Statistical mechanics of dissipative particle dynamics," *EPL*, vol. 30, no. 4, pp. 191–196, 1995.

[140] J. Bonet-Avalós and A. D. Mackie, "Dissipative particle dynamics with energy conservation," *EPL*, vol. 40, no. 2, pp. 141–146, 1997.

[141] P. Español, "Dissipative particle dynamics with energy conservation," *EPL*, vol. 40, no. 6, pp. 631–636, 1997.

[142] M. Ripoll, P. Español, and M. H. Ernst, "Dissipative particle dynamics with energy conservation: Heat conduction," *Int. J. Mod. Phys. C*, vol. 09, no. 08, pp. 1329–1338, 1998.

[143] A. Malevanets and R. Kapral, “Solute molecular dynamics in a mesoscale solvent,” *J. Chem. Phys.*, vol. 112, no. 7260, 2000.

[144] E. Allahyarov and G. Gompper, “Mesoscopic solvent simulations: Multiparticle-collision dynamics of three-dimensional flows,” *Phys. Rev. E*, vol. 66, no. 036702, 2002.

[145] R. Kapral, “Multiparticle collision dynamics: simulation of complex systems on mesoscale,” *Adv. Chem. Phys.*, vol. 140, no. 89, 2008.

[146] G. Gompper, T. Ihle, D. Kroll, and R. Winkler, *Advanced Computer Simulation Approaches for Soft Matter Sciences III*, vol. Advances in Polymer Science, 221 of *Advanced Computer Simulation Approaches for Soft Matter Sciences III*, pp. 1–87. Springer Berlin Heidelberg, 2009.

[147] T. Ihle and D. M. Kroll, “Stochastic rotation dynamics: A Galilean-invariant mesoscopic model for fluid flow,” *Phys. Rev. E*, vol. 63, no. 020201, 2001.

[148] T. Ihle and D. M. Kroll, “Stochastic rotation dynamics. I. formalism, Galilean invariance, and Green-Kubo relations,” *Phys. Rev. E*, vol. 67, p. 066705, 2003.

[149] A. Lamura, G. Gompper, T. Ihle, and D. M. Kroll, “Multi-particle collision dynamics: Flow around a circular and a square cylinder,” *EPL*, vol. 56, no. 3, pp. 319–325, 2001.

[150] D. Lüsebrink and M. Ripoll, “Temperature inhomogeneities simulated with multiparticle-collision dynamics,” *J. Chem. Phys.*, vol. 136, no. 8, p. 084106, 2012.

[151] F. Müller-Plathe, “A simple nonequilibrium molecular dynamics method for calculating the thermal conductivity,” *J. Chem. Phys.*, vol. 106, no. 14, pp. 6082–6085, 1997.

[152] N. Kikuchi, C. M. Pooley, J. F. Ryder, and J. M. Yeomans, “Transport coefficients of a mesoscopic fluid dynamics model,” *J. Chem. Phys.*, vol. 119, no. 12, pp. 6388–6395, 2003.

[153] E. Tüzel, S. M., T. Ihle, and D. M. Kroll, “Transport coefficients for stochastic rotation dynamics in three dimensions,” *Phys. Rev. E*, vol. 68, no. 036701, 2003.

[154] T. Ihle, E. Tüzel, and D. M. Kroll, “Equilibrium calculation of transport coefficients for a fluid-particle model,” *Phys. Rev. E*, vol. 72, p. 046707, 2005.

[155] E. Tüzel, T. Ihle, and D. M. Kroll, "Dynamic correlations in stochastic rotation dynamics," *Phys. Rev. E*, vol. 74, p. 056702, 2006.

[156] C. C. Huang, A. Chatterji, G. Sutmann, G. Gompper, and R. G. Winkler, "Cell-level canonical sampling by velocity scaling for multiparticle collision dynamics simulations," *J. Comput. Phys.*, vol. 229, no. 1, pp. 168–177, 2010.

[157] J. F. Ryder, *Mesoscopic simulations of complex fluids.* PhD thesis, University of Oxford, United Kingdom, 2005.

[158] C. M. Pooley and J. M. Yeomans, "Kinetic theory derivation of the transport coefficients of stochastic rotation dynamics," *J. Phys. Chem. B*, vol. 109, pp. 6505–6513, 2005.

[159] I. O. Götze, H. Noguchi, and G. Gompper, "Relevance of angular momentum conservation in mesoscale hydrodynamics simulations," *Phys. Rev. E*, vol. 76, no. 046705, 2007.

[160] H. Noguchi and G. Gompper, "Transport coefficients of off-lattice mesoscale-hydrodynamics simulation techniques," *Phys. Rev. E*, vol. 78, no. 016706, 2008.

[161] M. Yang, R. Liu, M. Ripoll, and K. Chen, "A microscale thermophoretic turbine driven by external diffusive heat flux," *Nanoscale*, vol. 6, no. 13550, 2014.

[162] R. B. Bird, E. S. Warren, and E. N. Lightfoot, *Transport Phenomena, Revised 2nd Edition.* Wiley, 2002.

[163] G. F. Hewitt, G. L. Shires, and T. R. Bott, *Process heat transfer.* Boca Raton, CRC Press, Begell House, 1994.

[164] L. Verlet, "Computer "experiments" on classical fluids. I. thermodynamical properties of lennard-jones molecules," *Phys. Rev.*, vol. 159, no. 98, 1967.

[165] D. Frenkel and B. Smit, *Understanding molecular simulations.* Academic Press, 1996.

[166] M. P. Allen and D. J. Tildesley, *Computer Simulation of Liquids.* Oxford University Press, 2nd edition ed., 2017.

[167] M. P. Allen, *Introduction to Molecular Dynamics Simulation*, vol. 23 of *NIC*. John von Neumann Institute for Computing, Jülich, 2004.

[168] J. P. Mahalik, B. Hildebrandt, and M. Muthukumar, "Langevin dynamics simulation of DNA ejection from a phage," *J. Biol. Phys.*, vol. 39, 2013.

[169] W. C. Swope and D. M. Ferguson, “Alternative expressions for energies and forces due to angle bending and torsional energy,” *J. Comp. Chem.*, vol. 13, 1992.

[170] V. L. Kulinskii, “The Vliegenthart-Lekkerkerker relation: The case of the Mie-fluids,” *J. Chem. Phys.*, vol. 134, 2011.

[171] J. E. Lennard-Jones, “On the determination of molecular fields,” *Proc. R. Soc. Lond. A*, vol. 106, no. 738, pp. 463–477, 1924.

[172] J. D. Weeks, D. Chandler, and H. C. Andersen, “Role of repulsive forces in determining the equilibrium structure of simple liquids,” *J. Chem. Phys.*, vol. 54, 1971.

[173] H. N. W. Lekkerkerker and R. Tuinier, *Colloids and the Depletion Interaction.* Springer Science+Business Media B. V., 2011.

[174] T. N. Shendruk, M. Bertrand, J. L. Harden, G. W. Slater, and H. W. de Haan, “Coarse-grained molecular dynamics simulations of depletion-induced interactions for soft matter systems,” *J. Chem. Phys.*, vol. 141, no. 244910, 2014.

[175] S. Asakura and F. Oosawa, “On interaction between two bodies immersed in a solution of macromolecules,” *J. Chem. Phys.*, vol. 22, no. 7, pp. 1255–1256, 1954.

[176] S. Asakura and F. Oosawa, “Interaction between particles suspended in solutions of macromolecules,” *J. Polym. Sci.*, vol. 33, no. 126, pp. 183–192, 1958.

[177] T. Biben, P. Bladon, and D. Frenkel, “Depletion effects in binary hard-sphere fluids,” *J. Phys.: Condens. Matter*, vol. 8, no. 50, pp. 10799–10821, 1996.

[178] Y. Mao, M. E. Cates, and H. N. W. Lekkerkerker, “Depletion force in colloidal systems,” *Physica A*, vol. 222, no. 1, pp. 10–24, 1995.

[179] C. Bechinger, D. Rudhardt, P. Leiderer, R. Roth, and S. Dietrich, “Understanding depletion forces beyond entropy,” *Phys. Rev. Lett.*, vol. 83, pp. 3960–3963, 1999.

[180] M. Wagner and M. Ripoll, “Hydrodynamic front-like swarming of phoretically active dimeric colloids,” *EPL*, vol. 119, p. 66007, 2017.

[181] M. Wagner and M. Ripoll, “Solvent-induced depletion interactions in multiparticle collision dynamic simulations,” *Int. J. Mod. Phys. C*, vol. 30, 2019.

[182] D. Lüsebrink and M. Ripoll, "Collective thermodiffusion of colloidal suspensions," *J. Chem. Phys.*, vol. 137, no. 194904, 2012.

[183] M. Ripoll, R. G. Winkler, and G. Gompper, "Star polymers in shear flow," *Phys. Rev. Lett.*, vol. 96, p. 188302, 2006.

[184] S. Plimpton, "Fast parallel algorithms for short-range molecular dynamics," *J. Comput. Phys.*, vol. 117, 1995.

[185] M. K. Petersen, J. B. Lechman, S. J. Plimpton, G. S. Grest, P. J. in't Veld, and P. R. Schunk, "Mesoscale hydrodynamics via stochastic rotation dynamics: Comparison with lennard-jones fluid," *J. Chem. Phys.*, vol. 132, no. 174106, 2010.

[186] A. Rojnuckarin, S. Kim, and S. Subramaniam, "Brownian dynamics simulations of protein folding: Access to milliseconds time scale and beyond," *Proc. Natl. Acad. Sci.*, vol. 95, no. 8, pp. 4288–4292, 1998.

[187] H. Behringer and R. Eichhorn, "Brownian dynamics simulations with hard-body interactions: Spherical particles," *J. Chem. Phys.*, vol. 137, no. 16, p. 164108, 2012.

[188] F. Höfling and T. Franosch, "Anomalous transport in the crowded world of biological cells," *Rep. Prog. Phys.*, vol. 76, no. 4, p. 046602, 2013.

[189] M. Aznar, S. Roca-Bonet, and D. Reguera, "Viral nanomechanics with a virtual atomic force microscope," *J. Phys.: Condens. Matter*, vol. 30, no. 26, pp. 264001–264001, 2018.

[190] G. A. Huber and J. A. McCammon, "Brownian dynamics simulations of biological molecules," *Trends Chem.*, vol. 1, no. 8, pp. 727–738, 2019.

[191] M. Yang, M. Theers, J. Hu, G. Gompper, R. G. Winkler, and M. Ripoll, "Effect of angular momentum conservation on hydrodynamic simulations of colloids," *Phys. Rev. E*, vol. 92, no. 013301, 2015.

[192] J. P. Hansen and I. R. McDonald, *Theory of Simple Liquids.* Academic Press, 4th ed., 2013.

[193] O. Pohl and H. Stark, "Dynamic clustering and chemotactic collapse of self-phoretic active particles," *Phys. Rev. Lett.*, vol. 112, p. 238303, 2014.

[194] T. Speck, "Collective behavior of active Brownian particles: From microscopic clustering to macroscopic phase separation," *Eur. Phys. J. Spec. Top.*, vol. 225, no. 11, pp. 2287–2299, 2016.

[195] F. Peruani and L. G. Morelli, “Self-propelled particles with fluctuating speed and direction of motion in two dimensions,” *Phys. Rev. Lett.*, vol. 99, p. 010602, 2007.

[196] R. Golestanian, “Anomalous diffusion of symmetric and asymmetric active colloids,” *Phys. Rev. Lett.*, vol. 102, p. 188305, 2009.

[197] S. Thakur and R. Kapral, “Dynamics of self-propelled nanomotors in chemically active media,” *J. Chem. Phys.*, vol. 135, p. 024509, 2011.

[198] M. N. Popescu, M. Tasinkevych, and S. Dietrich, “Pulling and pushing a cargo with a catalytically active carrier,” *EPS*, vol. 95, no. 28004, 2011.

[199] S. Y. Reigh and R. Kapral, “Catalytic dimer nanomotors: continuum theory and microscopic dynamics,” *Soft Matter*, vol. 12, pp. 3149–3158, 2015.

[200] G. S. Klindt and B. M. Friedrich, “Flagellar swimmers oscillate between pusher- and puller-type swimming,” *Phys. Rev. E*, vol. 92, no. 063019, 2015.

[201] E. Lushi, V. Kantsler, and R. E. Goldstein, “Scattering of biflagellate microswimmers from surfaces,” *Phys. Rev. E*, vol. 96, no. 023102, 2017.

[202] G. S. Klindt, *Hydrodynamics of flagellar swimming and synchronization.* PhD thesis, Technische Universität Dresden, 2018.

[203] K. Drescher, J. Dunkel, L. H. Cisneros, S. Ganguly, and R. E. Goldstein, “Fluid dynamics and noise in bacterial cell–cell and cell–surface scattering,” *Proc. Natl. Acad. Sci.*, vol. 108, no. 27, 2011.

[204] J. Hu, M. Yang, G. Gompper, and R. G. Winkler, “Modelling the mechanics and hydrodynamics of swimming E. coli,” *Soft Matter*, vol. 11, 2015.

[205] I. O. Götze and G. Gompper, “Mesoscale simulations of hydrodynamic squirmer interactions,” *Phys. Rev. E*, vol. 82, no. 041921, 2010.

[206] M. E. Cates and J. Tailleur, “Motility-induced phase separation,” *Annu. Rev. Condens. Matter Phys.*, vol. 6, no. 1, pp. 219–244, 2015.

[207] I. Theurkauff, C. Cottin-Bizonne, J. Palacci, C. Ybert, and L. Bocquet, “Dynamic clustering in active colloidal suspensions with chemical signaling,” *Phys. Rev. Lett.*, vol. 108, p. 268303, 2012.

[208] S. Thakur and R. Kapral, “Collective dynamics of self-propelled sphere-dimer motors,” *Phys. Rev. E*, vol. 85, no. 026121, 2012.

[209] M. D. Haw, W. C. K. Poon, and P. N. Pusey, “Structure factors from cluster-cluster aggregation simulation at high concentration,” *Physica A*, vol. 208, pp. 8–17, 1994.

[210] F. Alarcón, C. Valeriani, and I. Pagonabarraga, “Morphology of clusters of attractive dry and wet self-propelled spherical particle suspensions,” *Soft Matter*, vol. 13, pp. 814–826, 2017.

[211] Z. Shen and J. S. Lintuvuori, “Hydrodynamic clustering and emergent phase separation of spherical spinners,” *Phys. Rev. Research*, vol. 2, p. 013358, 2020.

[212] M. Wagner, S. Roca-Bonet, and M. Ripoll, “Collective behavior of thermophoretic dimeric active colloids in three-dimensional bulk,” *Eur. Phys. J. E*, vol. 44, no. 3, p. 43, 2021.

[213] P. H. Colberg and R. Kapral, “Many-body dynamics of chemically propelled nanomotors,” *J. Chem. Phys.*, vol. 147, no. 6, p. 064910, 2017.

[214] R. Matas-Navarro, R. Golestanian, T. B. Liverpool, and S. M. Fielding, “Hydrodynamic suppression of phase separation in active suspensions,” *Phys. Rev. E*, vol. 90, p. 032304, 2014.

[215] K. Drescher, K. C. Leptos, I. Tuval, T. Ishikawa, T. J. Pedley, and R. E. Goldstein, “Dancing volvox: Hydrodynamic bound states of swimming algae,” *Phys. Rev. Lett.*, vol. 102, p. 168101, 2009.

[216] B. A. Grzybowski, H. A. Stone, and G. M. Whitesides, “Dynamic self-assembly of magnetized, millimetre-sized objects rotating at a liquid–air interface,” *Nature*, vol. 405, no. 6790, pp. 1033–1036, 2000.

[217] B. A. Grzybowski and G. M. Whitesides, “Dynamic aggregation of chiral spinners,” *Science*, vol. 296, no. 5568, pp. 718–721, 2002.

[218] S. Bleil, D. W. M. Marr, and C. Bechinger, “Field-mediated self-assembly and actuation of highly parallel microfluidic devices,” *Appl. Phys. Lett.*, vol. 88, no. 26, p. 263515, 2006.

[219] B. Kavčič, D. Babič, N. Osterman, B. Podobnik, and I. Poberaj, “Magnetically actuated microrotors with individual pumping speed and direction control,” *Appl. Phys. Lett.*, vol. 95, no. 2, p. 023504, 2009.

[220] N. Elsner, C. P. Royall, B. Vincent, and D. R. E. Snoswell, “Simple models for two-dimensional tunable colloidal crystals in rotating ac electric fields,” *J. Chem. Phys.*, vol. 130, no. 15, p. 154901, 2009.

[221] A. Terray, J. Oakey, and D. W. M. Marr, “Microfluidic control using colloidal devices,” *Science*, vol. 296, no. 5574, pp. 1841–1844, 2002.

[222] G. Quincke, “Ueber rotationen im constanten electrischen felde,” *Ann. Phys.*, vol. 295, no. 11, pp. 417–486, 1896.

[223] A. O. Tsebers, “Internal rotation in the hydrodynamics of weakly conducting dielectric suspensions,” *Fluid Dyn.*, vol. 15, no. 2, pp. 245–251, 1980.

[224] B. Zhang, A. Sokolov, and A. Snezhko, “Reconfigurable emergent patterns in active chiral fluids,” *Nat. Commun.*, vol. 11, no. 1, p. 4401, 2020.

[225] Y. Fily, A. Baskaran, and M. C. Marchetti, “Cooperative self-propulsion of active and passive rotors,” *Soft Matter*, vol. 8, pp. 3002–3009, 2012.

[226] J. E. Scott, V. M. Kenkre, and A. J. Hurd, “Nonlocal approach to the analysis of the stress distribution in granular systems. ii. application to experiment,” *Phys. Rev. E*, vol. 57, pp. 5850–5857, 1998.

[227] G. Coupier, M. Saint Jean, and C. Guthmann, “Single file diffusion in macroscopic wigner rings,” *Phys. Rev. E*, vol. 73, p. 031112, 2006.

[228] L. Giuggioli, J. R. Potts, and S. Harris, “Predicting oscillatory dynamics in the movement of territorial animals,” *J. R. Soc. Interface*, vol. 9, no. 72, pp. 1529–1543, 2012.

[229] L. Van Hove, “Correlations in space and time and born approximation scattering in systems of interacting particles,” *Phys. Rev.*, vol. 95, pp. 249–262, 1954.

[230] A. Rahman, “Correlations in the motion of atoms in liquid argon,” *Phys. Rev.*, vol. 136, pp. A405–A411, 1964.

[231] A. L. Thorneywork, D. G. A. L. Aarts, J. Horbach, and R. P. A. Dullens, “On the gaussian approximation in colloidal hard sphere fluids,” *Soft Matter*, vol. 12, pp. 4129–4134, 2016.

[232] Z. Ghannad, “Fickian yet non-gaussian diffusion in two-dimensional yukawa liquids,” *Phys. Rev. E*, vol. 100, p. 033211, 2019.

Erklärung zur Dissertation
gemäß der Promotionsordnung vom 12. März 2020

"Hiermit versichere ich an Eides statt, dass ich die vorliegende Dissertation selbstständig und ohne die Benutzung anderer als der angegebenen Hilfsmittel und Literatur angefertigt habe. Alle Stellen, die wörtlich oder sinngemäß aus veröffentlichten und nicht veröffentlichten Werken dem Wortlaut oder dem Sinn nach entnommen wurden, sind als solche kenntlich gemacht. Ich versichere an Eides statt, dass diese Dissertation noch keiner anderen Fakultät oder Universität zur Prüfung vorgelegen hat; dass sie - abgesehen von unten angegebenen Teilpublikationen und eingebundenen Artikeln und Manuskripten - noch nicht veröffentlicht worden ist sowie, dass ich eine Veröffentlichung der Dissertation vor Abschluss der Promotion nicht ohne Genehmigung des Promotionsausschusses vornehmen werde. Die Bestimmungen dieser Ordnung sind mir bekannt. Darüber hinaus erkläre ich hiermit, dass ich die Ordnung zur Sicherung guter wissenschaftlicher Praxis und zum Umgang mit wissenschaftlichem Fehlverhalten der Universität zu Köln gelesen und sie bei der Durchführung der Dissertation zugrundeliegenden Arbeiten und der schriftlich verfassten Dissertation beachtet habe und verpflichte mich hiermit, die dort genannten Vorgaben bei allen wissenschaftlichen Tätigkeiten zu beachten und umzusetzen. Ich versichere, dass die eingereichte elektronische Fassung der eingereichten Druckfassung vollständig entspricht."

(Ort, Datum)	Sergi Roca Bonet

Teilpublikation

[1] M. Wagner, S. Roca-Bonet, M. Ripoll, "Collective behavior of thermophoretic dimeric active colloids in three-dimensional bulk", *Eur. Phys. J. E*, **44**, 3 (2021).

[2] S. Roca-Bonet, M. Wagner, M. Ripoll, "Hydrodynamic effect on the clustering of self-thermophilic asymmetric dimers", *to be submitted*, 2021.

[3] S. Roca-Bonet, M. Wagner, M. Ripoll, "Collective swimming of multimeric self-propelled thermophobic colloids", *in preparation*, 2021.

[4] S. Roca-Bonet, J. Oller, M. Ripoll, "Interplay of geometry and hydrodynamics on the aggregation of thermophilic multimeric self-propelled colloidal swimmers", *in preparation*, 2021.

Sergi Roca Bonet

Curriculum Vitae

Personal information

Birthdate: **14th of September 1994**.
Birthplace: **Barcelona**, *Spain*.

Education

Sept. 2017 – June 2021 **Ph.D. in Theoretical Physics**, Forschungszentrum Jülich, Jülich and Universität zu Köln, Cologne, Germany.

- **Ph.D. Thesis:** "*Thermophoretic microswimmers: Interplay of phoresis, geometry and hydrodynamics*," under supervision of **PD Dr. Marisol Ripoll**

Oct. 2016 – July 2017 **M.Sc. in Atomistic and Multiscale Computational Modelling in Physics, Chemistry and Biochemistry**, Universitat de Barcelona and Universitat Politècnica de Catalunya, Barcelona, Spain.

- **M.Sc. Thesis:** "*Translocation of a polymer chain using Brownian Dynamics simulations*," under supervision of **Prof. Dr. David Reguera López**

Sept. 2012 – July 2016 **B.Sc. in Physics**, Universitat de Barcelona, Barcelona, Spain.

- **B.Sc. Thesis:** "*Evaluation of the binding energy of viral capsid proteins using a Virtual AFM*," under supervision of **Prof. Dr. David Reguera López**

Sept. 2006 – June 2012 **High school and pre-university**, ICCIC Escola Thau and ICCIC Batxillerats, Barcelona, Spain.

Publications

- M. Aznar, S. Roca-Bonet, D. Reguera, "Viral nanomechanics with a virtual atomic force microscope", *J. Phys.: Condens. Matter*, **30**, 26, pp. 264001-264001 (2018).
- M. Wagner, S. Roca-Bonet, M. Ripoll, "Collective behavior of thermophoretic dimeric active colloids in three-dimensional bulk", *Eur. Phys. J. E*, **44**, 3, p. 43 (2021).

- S. Roca-Bonet, M. Wagner, M. Ripoll, “Hydrodynamic effect on the clustering of self-thermophilic asymmetric dimers”, *to be submitted* (2021).
- S. Roca-Bonet, M. Wagner, M. Ripoll, “Collective swimming of multimeric self-propelled thermophobic colloids”, *in preparation* (2021)
- S. Roca-Bonet, J. Oller, M. Ripoll, “Interplay of geometry and hydrodynamics on the aggregation of thermophilic multimeric self-propelled colloidal swimmers”, *in preparation* (2021).